An Investigation of Isotropic and Anisotropic Magnetic Field Effects in Fluorescent Systems

by

Kelly-Anne Ferguson

A Thesis Submitted for

The Final Honour School of Natural Science:

D.Phil Thesis

Trinity 2013

University of Oxford
Inorganic Chemistry Laboratory and Magdalen College

The most difficult thing is the decision to act, the rest is merely tenacity. The fears are paper tigers. You can do anything you decide to do. You can act to change and control your life; and the procedure, the process is its own reward. - *Amelia Earhart*

To my brothers and sister, TJ, Charlie and Wendy. This is for you. To show you that anything in life is possible when you put your mind to it. It does not matter where you were born, and who you were born to but what you do with the rest of your life. I am proud of you all, for what you have achieved in life and the hardships you have overcome. Never stop believing. Lots of love, Big Sis.

An Investigation of Isotropic and Anisotropic Magnetic Field Effects in Fluorescent Systems

Kelly-Anne Ferguson
A thesis submitted for the degree of Doctor of Philosophy
Trinity Term 2013
University of Oxford

Abstract

Interest into the effects of weak static magnetic fields on chemical reactions involving spin correlated radical pairs has increased over the last few decades, particularly as scientists have become more curious about the mechanisms by which animals can sense and respond to small variations in the Earth's weak (50 μT) magnetic field. The magnetosensitivity of radical pairs, as dictated by the radical pair mechanism, lies at the heart of the most heavily supported hypothesis of this magnetoreception phenomenon.

This thesis is concerned with the spectroscopic investigations of isotropic and anisotropic magnetic field effects in fluorescent systems. First of all, an introduction to spin chemistry and magnetoreception is presented. In chapter 3, the effects of weak radiofrequency oscillating fields when applied in combination with weak static fields are explored in isotropic solutions. The validity of the high-field model, typically used to describe spin dynamics in magnetic resonance, is tested and the effects of orientation and field strength on magnetic field effects are discussed in detail.

In Chapter 4, a range of exciplex systems are studied by fluorescence methods and their energetics are explored. The factors which determine the formation of an exciplex, i.e. the complex equilibrium between the exciplex and the spin-correlated radical pair, are considered and used to assess the existence and magnitude of MFEs.

Radical pair systems investigated, using MARY spectroscopy, with respect to their potential to act as model chemical compasses are introduced in chapter 5. Solid-state media are used to align the exciplex systems to detect any magnetic field direction dependence. Finally, in chapter 6, AMELIA, an experiment which can directly measure the anisotropic magnetic field response of a system, is presented and applied successfully to systems to detect directly the anisotropic field response of a photoexcited anthracene crystal.

Acknowledgements

I must first express my sincere thanks to my supervisor, Christiane Timmel, who welcomed me into her group and has supported me throughout. For her efforts, suggestions and for guiding me through my work. Without her constant encouragement for me to strive to be my best this thesis would not be as significant. I have been truly blessed to have had such an amazing person in my life, not just a supervisor but also a friend.

I owe much gratitude to everyone in the Timmel group, past and present, for making the last 5 years very enjoyable. It has been so much fun and I will cherish the fond memories of our time together. Particularly the soup kitchen and the plethora of conversations that have left me in fits of laughter. A special mention must go to the following people:

- Kim and Kevin for their continuous support in the lab. Kevin for help and discussion with optics and experiments and Kim for very helpful discussions about spin chemistry.
- Jonathan for his help with the AMELIA work and for sharing his expertise in Matlab coding.
- Claudia, for help with DFT calculations and also for proof reading parts of this thesis. Thank you for all of the delicious cakes!
- Emrys and Neil for proof reading parts of my thesis and for your general camaraderie.
- Jason for all his help with the simulations of RYDMR spectra and discussions.
- Christopher Wedge for mentoring me through my initial years in the Timmel group and for help with my RYDMR work.
- Pip and Matthew for help collecting data during their Part II year.
- Simon, just so he knows that I will never forget our pact.
- Last but not least, Alice, for help with DFT and many more things which would be exhausting to list. But most of all for being a great friend through the years.

To Rachel Bull, you are the best wifey a girl could ask for. You were always there to pick me up when work got too much. Be it a cup of tea or a glass of wine. It's been fantastic knowing you. We otter be friends forever!

Last but not least OUWRFC and Henley Hawks RFC, without you I would have gone insane!

Contents

1 An Introduction to Spin Chemistry **1**
1.1 Spin . . . 2
1.1.1 Properties of Spin . . . 2
1.1.2 Interaction with a Magnetic Field . . . 3
1.1.3 Corrections to the g-Factor . . . 4
1.1.4 Coupling of Spins . . . 5
1.2 The Spin Hamiltonian . . . 8
1.2.1 Spin Operators . . . 8
1.2.2 Zeeman Interaction . . . 10
1.2.3 Hyperfine Interaction . . . 11
1.2.4 Coupling Between Electron Spins . . . 13
1.3 The Radical Pair Mechanism . . . 16
1.3.1 Radical Pair Formation . . . 16
1.3.2 Radical Pair Diffusion and Recombination . . . 17
1.4 Magnetic Field Effects . . . 18
1.4.1 Zeeman Mechanism . . . 18
1.4.2 Hyperfine Mechanism . . . 19
1.4.3 Δg Mechanism . . . 20
1.4.4 The Low Field Effect . . . 21
1.4.5 Relaxation Mechanism . . . 22
1.4.6 Oscillating Magnetic Field Effects . . . 23
1.4.7 Magnetic Field Effects: An Overview . . . 24

2 Introduction to Animal Migration **25**
2.1 The Geomagnetic Field: What We Know . . . 26
2.2 Inclination Compass . . . 28
2.3 Mechanisms of Magnetoreception . . . 29
2.3.1 Magnetite . . . 30
2.3.2 Radical Pair Mechanism . . . 31
2.4 Evidence Supporting the Radical Pair Mechanism . . . 33
2.4.1 Wavelength-dependence . . . 33
2.4.2 The Effects of Radio Frequency Fields . . . 34
2.4.3 Overview . . . 35

3 Rotary RYDMR **37**
3.1 Introduction . . . 37
3.1.1 Theory . . . 39
3.1.2 Spin-Locking . . . 42
3.1.3 Experimental . . . 45

3.1.4 The Coils . . . 46
3.1.5 The RF system . . . 47
3.1.6 Sensitivity . . . 48
3.1.7 Static Field Strength . . . 49
3.1.8 Oscillating Field Strength . . . 49
3.2 Systems studied . . . 50
3.3 Theoretical Methods . . . 51
3.3.1 γ-COMPUTE . . . 51
3.4 Results and Discussion . . . 54
3.5 Conclusion . . . 81

4 Exploring New Exciplex Systems 85
4.1 Optical Spectroscopy . . . 86
4.1.1 Ground State UV/Vis Absorption Spectroscopy . . . 86
4.1.2 Steady State Fluorescence Emission Spectra . . . 86
4.2 MARY . . . 87
4.2.1 Introduction . . . 87
4.2.2 The Technique of Magnetically Altered Reaction Yield Experiments 88
4.2.3 Modulation Techniques . . . 89
4.2.4 MARY Plots . . . 90
4.2.5 Electron Self Exchange . . . 91
4.2.6 Experimental Apparatus . . . 93
4.3 Results and Discussions . . . 96
4.3.1 Polyarenes . . . 96
4.3.2 Energetics of Photoinduced Electron Transfers . . . 102
4.3.3 Frontier Molecular Orbital Theory for Photoinduced Electron Transfer Reactions . . . 108
4.4 Conclusion . . . 117

5 Exploring New Chemical Compass Systems 119
5.1 Introduction . . . 120
5.1.1 Photoselection . . . 120
5.1.2 Liquid Crystals . . . 121
5.1.3 Polymers . . . 122
5.1.4 Single Crystals . . . 122
5.2 Experimental Considerations . . . 124
5.2.1 Liquid Crystals . . . 124
5.2.2 Polymers . . . 126
5.2.3 Anthracene Single Crystals . . . 129
5.3 Results . . . 130
5.3.1 Pyrene/DCB in a Glass Matrix . . . 130
5.3.2 Liquid Crystals . . . 132
5.3.3 Polymers . . . 139
5.3.4 Single Crystals . . . 148
5.4 Conclusion . . . 155

6 AMELIA **159**
6.1 Experimental Procedure . . . 160
6.1.1 The Coils . . . 161
6.1.2 The Frequency Generator and Field Box . . . 164
6.1.3 The Graphical User Interface . . . 164
6.2 Calibration . . . 165
6.2.1 Static Field Strength . . . 165
6.2.2 Lock-In Amplifier Settings . . . 166
6.3 Preliminary Results . . . 168
6.4 Conclusion . . . 176

A RotRYDMR Data **179**

B RYDMR Data **187**

C Modulation Techniques **195**

D Fluorescence **199**

E Hyperfine Coupling Data **205**

F Matlab Code for Calculating Maximum Overlap **207**

G HOMO and LUMO 2-D Contour Plots **219**

H Exciplex Geometry **221**

I Photoselection **229**

Chapter 1

An Introduction to Spin Chemistry

In the 1920s experimental evidence arose which proved the existence of a previously unrecognised property of the electron. A high resolution emission spectrum of hydrogen showed unexpected, closely spaced splitting of the lines, called fine structure. After analysing these results Uhlenbeck and Goudsmit [1] proposed that the electron must possess an extra degree of freedom, an intrinsic angular momentum. This realisation shed some light on an experiment performed several years earlier by Stern and Gerlach [2] which also proved the existence of quantised spin angular momentum resulting from unpaired electrons. This experiment consisted of preparing a beam of silver atoms and passing them through a strong, inhomogeneous magnetic field. Stern and Gerlach found that the beam was deflected into two directions and ascribed this effect to the existence of an half-integer quantum number describing the intrinsic spin angular momentum.

Both of these experimental scenarios were consistent with the possession of an intrinsic angular momentum and a magnetic moment by individual electrons. This fundamental quantum-mechanical property came to be known as 'spin' and is intrinsic to the electron as well as other elementary particles.

1.1 Spin

1.1.1 Properties of Spin

The spin of a particle is a form of angular momentum which is purely quantum mechanical in origin. Analogous to other forms of angular momentum, spin can be described by a vector, $\boldsymbol{s}$, whose magnitude is given by;

$$|\boldsymbol{s}| = \hbar\sqrt{s(s+1)} \tag{1.1}$$

where s is the *spin quantum number* which may take integer or half-integral values. The projection of s onto a given axis (conventionally the z-axis) is given by $\hbar m_s$; the component, m_s, of the spin vector onto this axis can only take up a set of discrete values given by $+s, (s-1), ..., (-s+1), -s$. The spin magnetic quantum number, m_s, may therefore have $2s+1$ values.

The electron spin has a quantum number, $s = \frac{1}{2}$ giving rise to two states; $m_s = +\frac{1}{2}$, denoted α or 'spin-up' and $m_s = -\frac{1}{2}$, denoted β or 'spin-down'. For an electron in an atom or molecule there is a magnetic moment associated with its orbital angular momentum. The magnetic dipole moment, μ_l, resulting from the electron's orbital momentum, l, is given by

$$\boldsymbol{\mu}_l = \gamma_e \boldsymbol{l} \quad \text{where} \quad \gamma_e = -\frac{e}{2m_e} \tag{1.2}$$

where γ_e is the magnetogyric ratio of the electron, e is the charge of the electron and m_e is the mass of the electron. Quantisation of the orbital momentum results in the z-component of the electron's orbital magnetic moment, $\boldsymbol{\mu}_{z,l}$, also being quantised; it may take the following values

$$\mu_{z,l} = \gamma_e \hbar m_l = -\mu_B m_l \tag{1.3}$$

where m_l is the magnetic quantum number corresponding to l and μ_B is the Bohr magneton.

$$\mu_B = \frac{e\hbar}{2m_e} \tag{1.4}$$

The magnetic moment, $\boldsymbol{\mu}_s$[1], associated with the spin angular momentum, s, of the electron is similar but with the additional inclusion of g_e, the g-factor for a free electron (the g-factor will later be discussed in Section 1.1.3). This is included to account for the quantum mechanical properties of the electron:

$$\boldsymbol{\mu}_s = \frac{-g_e \mu_B \boldsymbol{s}}{\hbar} \tag{1.5}$$

and hence, by analogy with orbital angular momentum

$$\mu_z = -g_e \mu_B m_s \tag{1.6}$$

where $g_e = 2.002319$ [3]. The minus sign is required as $\boldsymbol{\mu}_s$ and $\boldsymbol{s}$ are anti parallel to each other as the electron charge is negative.

1.1.2 Interaction with a Magnetic Field

In the absence of a magnetic field the electron ($s = 1/2$) spin states for different m_S are degenerate. However, upon application of a static magnetic field, $\boldsymbol{B}$, the magnetic moment of the electron and the field will interact according to the Hamiltonian:

$$\hat{H} = -\hat{\boldsymbol{\mu}}_e \cdot \boldsymbol{B} = \frac{g_e \mu_B \hat{\boldsymbol{s}} \cdot \boldsymbol{B}}{\hbar} \tag{1.7}$$

where $\hat{\boldsymbol{s}}$ is the operator for spin angular momentum. For a sufficiently strong magnetic field, the direction of $\boldsymbol{B}$ defines the quantisation axis (conventionally taken as the z-axis) and $\hat{\boldsymbol{\mu}_e}$ can be replaced by $\hat{\mu_z}$, the operator for the z-component of the spin magnetic moment. The Hamiltonian is now simplified to

$$\hat{H} = \frac{g_e \mu_B \hat{s}_z B}{\hbar} \tag{1.8}$$

where $\hat{s}_z$ is the operator for the z-component of spin and B is the magnitude of $\boldsymbol{B}$ along the z-axis. The eigenvalues of the operator $\hat{s}_z$ are $m_s\hbar$ and hence the energy of the state

[1]Note that $\boldsymbol{\mu}_s$ is commonly denoted $\boldsymbol{\mu}_e$, this notation will be used from now on.

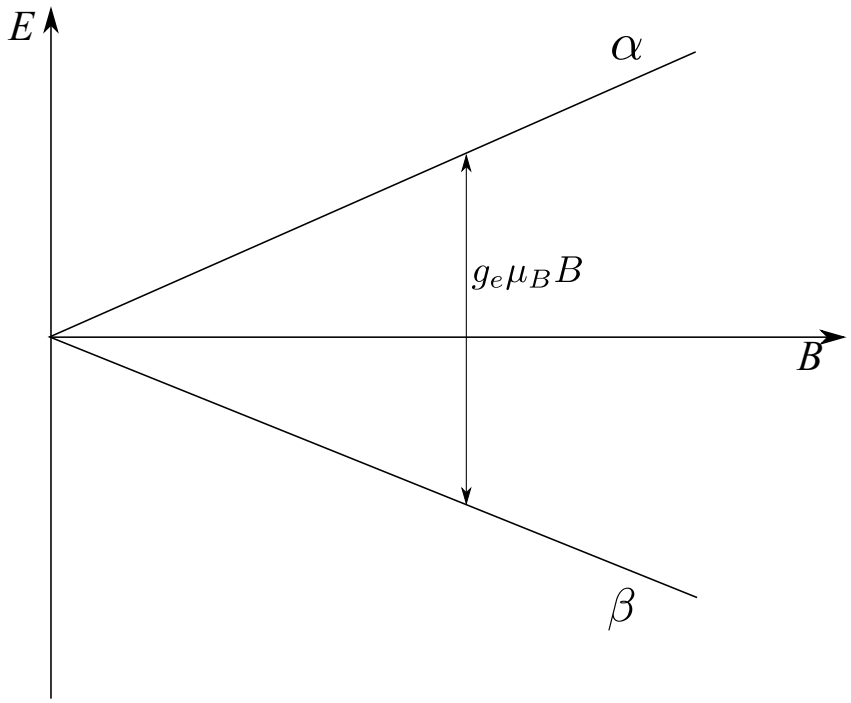

Figure 1.1: The Zeeman effect for a free-electron. Application of a magnetic field causes the energy of the α state to increase and the energy of the β state to decrease. Both states are degenerate for $B = 0$.

for a given m_s is given by

$$E = g_e \mu_B m_s B. \tag{1.9}$$

The energy gap between the two spin levels of the electron, α and β, is given by

$$\Delta E = E_\alpha - E_\beta = g_e \mu_B B \tag{1.10}$$

This is called the *Zeeman* splitting (Figure 1.1), and leads to a resonance condition where $\Delta E = h\nu$.

$$\nu \approx 28\,\mathrm{MHz\,mT^{-1}} \times B. \tag{1.11}$$

1.1.3 Corrections to the g-Factor

For electrons in atoms and molecules the g-value deviates from g_e. An electron in an atom or molecule is not only exposed to an applied field but also to the local magnetic fields from the surrounding environment. This means that an electron experiences an effective field, $\boldsymbol{B}_{\mathrm{eff}}$, that can be greater or smaller than $\boldsymbol{B}$. The surrounding environment and spin-orbit coupling (interaction of the spin and orbital magnetic moments) all contribute to the

effective field, $\boldsymbol{B}_{\text{eff}}$, experienced by the electron. This effect is similar to 'shielding' and 'de-shielding' in NMR spectroscopy where the external field will induce orbital circulation of the electrons creating a local field in opposition to the applied field.

The free-electron g-factor, g_e, can now be replaced by an effective g-factor, g, where deviations of $\boldsymbol{B}_{\text{eff}}$ from $\boldsymbol{B}$ are accounted for in the deviation of g from g_e.

The most significant contribution to the g-factor is from spin-orbit coupling effects which can be large, particularly in heavy atoms (the spin-orbit coupling parameter is proportional to Z^4, where Z is the nuclear charge). However, for organic carbon centred radicals spin-orbit coupling is weak and the orbital angular momentum is 'quenched'. Hence the deviation between g and g_e is typically small and in this thesis, which concentrates on low field studies of C-centred radicals, it will mainly be ignored.

1.1.4 Coupling of Spins

So far, we have only considered a single electron but the body of work discussed in this thesis is concerned with magnetic field effects arising from a radical pair (RP), a system containing two unpaired electrons which can be described by the mutual spin state of the partners. Radical pairs fall into two categories:

1. Uncorrelated RP (URP) where the electron spins are randomly orientated with respect to each other

2. Spin-correlated RP (SCRP) where the spins are correlated in a certain way, often by being created with conservation of total angular momentum.

These different types of RP will be discussed later in this chapter (Section 1.3) but it is only the latter, SCRP, that will give rise to the effects discussed in this thesis.

Consider two electrons, each with $s = \frac{1}{2}$ and in the α or β state ($|\alpha\rangle = \left|\frac{1}{2}\right\rangle$ or $|\beta\rangle = \left|-\frac{1}{2}\right\rangle$), there are four possible spin states

$$|\alpha\alpha\rangle \quad |\alpha\beta\rangle \quad |\beta\alpha\rangle \quad |\beta\beta\rangle\,. \tag{1.12}$$

This is called the *uncoupled* representation where the magnitude and z-component of the individual angular momenta are described but the total angular momenta is unspecified.

An alternative representation, where the magnitude and z-component of the overall angular momentum are known but information of the electrons' individual angular momenta are not is called the coupled representation. The total spin angular momentum, $\boldsymbol{S}$, is defined as $\boldsymbol{s_1} + \boldsymbol{s_2}$ and the corresponding overall spin quantum number, S, is obtained from a summation of s_1 and s_2 according to the Clebsch-Gordan series $(s_1 + s_2, s_1 + s_2 - 1, ..., |s_1 - s_2|)$. The spins of the two electrons may add ($S = 1$) or subtract ($S = 0$) and are called a 'Triplet' (T) or 'Singlet' (S) state, respectively after the spin multiplicity of the system, given by $2S + 1$. The state of the electron can be described by $|S, M_S\rangle$ where M_S is given by $(S, S-1, ..., 1-S, -S)$. S and T states will therefore differ because of their local spin angular momentum. The states of the coupled representation can be found by taking linear combinations of the states of the uncoupled representation. For two electrons these states can be represented by

$$|\mathrm{T}_+\rangle = |1, +1\rangle = |\alpha_1, \alpha_2\rangle \tag{1.13}$$

$$|\mathrm{T}_0\rangle = |1, 0\rangle = \frac{1}{\sqrt{2}}(|\alpha_1\beta_2\rangle + |\beta_1\alpha_2\rangle) \tag{1.14}$$

$$|\mathrm{T}_-\rangle = |1, -1\rangle = |\beta_1, \beta_2\rangle \tag{1.15}$$

$$|\mathrm{S}\rangle = |0, 0\rangle = \frac{1}{\sqrt{2}}(|\alpha_1\beta_2\rangle - |\beta_1\alpha_2\rangle) \tag{1.16}$$

The Vector Model

In the uncoupled states for two electrons, described in Equation 1.12, the magnitude of the total angular momenta for each electron, $\boldsymbol{s}$, is represented as a vector with length $\hbar\sqrt{s(s+1)}$ and the projection on the z-axis is given by $m_s\hbar$. The individual angular momenta lie at unspecified positions on a cone and the total angular momentum is unknown (because s_x and s_y cannot be specified if s_z has been specified due to the uncertainty principle). The precession of the electron spin on this cone is known as the *Larmor Precession*

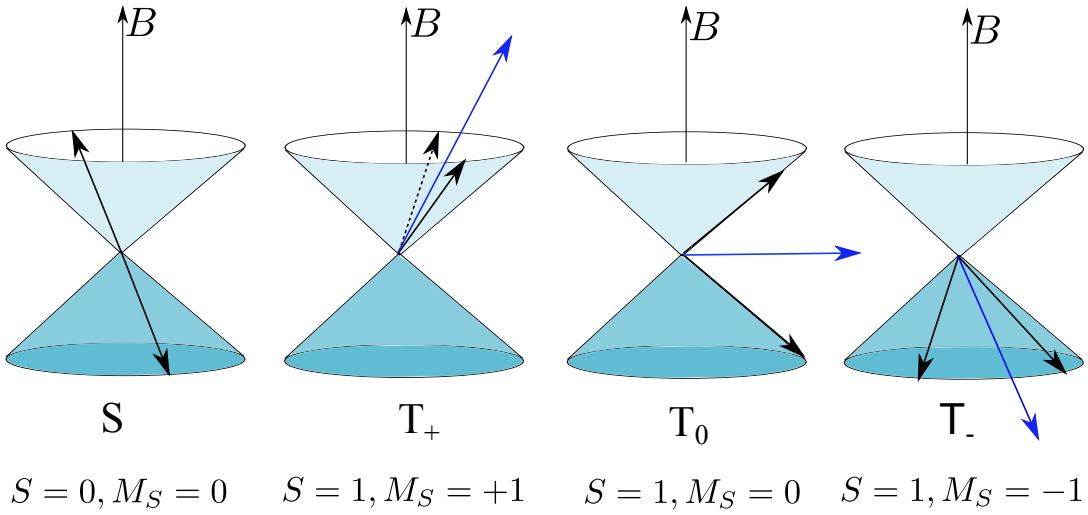

Figure 1.2: The coupled representation of the four spin states. The first state ($S = 0$) represents the singlet state and the next three ($S = 1$) represent the triplet states $M_S = +1, 0, -1$ (T_+, T_0 and T_- respectively). Black arrows represent the individual spin angular momenta vectors of each electron spin. The blue arrow represents the resultant of these vectors described by S and M_S.

and occurs at the Larmor frequency:

$$\omega_L = \gamma_e B. \tag{1.17}$$

Now consider the coupled picture, Figure 1.2. The vector model of the singlet represents a state in which the spin angular momenta vectors sum to give a resultant of zero hence the two spins are antiparallel. In order to achieve a resultant, $S = 1$, using component vectors of $s = \frac{1}{2}$, the vectors must lie at a definite angle relative to each other in the same plane. Note that in the T_+ and T_-, although the spins are said to be 'parallel' they are in fact at an acute angle ($\approx 70°$).

It is clear from this model that although the absolute orientation of the two electron spins on their cones is unknown, the relative orientation between them remains fixed, i.e. in the S state the two spin vectors are always antiparallel with a resultant angular momentum of zero. It can also be seen that the S and T_0 are related to each other by a rotation of π of the two component spin vectors relative to each other. The various triplet states are related to each other by 'spin-flips' of one or more electron spins, changing the M_s value of the state. This provides some insight as to the mechanism that would cause $S - T$ mixing and is the basis for the magnetic field effects discussed later on in this chapter (Section 1.4).

1.2 The Spin Hamiltonian

Having discussed how a single free-electron interacts with a magnetic field and having briefly outlined the Zeeman interaction, it is now necessary to discuss how the electrons in a SCRP interact with each other, with magnetic nuclei and with the magnetic field. It is conventional in magnetic resonance to discuss these interactions in terms of a spin Hamiltonian containing contributions arising from spin interactions only.

1.2.1 Spin Operators

Three operators, $\hat{S}_x$, $\hat{S}_y$ and $\hat{S}_z$ may be defined which represent spin projection operators in the x, y and z directions, respectively. The operator for the total spin angular momentum is given by:

$$\hat{S} = \hat{S}_x\mathbf{i} + \hat{S}_y\mathbf{j} + \hat{S}_z\mathbf{k} \tag{1.18}$$

where $\mathbf{i}$, $\mathbf{j}$ and $\mathbf{k}$ are the unit vectors along the x, y and z axes, respectively. We can represent the magnitude squared of the spin angular momenta vector by the operator

$$\hat{S^2} = \hat{S_x}^2 + \hat{S_y}^2 + \hat{S_z}^2. \tag{1.19}$$

It can be shown that $\hat{S^2}$ commutes with all spin projection operators and hence the magnitude of the spin angular momenta and any one projection onto the axis can be measured precisely and simultaneously. By convention we always choose to take the spin projection operator in the direction of the field B_z, $\hat{S}_z$. We can also define shift operators

$$\hat{S}_\pm = \hat{S}_x \pm i\hat{S}_y \tag{1.20}$$

which are useful for manipulating spin projection operators and allow us to rewrite the operator $\hat{S}_x\hat{I}_x + \hat{S}_y\hat{I}_y$,

$$\hat{S}_x\hat{I}_x + \hat{S}_y\hat{I}_y = \frac{1}{2}(\hat{S_+}\hat{I_-} + \hat{S_-}\hat{I_+}). \tag{1.21}$$

In Section 1.1.1 it was shown that the electron has a spin quantum number $s = 1/2$ and that there are two allowed components of the spin along the z direction (field direction,

B_z) whose spin functions can be denoted by the symbols $|\alpha\rangle$ and $|\beta\rangle$ with spin quantum numbers $m_s = +1/2$ and $-1/2$, respectively. The operator equations for these are given by the following equations when working in a basis where $\hbar = 1$.

$$\hat{S}_z |\alpha_e\rangle = +\frac{1}{2} |\alpha_e\rangle \quad \hat{S}_z |\beta_e\rangle = -\frac{1}{2} |\beta_e\rangle \tag{1.22}$$

and the shift operators are given by:

$$\begin{aligned} &\hat{S}^+ |\alpha_e\rangle = 0 \\ &\hat{S}^+ |\beta_e\rangle = |\alpha_e\rangle \quad \text{such that} \quad \langle\alpha_e| \hat{S}^+ |\beta_e\rangle = 1 \\ &\hat{S}^- |\beta_e\rangle = 0 \\ &\hat{S}^- |\alpha_e\rangle = |\beta_e\rangle \quad \text{such that} \quad \langle\beta_e| \hat{S}^- |\alpha_e\rangle = 1 \end{aligned} \tag{1.23}$$

Considering the coupling of one electron to a spin-$\frac{1}{2}$ nucleus it is necessary to introduce the nuclear spin, I. Nuclear spins are described analogously with nuclear spin operators, $\hat{I}$. For an $I = \frac{1}{2}$ nucleus

$$\hat{I}_z |\alpha_N\rangle = +\frac{1}{2} |\alpha_N\rangle \quad \hat{I}_z |\beta_N\rangle = -\frac{1}{2} |\beta_N\rangle \tag{1.24}$$

and similarly for the nuclear spin shift operators. For a system of an electron spin coupled to a nuclear spin we can define appropriate basis functions, written as products of an electron and nuclear part

$$\phi_1 = |\alpha_e \alpha_N\rangle \quad \phi_2 = |\alpha_e \beta_N\rangle \quad \phi_3 = |\beta_e \alpha_N\rangle \quad \phi_4 = |\beta_e \beta_N\rangle \tag{1.25}$$

If the coupling between the electron and nuclear spin is zero these four states will be degenerate in the absence of a field. The effect of applying a static magnetic field, however, is to separate the energy levels through different interactions.

1.2.2 Zeeman Interaction

The Zeeman interaction between the unpaired electron spins on each radical and an externally applied magnetic field is very important for the study of magnetic field effects. This interaction is linear in spin since it arises from the coupling of the electron spin with an external vector (magnetic field). The most general expression representing the Zeeman interaction (see Section 1.1.2) is given by

$$\hat{H}_{zee} = \mu_B \boldsymbol{B} \cdot \boldsymbol{g} \cdot \hat{\boldsymbol{S}} \tag{1.26}$$

where $\boldsymbol{B}$ is the magnetic field vector, $\hat{\boldsymbol{S}}$ is the spin vector operator and $\boldsymbol{g}$ is a three dimensional tensor, describing the anisotropy of the interaction. The expression $\boldsymbol{B}\cdot\boldsymbol{g}\cdot\hat{\boldsymbol{S}}$ is written fully as

$$\begin{bmatrix} B_x & B_y & B_z \end{bmatrix} \begin{bmatrix} g_{xx} & g_{yx} & g_{zx} \\ g_{xy} & g_{yy} & g_{zy} \\ g_{xz} & g_{yz} & g_{zz} \end{bmatrix} \begin{bmatrix} \hat{S}_x \\ \hat{S}_y \\ \hat{S}_z \end{bmatrix}$$

It is often found that the g-tensor is symmetric and can thus be diagonalized by means of an appropriate matrix transformation [4]. The Zeeman Hamiltonian may then be written as

$$\hat{H}_{zee} = \mu_B \left[g_{xx} B_x \hat{S}_x + g_{yy} B_y \hat{S}_y + g_{zz} B_z \hat{S}_z \right]. \tag{1.27}$$

The principal values of the g-tensor (g_{xx}, g_{yy} and g_{zz}) can be determined experimentally from solid state EPR studies. Alternatively it can be calculated from density functional theory (DFT) methods and can be determined for molecules as large as a small protein [5]. For magnetic field effect (MFE) studies, small organic molecules and weak fields are studied where it is reasonable to assume that the g-tensor is isotropic and equal to that of a free electron.

$$\hat{H}_{zee} = \frac{g_e \mu_B \hat{\boldsymbol{S}} \cdot \boldsymbol{B}}{\hbar}. \tag{1.28}$$

The interactions between a nucleus and an externally applied magnetic field are assumed to be negligible since the nuclear magnetogyric ratios are many times smaller than that of an electron.

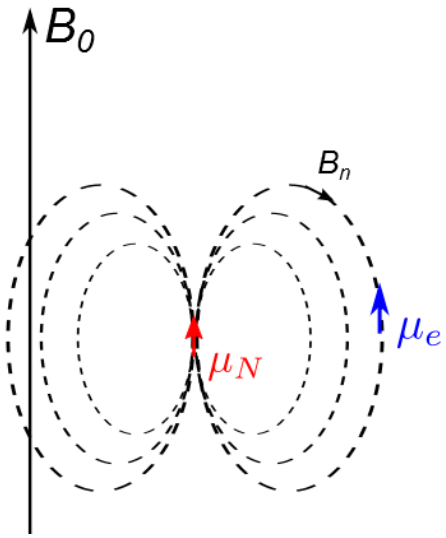

Figure 1.3: The nuclear magnetic moment leads to a nuclear magnetic field, $B_n(r)$ and the electron magnetic moment will interact with this nuclear field.

1.2.3 Hyperfine Interaction

The hyperfine interaction arises from the coupling of an unpaired electron spin with the internal magnetic field due to the spins of magnetic nuclei ($I > 0$) in the radical and is bi-linear in spin. This interaction can be visualised as the motion of an electron in the magnetic dipole field of the nucleus (Figure 1.3). The nuclear magnetic moment leads to a magnetic field, $B_n(r)$, which is called the nuclear field and the electron magnetic moment interacts with this nuclear field, $B_n(r)$. There are two contributions to the hyperfine mechanism: the dipolar hyperfine coupling and the Fermi contact interaction.

The first interaction arises from the magnetic coupling between the magnetic moments of the nucleus and the electron. This can be compared to the classical dipolar coupling between two bar magnets. The classical interaction energy, E, between two magnetic moments $\boldsymbol{\mu_e}$ and $\boldsymbol{\mu_N}$ is given by

$$E = \frac{\boldsymbol{\mu_e}.\boldsymbol{\mu_N}}{r^3} - \frac{3(\boldsymbol{\mu_e}\cdot\boldsymbol{r})(\boldsymbol{\mu_N}\cdot\boldsymbol{r})}{r^5} \tag{1.29}$$

where r is the distance between the electron and nucleus, $\boldsymbol{r}$ is the vector connecting the electron and nucleus and $\boldsymbol{\mu_N} = -g_N\mu_N\boldsymbol{I}$. The Hamiltonian for the dipolar interaction is given by

$$\hat{H}_{dip} = -\frac{\mu_0 g_e \mu_B g_N \mu_N}{4\pi}\left\{\frac{\boldsymbol{I}\cdot\boldsymbol{S}}{r^3} - \frac{3(\boldsymbol{I}\cdot\boldsymbol{r})(\boldsymbol{S}\cdot\boldsymbol{r})}{r^5}\right\}. \tag{1.30}$$

For studies in isotropic liquids this dipolar contribution is averaged to zero by rapid tumbling of radicals in solution. In the solid state and in orientated media, such as a liquid crystals, the hyperfine interaction is anisotropic. Hence, the angle between the two spins and the external magnetic field, B, will be important.

The second contribution to the hyperfine interaction is known as the Fermi contact interaction. This contact interaction occurs when the electron has a finite probability density at the nucleus; since *p*, *d*, *f*, or higher orbitals have nodes at the nucleus the electron must have some *s*-orbital character (the contact interaction is proportional to the *s*-orbital character in the singly occupied molecular orbital (SOMO) around the nucleus in question). The Fermi contact interaction is isotropic and is described by

$$\hat{H}_{\mathrm{HFI}} = a\hat{\boldsymbol{I}} \cdot \hat{\boldsymbol{S}} \tag{1.31}$$

where a is the isotropic hyperfine coupling constant (HFC) for the interaction between an electron and nuclear spin. The overall hyperfine interaction can be described by

$$\hat{H}_{\mathrm{HFI}} = \hat{\boldsymbol{I}} \cdot \boldsymbol{A} \cdot \hat{\boldsymbol{S}} \tag{1.32}$$

where $\boldsymbol{A}$ is the complete hyperfine tensor and $a = \mathrm{trace}(\boldsymbol{A})/3$. The coupling constant, a, is proportional to γ_N and therefore replacing any hydrogens with a deuterium will reduce the hyperfine interaction by $\gamma_H/\gamma_D \approx 6.5$. Hyperfine coupling constants can be determined experimentally by EPR spectroscopy or theoretically by DFT from the spin density in the SOMO.

The overall Hamiltonian for a molecule containing a number of magnetic nuclei with hyperfine coupling constants, a, and nuclear spin quantum number, I, can be written as [6]

$$\hat{H}_{\mathrm{HFI}} = \sum_i a_i \boldsymbol{I_i}.\boldsymbol{S} \tag{1.33}$$

where a_i and I_i are the hyperfine coupling constants and nuclear spin quantum numbers for the individual nuclei, i. For a molecule with multiple hyperfine couplings it is often

more convenient to define the effective molecular hyperfine coupling constant, a_{mol}:

$$a_{\text{mol}} = \sqrt{\sum_i a_i^2 I_i(I_i+1)}. \tag{1.34}$$

This has been shown to be a good approximation for reproducing coherent dynamics [6]. For a radical pair with two effective molecular hyperfine coupling constants to consider, the effective radical pair hyperfine coupling is then simply given by

$$a_{\text{eff}} = \sqrt{a_1^2 + a_2^2} \tag{1.35}$$

where a_1 and a_2 are the effective molecular hyperfine coupling constants for radical 1 and radical 2 respectively.

In a semiclassical picture the effective magnetic field, $\boldsymbol{B}_{\mathbf{eff}}$, experienced by an electron is now given by the vector sum of the external static magnetic field, $\boldsymbol{B}_{\mathbf{0}}$, and an additive magnetic field, $\boldsymbol{B}_{\mathbf{hfc}}$. $\boldsymbol{B}_{\mathbf{hfc}}$ arises from the sum of the hyperfine couplings of the various nuclear spins in the corresponding radical

$$\boldsymbol{B}_{\mathbf{eff}} = \boldsymbol{B}_{\mathbf{0}} + \boldsymbol{B}_{\mathbf{hfc}} \tag{1.36}$$

For reasons of simplicity, consider a hypothetical one-proton RP. That is, a RP consisting of two electrons, one of which is coupled to a single nuclear spin with $I = 1/2$ with a hyperfine coupling constant, a. The strength of the field experienced by the coupled electron is given by;

$$B_{\text{eff}} = B_0 + am_I \tag{1.37}$$

where $m_I = 1/2$ for a proton and a as a hyperfine coupling will be quoted in mT.

1.2.4 Coupling Between Electron Spins

The interactions between electron and nuclear spins within a radical and how these contribute to the spin Hamiltonian have so far been discussed. However, for a complete picture the interactions between the two electron spins must also be considered. There

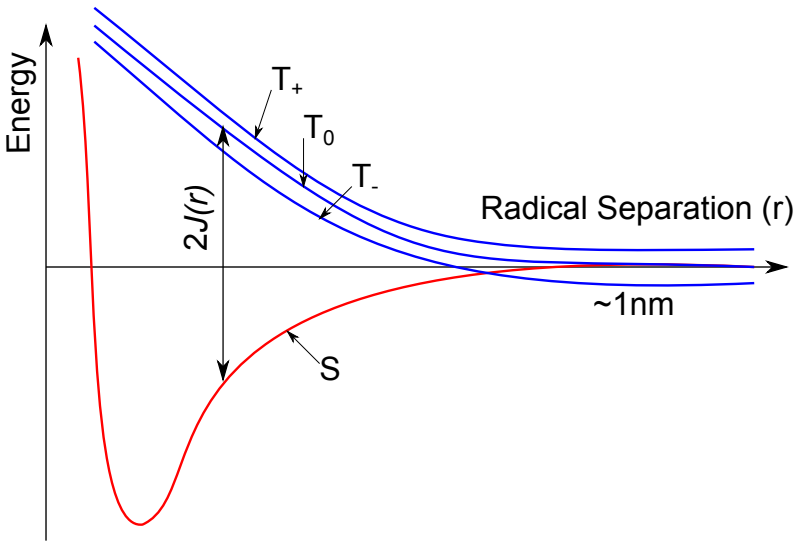

Figure 1.4: Energy of the S and T coupled spin states as a function of RP separation. The difference in energy is known as the exchange interaction given by $2J(r)$.

are two types of electron spin-spin interactions: the exchange and dipolar interactions. The exchange interaction is purely quantum mechanical in nature and causes a splitting in the energy levels of the singlet and triplet states. This effect arises because of the Pauli principle which states that the total wavefunction (including spin) must be antisymmetric with respect to the interchange of coordinates for any pair of indistinguishable electrons.

To describe the spin evolution of the RP, where the radicals are close enough for inter-radical electron correlation and bonding effects to act, we use the Hamiltonian:

$$\hat{H}_{ex} = -2J\hat{S}_A\hat{S}_B \tag{1.38}$$

where J is the exchange energy. The splitting of the spin states is shown schematically in Figure 1.4. The exchange interaction is assumed to decrease exponentially with increasing RP separation and to be independent of the radical and solvent orientation.

$$J(r) = J_0 e^{-\frac{r}{r_j}} \tag{1.39}$$

where J_0 is the magnitude of the exchange, r is the inter-radical separation and r_j is a range parameter. The values of these parameters vary considerably with the nature of the radicals and the solvent. In solution the exchange interaction acts to prevent S − T

mixing such that in the case where radicals are close enough and the exchange dominates the RP spin Hamiltonian, no MFEs will be observed [7]. For a separation of $\approx 1\,\text{nm}$ the exchange interaction is assumed to be negligible.

Dipolar Interaction

The electron spin magnetic dipolar interaction is the interaction between the magnetic moments of two electrons through space. The strength of the interaction depends on the inter-radical separation, r and on the orientation of the vector, $\boldsymbol{r}$, connecting the two electron spins of the RP with respect to the magnetic field.

$$\hat{H}_D = \frac{\mu_0}{4\pi}\gamma_e^2\hbar^2 g_A g_B \left[\frac{\hat{\boldsymbol{S}}_{\boldsymbol{A}}.\hat{\boldsymbol{S}}_{\boldsymbol{B}}}{r^3} - \frac{(\hat{\boldsymbol{S}}_{\boldsymbol{A}}.\boldsymbol{r})(\hat{\boldsymbol{S}}_{\boldsymbol{B}}.\boldsymbol{r})}{r^5}\right]. \tag{1.40}$$

where g_A and g_B are the electron g-factors for the two electrons, $\hat{\boldsymbol{S}}_{\boldsymbol{A}}$ and $\hat{\boldsymbol{S}}_{\boldsymbol{B}}$ are the electron spin vector operators and $\boldsymbol{r}$ is the vector connecting the two electron spins. Under high field conditions, the spin magnetic moments align parallel to the field direction and the Hamiltonian becomes:

$$\hat{H}_D = \frac{\mu_0}{4\pi}\gamma_e^2\hbar^2 g_A g_B \left[\frac{1-3cos^2\theta}{r^3}\right]\hat{S}_{Az}\hat{S}_{Bz} \tag{1.41}$$

where θ is the angle between $\boldsymbol{r}$ and the applied field. Averaging out of the dipolar interaction, which occurs in solution, cannot always be assumed since in solid state there is no motion of the radicals. Also, in weak fields, the electron spin is quantized along the vector connecting the two electrons (and not the applied field direction) and is therefore independent of θ [8]. Hence dipolar interactions cannot always be ignored allowing them to have a strong influence at weak fields, particularly on the low field effect, Section 1.4.4.

The exchange and dipolar interactions hinder $\text{S} - \text{T}$ mixing when the radicals are in close proximity, immediately after generation or upon re-encounter. Diffusion of the radicals will then separate the RP to a distance at which these interactions may be neglected and unhindered spin mixing may occur. In order to observe an appreciable MFE, it is important that the radicals are in an environment which will allow the molecules

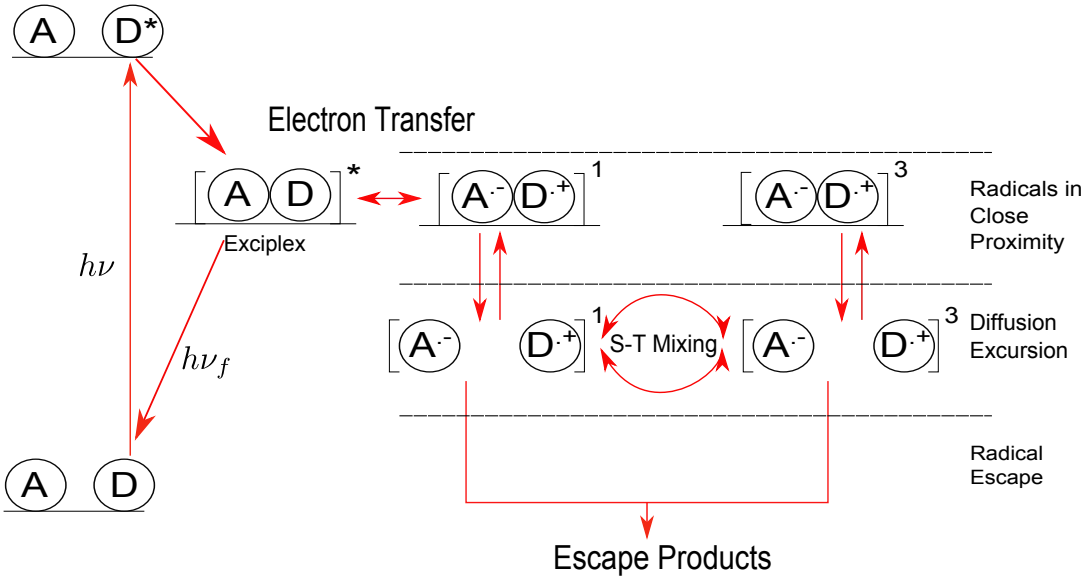

Figure 1.5: A generic scheme for the RPM in liquid state including the reactions during geminate phase.

to separate efficiently yet still have a high probability of re-encounter within a geminate cage (solvent molecules surrounding the RP). This can be achieved using media such as micelles which encapsulate the RP or by using radical ion pairs (RIP) which are subject to coulombic interactions.

1.3 The Radical Pair Mechanism

The Radical Pair Mechanism (RPM) was proposed by Kaptein in 1969 [9], initally as an explanation for the observation of Chemically Induced Dynamic Nuclear Polarization (CIDNP). This theory relied on the ability of nuclear spin interactions to alter the recombination probability in reactions that proceed through radical pairs. The RPM has become the only known mechanism by which magnetic fields can affect the yield of a chemical reaction [10]. An example scheme for reactions occurring in the liquid state, which is used throughout this thesis, is shown in Figure 1.5 and the essential features are described below.

1.3.1 Radical Pair Formation

Absorption of energy - from a photon in the case of all the reactions involved in this thesis - causes excitation of a ground state molecule, for example D (a donor), to form an excited

molecule, D*. There are a number of processes now available to this high-energy molecule, they are: radiative decay, hydrogen abstraction, bond cleavage or electron transfer. The majority of precursor molecules have a singlet excited state and most RPs are therefore initially created in the singlet state. However, intersystem crossing (ISC) may produce a triplet excited state, D^{3*}, if it is faster than electron transfer, and hence the RP can be formed in the triplet state. Of all the different pathways available to the excited molecule while the first generates the ground state molecule, only hydrogen abstraction, bond cleavage and electron transfer reactions produce a RP species. All the reactions investigated in this work (unless otherwise stated) are electron transfer reactions in which the excited molecule either donates (D) or receives (A) an electron to form a radical ion pair (RIP) with correlated spins.

1.3.2 Radical Pair Diffusion and Recombination

Immediately after their creation the RPs are trapped in very close proximity inside a solvent cage, the processes occuring during this 'geminate stage' are shown in Figure 1.5. Within this 'cage' the radical pairs are trapped within a loosely bound collection of solvent molecules, where they collide frequently with each other and stand a high chance of re-encounter and recombination. This is known as 'primary geminate recombination'. Some RPs, however, do not react immediately after creation and will instead separate and diffuse within the liquid. During these diffusion excursions, the exchange interaction may become negligible and the RP spin state evolves under the influence of molecular hyperfine interactions and externally applied magnetic fields. After a diffusion excursion the RPs may separate completely and form escape products or diffuse back into close proximity and re-encounter. Upon re-encounter the radicals are once again trapped inside a solvent cage and frequently collide with one another. The probability of reaction on re-encounter depends on the spin state of the RP and hence on the spin evolution of the RP during the diffusion excursion. Spin must be conserved in the back electron transfer to form the recombination product, i.e. exciplex, therefore only RPs with an overall singlet state may recombine and luminesce to produce the original ground state molecules. RPs in the triplet state are deemed 'unreactive', unless there are triplet recombination products, and

can do nothing but separate once more.

Spin evolution between S and T states during the diffusion excursion stage is key to the RPM. This evolution is mostly driven by hyperfine interactions and the effect of external and local magnetic fields. The interactions through which a field can affect the reaction are weak in the sense that their energies are far less than the thermal energy, k_BT. Therefore any MFE on a chemical reaction is an entirely kinetic effect which manifests itself as a change in the distribution of the reaction products.

1.4 Magnetic Field Effects

Having discussed in detail the various magnetic interactions within a radical pair (Section 1.2) it is now necessary to discuss the mechanisms by which magnetic field effects (MFEs) will arise. It has already been mentioned that spin evolution between S and T states are key to the observation of an MFE and hence it is important to understand the mechanisms which will cause interconversion between spin states. The processes which govern interconversion between the spin states (also known as singlet - triplet (S − T) mixing), fall into two types:

- Coherent mixing - where S − T mixing is caused by differences in the local fields experienced by the RP electrons.
- Incoherent mixing - where changes in the spin state may occur due to spin relaxation processes induced by random field oscillations caused by molecular motion.

All MFEs studied will be described in terms of singlet yield, ϕ_S, with the assumption that the RP is singlet born.

1.4.1 Zeeman Mechanism

The conceptually most accessible MFE to arise is that due to the Zeeman interaction which acts to progressively isolate the $T_\pm$ from the S/T_0 manifold as the strength of the static magnetic field increases. For a singlet born RP the Zeeman interaction will cause an increase in ϕ_S with increasing static field strength, see Figure 1.6, as the efficiency of

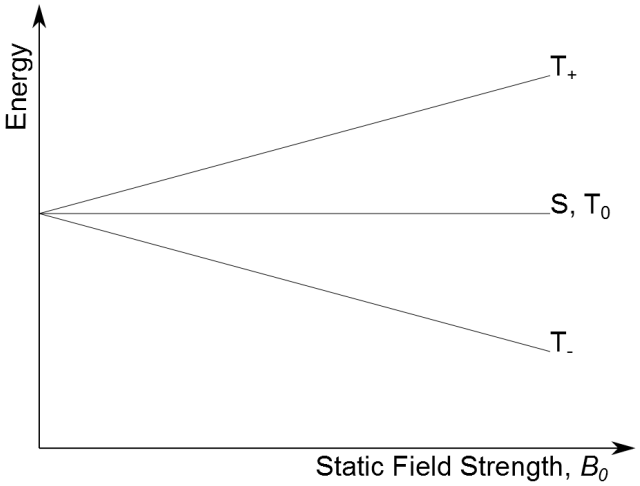

Figure 1.6: The Zeeman interaction on the spin states as a function of static field strength. The exchange interaction has been assumed to be negligible.

the S − T mixing is decreased. Eventually the $T_{\pm}$ will be so far removed from the S/T_0 manifold that the mixing pathway becomes completely inactive.

1.4.2 Hyperfine Mechanism

For the field strengths and chemical systems studied in this thesis the hyperfine mechanism is the dominant process of spin mixing in the RP, especially in the case of zero or low fields.

It is insightful to first examine a simple two-electron-one-proton system in a strong magnetic field. Consider a pair of radicals with identical g values but with one of the electrons coupled to a single spin-1/2 nucleus with hyperfine coupling constant, a. Both the electron and nuclear spin will be quantized along the direction of the applied field and will precess around it. The magnetic moment of the nucleus produces an additional field which will be experienced by the electron spin it is coupled to, resulting in an effective field $B \pm \frac{a}{2}$ at the electron spin, depending on the alignment of the nuclear spin. Since the other (non-coupled) electron precesses around the field, unperturbed by the magnetic moment of the nucleus there will be a field independent difference in the precession frequencies (Larmor frequency, ω_L) of the two electron spins. This difference is given by

$$\Delta\omega_L = \frac{g\mu_B \Delta B}{\hbar} = \pm\frac{g\mu_B a}{2\hbar} \tag{1.42}$$

This leads to a coherent $S - T_0$ mixing since the two states only differ in the relative precession phase of the two electron spins (Figure 1.2).

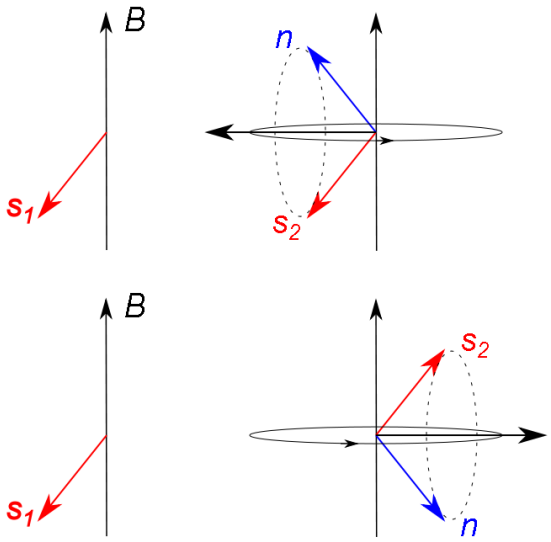

Figure 1.7: The hyperfine mechanism; in a frame of reference with a fixed spin, s_1. The coupled electron, s_2, and the nucleus, n, precess around their resultant which, in turn, precesses around the field direction. In this mechanism the S state may interconvert between all three T states with time.

When the applied static field is comparable in size to the hyperfine coupling constants within the RP, the field axis is no longer a good quantization axis. The electron spin will now precess around the vector sum of the applied static and hyperfine fields, resulting in a change of the relative orientation of the two electron spins with time. The uncoupled electron, s_1 is assumed to be static and the coupled electron, s_2, is shown to be precessing around the resultant of the electron spin, s_2 and the nuclear spin, n, which in turn precesses around the applied field. In this mechanism both spin flip and rephasing transitions are allowed, see Figure 1.7.

1.4.3 Δg Mechanism

The Δg mechanism is another example of coherent spin mixing. If the g-factors of the electrons in the two radicals differ, then their Larmor frequencies will also differ

$$\Delta\omega_L = \frac{(g_1 - g_2)\mu_B B}{\hbar} \tag{1.43}$$

where g_1 and g_2 are the g-factors of the electron on radical 1 and radical 2 respectively. This will result in a fluctuating difference in the phase between the two electrons and lead to $S - T_0$ mixing on a timescale of $\Delta t = \pi/\Delta\omega_L$. In contrast to the hyperfine mechanism, the difference in precession frequencies (and hence timescale of mixing) is dependent on the strength of the magnetic field. By applying a magnetic field of sufficient strength it should be possible to induce $S - T_0$ mixing.

In the case of organic radicals, the difference in the g-factors is very small (of the order of 10^{-4}) and for this reason the Δg mechanism is assumed to be insignificant for the field strengths used throughout this thesis.

1.4.4 The Low Field Effect

It has already been shown that at weak field strengths, $B \leq a$, the field direction is no longer a suitable quantisation axis and instead the electron spin will precess around the resultant of the applied static and hyperfine fields (Figure 1.7). This mechanism will cause not only $S - T_0$ mixing but also mixing with the T_+ and T_- states. However, this is not the only mechanism to be observed at low fields. In 1976 Brocklehurst [11] observed and predicted a phenomenon called the 'low-field effect' (LFE), which produced an effect opposite in sign to the normal MFE arising from the hyperfine mechanism.

The LFE can be understood as a consequence of the difference in the selection rules between zero and applied static fields. Consider the total angular momentum $\boldsymbol{F} = \boldsymbol{S} + \boldsymbol{I}$ whose projection onto the static field axis is time independent ($\Delta M_F = 0$). At field strengths $B_0 > 0$ the selection rules state that $\Delta M_F = 0$, but at zero fields, $B_0 = 0$, there is an additional selection rule such that the total angular momentum must also be conserved, $\Delta M_F = 0$ and $\Delta F = 0$. Consider again a one-proton radical pair where the coupled states are shown in Table 1.1. In this table it can be seen that at zero field only two $S - T_0$ transitions are allowed. However, at non-zero field, $B_0 > 0$, two more transitions to the $T_\pm$ are allowed. Hence, the efficiency of $S - T$ mixing is increased at low fields as compared to zero fields, resulting in a decrease in ϕ_S as B_0 increases. This changes when the energetic isolation of the $T_\pm$ states by the Zeeman interaction reduces the mixing efficiency again.

	$S\alpha$	$S\beta$	$T_0\alpha$	$T_0\beta$	$T_+\alpha$	$T_+\beta$	$T_-\alpha$	$T_-\beta$
F	$+\frac{1}{2}$	$+\frac{1}{2}$	$+\frac{1}{2}$	$+\frac{1}{2}$	$+\frac{3}{2}$	$+\frac{3}{2}$	$+\frac{3}{2}$	$+\frac{3}{2}$
M_F	$+\frac{1}{2}$	$-\frac{1}{2}$	$+\frac{1}{2}$	$-\frac{1}{2}$	$+\frac{3}{2}$	$+\frac{1}{2}$	$-\frac{1}{2}$	$-\frac{3}{2}$

Table 1.1: The coupled spin states of a one-proton radical pair. α and β denote the spin state of the nucleus and S or $T_0/T_\pm$ denotes the paired electron spin state.

1.4.5 Relaxation Mechanism

Relaxation mechanisms are incoherent spin mixing processes which cause interconversion between S and T states in the RP. Incoherent processes tend to reduce the critical spin polarisation. They are field dependent mechanisms and give rise to specific types of MFEs. Relaxation processes can be neglected if radical recombination happens on a much faster timescale. However for a long-lived RP relaxation processes may be significant and cannot therefore be ignored.

A common feature of relaxation mechanisms is that they involve random fluctuations of the local field experienced by the radicals caused by molecular motion. The resulting randomised spin-mixing acts to restore a Boltzmann equilibrium between the different spin states of the RP, originally created with a non-Boltzmann, polarised distribution of spins amongst the S and T energy levels. Contributions to the relaxation may arise due to interactions which are internal or external to the individual radical. The net result of these internal and external interactions is to cause randomised fluctuations in the local magnetic field. These fluctuations can lead to two forms of spin relaxation

- **Spin - Lattice Relaxation**

  If the frequency, ω, at which the local magnetic field is fluctuating is in resonance with the Zeeman splitting between S/T_0 and the $T_\pm$ states, 'spin flip' transitions between these energy levels will be induced. This mechanism is analogous to oscillating magnetic field effects described in Section 1.4.6 and acts to restore the Boltzmann distribution between the S and T states and causes a loss of spin polarisation over time with a time constant, T_1.

- **Spin - Spin Relaxation**

  Spin - spin relaxation destroys the coherence between the two electron spins in the radical pair. The random field fluctuations caused by molecular motion contain

components at all frequencies and hence there must be a component that will be effectively static on the timescale of the RP lifetime. This extra 'static' field will cause one of the electrons in the RP to experience an effective field different to that of its partner and hence its precession frequency will change. Through this dephasing $S \leftrightarrow T_0$ interconversion will occur. This is characterised by a time constant, T_2.

1.4.6 Oscillating Magnetic Field Effects

All of the mechanisms described so far have focused on the effects arising from static magnetic fields which have been studied for many decades [12]. However, throughout the 1990s [13] was shown that an oscillating field, applied in isolation and also in addition to a static magnetic field, may also affect the yield of a reaction under favourable conditions. The theoretical and experimental details describing the interaction between RPs and oscillating fields are much more complex than the interactions with static fields only.

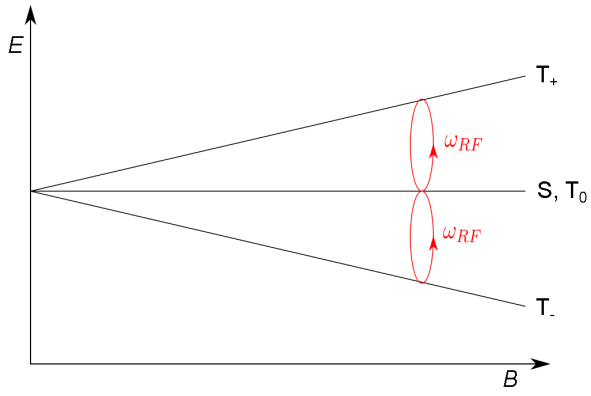

Figure 1.8: The application of an oscillating magnetic field will reconnect the S/T_0 manifold with the $T_\pm$ states. Here, J is assumed to be zero.

Consider a RP which is subject to a static magnetic field. The Zeeman interaction (Section 1.4.1) will act to increasingly isolate the $T_\pm$ from the S/T_0 manifold as the static field is increased. This results in a decrease in spin-mixing and in an increase in singlet yield. Application of an oscillating field can reconnect the S/T_0 manifold with $T_\pm$ states when a resonance condition is met, see Figure 1.8. This so-called resonance will occur when the frequency, ω_{RF}, of the oscillating field is equal to the Zeeman splitting:

$$\omega_{\mathrm{RF}} = \frac{g\mu_B B}{\hbar}. \tag{1.44}$$

For a singlet-born RP, this reconnection of the states will result in an increase in spin-mixing and a decrease in ϕ_S. For high fields ($B > a$), this effect is analogous to traditional electron spin resonance methods and is typically called Reaction Yield Detected Magnetic Resonance (RYDMR) .

1.4.7 Magnetic Field Effects: An Overview

The effects of static magnetic fields on chemical reaction yields have been investigated for many decades [10, 12, 14]. These reactions are known to include free radical intermediates as described in the radical pair mechanism (RPM) (Section 1.3).

Consider a singlet born radical pair in zero field, $\mathrm{S}-\mathrm{T}$ mixing may occur between the singlet and triplet states. Application of a static magnetic field the $\mathrm{T}_{\pm}$ levels split from the S/T_0 manifold due to the Zeeman effect, becoming progressively decoupled and an increase in the singlet yield will occur. This is known as the 'normal' magnetic field effect (MFE).

It is of great interest to investigate the effects of applied magnetic fields comparable in strength to the Earth's field ($\approx 50\,\mu\mathrm{T}$). However, the theory concerning fields this weak is very complex. Nevertheless such effects have been observed for a variety of reactions in solution [15–17]. In 1976, Brocklehurst [11] proposed a magnetic field effect opposite in sign to the normal effect at low fields, e.g. field strengths weaker than the effective RP hyperfine couplings of the system. This phenomenon is referred to as the low field effect (LFE) and has been previously described Section 1.4.4.

Chapter 2

Introduction to Animal Migration

Many animals possess the ability to sense the Earth's magnetic field for directional (compass) information [18]. This sense, called magnetoreception, is believed to enable the navigational abilities of several animal species; it has been postulated as a method by which animals might develop regional maps. Magnetoreception is widespread amongst animals [19]; examples include birds [20–22], insects (including fruit flies and honeybees) [23, 24] and species such as turtles [25], lobsters, sharks and stingrays [20]. It is most commonly studied in birds [26], where magnetoreception may be important in migration. Whilst a wide range of behavioural studies have supported the existence of various animal compasses and magnetic maps [20], the underlying mechanism remains unknown.

Since bird species are most commonly associated with magnetosensitivity, their proposed fundemantal mechanisms provide the subject of this review. More than five thousand species of birds undergo annual round trip migration of thousands of miles, often returning to precisely the same nesting and wintering locations from year to year [27]. The main reason for the annual migration is the change in season, causing the birds to relocate to maintain their food supply. The birds are thought to gauge the change of seasons by sensing the change in the light level from the angle of the sun in the sky, as well as the total hours of daylight. When their needs are no longer met by their current habitat, they will begin their journey. Several minor factors can affect the precise day any bird species begins its migration, including: level of available food supplies, weather patterns, air temperatures and wind patterns.

One of the greatest mysteries of migration is exactly how birds find their way from one location to the next. Scientific studies have been conducted on a number of bird species and different mechanisms of bird navigation have been proposed.

- **Magnetic Sensing**: Many birds are reported to have special chemical compounds in their brains [21], eyes, or bills that enable them to sense the Earth's magnetic field. This helps the birds orient for long journeys [21].
- **Geographic Mapping**: Birds follow the same migration routes from year to year; their keen eyesight allows them to map their journey by different landforms and geographic features such as rivers, coastlines, and mountain ranges [27].
- **Star Orientation**: For birds that migrate at night, star positions and the orientation of constellations can provide necessary navigational directions.
- **The Sun Compass**: During the day, birds also use the sun to navigate [27]. The primary compass sense that migrants rely on to orient south is the use of a sun compass i.e. the position of the sun.

Magnetosensitivity will be the focus of the discussion that follows in this chapter and thesis.

2.1 The Geomagnetic Field: What We Know

Before discussing the possible biophysical mechanisms underpinning magnetoreception, it is helpful to understand the stimulus of magnetoreception: the geomagnetic field. The geomagnetic field is approximately defined as a magnetic dipole tilted at an angle of 11° with respect to the Earth's rotational axis, as if there were a bar magnet placed at that angle at the centre of the Earth (Figure 2.1). The magnetic field lines emanate from the centre of the Earth, leave the surface at the southern magnetic pole, surround the globe and re-enter at the northern magnetic pole. Consequently, the magnetic field lines point away from the Earth at the southern hemisphere, towards the Earth at the northern hemisphere, and run parallel to the Earth's surface near the magnetic equator. Hence,

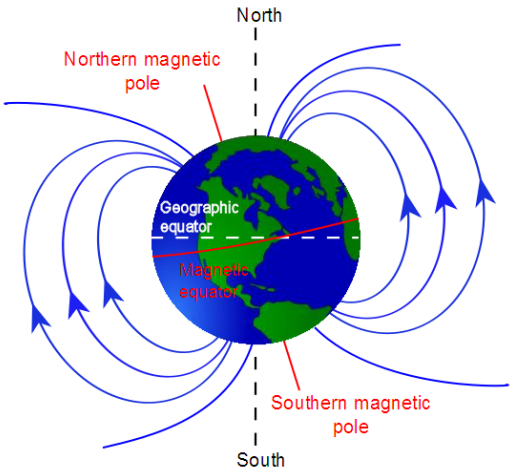

Figure 2.1: Schematic of the Earth's magnetic field. The solid blue lines represent the magnetic flux lines and dashed black lines indicates the rotational axis.

the angle of the magnetic field vector and the horizontal (magnetic) inclination change continuously (with a regular gradient) from $-90°$ at the southern magnetic pole to $+90°$ at the northern magnetic pole. The intensity of the geomagnetic field is highest at the two poles and lowest near the magnetic equator. Its magnitude ranges from about 0.025 mT to 0.065 mT.

There are slight variations in the magnitude of the geomagnetic field across the surface of the earth [20]. These variations arise from distortions caused by material in the upper crust resulting in magnetic anomalies with slight increase or decrease in intensity. The geomagnetic field is also temporarily altered by electromagnetic radiation originating from the sun, causing a slight decrease in intensity around noon. Occasional magnetic storms may cause changes in all magnetic parameters. However, these changes have a negligible effect on the overall intensity of the geomagnetic field [28].

Thus, the geomagnetic field represents a reliable, omnipresent source of navigational information. The magnetic field vector provides information that may be used as a compass and the intensity provides information that could be used in a potential navigational 'map'.

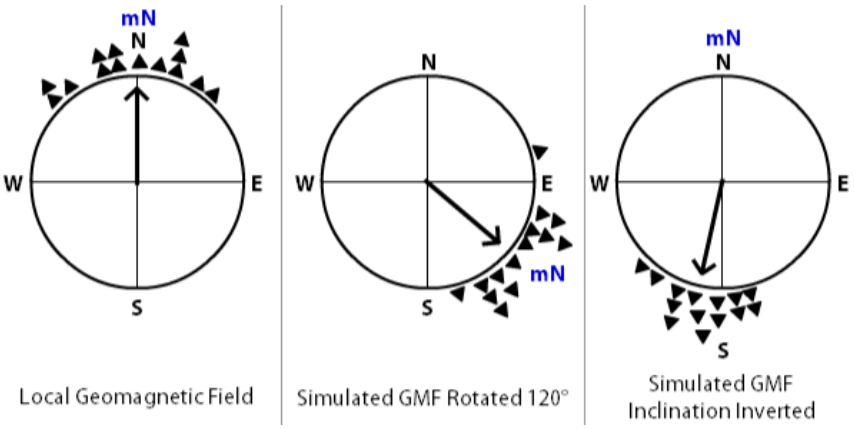

Figure 2.2: Orientation behaviour of migrating European robins in spring. The first tests were conducted in a local geomagnetic field and the second tests were conducted with simulated fields (magnetic North (mN)). The triangles at the periphery of the circle mark the headings of the birds with the arrows showing the mean vector. N, S, W, E indicate geographic North, South, East and West respectively. Data from [20].

2.2 Inclination Compass

Extensive studies have attempted to pinpoint how the geomagnetic field is used in the avian magnetic compass. The avian magnetic compass has been hypothesised to be an '*inclination compass*', meaning that it is based on the inclination of the field lines, rather than polarity. It follows that birds can only perceive the axial course of the field lines and interpret the inclination of the field with respect to up and down. From this however, they are able to derive non-ambiguous directional information [29]. This finding resulted from an experiment in which the vertical component of the magnetic field was inverted: under the experimental conditions, the birds that initially headed towards magnetic North under the geomagnetic field reversed their headings for magnetic 'South' (Figure 2.2). In contrast, the birds did not alter their course when the horizontal and vertical component of the magnetic field was reversed and inverted respectively [20]. Thus, a bird unable to perceive the polarity of the magnetic field would not realise any difference (Figure 2.3). The avian magnetic compass does not distinguish between magnetic 'North' and 'South', as indicated by polarity, but between 'poleward' and 'equatorward'. For example the direction of the field depends on the proximity to the magnetic North pole.

Another surprising finding concerning the bird's magnetic compass is that it is closely tuned to the total intensity of the ambient field, as supported by experiments which suggest a rather narrow functional window [20]. Experiments show that even in artificial

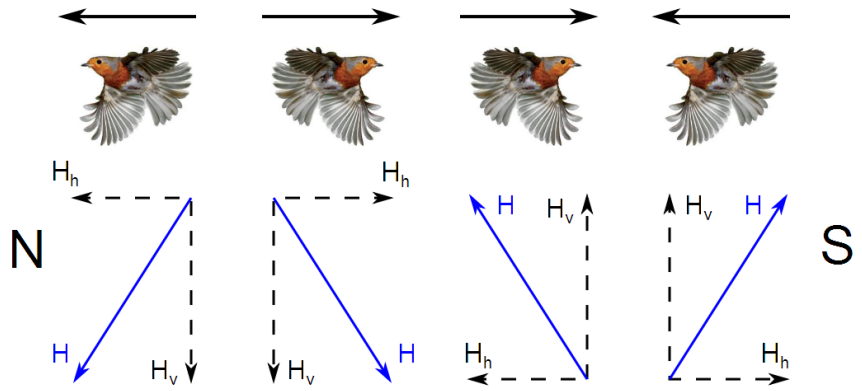

Figure 2.3: Scheme shows the orientation of robins when different components of the geomagnetic field were varied. H_h and H_v are the horizontal and vertical components of the field and H is the magnetic vector. N and S illustrate magnetic North and South, respectively.

geomagnetic fields birds could not orient to their normal migratory direction if the intensity of the magnetic field was either increased or decreased by ≈20-30%. However, if the birds were exposed to a higher intensity magnetic field for three days prior to testing, they could orient at the higher intensity level, as well as at the normal intensity levels but not at an intermediate level in-between, which they had not yet become accustomed to [30].

One hypothesis is that birds use the magnetic intensity to map their location [28]. For example, in the northern hemisphere birds know by experience that magnetic intensity increases the further North they are. Hence, when finding themselves at a location with higher magnetic intensity than at home, they would conclude that they are North of home and must head South to return.

Behavioural evidence suggests that magnetoreception is not a uniform phenomenon: animals use different parameters of the geomagnetic field for different tasks. It is therefore sensible to assume that these different parameters will be detected by different mechanisms. Just as a boy scout would use a map to work out his location and a compass to figure out in which direction he should go.

2.3 Mechanisms of Magnetoreception

To understand magnetoreception fully, there are three aspects that one must consider: (1) details of the primary biophysical processes which respond to magnetic fields; (2) the

location of the sensory organ, its structure and its neurological connections; and (3) the parts of the brain involved in processing the magnetic information. Although our research is mostly concerned with the first of these points, it is important that we acknowledge the other aspects.

The most commonly proposed models for magnetoreception are (1) induction [25], (2) the magnetite based mechanism [31], and (3) the radical pair mechanism [21]. The induction mechanism is a model limited to marine animals because it requires sea water as a surrounding medium with high conductivity. Skates and rays have been shown to use this mechanism [32]. Under this model, when the animals swim in different directions, they cross the field lines of the geomagnetic field at different angles, inducing different voltages at their electric organs. The other two models, the radical pair mechanism and the magnetite mechanism, are the two main hypotheses amongst terrestrial animals and those living in fresh water and will be discussed in more detail. It is unknown whether only one of these mechanisms is responsible for magnetosensitivity in birds or whether both of these mechanisms work together in order to elucidate different information.

2.3.1 Magnetite

Magnetite is a specific form of iron oxide, Fe_3O_4, whose magnetisation depends on the size and shape of the particles [33]. Iron (II, III) oxide remains permanently magnetised when its length is larger than 50 nm and becomes magnetised when exposed to a magnetic field if its length is less than 50 nm. In both of these situations the Earth's magnetic field leads to a transducible signal via a physical effect on this magnetically sensitive oxide [31]. Spin interactions cause the spin of adjacent atoms to align, thus forming domains with all spins parallel. Large particles include multiple domains with their magnetic moments largely cancelling out. Particles typically of the size 1.2 µm - 0.05 µm may consist of a single domain and have a stable magnetic moment, acting as a tiny permanent magnet.

A uniform concept of how magnetite-based magnetoreceptors might work does not yet exist, but theoretical models have been proposed. Kirschvink [34] proposed a model in which the magnetic particles in the organisms were single-domain magnetite. It is proposed that the external magnetic field will exert a magnetic-torque on the particle,

which can rotate the particle to open or close an ion channel and produce the nerve signals. Another model is based on superparamagnetic nanoparticles that can be magnetised such that the local magnetic field in the cell would be amplified by orders of magnitudes by an external field. Hence magnetic particles experience an attractive or repulsive force to induce their displacement, which might induce primary receptor potential via strain-sensitive membrane channels to create the nerve signal [35]. These models suggest that the nerve signals will transmit through the ophthalmic branch of the trigeminal nerve to the brain, and use the magnetic field as a compass or as a component of the navigational map for navigation in birds [36]. However, Zapka et al. [37] reported that disconnection of the ophthalmic branch of the trigeminal nerve did not influence the birds ability to use their magnetic compass for orientation.

Magnetite structures, associated with the trigeminal nerve (ophthalmic branch), were located in the beak of pigeons and found to be involved in the magnetoreception capabilities of birds [31], but did not explain all observed behaviour. In 2011, [38] research using magnetic resonance imaging and computed tomography confirmed the presence of iron-rich cells in the upper beak of pigeons, however, these cells were discovered to be macrophages and not magnetosensitive neurons, an observation which was inconsistent with a role in magnetoreception.

2.3.2 Radical Pair Mechanism

In 1978, Schulten [39] proposed the radical pair mechanism (RPM) as a potential mediator of directional magnetic field information for animal magnetoreception. To obtain magnetic compass information by a radical pair mechanism, animals must be able to distinguish between singlet and triplet products, and be able to compare the yields in different directions with respect to the Earth's geomagnetic field. This would require an aligned array of photopigments; a condition that could be met by the alignment of receptors in the eyes of birds [21]. It is hypothesised that a radical pair process would generate characteristic patterns of activation across the retina (Figure 2.4) which would enable animals to detect the direction of the field. This would be a light dependent process requiring absorption of photons and results in photoinduced RP formation.

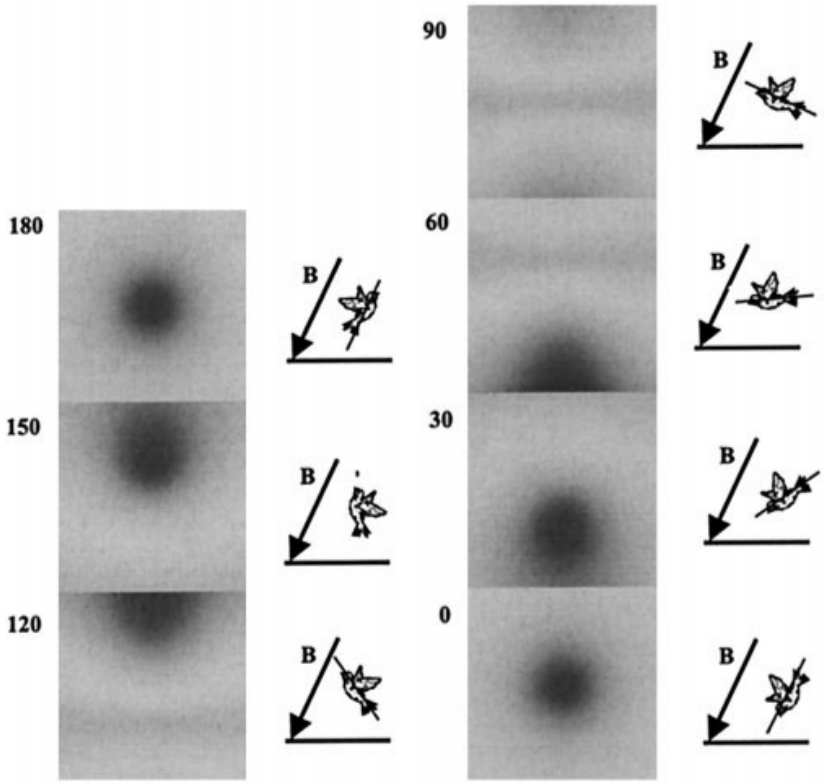

Figure 2.4: Visual modulation patterns through the geomagnetic field (0.05 mT) for a bird looking into different directions at angles 0°, 30°, 60°, 90°, 120°, 150°, and 180° with respect to the magnetic field vector [21].

The hypothesis of a 'chemical compass' requires a specific protein molecule suitable as acting as a photoreceptor and in 2000 Ritz et al. [21] suggested cryptochrome (CRY) as the candidate molecule. It was later suggested [40] that blue light photoinduced radical pairs formed magnetic field dependent yields of products which associate with nerve cells. In this paper, it was proposed that the RP reactions occur in CRY molecules that are regularly spaced, and orientationally ordered, at the bird's retina. The reaction yield at each point on the retina will depend on the relative direction of the magnetic field compared to the CRY axis at that point. Across the whole eye, a visual modulation pattern could be envisaged which would show a brighter spot when the animal looks in a particular direction (Figure 2.4).

2.4 Evidence Supporting the Radical Pair Mechanism

The radical pair model is only applicable to animals whose magnetosensitivity is based on an inclination compass, i.e. birds and amphibians [20]. However, if the radical pair mechanism is thought to be solely responsible for magnetoreception, the animal's ability to migrate should be light-dependent. The first evidence of this dependence was found by Wiltschko and Wiltschko [22] who showed, through behavioural experiments, that young homing pigeons were disorientated in total darkness. This disorientation was also shown in salamanders [41]. Later tests revealed not only was there a light dependence but also a wavelength dependence of the magnetic compass in amphibians [42], migratory birds, and pigeons [43], which is also consistent for the RPM.

2.4.1 Wavelength-dependence

European robins were shown to exhibit magnetic orientation under 424 nm (blue), 510 nm (turquoise) and 565 nm (green) light but were disorientated in 590 nm (yellow) and 635 nm (red) light (Figure 2.5) [44]. This is consistent with the absorption of FAD (flavin adenine dinucleotide), the cofactor which is essential for the physiological function of cryptochromes in magnetosensitivity. This onset of disorientation was narrowed down to between 561 nm and 568 nm using interference filters with a half-band width of only 10 mm [45]. This indicates that the light-dependent magnetoreception is only activated by the UV to green part of the spectrum, and fails to be effective in the yellow to red range.

If birds were tested in light from the blue-green region of the spectrum, they oriented to their migratory direction without problems. In the extensive tests with European robins in blue or green light, they would orient to the North in the spring and to the south in the autumn. Even in UV light (at 373 nm) the robins were able to find their proper orientation. However, when yellow and red light were used, the birds could not orient in the proper directions, and they showed a general random disorientation, Figure 2.5.

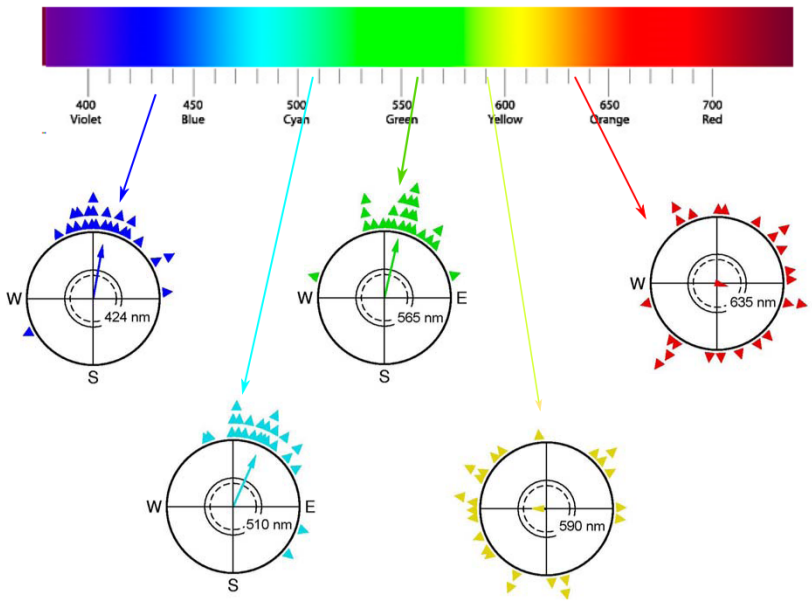

Figure 2.5: Image adapted from [20], shows the orientation behaviour of European robins in spring under different wavelengths of monochromatic light.

2.4.2 The Effects of Radio Frequency Fields

The radical pair model of magnetoreception predicts that magnetic compass orientation can be disrupted by high frequency magnetic fields in the Megahertz range. If indeed, the reaction yield is crucial for magnetoreception, interfering with the singlet-triplet interconversion would alter the output of the receptors markedly and therefore disrupt magnetoreception. These findings are inconsistent with a magnetite-only mechanism [21, 46] and, hence, investigations into the effects of radio-frequency fields on magnetic orientation might be diagnostic for the involvement of the radical pair mechanism.

It is not an easy task to predict which specific frequencies will interfere with the radical pair mechanism underlying magnetoreception because the chemical composition and the geometric structures of molecules are not yet known. However, theoretical and experimental studies have shown that they are expected in the region $0.1 - 10\,\mathrm{MHz}$ [20] where the frequency of the oscillating field matches the energetic splitting induced by the static geomagnetic field.

European robins were tested under monochromatic 365 nm green light in $1.315\,\mathrm{MHz}$ fields of $0.48\,\mu\mathrm{T}$ during spring and autumn. $1.315\,\mathrm{MHz}$ is chosen because it matches the Zeeman splitting induced by the geomagnetic field. The results show that the bird's response was dependent on the orientation between the oscillating and static geomagnetic

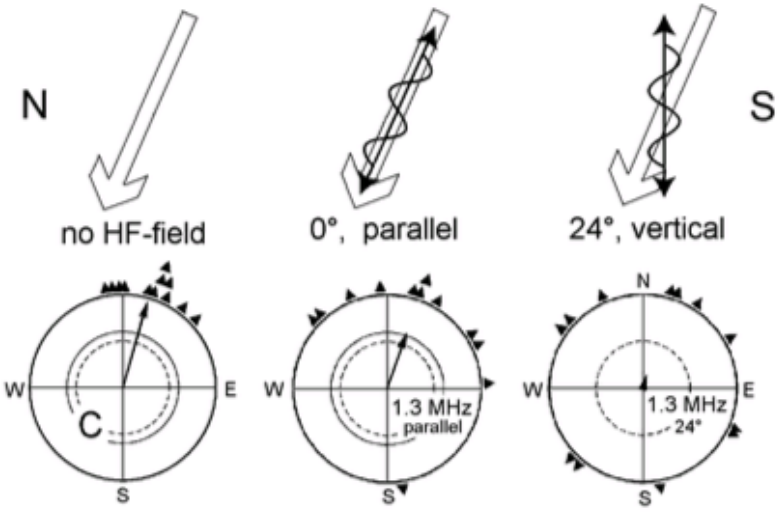

Figure 2.6: Orientation preferences of European robins in the geomagnetic field (control, C) and in high-frequency fields added to the geomagnetic field in two different orientations. The upper part of the diagram illustrates the orientation of the geomagnetic field and the high-frequency field under the three test conditions [20]

field [47]. When the oscillating field was aligned parallel to the field lines, the birds were able to orientate North in spring and South in autumn, directions which reflect normal migratory patterns. However, when the 1.315 MHz field is aligned at a 24° angle to the field lines the birds were completely disorientated, indicating that the high frequency field interferes with the magnetorecpetion mechanism.

2.4.3 Overview

Many classes of animal species are known to possess a magnetic compass sense. Behavioural studies conducted have confirmed the existence of this sense but the physiological basis of magnetoreception remains unknown. Several investigations, whose results were outlined above, have shed some light to the operation of the avian compass sense and the physiological mechanisms involved.

The evidence supporting the involvement of the RPM in the magnetosensitivity of some bird species is consistent with the available behavioural investigations; in particular, effects of wavelength of light and the effects of RF fields fit well with a photoinduced RP reaction model. The work to be presented in the following chapters aims to further investigate the consistency of this model with current behavioural evidence.

Chapter 3

Rotary RYDMR

3.1 Introduction

Optically Detected Electron Spin Resonance (ESR) is a technique first proposed and used by Sharnoff in 1967 [48] to investigate the combined effects of static and oscillating magnetic fields on the rate of a chemical reaction proceeding via a radical pair intermediate. Methods of optical detection of ESR spectra (OD ESR) of short lived radical-ion pairs (RPs) represent the wide family of so-called reaction yield detected magnetic resonance (RYDMR) [49]. In a traditional RYDMR experiment a strong, static magnetic field (typically that of an X-band ESR spectrometer, 340 mT) energetically isolates the $T_{\pm}$ states from the S/T_0 manifold by the Zeeman interaction. Application of resonant microwave radiation excites transitions between these two sets of states, altering the yield of the reaction [50]. In 2002, new experiments were reported which showed the effects of weak radiofrequency fields ($B_1 < 0.3\,\mathrm{mT}$) in the range 1 - 80 MHz applied orthogonally to weak static magnetic fields ($B_0 \leq 3.0\,\mathrm{mT}$) [50]. These experiments tested the viability of RYDMR in low fields (hence low-field RYDMR) and also provided insight into the crossover region between the zero static field (oscillating magnetic field effects (OMFE)) and high field (RYDMR) cases.

In an attempt to test for the involvement of the radical pair mechanism in magnetoreception (see Chapter 2) a series of experiments were conducted on the birds where a weak, oscillating magnetic field was superimposed on an Earth-strength static magnetic

field [46, 47, 51, 52]. In these experiments, the ability of caged birds to orient in the seasonally appropriate migration direction was tested under the influence of these magnetic fields. The results may be summarized as follows:

1. Experiments performed using a broadband 'noise' radio-frequency magnetic field in the presence of the Earth's static field showed that oscillating fields in the MHz range disrupted the orientation of birds.

2. The orientation of birds was also disrupted by monochromatic oscillating fields in the frequency range 1 - 7 MHz (0.47 µT amplitude) where the oscillating field was applied at an angle of 24° to the local geomagnetic field. However, oscillating fields with the same amplitude applied parallel to the geomagnetic field did not disrupt the orientation of the birds.

3. The orientation ability of the birds was dependent on the frequency of the oscillating field [53]. RF fields with frequencies of 0.66 MHz and higher caused the birds to be disorientated indicating that the RP involved in magnetoreception will have a fairly long life time of 2 - 10 µs.

4. The most sensitive response to oscillating fields was found for 1.315 MHz fields which matches the electron ($g = 2$) Larmor frequency of the geomagnetic field. Thus a strong resonance at a frequency proportional to the intensity of the static field is observed, arising from the Zeeman interaction.

In order to understand how a radio-frequency field can disturb a radical pair based magnetic compass, a quantitative understanding of oscillating and static magnetic field effects is necessary, particularly at strengths of the order of the geomagnetic field. Conventional RYDMR is a high field technique and the theory typically applied for its interpretation (such as the 'high-field approximation' and 'rotating frame' approach) is not applicable for the 'low-field' regime, when the hyperfine couplings within the molecule $a \geq B$, as in the case of the bird experiments. Consequently the physical techniques and theoretical models exploring weak magnetic field effects need to be investigated.

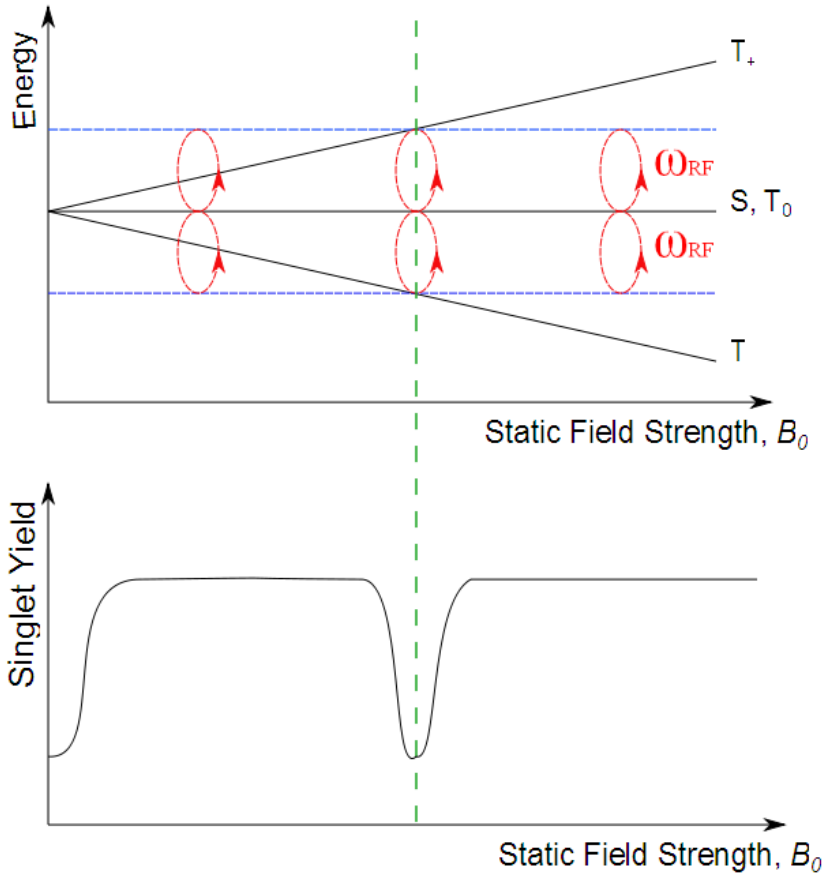

Figure 3.1: The top illustration shows a simple energy diagram, showing the reconnection of the Zeeman split states by the RF field. The exchange interaction which splits S and T_0 is assumed to be zero. The bottom illustration shows the resulting singlet yield of an S-born radical pair.

In this chapter a new experiment, rot-RYDMR, will be discussed which probes the effect an oscillating magnetic field has on the rate of the radical recombination reaction in the presence of a static field. This experiment will gain more detailed angular information than previous experiments because of the ability to alter the relative angle (hence 'rot'-RYDMR) between the static and RF fields smoothly.

3.1.1 Theory

In a typical RYDMR experiment (fixed relative angle of the two fields is 90°) a static field, B_0, induces a Zeeman splitting between the T_+ and T_- spin states and the S/T_0 manifold (analogous to a MARY experiment [54]). This separates the S/T_0 and the $T_\pm$ manifolds by an energy, ΔE, which is proportional to B_0. This picture is valid in the limit where B_0 is larger than the hyperfine couplings within the radical pair (high-field regime). If an

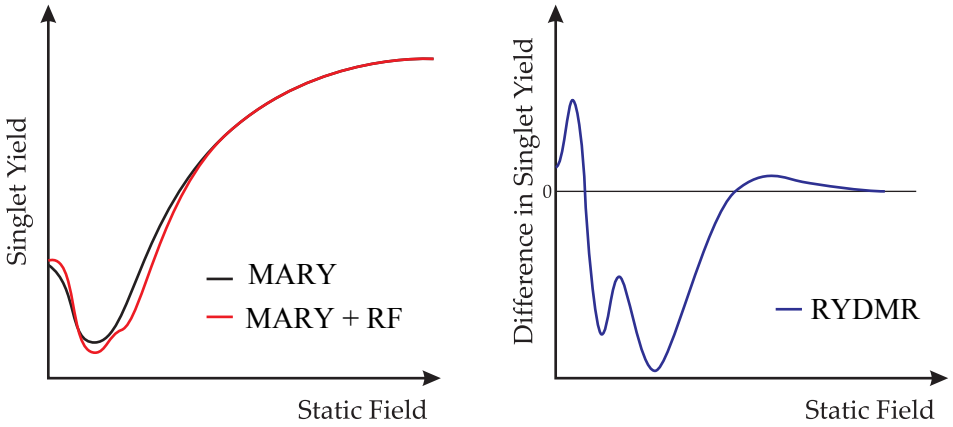

Figure 3.2: Representation showing that a RYDMR signal (right) is the difference between the MARY response and the singlet yield produced with both static and oscillating fields present.

oscillating field with fixed strength (amplitude), B_1, and frequency, ω_{RF}, is also applied it acts as a perturbation, reconnecting the S/T_0 and the $T_\pm$ manifolds when the resonance condition is met, Figure 3.1. For example, for a 36 MHz RF field this resonance will occur at 1.28 mT. This will cause an increase in the rate of $S - T$ mixing and subsequently a decrease in the singlet yield for an S-born radical pair. In a typical RYDMR experiment the frequency, ω_{RF}, strength, B_1, and angle θ (with respect to the static field) of the oscillating field are held constant and the signal intensity is recorded as a function of static field strength. In the RYDMR experiments performed in this thesis, the singlet yield is monitored by measuring the exciplex fluorescence. This is proportional to the yield of singlet RP since only RPs in the singlet state can recombine via back electron transfer to give the exciplex precursor. The oscillating field is modulated to allow for the small RF effect to be observed and the signal recorded is a representation of the effect of the oscillating field in the presence of the static field. The resulting spectrum measured shows the effect of an oscillating field at a given static field strength (Figure 3.2). Both positive and negative signals correspond to a change in the rate of $S - T$ mixing with respect to zero field they correspond to an increase and a decrease, respectively in the static-field singlet yield upon addition of the radio-frequency field.

Due to the versatility of the technique and the increased number of experimental variables when combining static and RF fields, a variety of different RYDMR experiments can be conducted [55]. To characterise the effects of the oscillating field strength, an alternative approach can be taken, and the spectra displayed in a different way by sweeping

the oscillating field strength, B_1, under the influence of a fixed static field strength, B_0, at a fixed frequency, ω_{RF}, and fixed angle, θ. This kind of experiment yields so-called RYDMR-B_1 spectra and can be compiled by extracting data points from RYDMR-B_0 curves.

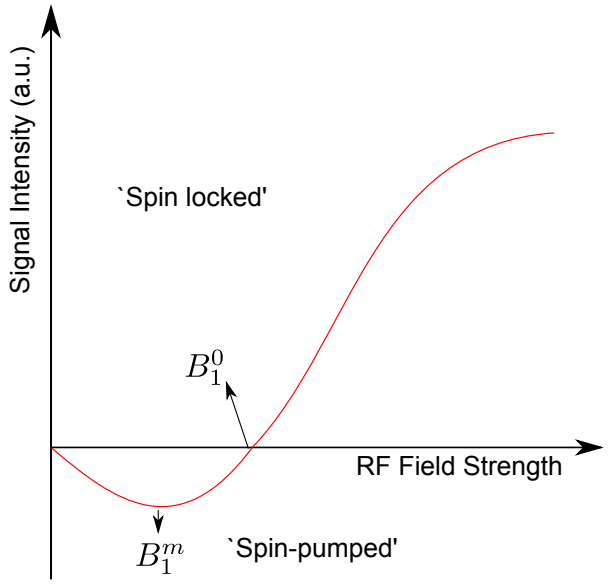

Figure 3.3: Schematic of a typical RYDMR-B_1 spectrum. The zero-crossing is characterised by B_1^0 and the minimum in the curve is characterised by B_1^m. Positive signals refer to the 'spin-locking' regime and negative signals refer to the 'spin-pumping' regime. See Section 3.1.2 for details.

In order to compare RYDMR-B_1 spectra under different conditions two values are used. The first, B_1^m, defines the minimum in the RYDMR-B_1 spectrum and corresponds to the greatest RF-induced increase in the rate of S − T mixing. The second parameter, B_1^0, defines the point at which the curve passes through zero signal intensity, i.e. when the rate of S − T mixing on addition of an oscillating field is equal to that of the static field only case. Both of these parameters are shown in (Figure 3.3) and can be extracted from conventional RYDMR-B_0 spectra when conducted at different B_1 field strengths. This is achieved by plotting the signal intensity at a given static field strength as a function of B_1 (Figure 3.4). Positive signals in the RYDMR spectra correspond to a decrease in the rate of S − T interconversion in the presence of an oscillating field and are known as spin-locking signals (see below). Negative RYDMR signals correspond to an increase in the rate of S − T interconversion and are known as spin-pumping signals. See Section 3.1.2.

The final form of RYDMR experiment presented in this thesis allows one to characterise the effects of the angle between the static and oscillating fields, θ. This experiment is

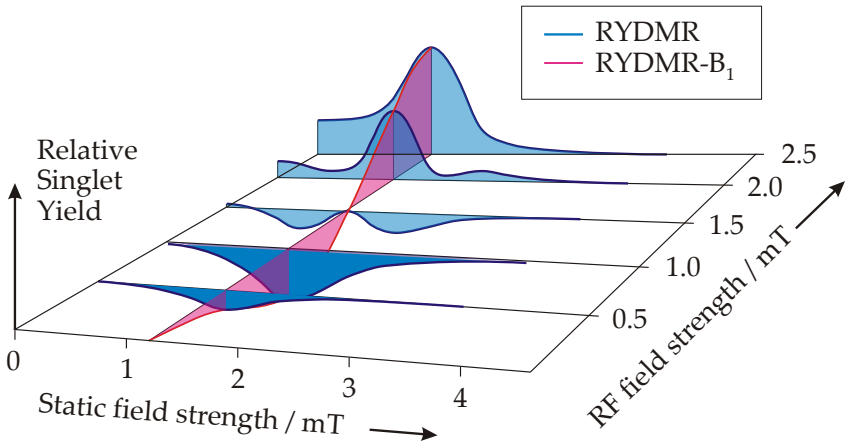

Figure 3.4: The relationship between RYDMR and RYDMR-B_1 spectra, shown schematically for a 36 MHz RF field. The figure has been adapted from [54].

called rot-RYDMR (rotary-RYDMR) and is recorded as a function of θ whilst the static field strength, B_0, the oscillating field strength, B_1, and the frequency, ω_{RF}, are held constant.

3.1.2 Spin-Locking

The effect of the RF field strength, B_1, and also its orientation with respect to the static field, B_0 was previously investigated by Koptyug [56] in optically detected ESR and by Batchelor *et al.* [57] in high field RYDMR experiments. In both these papers an inversion of the signal was observed if the strength of the RF field was sufficiently large but was only observed for perpendicular orientations of the two fields. This phenomenon is called 'spin-locking' and occurs when the applied RF field strengths impedes $\mathrm{S} - \mathrm{T}_0$ mixing.

In 1992 Batchelor [57] described 'spin-locking' as being similar to the MARY effect with the use of the rotating frame approximation. This model suggested that strong oscillating fields can no longer be treated as a perturbation of the system and thus the rotating frame states should be used which are a linear combination of the laboratory frame states. As resonance is approached the mixing of these states and their energy level separations change and so do the transition probabilities between them altering the rate of $\mathrm{S} - \mathrm{T}$ mixing. In the rotating frame when the system is at exact resonance the effective field in the B_0 direction is negligible and the system experiences a static B_1 only. This is hence analogous to the MARY effect resulting from the static field in the laboratory

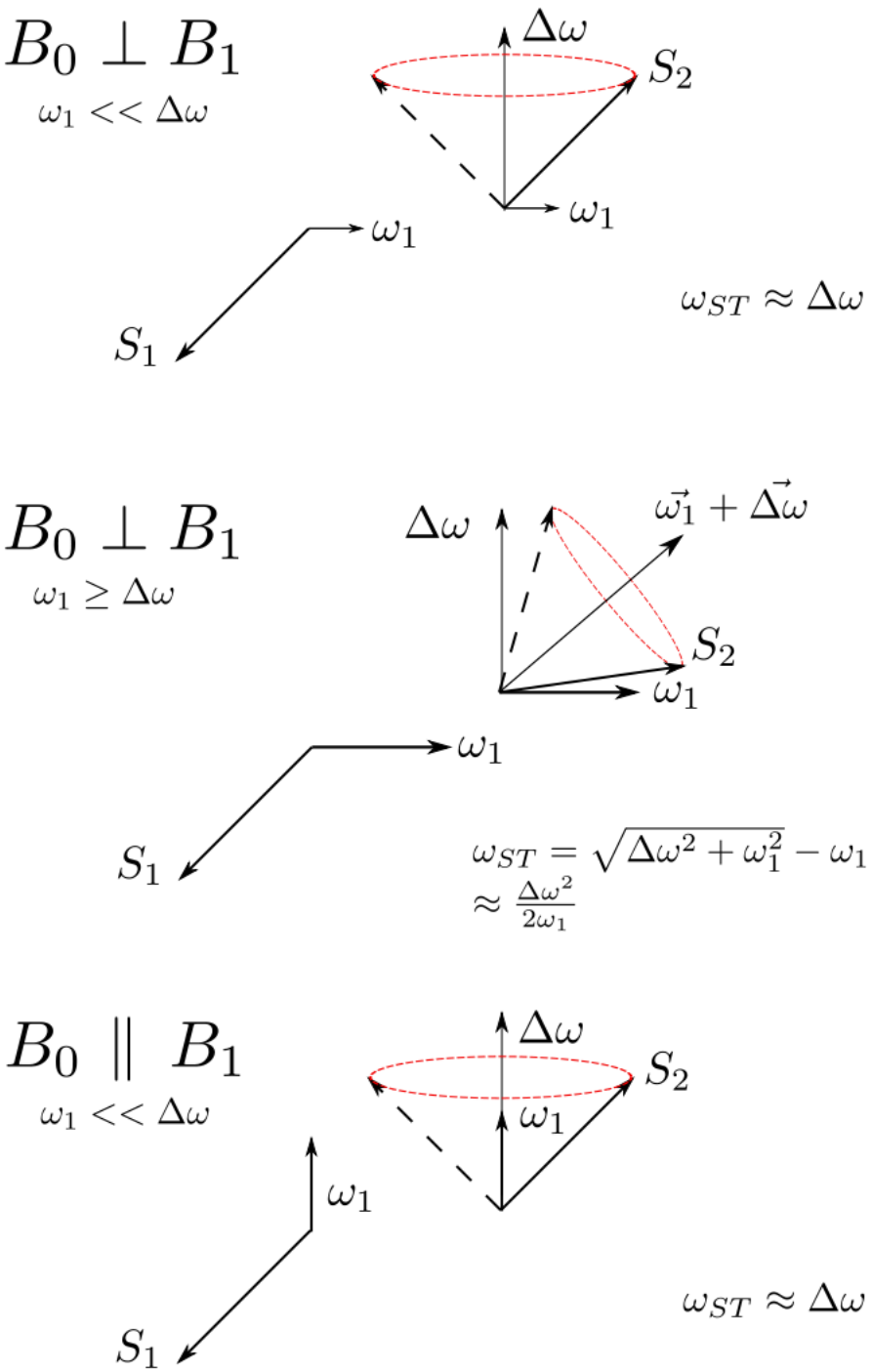

Figure 3.5: A vector model of spin-locking in the rotating frame [56].

frame. Recall that in the MARY experiment the $S - T_0$ states are unaffected by the increasing static field but the $T_\pm$ states are isolated by B_0 (the Zeeman effect). In this model, for the RYDMR experiments considered in the rotating frame, an increasing B_1 will isolate the rotating frame triplet states, $X_\pm$, from the rotating frame triplet state X_0. Since X_0 is formed from mixing of the $T_\pm$ laboratory frame states any mixing between the S and the X_0 is forbidden. This inhibits any $S - T$ mixing in a presence of an oscillating field of sufficient strength. A theoretical comparison of MARY and RYDMR-B_1 spectra showed that this theory did not hold in the general case [55, 58].

Earlier in 1989, Koptyug [56] proposed another high field theory of 'spin-locking' in the rotating frame using a vector model (Figure 3.5). Consider a radical pair first in the absence of a RF field: the electron spin of radical one, S_1, is considered stationary in the rotating frame and the electron spin of radical two, S_2, precesses about B_0 with a frequency, $\Delta\omega$. $\Delta\omega$ is approximately equal to the difference in precession frequencies of the two spins and is proportional to B_0 in the absence of any hyperfine interactions. $\Delta\omega$ arises because of differences in hyperfine couplings of the two radicals or g-value differences if at higher fields. $S - T_0$ mixing will occur with a frequency, ω_{ST}, approximately equal to $\Delta\omega$. If an RF field is applied perpendicular to B_0 at the Larmor resonance frequency, such that $\omega_1 \ll \Delta\omega$ ($\omega_1 = g\beta B_1$, where B_1 is the strength of the RF field), $S - T_0$ mixing will occur with a frequency $\omega_{ST} = \Delta\omega$. This is the 'spin pumping' effect of an oscillating field. In this regime, negative resonances will be observed because the S/T manifolds are reconnected with $T_\pm$ and hence cause an increase in $S - T$ interconversion.

If the strength of B_1 is increased, such that $\omega_1 \geq \Delta\omega$, S_1 now precesses around the ω_1 direction and S_2 precesses around the vector sum $\omega_1 + \Delta\omega$. If the spins precess with frequencies ω_1 and $\sqrt{\omega_1^2 + \Delta\omega^2}$, respectively the frequency of $S - T_0$ mixing will be given by,

$$\omega_{ST} = \sqrt{\omega_1^2 + \Delta\omega^2} - \omega_1 \tag{3.1}$$

$$\omega_{ST} = \omega_1 \left(1 + \frac{1}{2}\left(\frac{\Delta\omega^2}{\omega_1^2}\right) - \frac{1}{8}\left(\frac{\Delta\omega^2}{\omega_1^2}\right)^2 \text{.....}\right) - \omega_1 \tag{3.2}$$

$$\omega_{ST} \approx \frac{\Delta\omega^2}{2\omega_1} \tag{3.3}$$

This is less than rate of $S - T_0$ mixing, $\omega_{ST} = \Delta\omega$, obtained in the presence of a small oscillating magnetic field. Consequently a decrease in $S - T_0$ mixing occurs for strong oscillating field strengths and a 'spin-locking' effect is observed. In this regime, positive resonances are observed because the rate of $S/T - T_\pm$ mixing (as caused by reconnection of states upon application of an RF field) is reduced. If the strength of B_1 is increased further, it is expected that spin mixing would cease as both spins precess with a frequency, ω_1. This is analogous to NMR spin-locking [59].

Finally, if the RF field is parallel to the static field, B_0, 'spin-locking' is not possible. This is because $\Delta\omega$ and ω_1 are always additive, so the strength of the RF field has no other effect on the rate of $S - T$ mixing, ω_{ST}. For parallel fields negative resonances are observed, consistent with the reconnection of the S/T with $T_\pm$ as caused by application of an RF field.

3.1.3 Experimental

In this new experiment, the angle, θ, between the static and oscillating fields can be altered and spectra can be recorded as a function of θ for fixed field strengths, B_0 and B_1. This is possible due to the special design of the static field coils as described below and constitutes a significant further development of previous apparatus used [54, 55].

A block diagram shows the set up of the rot-RYDMR experiment, (Figure 3.6). Continuous illumination is provided by UV light from a Thermo-Oriel 6293 1000 W Xenon arc lamp and is powered by a Thermo-Oriel 69920 power supply unit which maintains constant light output. An electro-mechanical shutter allows the irradiation time to be controlled using a PC via the graphical interface, LabView. A water filter removes infra-red (IR) radiation that would otherwise heat the sample and a UG-5 250-400 nm band-pass filter selects the correct wavelength of light for photolysis. Light is directed to and from the sample using a 40 mm diameter glass lens. Sample fluorescence is detected perpendicular to the excitation radiation and is focused onto a photomultiplier tube (PMT) (Hamamatsu, R928) using a glass lens. A suitable band pass interference filter was used before the PMT to select the correct wavelength of detection that matches the emission maximum of the exciplex. For all systems studied in this chapter an interference filter

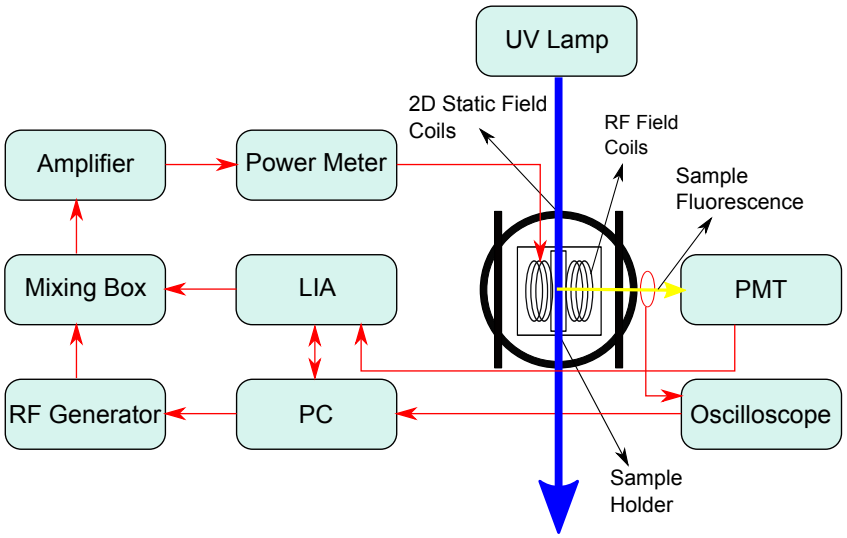

Figure 3.6: A block diagram of the rot-RYDMR apparatus.

(100 nm bandwidth, centred at 548 nm) was used. For each experiment, the gain, and hence the voltage applied to the PMT, was adjusted such that the total output was constant across all experiments. This gave the maximum sensitivity without saturation of the PMT detector such that the light intensity gave a linear response with the PMT output.

The solution under investigation is contained within a 3 mm × 3 mm (cross section) SUPRASIL quartz flow cell with short lengths of 3 mm internal diameter glass tubes at each end to allow for the attachment of silicone tubing. The solution is re-circulated, using a flow system and pump, through 3 mm (internal diameter) polytetrafluoroethylene (PTFE) tubing, used because of its compatibility with most organic solvents. Short lengths of a more flexible, minimally deteriorating silicone tube were used to connect the ends of the PTFE to the cuvette. The design of the flow system was optimised to minimise sample degradation through circulation of the sample.

3.1.4 The Coils

The static field coils consist of two sets of large, water cooled Helmholtz coils which are locked perpendicular to each other (Figure 3.7). The static field is produced by two time-dependent sinusoidal voltages which are applied to each set of coils. If the amplitudes of the two fields from each set of coils are given by B_{perp} and B_{par} then the overall field is given by the resultant of these two fields, $B_0^2 = B_{perp}^2 + B_{par}^2$ and the angle of the static

field relative to the RF field, θ, will be given by $\arctan(B_{perp}/B_{par})$. The coils are water cooled by a flow system to avoid overheating.

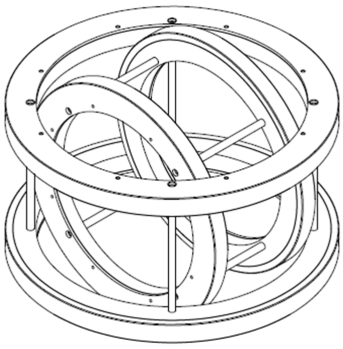

Figure 3.7: Design of the static field coils [55].

3.1.5 The RF system

Radio-frequency electronics are a highly specialised field and the design of RF systems is complex and time consuming. A major redesign of the apparatus was required such that it was possible to attain larger RF field strengths compared to previous experiments [55]. The best method to do this was to generate a fixed RF frequency with a tuned coil circuit so that a greater proportion of amplified output power could be used to generate a magnetic field. A fixed-frequency of 36 MHz was chosen because this resonance was found to be comparable to the hyperfine couplings in many of the systems studied, [60]. This frequency also offers a compromise between a higher frequency field which would resonate at larger field strengths producing larger signal intensities and the desire to use lower frequency fields to study the effects in the low field effect region.

Within the sample box (Figure 3.8), the cuvette containing the sample solution fits between a pair of small Helmholtz coils which produce the RF field. Two capacitors, one in parallel with the RF coils, one in series, allow for tuning and impedance matching over a small range of frequencies and powers. Impedance matching is necessary in order to allow loss-less transmission of RF power. In a non-matched circuit, energy would be used to set up a standing wave in the transmission line. This will cause the power to be reflected back to the amplifier output causing a high standing wave ratio (SWR). If the SWR is high, the voltage associated with it could damage the amplifier. A radio frequency power/SWR

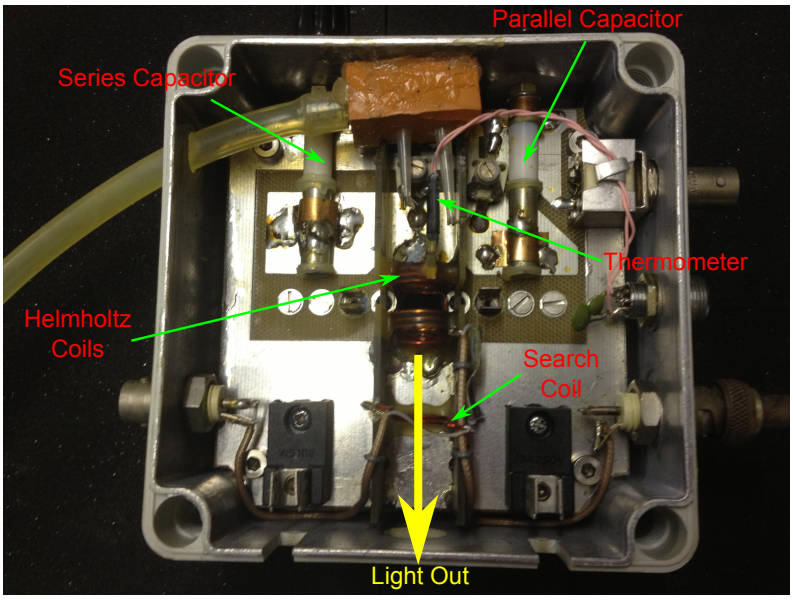

Figure 3.8: The sample box which is normally covered with a screw down lid. UV light enters the box from behind the sample cuvette and fluorescence is detected perpendicularly to this through the hole shown on the box.

meter (Diamond Antenna SX-200) is connected in series between the amplifier and sample block so that the measurement of the power and quality of tuning was possible. The tuned circuit matches the 50 Ω output impedance of the amplifier meaning that the amplifier output could be terminated at the coils and all available radio-frequency power could be dissipated to the coil and produce a strong oscillating magnetic field. Other features of the system include a platinum thermometer, affixed to the coils, allowing real-time monitoring of the temperature and the addition of a probe coil to allow for monitoring of the field strength during the course of an experiment. The coils were cooled using a directed jet of compressed air to reduce the effect of heating. The maximum power that the coils could reach was found to be 30 W [55].

3.1.6 Sensitivity

In order to increase the sensitivity of the experiment, modulation techniques are used. Rot-RYDMR experiments rely on the modulation of the RF field. This is in contrast to modulated-MARY which employs an audio-frequency modulation of the static field. The consequence of modulating the static field in the modulated MARY experiment is to produce the first-derivative of the MFE plot. Modulation of the RF field may be (roughly) understood as the effect an oscillating field imposes on a MARY curve (i.e. the

difference between employing both static and oscillating fields and the effect of the static field alone).

A dual-channel, digital Lock-In Amplifier (LIA) (Stanford Research Systems SRS830) is used as a phase sensitive detector (PSD). The signal from the PMT is divided using a voltage divider at the output, with one branch going to the LIA signal input and the second to an auxiliary input. Phase sensitive detection is applied to the signal from the signal input and the total signal amplitude is measured at the auxiliary input.

RF modulation is achieved through the home built 'signal mixing' box. The 36 MHz RF signal is mixed with a 331 Hz reference output from the LIA. Ideally the RF signal would be 100% modulated by the audio-frequency signal. However, in reality this perfect modulation was not possible and only a 79% modulation (reproducible) could be obtained.

3.1.7 Static Field Strength

The static field was calibrated using a 3D gauss meter (SENSIS GmbH C-H3B-2m-E3D-10kHz) to ensure that the static field strength was constant over the full range of angles. The 3D gauss meter probe was placed in the centre of the two pairs of coils and was fixed in place using clamps. Signal averaging was performed to reduce noise and the probe was calibrated by placing it within a μ-metal enclosure. The calibration results for a 2.4 mT field are shown in Figure 3.9. The mean field measured was 2.39 mT with a standard deviation of 1.42%.

3.1.8 Oscillating Field Strength

The oscillating field strength was calibrated using a RF field probe, supplied by Aaronia AG. The voltage (Pk-Pk) across the RF field coils was measured and converted into a field strength (Pk-Pk) using a supplied program. The field strengths (Pk-Pk) were converted into rms values using a conversion factor 1 mT(Pk-Pk):0.453 mT(rms). This value was calculated by simulating the modulation of the RF field using [58];

$$A(t) = \left[1 - M \sin^2(\pi t/2)\right] A^{\max} \tag{3.4}$$

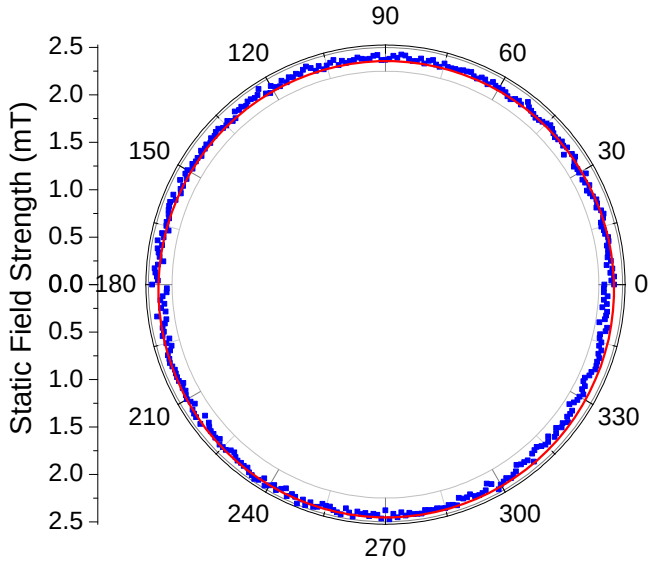

Figure 3.9: Calibration of the static field at 2.4 mT measured using a 3D gauss meter for 360 angles during a computer controlled field rotation in the xz plane.

where $A(t)$ is the modulated RF field, M is the fractional modulation depth (measured on the oscilloscope), $A^{\max}$ is the peak value of the modulated quantity and time, t, is measured in modulation cycles. An arbitrary value $A^{\max} = 1\,\mathrm{mT}$ and a modulation depth $M = 0.79$ is used.

3.2 Systems studied

Electron donors used were pyrene (Py) and chrysene (Chy) and their deuterated forms and electron acceptors used were 1,3-dicyanobenzene (1,3-DCB) and 1,4-DCB. Combinations of $\mathrm{Py_{h10}}$/1,3-DCB, $\mathrm{Py_{d10}}$/1,3-DCB, $\mathrm{Chy_{h12}}$/1,4-DCB and $\mathrm{Chy_{d12}}$/1,4-DCB (Table 3.1) were chosen in order to investigate systems with a range of hyperfine coupling constants. Details of the hyperfine coupling constants within these six molecules are shown in Appendix E. The solvent cyclohexanol:acetonitrile (9:1) (CH/ACN) was used and chosen because of its dielectric constant which favours the formation of both the exciplex and RP and its viscosity which favours recombination (Section 1.3.2). Unless otherwise stated, the concentration of the electron acceptor molecule in the sample was 0.4 mM and that of the electron donor was 40 mM (100 times in excess). These concentrations were optimised to give the best signal to noise of the field effects on fluorescence (data not shown). Samples were dissolved in acetonitrile and sonicated before the addition of cyclohexanol in order

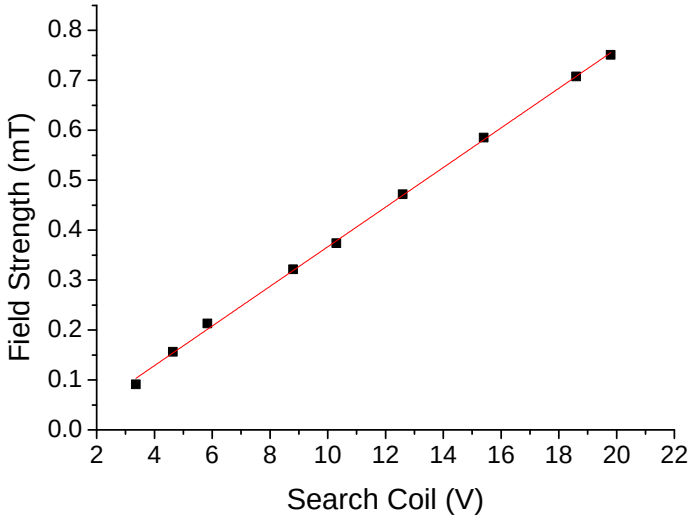

Figure 3.10: Calibration of the RF magnetic field where 1 V(Pk-PK) measured on the search coils corresponds to a field strength 0.04 mT(rms).

to ensure that mixing was complete and uniform. Degassing was not performed because this was shown to have little effect on the sample and the magnitude of the spectra [54]. Where necessary several scans were run and averaged in order to improve signal to noise ratio.

	a_D	a_A	a_{eff} for RP
$Py^{\bullet+}_{h10}$/1,3-DCB$^{\bullet-}$	1.01	1.04	1.45
$Py^{\bullet+}_{d10}$/1,3-DCB$^{\bullet-}$	0.25	1.04	1.07
$Chy^{\bullet+}_{h12}$/1,4-DCB$^{\bullet-}$	0.81	0.46	0.93
$Chy^{\bullet+}_{d12}$/1,4-DCB$^{\bullet-}$	0.20	0.46	0.50

Table 3.1: Hyperfine couplings, a_{eff}, (mT) for four RP systems calculated from literature values [61, 62]. It shows the range of effective hyperfine coupling constants of the RPs studied, Equation 1.34 - Equation 1.35. The effective hyperfine coupling constant for the electron donor and acceptor are given by a_D and a_A respectively.

3.3 Theoretical Methods

3.3.1 γ-COMPUTE

All theoretical results in this thesis were produced using a γ-COMPUTE (Calculation over One Modulation Period Using Time Evolution with γ-averaging) algorithm coded in Matlab. This was implemented by Rodgers [58] to model the effects of static and oscillating fields, and the orientation between them, efficiently in the low-field regime.

This algorithm has been adapted from the original, formulated by Hohwy *et al.* [63] to simulate solid-state NMR powder spectra.

All practical and theoretical details of γ-COMPUTE can be found in [58] but a brief summary will be given here.

Consider a spin correlated radical pair (SCRP) evolving under the influence of;

- isotropic electron-nuclear hyperfine interactions
- the isotropic Zeeman interactions of the electron spins with a static magnetic field $B_0 = \omega_0/\gamma_e$ and a linearly polarised RF field of peak strength, $B_1 = \omega_1/\gamma_e$ and frequency $\omega_{RF}/2\pi$ where γ_e is the magnetogyric ratio of the electron.

The coherent evolution of the radical pair, described by a spin density operator $\hat{\rho}(t)$, is determined by the spin Hamiltonian;

$$\hat{H}(t;\gamma) = \sum_{N=1}^{2}(\sum_{i} a_{iN}\hat{\mathbf{S}}_N.\hat{\mathbf{I}}_{iN} + \omega_1\hat{S}_{Nx}\sin(\omega_{RF}t+\gamma) + \omega_0[\hat{S}_{Nz}\sin\theta + \hat{S}_{Nx}\cos\theta]) \quad (3.5)$$

in which t is the time after formation of the radical pair and γ is the phase of the RF field at $t = 0$. N labels the radical and i labels the nuclear spin within that radical. $\hat{\mathbf{S}}$ and $\hat{\mathbf{I}}$ are the electron and spin nuclear angular momentum operators respectively and a_{iN} is the hyperfine coupling constant of nucleus, i, in the radical, N. The angle between the two magnetic fields is given by θ. The following assumptions which are valid for the weak fields employed here are made in the calculation;

- Anisotropic magnetic interactions are averaged in solution
- Spin evolution arising from Δg and from the nuclear Zeeman interaction can be neglected
- Exchange and dipolar interactions are assumed to be negligible

Although it is assumed that the exchange interaction is negligible it is acknowledged that since γ-COMPUTE is based on spin-selective reactions even weak exchange can interfere with the coherent spin evolution (e.g. CIDNP). The total probability that the

radical pair will recombine (the 'singlet yield') depends on the state that the RP is in at the moment of radical encounter and also the diffusion of the RP. The radicals are assumed to recombine in a diffusion controlled manner and are deemed reactive if they are in the S state and unreactive in the T state. This probability is given by;

$$\phi_S = \int_0^\infty \langle \hat{P}^S \rangle(t) f(t) dt \tag{3.6}$$

where $\langle \hat{P}^S \rangle(t)$ is the probability that the RP will be in a S state at the time of encounter, t, and $f(t)$ is the distribution of encounter times, $f(t) = ke^{-kt}$, where k is the first order recombination rate constant. The expectation value of the singlet projection operator, $\hat{P}^S$, is given by

$$\langle \hat{P}^S \rangle = \mathrm{Tr}[\hat{\rho}(t)\hat{P}^S] = \frac{1}{M}\mathrm{Tr}[U^\dagger(t,0;\gamma)\hat{P}^S U(t,0;\gamma)\hat{P}^S]. \tag{3.7}$$

The radical pair is assumed to be formed initially in a singlet state. For $M = 2^n$ (n spin-1/2 nuclei) $\hat{\rho}(0) = \frac{\hat{P}^S}{M}$. $U(t,0;\gamma)$ is the spin evolution operator describing the interval 0 $\rightarrow t$. Since the RP has equal probability of being created at any point during a cycle of the RF field $\langle \hat{P}^S \rangle(t)$ must be averaged over a uniform distribution of γ in the interval 0 - 2π. The Hamiltonian is periodic and hence the initial RF phase may be treated as a time shift

$$\hat{H}(t;\gamma) = \hat{H}(t + 2m\pi/\omega_{RF};\gamma) \quad \forall m \in \mathbb{Z} \tag{3.8}$$

$$\hat{H}(t;\gamma) = \hat{H}(t + \gamma/\omega_{RF}). \tag{3.9}$$

This property means that the spin evolution may be divided into contributions from each RF period, $T = 2\pi/\omega_{RF}$, into n time steps plus contributions arising due to spin evolution during the final, partially completed RF cycle. The unit propagator for one RF cycle, T, may therefore be found according to;

$$U(T,0;\gamma) = \exp[-\mathrm{i}\int_0^T \hat{H}(t;\gamma)dt] = \exp(-\mathrm{i}\bar{H}T) \tag{3.10}$$

where $\bar{H}$ is the zero RF phase average Hamiltonian.

This code has been further developed by Mr Jason Lau to further improve the performance of RYDMR simulations. This was achieved by assuming that the radicals are separated at a distance at which there are no interactions between them, that is

$$\hat{H}(t;\gamma) = \hat{H}_A + \hat{H}_B \tag{3.11}$$

where $\hat{H}_N$ is the time dependent Hamiltonian for the radical N.The spin-space can then be separated into two individual radical spin-spaces using Equation 3.7,

$$\langle \hat{P}^S \rangle(t) = \frac{1}{4} + \frac{1}{M} \sum_{q,r} \mathrm{Tr}\left[U_A(t;\gamma).\hat{S}_{Aq}.U_A(t;\gamma)^\dagger.\hat{S}_{Ar}\right].\mathrm{Tr}\left[U_B(t;\gamma).\hat{S}_{Bq}.U_B(t;\gamma)^\dagger.\hat{S}_{Br}\right] \tag{3.12}$$

where $\hat{S}_{Aq;r}$ and $\hat{S}_{Bq;r}$ are the electron spin operators in the x,y,z directions for radical A and B, respectively. The first trace in Equation 3.12 only contains interactions within the radical A and therefore the spin-space of the spin operators and spin propagators in the first trace are the electron and all the magnetic nuclei in radical A. Similarly, the same applies to the second trace in Equation 3.12. The effective total matrix size for Equation 3.12 is the sum of the spin-space for radical A and radical B whilst the matrix size for Equation 3.7 is the product of spin-space for radical A and B. This reduces the computer memory needed to store the spin matrices and allows for the inclusion of more nuclear spins in the calculations. γ-COMPUTE was used with Equation 3.12 and the singlet projection was calculated. The calculations were furthermore accelerated by exploiting any symmetry within the radical species used and including these within the simulations. Equivalent spins can be coupled and this reduces the spin-space of the radicals. The spin-space reduction of pyrene is 90% whilst for 1,3-DCB it is 37%.

The calculations in this work were therefore performed and implemented in conjunction with Mr Jason Lau.

3.4 Results and Discussion

Rot-RYDMR spectra were recorded for all four systems using a variety of B_1 field strengths (0.11 mT - 0.43 mT) and B_0 field strengths (0.0 mT - 4.0 mT). For each combination of

field strengths, the angle, θ, was swept from 0° - 180°. Rot-RYDMR data are shown in Figure 3.11 for $B_1 = 0.11\,\mathrm{mT}$ and $B_1 = 0.43\,\mathrm{mT}$. A complete set of data can be found in Appendix A. All experiments are performed using a 36 MHz RF field, chosen because this resonance was found to be comparable to the hyperfine couplings in many of the systems studied, [60]. This frequency corresponds to a timescale which is much shorter than the RP recombination lifetime and therefore oscillating field effects can be observed.

The data (Figure 3.11) clearly show that for all systems the rot-RYDMR signals have a strong dependence on the angle between the two fields and the strength of the applied RF field. It can be seen that for all systems the signal intensity increases with increasing RF field strength. This is the case because as the strength of the RF field increases it becomes an increasing perturbation on the system. For parallel orientations the size of spin-pumping signal will increase in magnitude as the efficiency of $\mathrm{S}-\mathrm{T}$ mixing becomes more efficient and for perpendicular orientations the signal intensity increases as the efficiency of $\mathrm{S}-\mathrm{T}$ mixing is reduced.

As expected, for a zero static field ($B_0 = 0.0\,\mathrm{mT}$) the plots show no orientation dependence (red flat lines) but do show a non zero signal intensity. This corresponds to the oscillating magnetic field effect (OMFE) for 36 MHz and indicates how an oscillating field affects the rate of $\mathrm{S}-\mathrm{T}$ mixing. The origin of the $\mathrm{S}-\mathrm{T}$ interconversion in the presence of RF fields arises when the oscillating field is on-resonance with the hyperfine induced splitting of energy levels. OMFEs are most pronounced when the frequency of the applied RF field matches a hyperfine splitting in one of the radicals [60]. For $\mathrm{Py}_{\mathrm{h10}}$/1,3-DCB the frequency corresponding to the hyperfine splitting is 28 MHz and 28.9 MHz whilst for $\mathrm{Chy}_{\mathrm{d12}}$/1,4-DCB it is 5.7 MHz and 12.7 MHz. So an OMFE corresponding to a 36 MHz RF field would be more pronounced for $\mathrm{Py}_{\mathrm{h10}}$/1,3-DCB.

The effect of the OMFE can be better visualised by plotting the signal intensity for $B_0 = 0\,\mathrm{mT}$ as a function of B_1 field strength. This data is shown in Figure 3.13 for $\mathrm{Py}_{\mathrm{h10}}$/1,3-DCB and $\mathrm{Chy}_{\mathrm{d12}}$/1,4-DCB alongside their respective simulations and shows that the OMFE is dependent on the hyperfine coupling constants within the system and also on the strength of the RF field strength, B_1. The agreement between experimental and theoretical data can be seen to be strong for the case of $\mathrm{Chy}_{\mathrm{d12}}$/1,4-DCB but not as

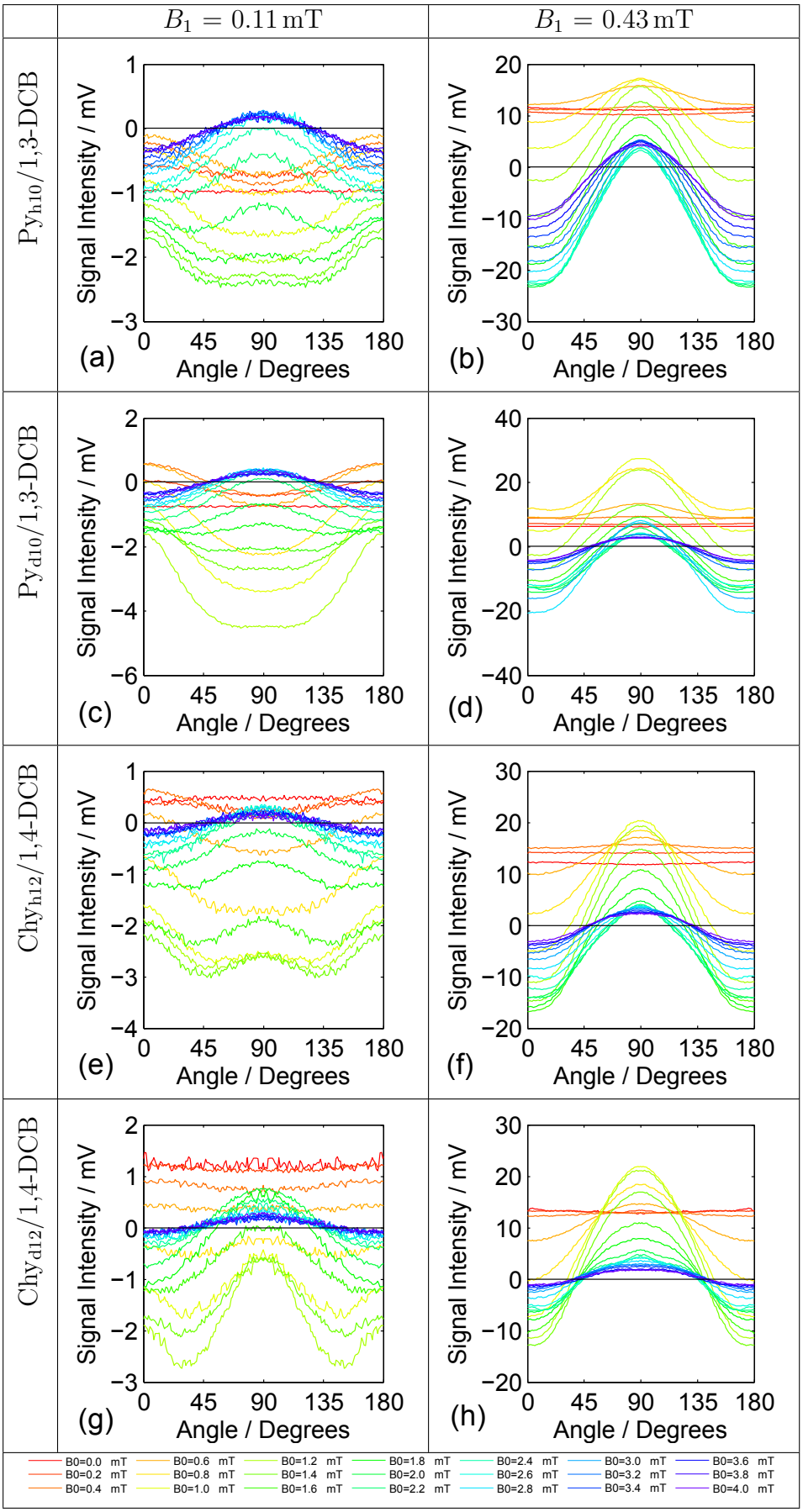

Figure 3.11: Experimental rot-RYDMR results for all systems studied. B_0 field strengths ranging from 0.0 - 4.0 mT are shown within panels. Spectra were recorded for different B_1 field strengths, 0.11 mT (left) and 0.43 mT (right), shown in different panels, and a frequency $\omega_{RF} = 36$ MHz.

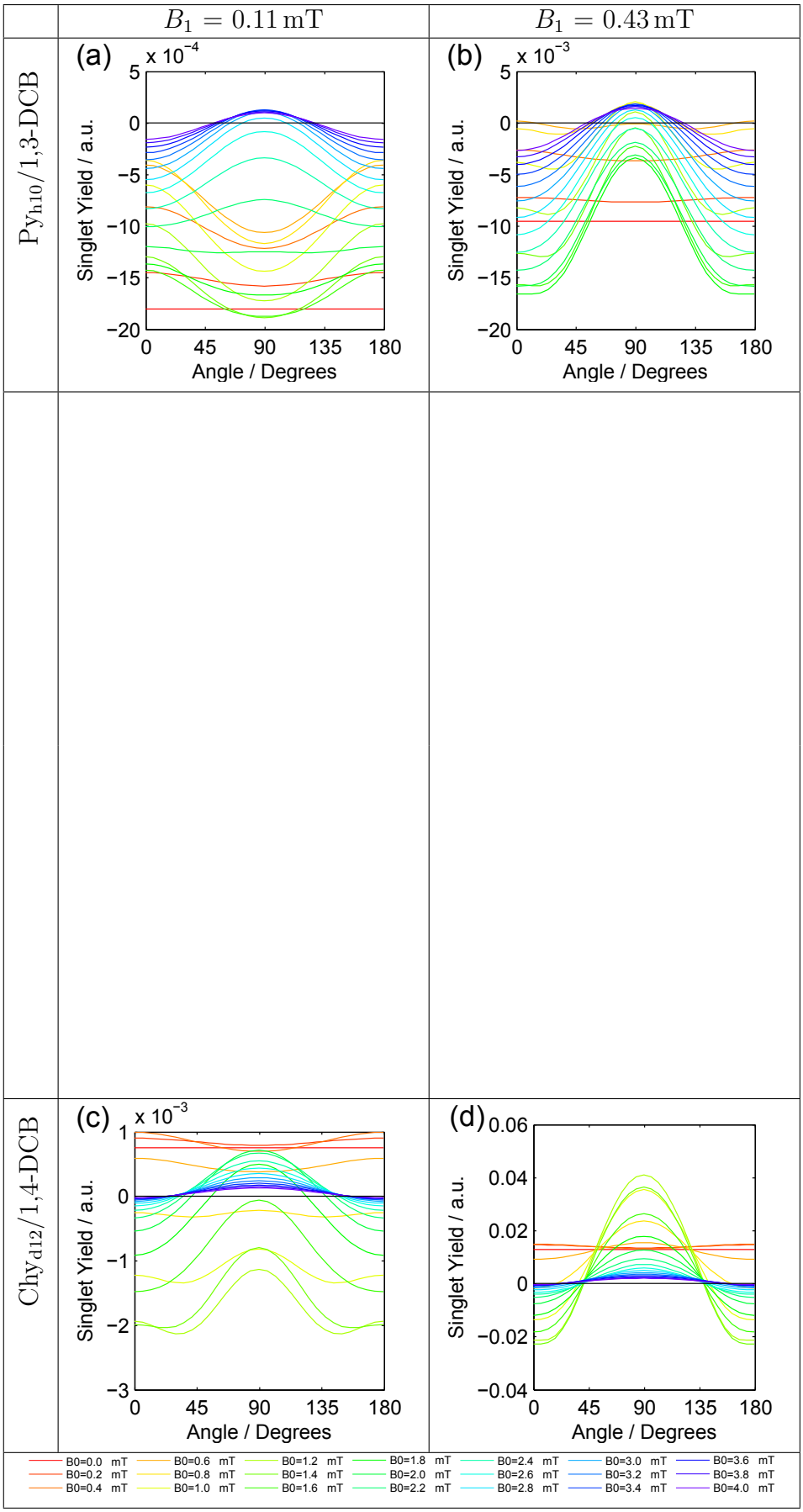

Figure 3.12: Theoretical rot-RYDMR results for $\mathrm{Py_{h10}}$/1,3-DCB (top) and $\mathrm{Chy_{d12}}$/1,4-DCB (bottom). Spectra were calculated for different B_1 field strengths, 0.11 mT (left) and 0.43 mT (right), shown in different panels, and a frequency $\omega_{RF} = 36\,\mathrm{MHz}$. Global optimisation of $\mathrm{Py_{h10}}$/1,3-DCB produced $k = 86.16\,\mu\mathrm{s}^{-1}$ and $k = 55.34\,\mu\mathrm{s}^{-1}$ for $\mathrm{Chy_{d12}}$/1,4-DCB. Calculations were performed using 32 time steps, n.

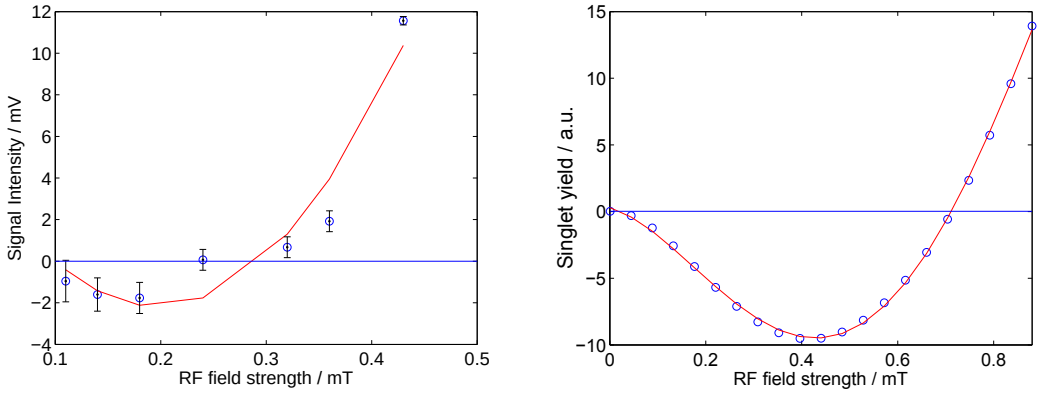

(a) Py_{h10}/1,3-DCB (exp)

(b) Py_{h10}/1,3-DCB (sim)

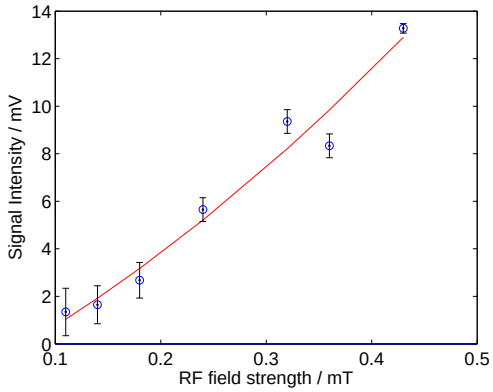

(c) Chy_{d12}/1,4-DCB (exp)

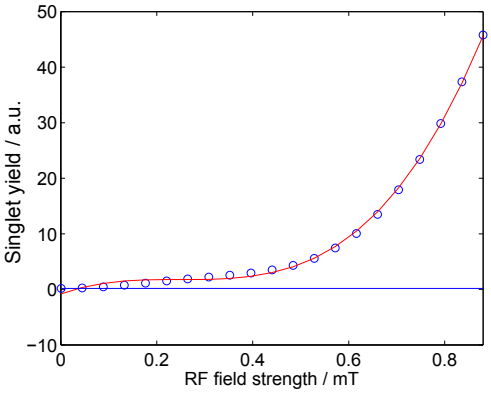

(d) Chy_{d12}/1,4-DCB (sim)

Figure 3.13: B_1-spectra ($B_0 = 0\,\mathrm{mT}$) for a 36 MHz oscillating field for Py_{h10}/1,3-DCB and Chy_{d12}/1,4-DCB experimental (extracted from rot-RYDMR data) (left) and theoretical data (right). Simulations were performed using $k = 86.16\,\mu s^{-1}$ and $k = 55.34\,\mu s^{-1}$ for Py_{h10}/1,3-DCB and Chy_{d12}/1,4-DCB, respectively.

strong for Py_{h10}/1,3-DCB. For Py_{h10}/1,3-DCB the B_1-spectra ($B_0 = 0$) show that the signal intensity of the OMFE initially decreases with increasing RF field strength and negative signals are observed (spin-pumping). It then reaches a minimum and subsequently rises, passing through zero intensity, and positive signals are observed (spin-locking). This effect is shown in both the experimental and theoretical signals but the field strength at which the signal intensity is zero is different, 0.28 mT and 0.70 mT, respectively. For Chy_{d12}/1,4-DCB the B_1-spectra ($B_0 = 0$) can be seen to become increasingly positive (spin-locking) as the RF field strength is increased. This is observed in both the experimental and theoretical data.

The data in Figure 3.14 shows the OMFEs for Py_{h10}/1,3-DCB and Chy_{d12}/1,4-DCB as a function of frequency for different B_1 field strengths. The broad resonance observed in the OMFE for Py_{h10}/1,3-DCB corresponds to the effective hyperfine coupling constant

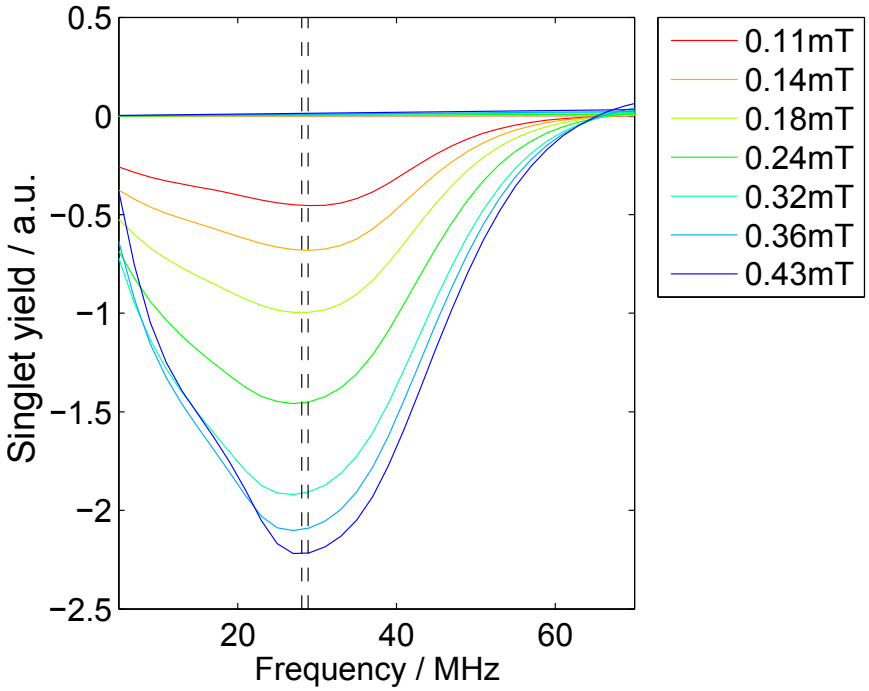

(a) Py_{h10}/1,3-DCB

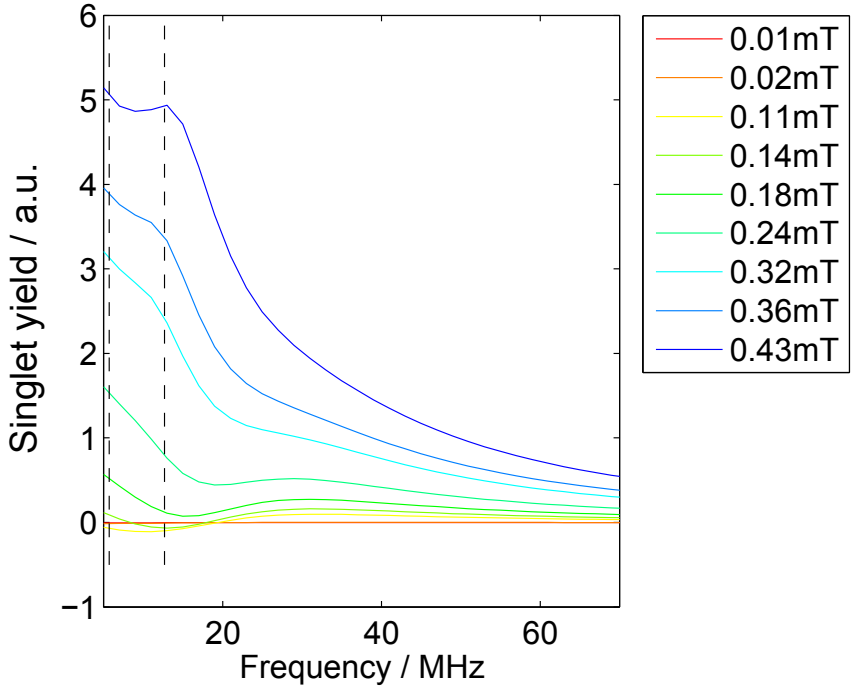

(b) Chy_{d12}/1,4-DCB

Figure 3.14: Simulated OMFE spectra ($B_0 = 0\,\mathrm{mT}$) for Py_{h10}/1,3-DCB (top) and Chy_{d12}/1,4-DCB (bottom) for various RF field strengths (see legend). Simulations were performed using $k = 86.16\,\mu s^{-1}$ and $k = 55.34\,\mu s^{-1}$ for Py_{h10}/1,3-DCB and Chy_{d12}/1,4-DCB, respectively. The black dashed lines correspond to the effective hyperfine coupling constant for each radical in the pair, see text for details.

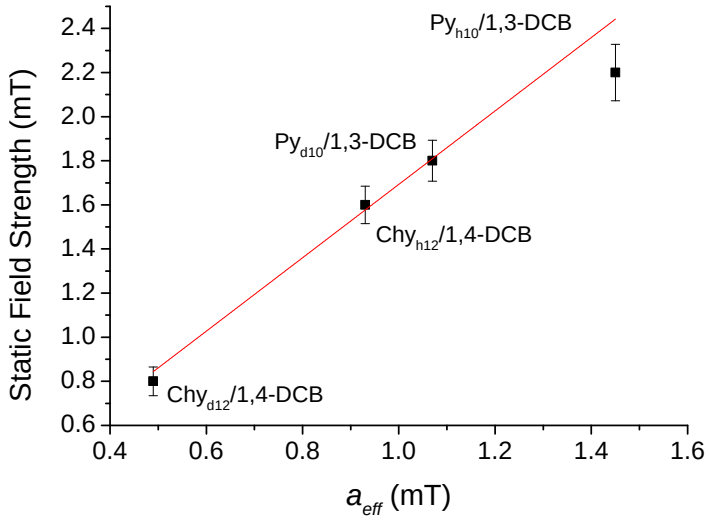

Figure 3.15: The field strength at which there is less S − T mixing in perpendicular orientations compared with parallel (i.e. signal 90° > 0°) as a function of effective hyperfine coupling. Data is shown for $B_1 = 0.11\,\mathrm{mT}$ in Figure 3.11((a), (c), (e) and (g)).

for Py (1.01 mT ≈ 28 MHz) and 1,3-DCB (1.03 mT ≈ 28.9 MHz). The OMFE spectra for Chy$_{d12}$/1,4-DCB shows a resonance peak at ≈ 13 MHz and a shoulder resonance at ≈ 3 MHz corresponding to the effective hyperfine coupling constants of 1,4-DCB and Chy$_{d12}$, respectively which are 12.7 MHz and 5.7 MHz. From these data it can be clearly seen that the resonance feature for Py$_{h10}$/1,3-DCB becomes more pronounced for stronger RF fields, identical to the effect observed with decreasing lifetime [64]. The oscillating field has no influence on the singlet yield at very high frequencies because it is too far off resonance to induce any transitions if there are no hyperfine couplings of similar magnitude. The effective hyperfine coupling constants in Py$_{h10}$/1,3-DCB are comparable in size to 36 MHz whereas those in Chy$_{d12}$/1,4-DCB are much smaller. The OMFE data for Chy$_{d12}$/1,4-DCB is shown in Figure 3.14(b). In contrast to the OMFE data for Py$_{h10}$/1,3-DCB whose resonance features are negative at all RF field strengths, the resonance features increase from negative to positive as the RF field strength is increased. This occurs when the field strength exceeds or becomes comparable to the hyperfine coupling and the data shows that the resonance due to Chy (3 MHz) becomes positive at a lower RF field strength than the resonance due to 1,4-DCB (12.7 MHz). This effect is identical to spin-locking effects observed when $B_0 \neq 0$.

For all systems at $B_1 = 0.43\,\mathrm{mT}$ (Figure 3.11), the response to an applied field shows

no angle dependence for $B_0 = 0.4\,\mathrm{mT}$ and lower, whilst at $B_1 = 0.11\,\mathrm{mT}$ (Figure 3.11) the response to an applied field shows no angle dependence for $B_0 = 0$ only. It can be concluded that for significant angle dependence to be observed, $B_0 \geq B_1$. As the static field strength increases the dependence on θ changes. Generally, for all systems at low RF field strengths, i.e. $B_1 = 0.11\,\mathrm{mT}$, increasing the static field strength to $0.20\,\mathrm{mT}$ induces an angle dependence θ and the spectra exhibit a $\cos 2\theta$ shape showing that a $0.20\,\mathrm{mT}$ field promotes more $\mathrm{S}-\mathrm{T}$ mixing in perpendicular orientations compared with parallel. As the field strength is increased further the trough at $\theta = 90°$ starts to flatten out and then inverts such that the spectra exhibit a $-\cos 2\theta$ shape indicating that there is less $\mathrm{S}-\mathrm{T}$ mixing in perpendicular orientations compared with parallel. This observed change in angle dependency will be discussed later.

The field strength at which this change in orientation dependence occurs decreases as the effective hyperfine coupling of the RP decreases (Figure 3.15). Take as an example, the data for $B_1 = 0.11\,\mathrm{mT}$, for $\mathrm{Py_{h10}}$/1,3-DCB, which has the largest effective hyperfine coupling constant (1.453 mT), the angle dependence changes at $B_0 = 2.2\,\mathrm{mT}$ whilst for $\mathrm{Chy_{d12}}$/1,4-DCB, which has the smallest effective hyperfine coupling (0.498 mT), the angle dependence changes at $B_0 = 0.8\,\mathrm{mT}$. This also holds true for $B_1 = 0.14\,\mathrm{mT}$ and $B_1 = 0.18\,\mathrm{mT}$, data shown in Appendix A.

In contrast at larger RF field strengths, $B_1 = 0.43\,\mathrm{mT}$ (Figure 3.11) all rot-RYDMR plots (with $B_0 > 0.4\,\mathrm{mT}$) exhibit the $-\cos 2\theta$ shape which means that $\mathrm{S}-\mathrm{T}$ mixing is more efficient in parallel orientations. Negative signals correspond to an increased rate of $\mathrm{S}-\mathrm{T}$ mixing and positive signals correspond to a decrease in the rate. For $B_1 = 0.43\,\mathrm{mT}$, the signal intensity at $\theta = 90°$ is always larger than that at 0° indicating that there is less $\mathrm{S}-\mathrm{T}$ mixing in perpendicular orientations compared with parallel. Furthermore, the signal intensity at 90° is always positive, corresponding to a decrease in the $\mathrm{S}-\mathrm{T}$ mixing compared with the static field only case. This a consequence of spin-locking which hampers $\mathrm{S}-\mathrm{T_0}$ mixing. For all systems, the signal intensity at parallel orientations is positive at low static field strengths but becomes negative as the static field strengths become larger than 1.2 mT corresponding to an increase in the rate of $\mathrm{S}-\mathrm{T}$ mixing compared with the static field only case (Figure 3.11((b), (d), (f) and (h))). For low

static field strengths positive signals correspond to a decrease in S − T mixing and the static field strength is no longer a good quantisation axis. At higher static field strengths, negative signals are observed because reconnection of the S/T_0 with the $T_\pm$ manifold at resonance increases the efficiency of S − T mixing.

Lastly, the signal intensity of the data at $B_0 = 1.2\,\mathrm{mT}$ (on resonance) should be discussed for all systems particularly at low B_1 field strengths ($B_1 = 0.11\,\mathrm{mT}$, Figure 3.11). Take the data for Py_{h10}/1,3-DCB and Py_{d10}/1,3-DCB: it can be seen that the signal intensity at perpendicular orientations is wide for $B_0 = 1.0\,\mathrm{mT}$, $1.2\,\mathrm{mT}$ and $1.4\,\mathrm{mT}$. In contrast, the signal intensity observed at perpendicular orientations for Chy_{h12}/1,4-DCB and Chy_{d12}/1,4-DCB is narrow for $B_0 = 1.0\,\mathrm{mT}$, $1.2\,\mathrm{mT}$ and $1.4\,\mathrm{mT}$. In Py_{h10}/1,3-DCB and Py_{d10}/1,3-DCB the appearance of the data is dominated by the large hyperfine coupling constants within the RP, even in the case for deuterated pyrene where the hyperfine coupling constants are small, the dominant hyperfine coupling constant for 1,3-DCB is $0.829\,\mathrm{mT}$. Whilst for Chy_{h12}/1,4-DCB and Chy_{d12}/1,4-DCB the dominant hyperfine coupling constants are small in comparison, $0.18\,\mathrm{mT}$ for 1,4-DCB, $0.49\,\mathrm{mT}$ for protonated chrysene and $0.08\,\mathrm{mT}$ for deuterated chrysene.

Simulations were performed for the systems Py_{h10}/1,3-DCB and Chy_{d12}/1,4-DCB (Figure 3.12) in order to compare the two systems with the largest and smallest effective hyperfine coupling constants. Whilst a full set of hyperfine coupling constants were used in the simulations for Py_{h10}/1,3-DCB it was not possible to use a full set of hyperfine coupling constants for Chy_{d12}/1,4-DCB and only the three largest hyperfine coupling constants of deuterated chrysene were used. The reason for this was because of insufficient memory to calculate singlet yields for a full set of hyperfine coupling constants for spin-1 nuclei due to the large dimensions of the resulting matrix. In previous investigations on Py_{h10}/1,3-DCB and Chy_{d12}/1,4-DCB [65] approximate k values (recombination rate) were used ($40\,\mu s^{-1}$ and $30\,\mu s^{-1}$ respectively). Here, it has been possible to globally fit k values using a large data set (θ, B_1, B_0) and the full set of hyperfine coupling constants, for Py_{h10}/1,3-DCB.

In general, the agreement of the theoretical simulations (Figure 3.12) with experimental results (Figure 3.11) is gratifying. Simulations show that the spectra are strongly dependent on the orientation of the two fields, θ, supporting this observation in the

experimental data. Other experimental details are also reproduced very well by the simulations, including the change in orientation dependence with increasing field strength and spin locking features.

The agreement between experimental and simulated data is weaker for Py_{h10}/1,3-DCB compared with that for Chy_{d12}/1,4-DCB, particularly at large RF field strengths. The reason for this has already been touched upon but will be discussed further. It is assumed that the singlet yield is linear in B_1 [58] such that the effects of modulation can be simulated by subtracting the singlet yield in the absence of an RF field from the singlet yield when both static and RF fields are applied. For weak RF fields ($B_1 < B_1^m$) this treatment is a good approximation despite the non-linearity of B_1 field dependence. For large RF field strengths ($B_1 \geq B_1^m$) this approximation breaks down because the signal would be averaged over the spin-pumping and spin-locking regimes. For Py_{h10}/1,3-DCB this approximation breaks down more than it does for Chy_{d12}/1,4-DCB because spin-locking occurs at a higher RF field strength and there is a greater spin-pumping signal. Hence, a weaker agreement between experimental and theoretical data for Py_{h10}/1,3-DCB is observed compared with Chy_{d12}/1,4-DCB, particularly at high RF field strengths $B_1 = 0.43\,\mathrm{mT}$.

As in the experimental data, the simulations show that at low RF field strengths, $B_1 = 0.11\,\mathrm{mT}$, and low static field strengths there is less $\mathrm{S}-\mathrm{T}$ mixing for parallel orientations compared to perpendicular (Figure 3.12((a) and (c))). As the static field strength increases the shape of the spectra changes and indicates that there is more $\mathrm{S}-\mathrm{T}$ mixing for parallel orientations compared to perpendicular. This change from $\cos\theta$ like to $-\cos\theta$ like dependence is observed in the theoretical data: at a static field strength $B_0 = 2.2\,\mathrm{mT}$ for Py_{h10}/1,3-DCB and $B_0 = 0.8\,\mathrm{mT}$ for Chy_{d12}/1,4-DCB, Figure 3.12((a) and (c)) for the same RF field strength, $B_1 = 0.11\,\mathrm{mT}$. Also in agreement for higher RF field strengths, $B_1 = 0.43\,\mathrm{mT}$ (Figure 3.12((b) and (d))), the signal intensity at 90° orientations is more positive than those at 0° orientations corresponding to a decrease in the efficiency of $\mathrm{S}-\mathrm{T}$ mixing compared with parallel orientations. In the simulated data for Chy_{d12}/1,4-DCB the signal intensities observed for 90° orientations are positive, also in agreement, corresponding to an decrease in the rate of $\mathrm{S}-\mathrm{T}$ mixing (spin-locking) compared with

the static-field only case. However, in the simulated data for Py_{h10}/1,3-DCB the signal intensities at $\theta = 90°$ are positive for static field strengths above 2.20 mT. This is in contrast to the experimental data for which *all* signal intensities are positive at 90°. Again highlighting the weaker agreement between experimental and theoretical data for Py_{h10}/1,3-DCB observed at large RF field strengths.

It is useful to present data in different forms in order to investigate different effects and properties of the systems. Therefore, in Figure 3.16 RYDMR-B_0 data are presented for all systems. All spectra for different angles and RF field strengths show a resonance at approximately 1.28 mT which corresponds to the resonance for a 36 MHz RF frequency. It can be seen from the data that this resonance is shifted to higher static field in systems with large hyperfine couplings (e.g. Py_{h10}/1,3-DCB ($a_{\text{eff}} = 1.453$ mT)) whereas for systems with small hyperfine couplings (e.g. Chy_{d12}/1,4-DCB ($a_{\text{eff}} = 0.489$ mT)) the resonance is not shifted and occurs at $B_0 = 1.28$ mT. In general, for all systems studied, the resonance shifts to higher static field strengths and becomes broad as the B_1 field strength increases. This shift and broadening in the resonance at higher B_1 field strengths is analogous to the Bloch-Siegert shift [66]. This effect is due to an additional contribution to the static field, B_0 that arises from the off-resonance component of the RF field, B_1, and is proportional to the square of the field strength, B_1.

All Zeeman like resonances in all systems observed (Figure 3.16, red data) for 0° orientations are negative, corresponding to an increase in the $S-T$ mixing compared with the static-field only case. This occurs when the resonance condition is met $\gamma_e B_0 \approx \omega_{RF}$ and reconnection of the S/T_0 states with the $T_\pm$ states is possible. For 90° orientations (Figure 3.16, blue graphs) the situation is different and the resonance changes sign with increasing RF field strengths. At low RF field strengths, $B_1 = 0.11$ mT, a negative resonance is observed for 90° orientations (blue graphs) corresponding to an increase in the rate of $S-T$ mixing compared with the static-field only case whilst at higher RF field strengths, $B_1 = 0.43$ mT, a positive resonance is observed corresponding to a decrease in the rate of $S-T$ mixing. This effect can be ascribed to 'spin-locking' and will be discussed later in this chapter. The effect of spin locking is more pronounced in Chy_{d12}/1,4-DCB because of smaller hyperfine couplings within the RP which results in spin-locking at

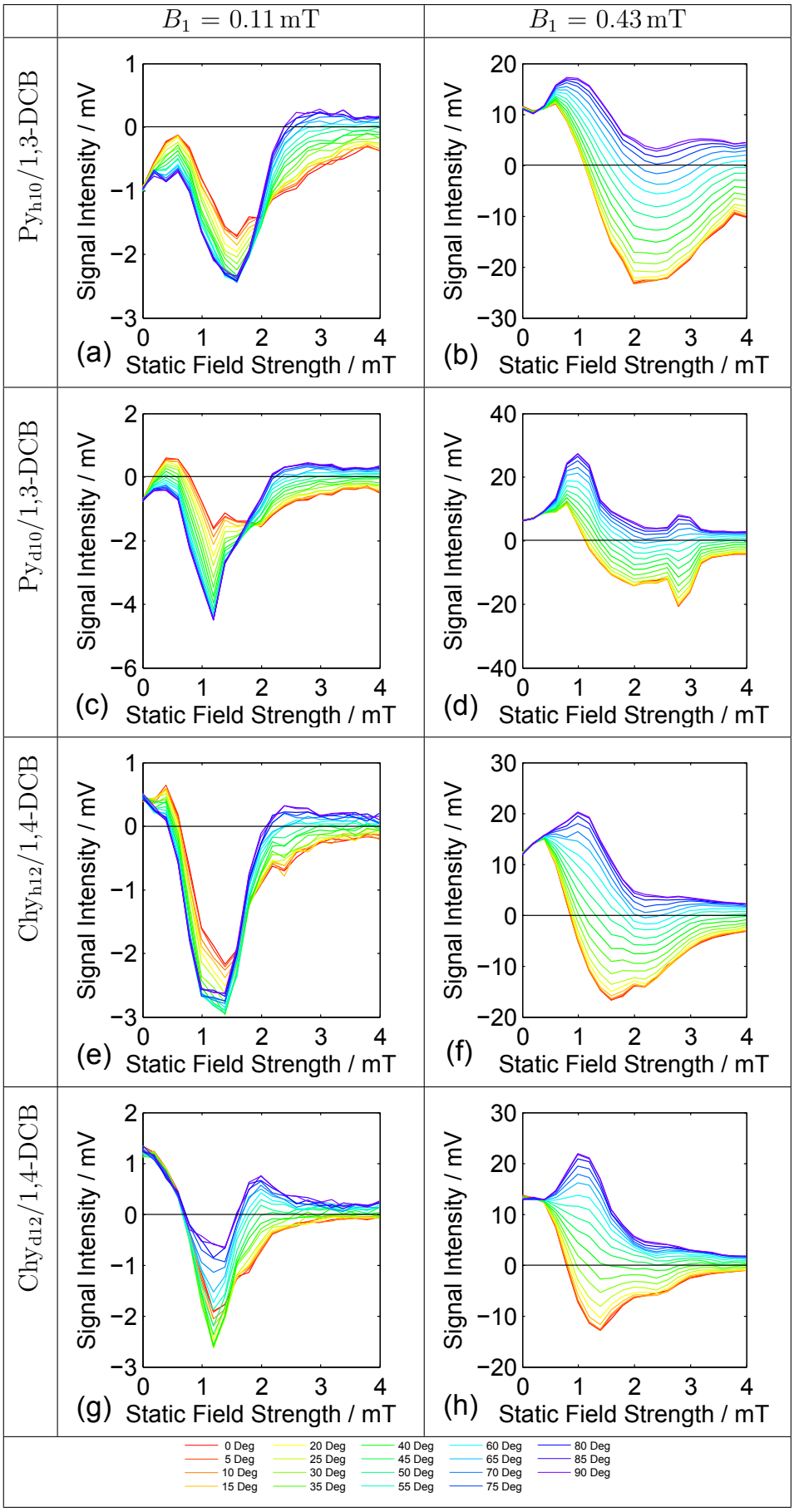

Figure 3.16: Experimental RYDMR results for all systems studied. B_0 field strengths ranging from 0.0 - 4.0 mT for different angles (0° - 90°) are shown within panels. Spectra were recorded for different B_1 field strengths, 0.11 mT (left) and 0.43 mT (right), shown in different panels, and a frequency $\omega_{RF} = 36$ MHz.

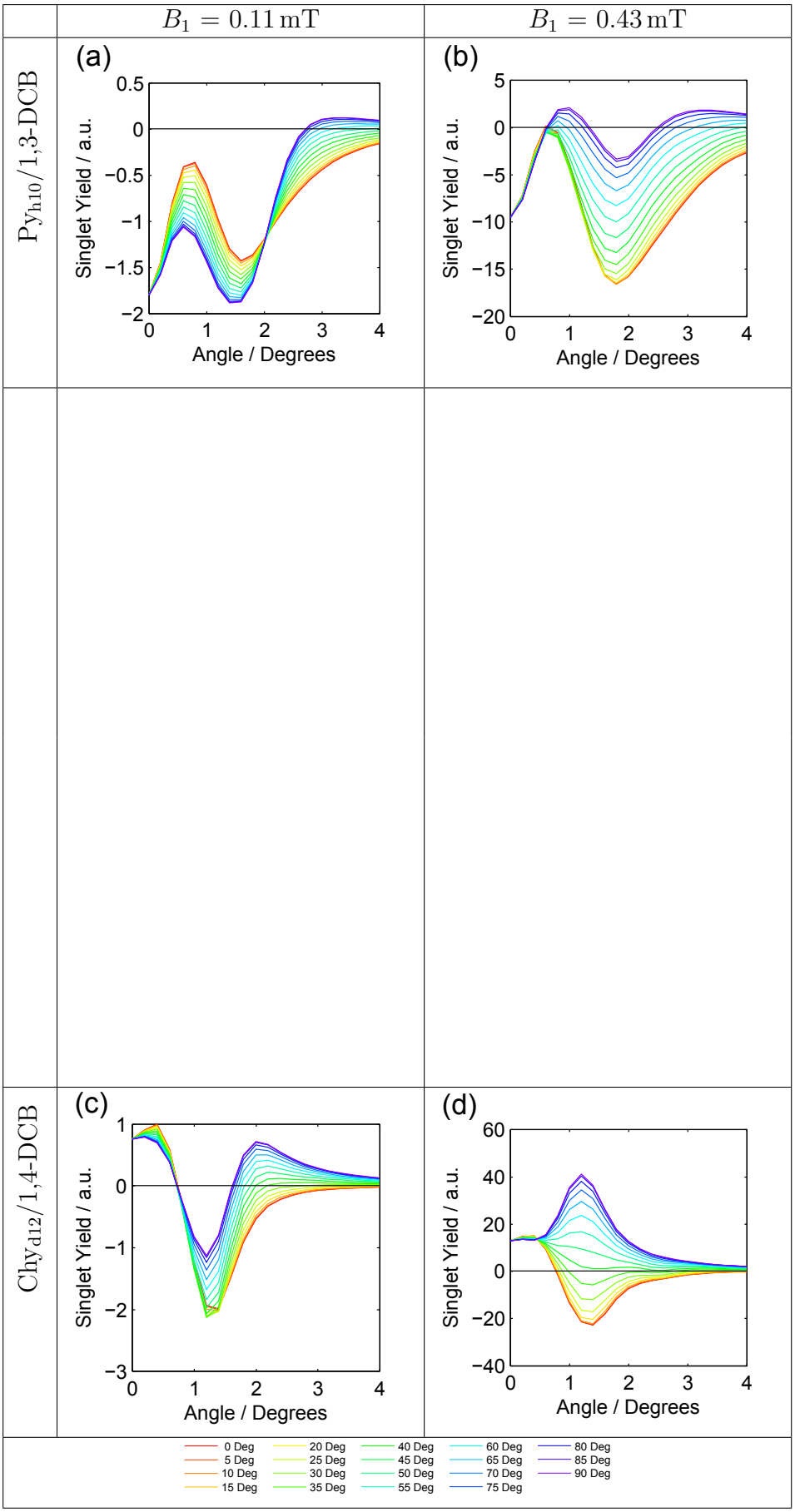

Figure 3.17: Theoretical RYDMR results for $\mathrm{Py_{h10}}$/1,3-DCB and $\mathrm{Chy_{d12}}$/1,4-DCB. Spectra were calculated for different B_1 field strengths, 0.11 mT (left) and 0.43 mT (right), shown in different panels, and a frequency $\omega_{RF} = 36\,\mathrm{MHz}$. Global optimisation of $\mathrm{Py_{h10}}$/1,3-DCB produced $k = 86.16\,\mu\mathrm{s}^{-1}$ and $k = 55.34\,\mu\mathrm{s}^{-1}$ for $\mathrm{Chy_{d12}}$/1,4-DCB identical to those found in Figure 3.12. Calculations were performed using 32 time steps, n.

lower RF field strengths.

The final observation is that the shapes of the spectra are also shown to be largely dependent on the effective hyperfine coupling constant of the RP. For Py_{h10}/1,3-DCB the resonance peak is asymmetric, as is expected for any system with unresolved hyperfine couplings, and can be described by the 'low-field' limit ($a_{\text{eff}} \geq B_0$) [65]. Whereas, for Chy_{d12}/1,4-DCB the resonance peak is more symmetric with respect to the centre of the peak compared with that for Py_{h10}/1,3-DCB. This is expected for any system with small hyperfine couplings which can therefore be described by the 'high-field' limit ($a_{\text{eff}} \leq B_0$) [57, 65]. An interesting observation of data for Chy_{d12}/1,4-DCB is that there appears another peak at $B_0 \approx 2.5\,\text{mT}$ for higher RF field strengths. This is due to an overtone resonance and has been previously observed in these systems, particularly at larger RF field strengths [55, 67].

Simulated RYDMR data for Py_{h10}/1,3-DCB and Chy_{d12}/1,4-DCB are shown in Figure 3.17 alongside the experimental data on the facing page. The agreement between experimental and theoretical data is striking with features, such as spin-locking and orientation dependence, observed in the experimental data (Figure 3.16) also reproduced in the the simulations. The data confirms the observation that the shape of the spectra largely depends on the effective hyperfine coupling constants of the system. In Figure 3.16 - Figure 3.17, a system with a large effective hyperfine coupling constant, Py_{h10}/1,3-DCB, is compared with a system which has a small effective hyperfine coupling constant, Chy_{d12}/1,4-DCB. The spectra clearly differ in resonance position, field strength at which spin-locking occurs and field strength at which the orientation dependence changes (Figure 3.15). Spin-locking in these systems will be discussed later.

For experimental and theoretical RYDMR data there exists a static field value at which the signal intensity shows negligible change on application of an RF field at different orientations [58]. For example, this 'nodal point' may be seen in the experimental data for Py_{h10}/1,3-DCB (Figure 3.16) (reproduced in the simulated data (Figure 3.17)) at $B_0 = 2.0\,\text{mT}$ for low RF field strengths, $B_1 = 0.11\,\text{mT}$ and moves to lower static field strengths, $B_0 = 0.7\,\text{mT}$, for higher B_1 field strengths ($0.43\,\text{mT}$). The simulated data for Chy_{d12}/1,4-DCB (Figure 3.17) shows that this 'nodal point' occurs at static field strengths

lower than those observed in the Py_{h10}/1,3-DCB system. For example, at low B_1 field strengths the 'nodal point' occurs at $B_0 \approx 0.8\,\mathrm{mT}$ (Figure 3.16(g)) and moves to lower static field strengths as the strength of the RF field is increased, $B_0 \approx 0.6\,\mathrm{mT}$ for $B_1 = 0.43\,\mathrm{mT}$ (Figure 3.16(h)). At static field strengths lower than this 'nodal point' the signal intensities observed for 0° orientations are larger than those observed for 90° orientations. At static field strengths larger than the 'nodal point' this situation is reversed. The 'nodal point' corresponds to the change in orientation dependence and it has been shown that the static field position at which it occurs depends on the effective hyperfine coupling constant of the system (Figure 3.15). Here, the static field strength at which the nodal point occurs has also been shown to decrease with increasing RF field strength another feature reproduced in the simulations [55, 58].

This change of orientation dependence with increasing static field strength observed in each system can be explained using 'high-field' and 'low-field' models where $B_1 > B_1^0$ or $B_1 < B_1^0$ respectively. When the applied RF field strength, B_1 ($B_1 = 0.43\,\mathrm{mT}$) is large enough to cause spin locking ('high-field') in the system, the signal intensity for perpendicular orientations is more positive than the signal intensity for parallel orientations because $\mathrm{S} - \mathrm{T}$ mixing will be less efficient. And hence, the change in orientation dependency for high RF fields is due to spin locking.

The observed orientation dependence at low RF field strengths, i.e. when the system is spin pumped and $B_1 \leq B_1^0$ (the RF field strength at which spin locking occurs), cannot be explained using spin-locking since the RF field strength is not strong enough to cause spin-locking in perpendicular orientations. At low RF field strengths, the change in orientation dependence with increasing static field strength illustrates a change in the selection rules between 'high field' ($B_0 \geq a_{\mathrm{eff}}$) and 'low field' ($B_0 \leq a_{\mathrm{eff}}$) limits as governed by Fermi's Golden Rule [4, 58]. This may be illustrated with the model of a simple 2-spin system $|m_e, m_n\rangle$. Ignoring the nuclear Zeeman interaction, consider the simple Hamiltonian;

$$\hat{H} = \omega_0 \hat{S}_z + 2\pi a \hat{\mathbf{S}}.\hat{\mathbf{I}} \tag{3.13}$$

where ω_0 is the static field strength (angular frequency units) applied in the z direction

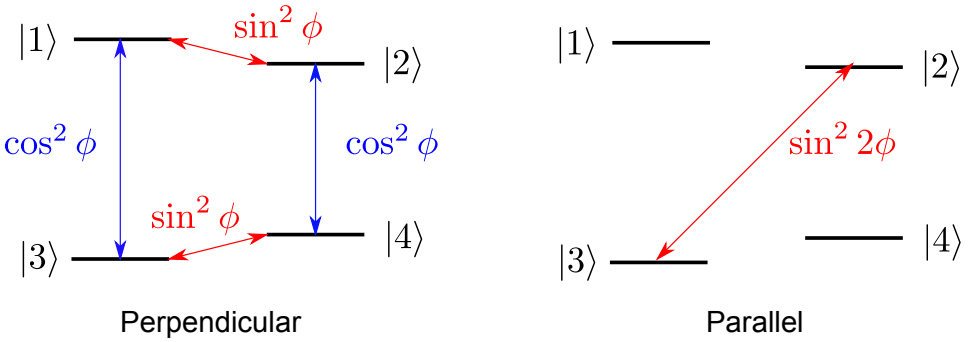

Figure 3.18: Schematic of energy levels for a simple two spin system. The arrows show the allowed transitions and their probabilities. Red arrows show transitions which are negligible when $a \ll \omega_0$.

and a is the electron-nuclear hyperfine coupling constant. The exchange and dipolar interaction have been assumed to be negligible. Solution of the secular determinant leads to the eigenvectors:

$$|1\rangle = |\alpha_e, \alpha_n\rangle \tag{3.14}$$

$$|2\rangle = \cos\phi\,|\alpha_e, \beta_n\rangle + \sin\phi\,|\beta_e, \alpha_n\rangle \tag{3.15}$$

$$|3\rangle = \cos\phi\,|\beta_e, \alpha_n\rangle - \sin\phi\,|\alpha_e, \beta_n\rangle \tag{3.16}$$

$$|4\rangle = |\beta_e, \beta_n\rangle \tag{3.17}$$

where $\tan 2\phi = -2\pi a/\omega_0$. These eigenvectors and their possible transitions are shown in Figure 3.18. If a weak oscillating field is applied parallel or perpendicular to the static field, the intensity of the transition from $|f\rangle \leftarrow |i\rangle$ is given by

$$I_\perp \propto (p_i - p_f)\left|\left\langle i\left|\hat{S}_+\right|f\right\rangle\right|^2 \tag{3.18}$$

$$I_{||} \propto (p_i - p_f)\left|\left\langle i\left|\hat{S}_z\right|f\right\rangle\right|^2 \tag{3.19}$$

where p_i and p_f denote the population of the initial and final state respectively and $\hat{S}_+ = \frac{1}{2}(\hat{S}_x + \mathrm{i}\hat{S}_y)$. For perpendicular orientations, considering only the transition probability, it can be seen that $|3\rangle \leftarrow |1\rangle$ and $|4\rangle \leftarrow |2\rangle$ transitions are allowed with a probability dependent on $\cos^2\phi$ and $|2\rangle \leftarrow |1\rangle$ and $|4\rangle \leftarrow |3\rangle$ are allowed with a probability dependent on $\sin^2\phi$. When the size of the static field strength is comparable in size to the hyperfine

coupling both types of transition should have equal probability (although their intensity may differ because of differences in populations) but when the static field strength is larger than the hyperfine coupling constant only the $|3\rangle \leftarrow |1\rangle$ and $|4\rangle \leftarrow |2\rangle$ transitions will have significant probability. For parallel alignments of the static and oscillating fields the $|3\rangle \leftarrow |2\rangle$ transition has a probability dependent on $\sin^2 2\phi = -a/\sqrt{a^2+\omega_0^2}$ and is only non-negligible when $a > \omega_0$ i.e. low static field strengths.

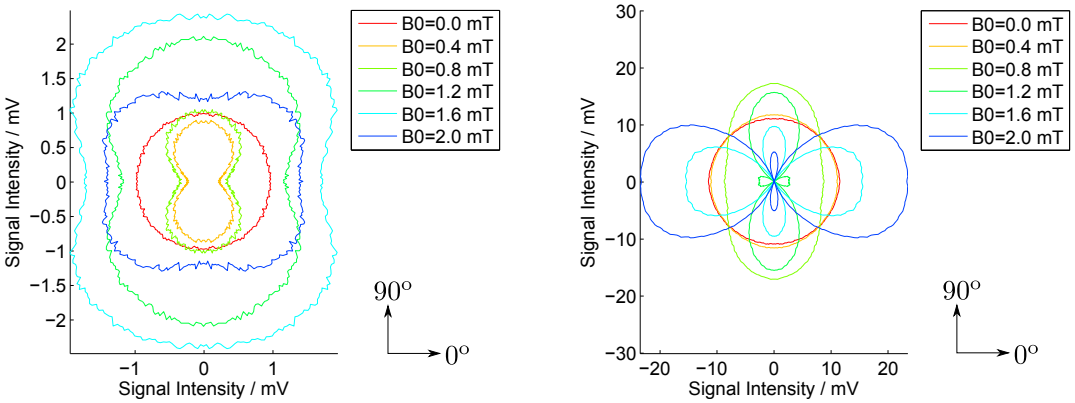

(a) $B_1 = 0.11\,\mathrm{mT}$ (b) $B_1 = 0.43\,\mathrm{mT}$

Figure 3.19: Experimental rot-RYDMR polar plots results for $\mathrm{Py_{h10}}$/1,3-DCB, recorded as a function of B_0 at 36 MHz for different angles, θ, between 0° and 90°. Spectra were recorded for different B_1 field strengths ranging 0.11 - 0.43 mT (rms).

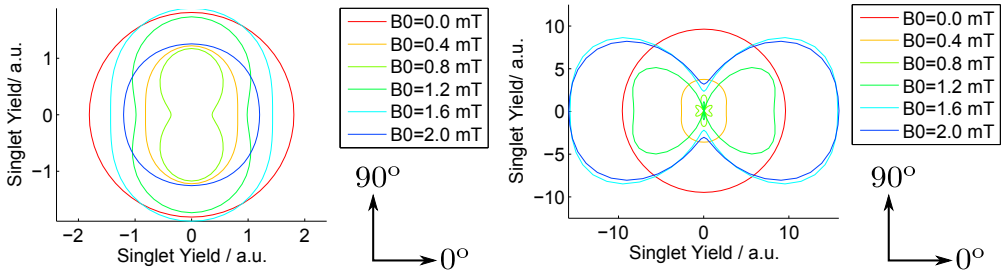

(a) $B_1 = 0.11\,\mathrm{mT}$ (b) $B_1 = 0.43\,\mathrm{mT}$

Figure 3.20: Theoretical rot-RYDMR polar plots results for $\mathrm{Py_{h10}}$/1,3-DCB, recorded as a function of B_0 at 36 MHz for different angles, θ, between 0° and 90°. Spectra were calculated for different B_1 field strengths ranging 0.11 - 0.43 mT (rms). Global optimisation of the system produced $k = 86.16\,\mu\mathrm{s}^{-1}$. Calculations were performed using 32 time steps, n.

To investigate this behaviour further simulations were performed for the system with largest hyperfine couplings, $\mathrm{Py_{h10}}$/1,3-DCB, and the system with the smallest hyperfine couplings, $\mathrm{Chy_{d12}}$/1,4-DCB. Rot-RYDMR spectra are presented in a polar coordinate plot, where the angle, θ is the angle between the static and RF fields and the radius is the signal intensity. The experimental and theoretical polar plots for the two systems

are shown in Figure 3.19 - Figure 3.22. In these plots, it is not possible to distinguish between spin pumping (negative) and spin-locking (positive) signals but the magnitude of the signals in parallel (0°) and perpendicular (90°) orientations can be compared. It can be seen that the general shape of the polar plot changes with increasing RF field strength.

At $B_1 = 0.11\,\mathrm{mT}$ (Figure 3.19(a)), corresponding to spin-pumping, the magnitude of the signal is largest for perpendicular orientations ($B_0 = 1.6\,\mathrm{mT}$), whereas for $B_1 = 0.43\,\mathrm{mT}$ (Figure 3.19(b)), the magnitude of the signal is largest for parallel orientations ($B_0 = 2.0\,\mathrm{mT}$) due to spin-locking. From the polar plot data it can also be seen that for $B_1 = 0.11\,\mathrm{mT}$ (Figure 3.19(a)) no angle dependence is observed for $B_0 = 0.0\,\mathrm{mT}$ whilst at higher RF field strengths, $B_1 = 0.43\,\mathrm{mT}$ (Figure 3.19(b)), no angle dependence is observed for $B_0 \leq 0.4\,\mathrm{mT}$. Hence, in order to observe significant anisotropy it can be concluded that $B_0 \gg B_1$. The polar plots for $B_1 = 0.11\,\mathrm{mT}$ show that there is a big change of shape between $B_0 = 0.0\,\mathrm{mT}$ and $B_0 = 0.4\,\mathrm{mT}$ suggesting that fields smaller than 0.4 mT would be capable of producing a significant anisotropy. Unfortunately, smaller field strengths were not investigated in the experiment in order to measure this limit.

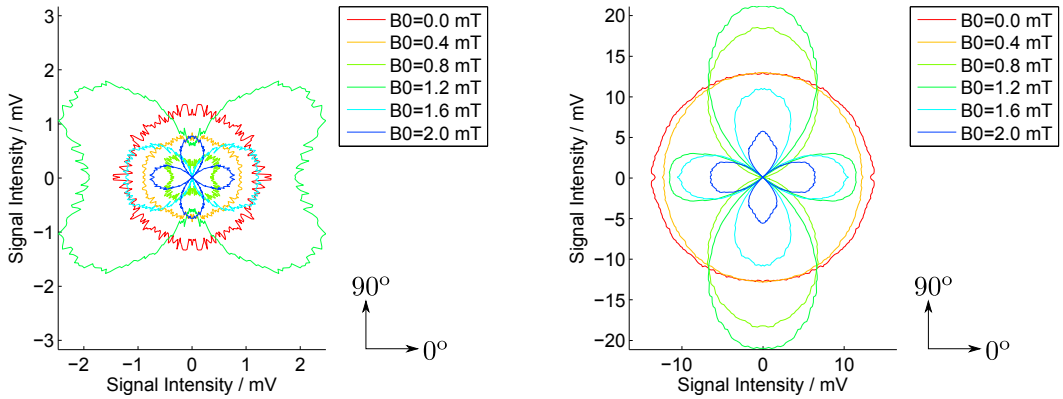

(a) $B_1 = 0.11\,\mathrm{mT}$ (b) $B_1 = 0.43\,\mathrm{mT}$

Figure 3.21: Experimental rot-RYDMR polar plots results for $\mathrm{Chy_{d12}}$/1,4-DCB, recorded as a function of B_0 at 36 MHz for different angles, θ, between 0° and 90°. Spectra were recorded for different B_1 field strengths ranging 0.11 - 0.43 mT (rms).

The simulated data for $\mathrm{Py_{h10}}$/1,3-DCB can be seen in Figure 3.20 and although the general shapes are consistent there are some clear differences between the experimental and theoretical polar plots. For $B_1 = 0.11\,\mathrm{mT}$, it can be clearly seen that the theoretically determined isotropic data dominates the appearance of the polar plot (Figure 3.20(a)) whereas in the experimental data the appearance of the polar plot is dominated by the

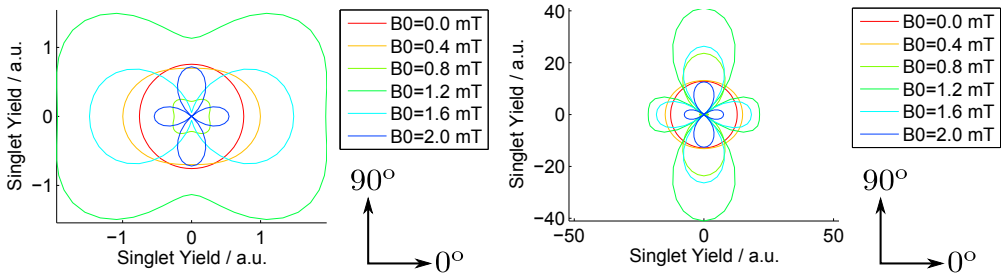

(a) $B_1 = 0.11\,\mathrm{mT}$ (b) $B_1 = 0.43\,\mathrm{mT}$

Figure 3.22: Theoretical rot-RYDMR polar plots results for $\mathrm{Chy_{d12}}$/1,4-DCB, recorded as a function of B_0 at 36 MHz for different angles, θ, between 0° and 90°. Spectra were calculated for different B_1 field strengths ranging 0.11 - 0.43 mT (rms). Global optimisation of the system produced $k = 55.34\,\mu\mathrm{s}^{-1}$. Calculations were performed using 32 time steps, n.

magnitude of anisotropic signal intensities (e.g. $B_0 = 1.6\,\mathrm{mT}$, Figure 3.19(a)). This being said, the simulated data do also show an agreement with the experimental data, where the shape of the polar plots are shown to vary as a function of RF field strength. At low RF field strengths ($B_1 = 0.11\,\mathrm{mT}$, Figure 3.20(a)) the signal intensities for perpendicular orientations are larger or equal to the signal intensity observed for parallel orientations. Whilst at higher RF field strengths ($B_1 = 0.43\,\mathrm{mT}$, Figure 3.20(b)) the magnitude of the signal intensities observed for parallel orientations are larger than those observed for perpendicular orientations agreeing with the observations from the experimental data (Figure 3.19(b)). In the simulated polar plots at low RF field strengths, $B_1 = 0.11\,\mathrm{mT}$ (Figure 3.20(a)), no orientation dependence is observed for $B_0 = 0\,\mathrm{mT}$ and for higher B_1 field strengths $B_1 = 0.43\,\mathrm{mT}$ (Figure 3.20(b)), no orientation dependence is observed for $B_0 = 0\,\mathrm{mT}$. Note that no orientation dependence is also observed for theoretical data $B_1 = 0.11$ and $B_0 = 2.0\,\mathrm{mT}$ (Figure 3.20(a)) and is due to the 'nodal point' as described above and shown in the RYDMR data for $\mathrm{Py_{h10}}$/1,3-DCB (Figure 3.17(a)).

Experimental rot-RYDMR data for $\mathrm{Chy_{d12}}$/1,4-DCB are presented as a polar plot in Figure 3.21 along side the simulated data (Figure 3.22). The agreement between the two sets of data, experimental and theoretical, is very gratifying. In both experimental and theoretical data it can be seen that the shape of the polar plots changes with increasing RF field strength. At low RF field strengths $B_1 = 0.11\,\mathrm{mT}$ (Figure 3.21(a) and Figure 3.22(a)), the largest (magnitude) signal intensity is observed for $B_0 = 1.2\,\mathrm{mT}$ and 1.0 mT in the experimental and theoretical polar plots respectively where the magnitude

of the signal is larger for parallel orientations compared with those of perpendicular orientations. For large RF field strengths $B_1 = 0.43\,\mathrm{mT}$ (Figure 3.21(b) and Figure 3.22(b)) the largest (magnitude) signal intensity is observed for $B_0 = 1.2\,\mathrm{mT}$ and $1.0\,\mathrm{mT}$ in the experimental and theoretical polar plots respectively, however, in contrast to observations at low RF field strengths the magnitude of the signal for perpendicular orientations is larger than those observed in parallel orientations. At low RF field strengths, $B_1 = 0.11\,\mathrm{mT}$ (Figure 3.21(a) and Figure 3.22(a)), isotropy is only observed for $B_0 = 0.0\,\mathrm{mT}$ and at higher B_1 field strengths, $B_1 = 0.43\,\mathrm{mT}$ (Figure 3.21(b) and Figure 3.22(b)), no significant orientation dependence is observed for $B_0 \leq 0.4\,\mathrm{mT}$. This data satisfies the conclusion that no significant orientation dependence will be observed for $B_0 \ll B_1$.

Rot-RYDMR data have been fitted with a Legendre polynomial to further investigate the orientation dependence of RYDMR. A fitting of the rot-RYDMR signal intensity, I, was performed using the following function:

$$I(B,\theta) = \sum_{l=0,2,4\ldots} a_{l0}(B)\sqrt{\frac{2l+1}{4\pi}}P_l^0(\cos\theta) \tag{3.20}$$

where θ is the angle between the RF and static field, a_{l0} is the spherical harmonic coefficient and $P_l^0(x)$ is the associated Legendre polynomial. The expansion is restricted to P^0 polynomials with even l because of the reflection symmetry in the signals. $P_l^0(x)$ is a polynomial in powers of x, including x^l, and therefore $I(B,\alpha)$ may also be written as

$$I(B,\theta) = \sum_{l=0,2,4\ldots} c_l \cos^l\theta. \tag{3.21}$$

If rot-RYDMR exhibits no orientation dependence then $a_{l0} = 0$ for $l > 0$ and the signal is well described by the first-order (isotropic) spherical harmonic. The results of these fittings are shown for $\mathrm{Py_{h10}}$/1,3-DCB and $\mathrm{Chy_{d12}}$/1,4-DCB in Figure 3.23 and Figure 3.24, respectively.

In these data it is shown that for $B_0 = 0\,\mathrm{mT}$ the major contribution to the polynomial is from the first (isotropic) spherical harmonic and that the contribution from the second and third is approximately zero. This is the same for both $\mathrm{Py_{h10}}$/1,3-DCB

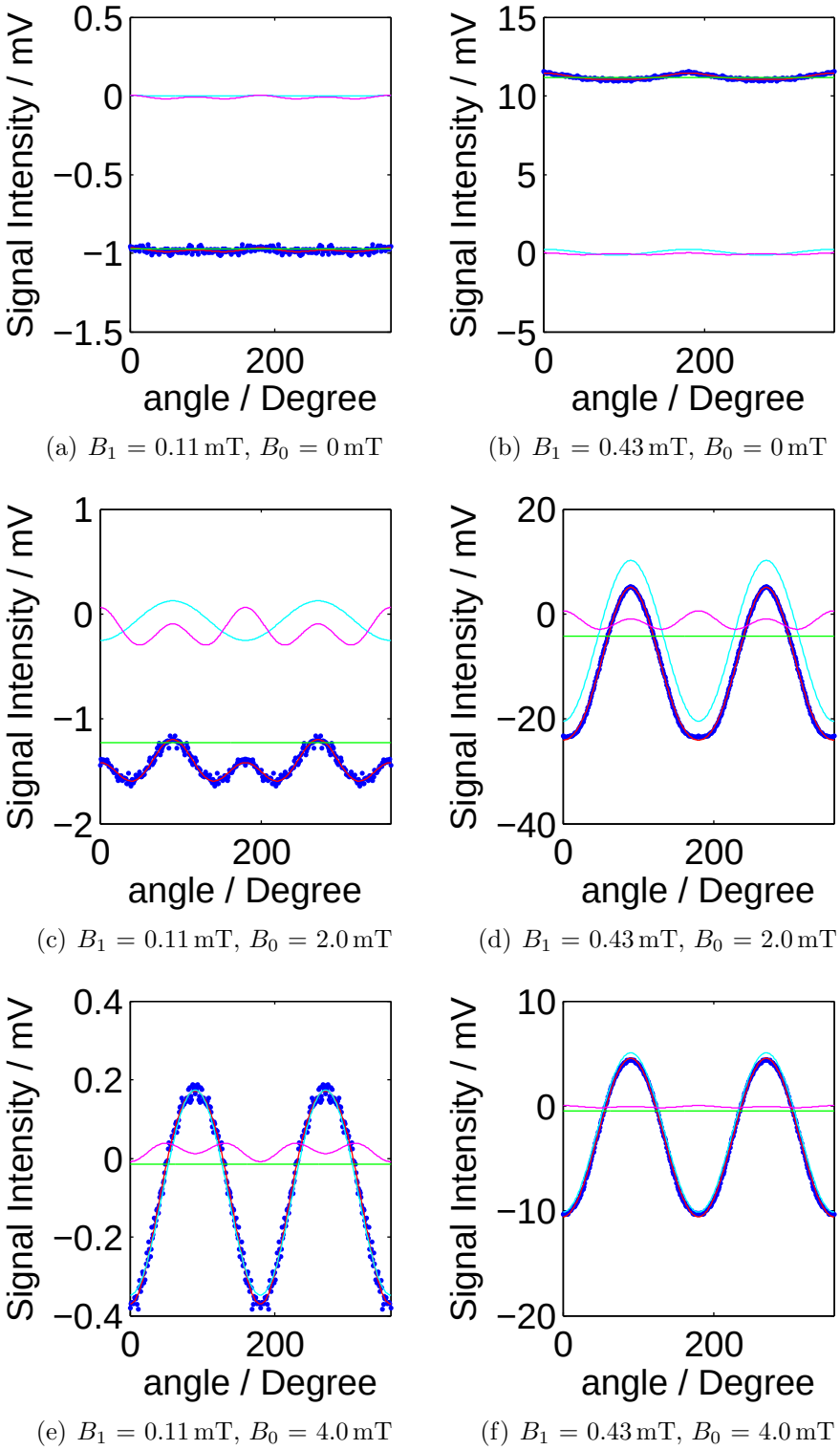

(a) $B_1 = 0.11\,\mathrm{mT}$, $B_0 = 0\,\mathrm{mT}$ (b) $B_1 = 0.43\,\mathrm{mT}$, $B_0 = 0\,\mathrm{mT}$

(c) $B_1 = 0.11\,\mathrm{mT}$, $B_0 = 2.0\,\mathrm{mT}$ (d) $B_1 = 0.43\,\mathrm{mT}$, $B_0 = 2.0\,\mathrm{mT}$

(e) $B_1 = 0.11\,\mathrm{mT}$, $B_0 = 4.0\,\mathrm{mT}$ (f) $B_1 = 0.43\,\mathrm{mT}$, $B_0 = 4.0\,\mathrm{mT}$

Figure 3.23: Rot-RYDMR data for $\mathrm{Py_{h10}}$/1,3-DCB for RF field strengths $B_1 = 0.11\,\mathrm{mT}$ (right) and $0.43\,\mathrm{mT}$ (left) and static field strengths $0\,\mathrm{mT}$ (top), $2.0\,\mathrm{mT}$ (middle) and $4.0\,\mathrm{mT}$ (bottom). The experimental data are shown by the blue dots, the polynomial fit is shown by the red line and the contributions from the first, second and third spherical harmonics are shown by the green, blue and magenta lines, respectively.

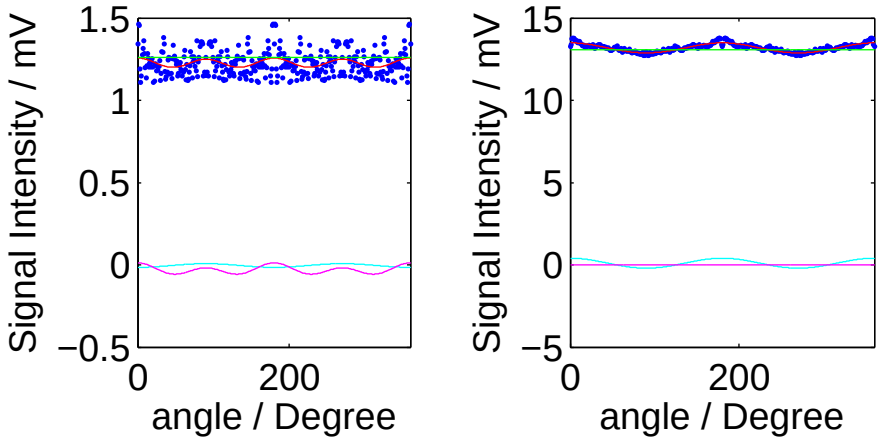

(a) $B_1 = 0.11\,\mathrm{mT}$, $B_0 = 0\,\mathrm{mT}$ (b) $B_1 = 0.43\,\mathrm{mT}$, $B_0 = 0\,\mathrm{mT}$

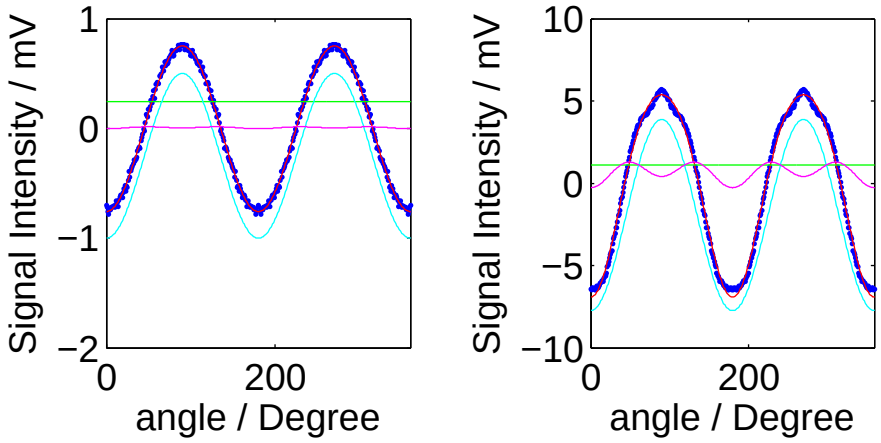

(c) $B_1 = 0.11\,\mathrm{mT}$, $B_0 = 2.0\,\mathrm{mT}$ (d) $B_1 = 0.43\,\mathrm{mT}$, $B_0 = 2.0\,\mathrm{mT}$

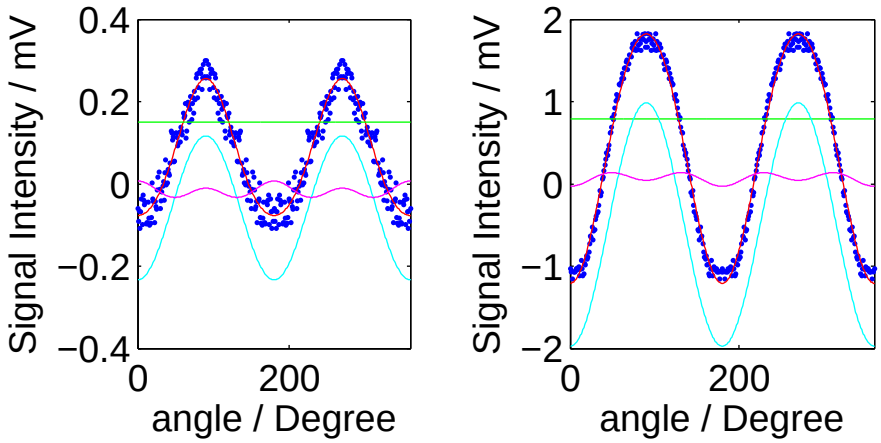

(e) $B_1 = 0.11\,\mathrm{mT}$, $B_0 = 4.0\,\mathrm{mT}$ (f) $B_1 = 0.43\,\mathrm{mT}$, $B_0 = 4.0\,\mathrm{mT}$

Figure 3.24: Rot-RYDMR data for $\mathrm{Chy}_{\mathrm{d12}}$/1,4-DCB for RF field strengths $B_1 = 0.11\,\mathrm{mT}$ (right) and $0.43\,\mathrm{mT}$ (left) and static field strengths $0\,\mathrm{mT}$ (top), $2.0\,\mathrm{mT}$ (middle) and $4.0\,\mathrm{mT}$ (bottom). The experimental data are shown by the blue dots, the polynomial fit is shown by the red line and the contributions from the first, second and third spherical harmonics are shown by the green, blue and magenta lines, respectively.

and Chy_{d12}/1,4-DCB and for all RF field strengths. The contribution from the spherical harmonic coefficients is dependent on the static field strength, RF field strength and also the system. For example, for Py_{h10}/1,3-DCB, $B_1 = 0.11\,\mathrm{mT}$ and $B_o = 2.0\,\mathrm{mT}$ (Figure 3.23(c)), it can be seen that there is an approximately equal contribution from the second and third spherical harmonics to the shape of the rot-RYDMR plot. Whilst for $B_1 = 0.43\,\mathrm{mT}$ (Figure 3.23(d)) there is a much larger contribution from the second harmonic coefficient. The shape of the rot-RYDMR plot for Py_{h10}/1,3-DCB $B_1 = 0.11\,\mathrm{mT}$ and $B_0 = 2.0\,\mathrm{mT}$ (Figure 3.23(c)) can be best explained by the change in the orientation dependence of the system (with increasing static field strength) as shown in Figure 3.15, and is dependent on the RF field strength and the hyperfine coupling constants within the system. For $B_1 = 0.43\,\mathrm{mT}$ this effect will be observed but at lower static field strengths and is also the case in Chy_{d12}/1,4-DCB, which has smaller hyperfine coupling constants than Py_{h10}/1,3-DCB. For the largest static field strength, $B_0 = 4.0\,\mathrm{mT}$, the largest contribution to the shape of the spectra is from the second harmonic coefficient. This is true for both systems at all RF field strengths.

The magnitude of the spherical harmonic coefficients are better summarised in Figure 3.25 and Figure 3.26 which show the magnitude of the coefficients as a function of static field strength. The first harmonic coefficient, a_{00}, which describes the isotropic contribution to the plot, looks very similar to that of a RYDMR curve Figure 3.16. This is not surprising since the first harmonic simply increases or decreases depending on the magnitude of the rot-RYDMR curve. In general, the second harmonic, a_{02}, which describes the angle dependence of rot-RYDMR, increases in magnitude as the field strength increases, reaches a peak magnitude and subsequently decreases. This is because at zero static field strength there is no angle dependence and at high static field strengths the angle dependence diminishes as the static field strength becomes much larger than that of the RF field. At resonance the largest angle dependence is observed and this is shown when the magnitude of the second harmonic coefficient is at its largest. For Py_{h10}/1,3-DCB, whose resonance is slightly shifted (Figure 3.16) from that of a 36 MHz RF field, a_{02} is largest (in magnitude) at approximately 2.0 mT (Figure 3.25) and for Chy_{d12}/1,4-DCB a_{02} is largest (in magnitude) at approximately 1.2 mT which corresponds to the resonance

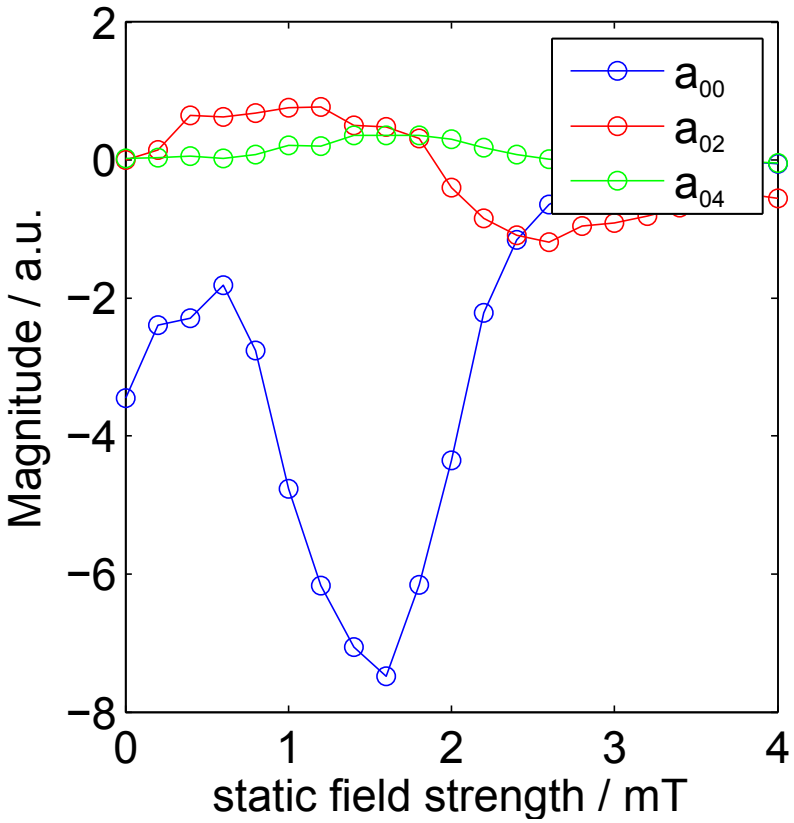

(a) $B_1 = 0.11\,\mathrm{mT}$

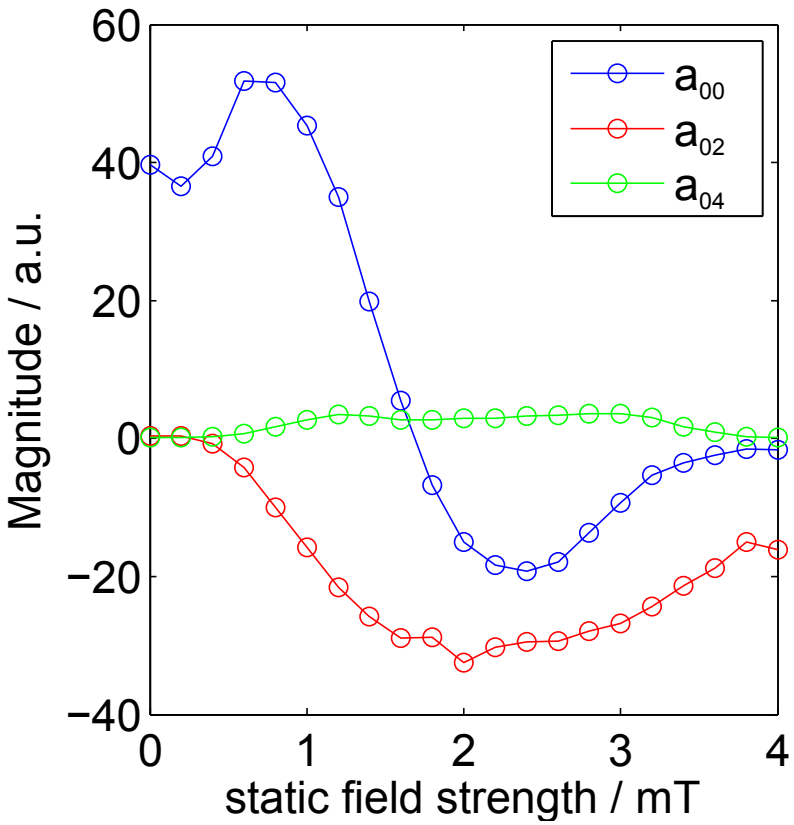

(b) $B_1 = 0.43\,\mathrm{mT}$

Figure 3.25: Spherical harmonic coefficients as a function of B_0 with a RF field strength $B_1 = 0.11\,\mathrm{mT}$ (top) and 0.43 mT (bottom) for $\mathrm{Py_{h10}}$/1,3-DCB.

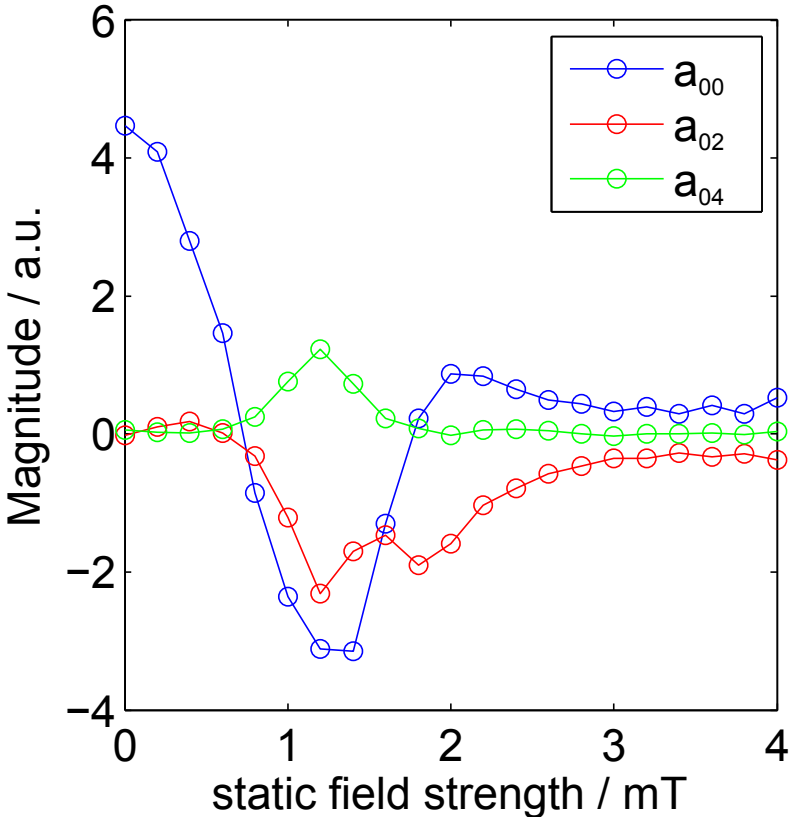

(a) $B_1 = 0.11\,\mathrm{mT}$

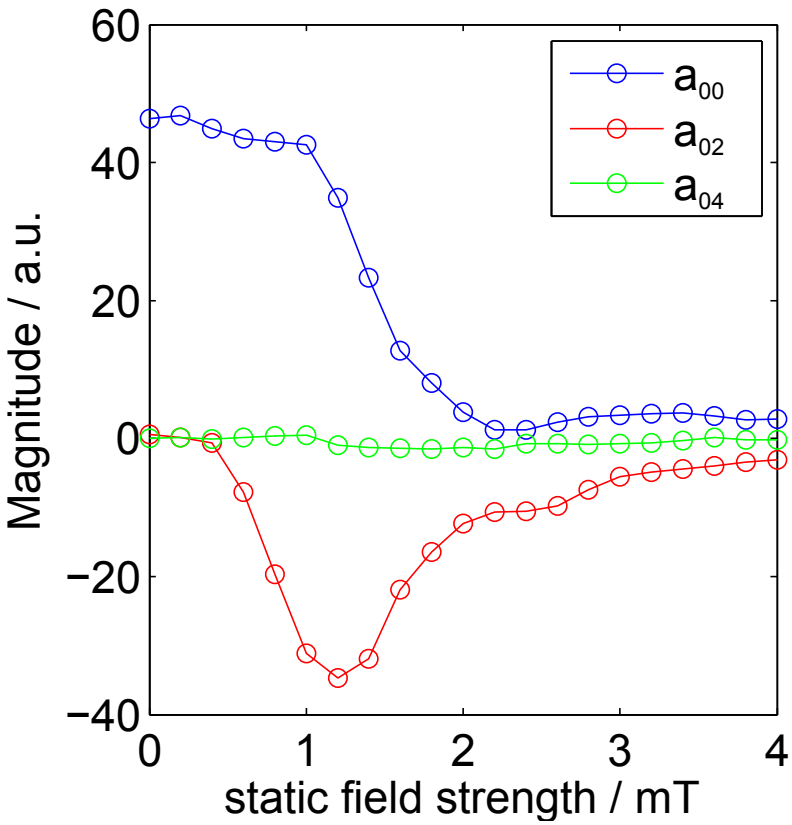

(b) $B_1 = 0.43\,\mathrm{mT}$

Figure 3.26: Spherical harmonic coefficients as a function of B_0 with a RF field strength $B_1 = 0.11\,\mathrm{mT}$ (top) and 0.43 mT (bottom) for $\mathrm{Chy}_{\mathrm{d12}}$/1,4-DCB.

frequency 36 MHz. The contribution from the third harmonic is, in general, smaller than the contribution from the first and second. The static field strength at which its contribution is the largest is when the orientation dependence of the rot-RYDMR changes (Figure 3.15) as shown in Figure 3.23(c). A large peak in its magnitude can be seen in Figure 3.26(a). This data is extremely useful when interpreting the angle dependence of rot-RYDMR spectra. For example, when $_{a02}$ and a_{04} are zero the spectra will not exhibit any anisotropy in the orientation dependence and when a_{02} is at its largest magnitude the spectra will exhibit the largest orientation dependence.

One of the most prominent discrepancies between the different systems, with regards to orientation dependence, can be seen when B_0 is on resonance, $B_0 = 1.20\,\mathrm{mT}$. The largest orientation dependence (i.e. the difference between the signal intensities at 0° and 90° orientations) for $B_0 = 1.2\,\mathrm{mT}$ is observed in $\mathrm{Chy_{d12}}$/1,4-DCB (Figure 3.21 - Figure 3.22) particularly at larger RF field strengths (Figure 3.16(h)). The increase in orientation dependence in systems with smaller effective hyperfine couplings is due to spin-locking effects for perpendicular orientations.

The effects of spin-locking can be best seen for RF field strengths, $B_1 \gg B_1^0$ and the orientation dependence at high RF fields can be described by the spin locking model. For RF field strengths, $B_1 \gg B_1^0$, when the system is on resonance, $B_0 = 1.28\,\mathrm{mT}$, it can be described by the rotating frame model, Section 3.1.2. Spin-locking effects can be quantified better using RYDMR-B_1 spectra which show the signal intensity for a given B_0 field strength (1.2 mT) at a fixed angle (90°) as a function of B_1 field strength. This data is shown in Figure 3.27 for the four systems investigated. For $\mathrm{Py_{h10}}$/1,3-DCB (Figure 3.27(a)), at small B_1 there is a significant negative signal (spin-pumping) ($B_1^m \approx 0.17\,\mathrm{mT}$) corresponding to an increase in the rate of $\mathrm{S-T}$, the signal becomes zero ($B_1^0 \approx 0.25\,\mathrm{mT}$) before it becomes positive (spin-locked) corresponding to a decrease in the rate of $\mathrm{S-T}$ mixing compared to the zero oscillating field case.

The simulated RYDMR-B_1 curve for $\mathrm{Chy_{d12}}$/1,4-DCB (Figure 3.27(c)) shows a different feature to that of the other systems namely the positive signal intensity begins to saturate and decrease again. Although this saturation limit is not reached within the range of experimental B_1 field strengths it has been predicted to occur for the $\mathrm{Chy_{d12}}$/1,4-DCB

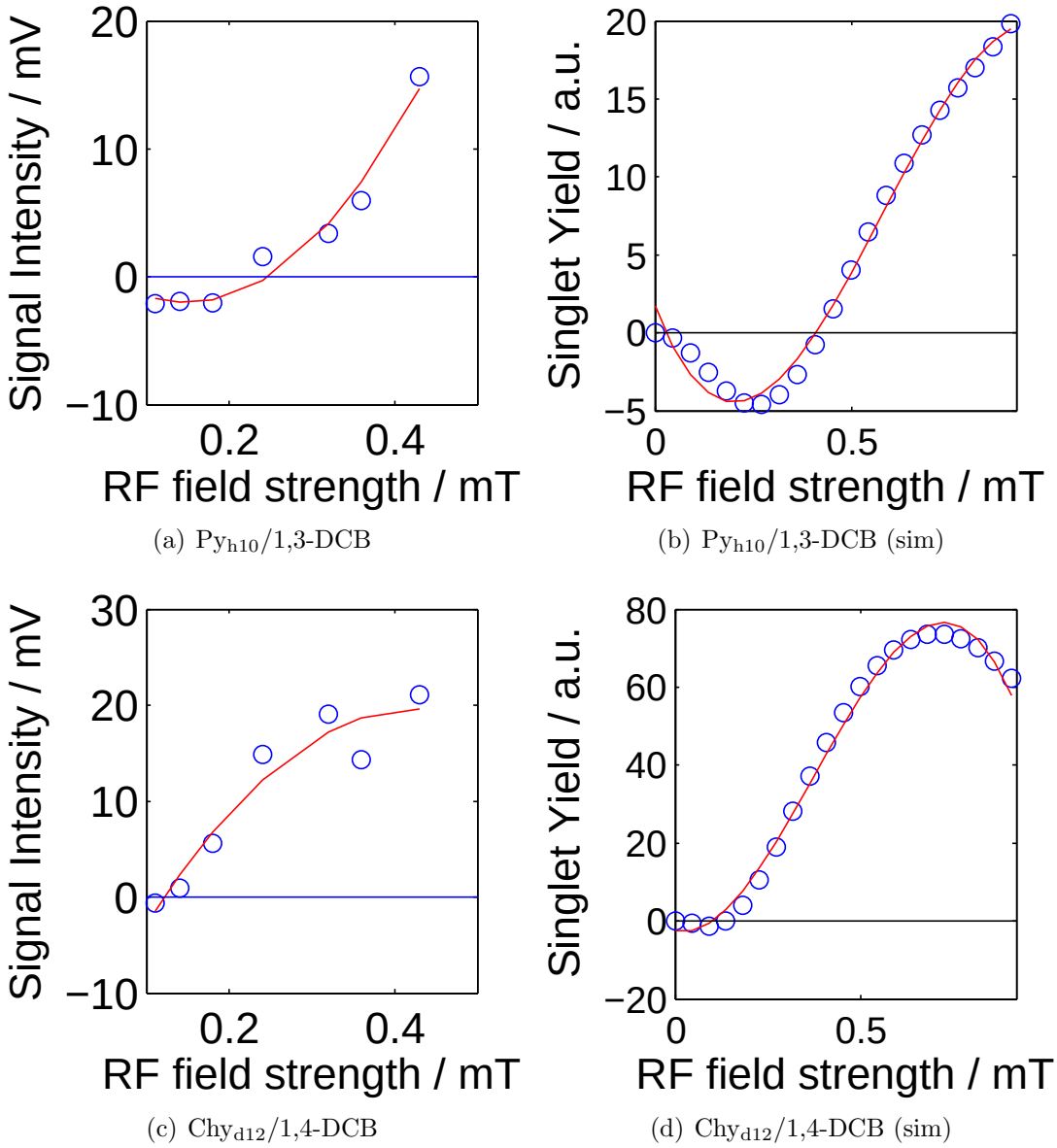

(a) Py_{h10}/1,3-DCB (b) Py_{h10}/1,3-DCB (sim)

(c) Chy_{d12}/1,4-DCB (d) Chy_{d12}/1,4-DCB (sim)

Figure 3.27: shows the RYDMR-B_1 spectra ($B_0 = 1.2\,\mathrm{mT}$) for a 36 MHz oscillating field for each of the system Py_{d10}/1,3-DCB (top) and Chy_{h12}/1,4-DCB (bottom) experimental (left) and simulated (right). The red line shows a best fit of the data using a second order polynomial.

system [55] (Figure 3.27(d)).

Chy_{d12}/1,4-DCB, the system with the smallest effective hyperfine couplings $a_{\mathrm{eff}} = 0.498\,\mathrm{mT}$, has a B_1^0 of $\approx 0.13\,\mathrm{mT}$. It can be clearly seen that the field strength at which spin-locking occurs, B_1^0, correlates with the effective hyperfine couplings within the radical pair. Plotting B_1^0 against the effective hyperfine coupling of the radical pair (Figure 3.28) shows that this correlation is approximately linear. This is not surprising since it would be expected that a larger RF field strength would be required to spin lock a system with larger hyperfine coupling constants. However, this is in contrast to that predicted by

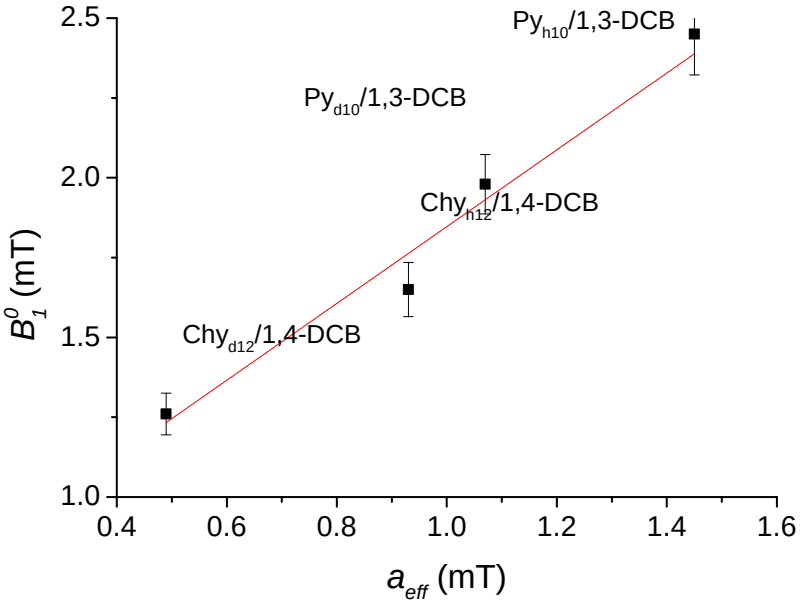

Figure 3.28: Graph shows the correlation between B_1^0 values obtained and the a_{eff} of the system.

Batchelor in 1992 [57], who predicted that the correlation between B_1^0 would be $a_{\text{eff}}^{3/2}$ in high-field RYDMR experiments but supports the findings by Wedge and Norman [54, 55], who showed that this relation would not hold, at least in the low-field limit. In the vector model proposed by Koptyug [56] the value of B_1^0 corresponds to the RF field strength at which ω_{ST} is equal to that in the zero oscillating field case. At high RF field strengths, taking the zero-field mixing rate as $\Delta\omega$ and equating with the rate for a strong RF field gives $\Delta\omega = 2\omega_1$ as the condition for equal mixing rates. Therefore, the dependence on B_1 is expected to be linear.

3.5 Conclusion

It is clear from all the data presented that the detected signals in rot-RYDMR spectra are highly sensitive to the relative orientation of the two fields (static and RF), the static field strength, the RF field strength, and the effective hyperfine coupling constant of the system using this rot-RYDMR technique. It has hence been possible to study the effects of a wide range of variables on the singlet yield and hence obtain a more comprehensive understanding of the limitations of the 'high-field' and 'low-field' approximations.

The agreement between the simulated and experimental spectra is, in general, excel-

lent. Despite the simplicity of the exponential model, used to approximate the kinetics of the system, it appears to provide an excellent basis for understanding the spectra and their dependence on the different parameters. Adaptation of the γ-COMPUTE [58] algorithm by Mr Jason Lau allowed for the use of more hyperfine coupling constants than in previous studies [65]. Using this alongside a large set of data for different parameters, B_0, B_1 and θ, it was possible to perform a global optimisation to find exponential rate constants, k. This is in contrast to previous studies [58, 65] where k values had been estimated and were less accurate because of the lack of hyperfine coupling constants used in the calculations.

Despite using a smaller set of hyperfine coupling constants for $\mathrm{Chy}_{\mathrm{d12}}$/1,4-DCB, where it was not possible to use a full set of hyperfine couplings due to lack of computer memory, the agreement between experimental and theoretical data was stronger than that observed for $\mathrm{Py}_{\mathrm{h10}}$/1,3-DCB. This suggests that inclusion of a full set of hyperfine coupling constants is not always necessary in order to produce accurate simulations, particularly in systems where the hyperfine couplings are small.

The agreement between the simulated and experimental data may be improved by correctly accounting for modulation effects. The modulation applied to the 36 MHz oscillating field means that the amplitude of the B_1 field oscillates with an audio frequency (AF) (in this work 331 Hz) and hence the signal measured by the LIA is also modulated. It is important to explore the relationship between the output signal of the LIA and the actual singlet yield that is to be measured. Experimental data can then be demodulated and the agreement with theoretical data improved. This has been implemented successfully in recent work [67], see Appendix C for further details.

The work presented in this chapter provides an extensive range of experimental data, investigating the effects of RF fields in the presence of an applied static field, whose results are supported by theoretical simulations. These investigations show that radical pair reactions are not only sensitive to magnetic fields but that they also respond to the direction and strength of an applied RF field. Together the results lay a solid foundation for the discussion of low-field, steady-state RYDMR. Experimental and theoretical data both show that RF field effects can be observed for a wide range of systems, varying

in their hyperfine coupling constants, but that different effects are observed for systems with small hyperfine coupling constants, e.g. Chy_{d12}/1,4-DCB, compared with those with large hyperfine coupling constants, e.g. Py_{h10}/1,3-DCB. In the latter case where $a_{\text{eff}} > \omega_{RF}$ the Zeeman resonance is shifted from that expected for a 36 MHz oscillating field and the spectra exhibit a shape characteristic of systems described by the 'low-field' approximation. In the former case, $a_{\text{eff}} < \omega_{RF}$, the Zeeman resonance is observed at $B_0 = 1.28\,\text{mT}$ as expected for a 36 MHz oscillating field and the spectra exhibit a shape characteristic of systems approaching the 'high-field' approximation.

Chapter 4

Exploring New Exciplex Systems

In this chapter model chemical systems are tested with regard to their potential to act as chemical compasses with properties akin to those of the avian magnetic compass and suitable for detection of any field effects using spectroscopic methods. Particular attention is devoted to exciplex systems that can be studied by fluorescent methods with high sensitivity. Different exciplex systems are used to investigate factors that determine the magnitude of the magnetic field effects and to determine how anisotropic responses can be observed and optimised. Close attention is paid to the study of long, thin molecules that have a preferential geometry in the exciplex system and thus higher possibility of a preferred direction in any aligning media. An example of a long, thin molecule is tetracene, which has already been shown to exhibit magnetic field effect with N,N-dimethylaniline (DMA) [68]. Unfortunately the use of DMA is not suitable for anisotropy investigations since the signal to noise in DMA systems is low and it is not possible to take multiple averages because DMA systems tend to deteriorate quickly, and anisotropic effects are likely to be small.

Previous research on fluorescent exciplex magnetic field effects have mainly concentrated on a few well known systems such as pyrene/N,N-dimethylaniline [7, 69] and pyrene/1,3-dicyanobenzene [70]. In this chapter an investigation will be presented which considers what factors determine the formation of exciplexes between a range of different electron donor molecules and electron acceptor molecules. The complex equilibrium between the exciplex and the spin-correlated RP as the source of the MFE is considered.

Fluorescence emission spectra, activation energies, redox potentials and spin density distributions are presented and used to predict which properties of the redox pair will determine if the formation of an exciplex from the RP is favourable and if these parameters can be used to quantitatively assess the existence and magnitude of MFEs.

4.1 Optical Spectroscopy

Experimental studies conducted during the course of this study included UV/Vis absorption spectroscopy to determine the ground state absorption spectra of the donor/acceptor pair and the optimum wavelength at which the system should be photoexcited. Steady state fluorescence spectra were recorded to determine the wavelengths and intensities of the exciplex emission bands. This allows comparison of the monomer and exciplex emission and highlights any quenching of the monomer, a good indication of strong interactions between donor and acceptor molecules.

4.1.1 Ground State UV/Vis Absorption Spectroscopy

A UV/Vis absorption spectrophotometer records the absorption of the sample as a function of the wavelength. The resulting UV/Vis ground state absorption spectrum is presented as a graph of absorbance, A, versus wavelength, λ, where absorbance is defined as below, according to the well known Beer-Lambert law:

$$A = \log_{10}(I_0/I) = \epsilon c l \tag{4.1}$$

where c is the concentration of the sample (mol dm^{-3}); l is the length of the light path (cm); ϵ is the molar absorptivity (mol dm^{-3}); I_0 is the intensity of the incident light at a given wavelength (λ) and I is the transmitted light at a given wavelength, λ.

4.1.2 Steady State Fluorescence Emission Spectra

An exciplex is an electronically excited complex of definite stoichiometry which is 'non-bonding' in the ground state. For example, a complex formed by the interaction of an

excited molecular entity with a ground state counterpart of a different structure. Exciplexes can be fluorescent species and therefore steady state fluorescence emission spectra can be used to quantify the exciplex formation. In these experiments the sample was excited at a wavelength corresponding to the ground state absorption of the donor or acceptor molecule and the emission of the exciplex was monitored. The wavelength (and thus the energy) of the light emitted is dependent on the energy gap between the ground state and the first excited singlet excited state (Figure 4.1). Other processes, which may compete with fluorescence, are phosphorescence, intersystem crossing, excited state isomerisation, photoionisation, photodissociation and acid-base equilibrium.

4.2 MARY

4.2.1 Introduction

Steady state [17, 71] and time resolved [72, 73] techniques have been used to investigate the effects of static magnetic fields on radical recombination reactions for a number of years. All of these techniques come under the heading of experiments monitoring Magnetically Altered Reaction Yield (MARY). In any MARY experiment the reaction is monitored using a variety of techniques; exciplex fluorescence [74], delayed fluorescence [75], absorption techniques [76] and photoconductivity [77]. The method described here is a steady state MARY experiment which monitors the singlet yield of the RP via exciplex fluorescence. The reaction scheme for this is described in Section 1.3. In this mechanism the MFE is observed by preparing the radicals in an environment that has restricted diffusion. This is achieved by firstly creating a charged radical pair (RP) in which the partners have a mutual Coulombic attraction and secondly by using viscous solvents or media which hinder diffusion and encourage recombination of the radicals within the solvent cage. Further methods currently used to maximize MFEs include using micelles and vesicles to contain the RP once formed [78], linked donor-acceptor systems (biradicals) [79] or the use of rigid molecules such as proteins [76] or polymers [80].

As shown in Figure 4.1, the exciplex is in equilibrium with the singlet RP and, since the singlet recombines via the exciplex, the exciplex fluorescence intensity is a direct

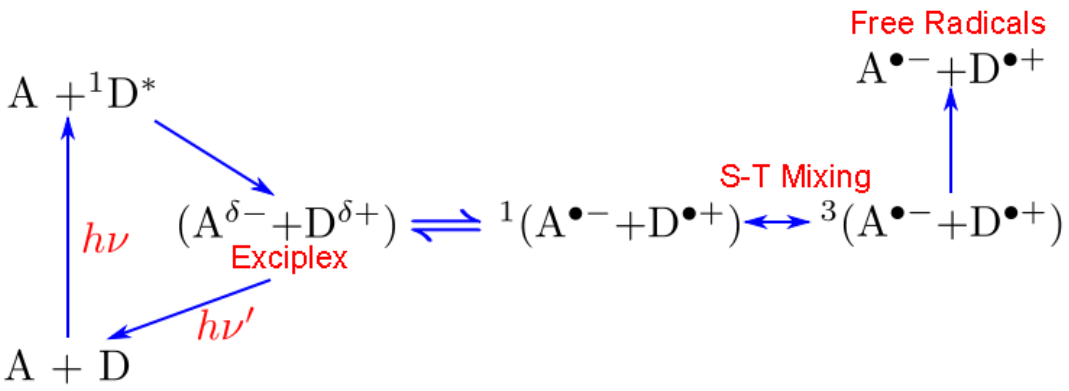

Figure 4.1: Schematic representation of the species involved in the formation of the magnetic field effect on the exciplex according to the radical pair mechanism. See Section 1.3 for further details.

measure of the concentration of RP in the singlet state. Therefore detection of exciplex fluorescence gives a direct indication of the singlet yield, ϕ_S.

4.2.2 The Technique of Magnetically Altered Reaction Yield Experiments

To produce a MARY curve the static magnetic field is swept whilst the yield of a radical reaction is measured. When detection of the reaction yield is achieved via singlet exciplex fluorescence the magnetic field effect (MFE), Γ, is calculated as

$$\Gamma = \left[\frac{I_B - I_0}{I_0}\right] \times 100 \tag{4.2}$$

where I_B and I_0 are the intensities of the exciplex fluorescence in the presence and absence of a static field respectively. It should be noted that the magnetic field effect on a chemical reaction can also be obtained by studying the concentration of the radicals as a function of the applied field, e.g. transient absorption techniques.

The shape of the MARY curve can be characterised by several features. If a low field effect (LFE) is observed there will be a minimum in the signal at low field strengths. This is characterized by two values Γ_{LFE} and B_{LFE}, the magnitude of the LFE and the field strength at which the maximum LFE occurs, respectively. At larger field strengths, up to 100 mT, the normal MFE tends to rise from zero to an asymptotic value. This is characterized by Γ_{MFE}, the maximum magnitude of the MFE, and also the field strength

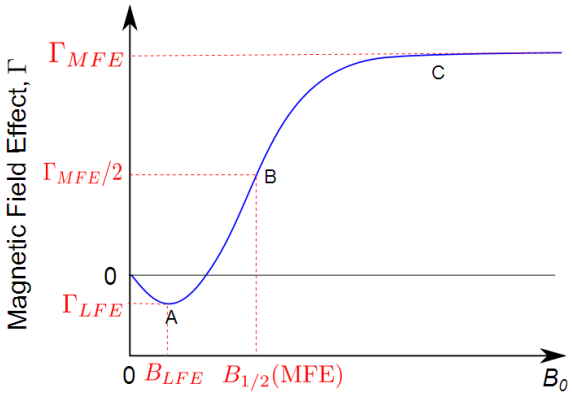

Figure 4.2: A typical MFE curve showing (A) the low field effect region, (B) $B_{1/2}$(MFE) field point and (C) saturation of the magnetic field effect at high fields.

at which Γ reaches half this limit, $B_{1/2}$(MFE). These values are shown graphically in Figure 4.2. In some cases, however, an asymptotic value is often not reached if the relaxation mechanism plays an important role.

4.2.3 Modulation Techniques

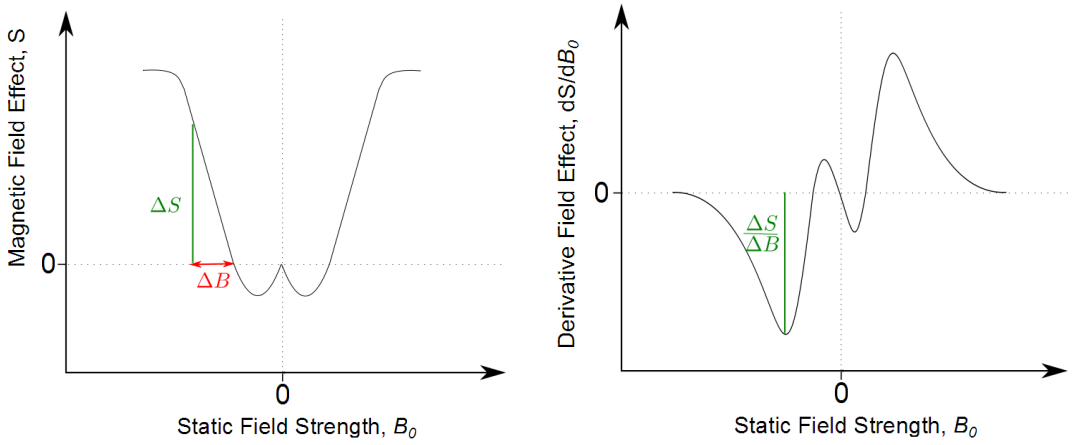

(a) MFE (b) First Derivative Spectra

Figure 4.3: Phase sensitive detection in the Modulated MARY experiment. The measurement recorded is the change in signal ΔS (green bar) when a modulated field ΔB (red bar) is applied on top of a static field. A first derivative curve is recorded, with a distinctive, opposite polarity LFE deflection.

There are innate sensitivity issues with MARY experiments in that the concentration of radicals produced are typically low, of the order of 10^{-5} - 10^{-5} mol dm^{-3}. Detecting the presence of these radicals and consequently measuring small changes in their concentration (which may only be a few percent) caused by the field is a difficult technical challenge. Another issue is that the RP may not be the only species which shows absorption or

fluorescence at a particular wavelength and often the characteristic bands overlap with those of starting materials, intermediates or products, making the measurement of the RP concentration more difficult. For example, the luminescence of a molecule may include fluorescence, phosphorescence, delayed fluorescence from triplet-triplet annihilation and excimer fluorescence. Thus a technique is needed which allows selective determination of a single magnosensitive species within a reaction scheme.

Consider a static field, B, upon which a modulation of amplitude of ΔB and known frequency, f_0, is applied, Figure 4.3. If it is assumed that (1) the S − T mixing in the RP is sensitive to the size of the total magnetic field and (2) the RP recombines from the singlet state only, then exciplex fluorescence will also dependent on the magnitude of the field. The modulation of the static field will therefore lead to a corresponding modulation in the field dependent property, i.e. exciplex fluorescence, S, with a frequency f_0 and an amplitude ΔS as shown in Figure 4.3. Since detection relies on the change in signal when modulation is applied the signal subsequently recorded is a first derivative spectrum. Although other non-field dependent characteristics may fluctuate over time, such as the fluorescence from an exciplex formed by one of the RP precursors, they are unlikely to oscillate with the same frequency, f_0. If detection is subsequently limited to only those properties that oscillate with frequency f_0, then the sensitivity of the experiment will be dramatically improved. This is known as 'phase-sensitive detection' where neglecting other properties, whether they be constant, oscillating with a different frequency, or randomly modulated will significantly improve the signal:noise (S:N) ratio for the experiment. The use of this technique on top of a swept magnetic field gives the experiment is subsequent name 'Modulated-MARY'.

4.2.4 MARY Plots

An important parameter when characterizing the shape of MARY plots is the $B_{1/2}$ value. This value corresponds to the static field strength at which the MFE reaches half of its saturation value, as illustrated in Figure 4.2. $B_{1/2}$ is related to the hyperfine couplings in

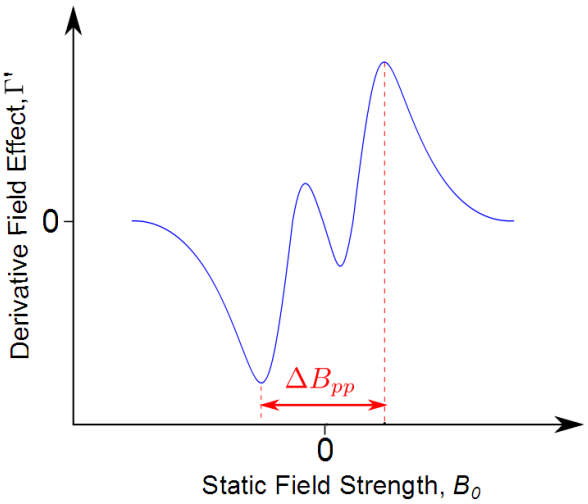

Figure 4.4: A first derivative MARY spectrum showing how to measure ΔB_{pp}

the RP [6] and is given by

$$B_{1/2} = 2\frac{(a_A^2 + a_B^2)}{(a_A + a_B)} \tag{4.3}$$

where a_A and a_B are the effective molecular hyperfine couplings for radical 1 and 2 respectively, as defined in Equation 1.34. This definition of $B_{1/2}$ is referred to as $B_{1/2}$(hfi). When analysing first derivative spectra (Modulated-MARY) it is more convenient to approximate $B_{1/2}$ as

$$B_{1/2} = \frac{\sqrt{3}}{2}\Delta B_{pp} \tag{4.4}$$

where ΔB_{pp} is the peak to peak separation of the recorded first derivative data [74], as shown in Figure 4.4. This definition of $B_{1/2}$ is referred to as $B_{1/2}$(Pk-Pk) and is approximated with the assumption that the MARY spectrum has a Lorentzian line shape and neglects the LFE. It is nevertheless often found to be the simplest method of providing a numerical parameter by which spectra can be characterised.

4.2.5 Electron Self Exchange

There is an additional reaction that can take place in the RPM which has to be considered when discussing MARY spectroscopy particularly when characterising MARY spectra using $B_{1/2}$ values. Electron self exchange is a mechanism where the transfer of an electron occurs between a neutral molecule and its radical ion counterpart according to the reaction

scheme:

$$Q^{\cdot\pm} + Q \rightleftharpoons Q + Q^{\cdot\pm} \tag{4.5}$$

and occurs with a rate constant k_{ex}. When self exchange is significant it will affect the size of the effective hyperfine coupling constants within the system and therefore affect the width of the MARY spectrum and hence $B_{1/2}$.

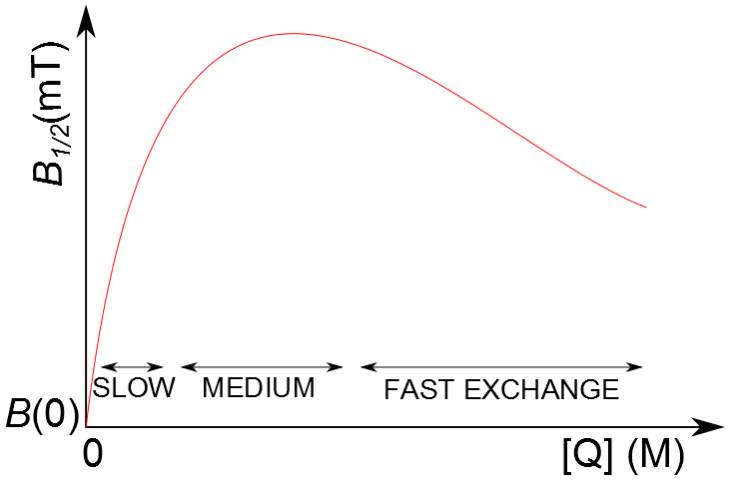

Figure 4.5: Schematic representation of the variation of $B_{1/2}$ with increasing concentration, [Q], of the radical undergoing exchanging adapted from [81].

The most widely used technique for investigating homogeneous electron self-exchange is ESR, where line broadening may be used to calculate the rate constant, k_{ex}, for electron self-exchange reactions [81]. More recently, however, MARY spectroscopy has been used to calculate the rate constants for a number of different fluorophore systems [74].

The rate of electron transfer is dependent on the concentration of the exchanging species, [Q], according to

$$\nu_{ex} = \frac{1}{\tau} = k_{ex}[Q] \tag{4.6}$$

where ν_{ex} is the rate of self exchange. In 2002, Justinek et al. [74] showed that $B_{1/2}$ varied with the concentration, and hence so did the rate of self-exchange, showing a linear increase in the low concentration regime, Figure 4.5. As the concentration is increased further a maximum in $B_{1/2}$ occurred. Theoretically, a subsequent decrease in $B_{1/2}$ is predicted at higher concentrations (Figure 4.5) but it is rarely observed, due to solubility issues. However, the effect has been characterised for a pyrene/1,3-dicyanobenzene system in THF:DMF solvents [74].

The initial rise in $B_{1/2}$ with concentration can be ascribed to energy level broadening of the radical pair spin levels according to Heisenberg's uncertainty principle. The $B_{1/2}$ value in this linear slow exchange region can be approximated by the expression [82]:

$$B_{1/2}([Q]) \approx B_{1/2}(0) + \frac{h}{g_e \mu_B} k_{ex}[Q] \tag{4.7}$$

and an estimate of k_{ex} can be obtained from the initial gradient of the curve, $\frac{\mathrm{d}B_{1/2}[Q]}{\mathrm{d}[Q]}$, at low concentrations. In the intermediate to fast exchange region, the rise in $B_{1/2}$ levels off and subsequently decreases as the increasing rate of electron self exchange causes the residence time of an electron on any radical to diminish.

4.2.6 Experimental Apparatus

A block diagram of the experimental MARY apparatus used in this thesis is shown in (Figure 4.6).

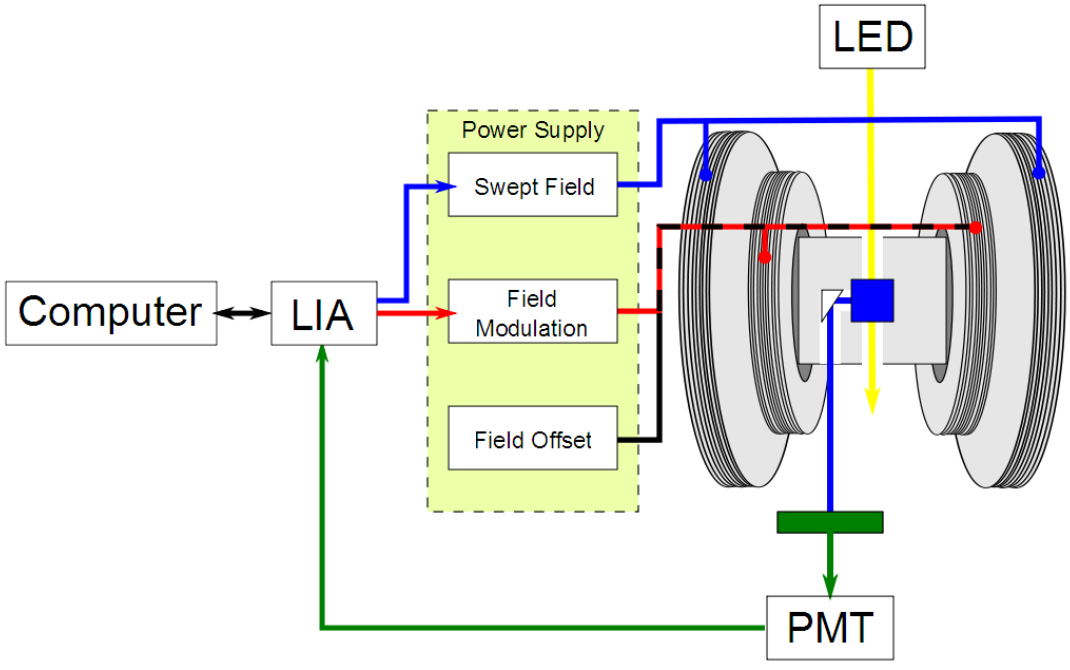

Figure 4.6: Schematic diagram showing the Modulated-MARY apparatus, the sample block mounted between two sets of Helmholtz coils. The larger of the coils produces a swept magnetic field; the smaller pair of coils provides the modulating field and a manual adjustable offset field. The lock-in amplifier (LIA) controls the swept field, demodulates the photomultiplier tube (PMT) voltage, the computer queries and sets the LIA parameters. Excitation is achieved using a light emitting diode (LED).

The sample is contained within a 10 mm by 10 mm cross-section quartz cuvette with four optical windows which holds approximately 3 cm^3 of solution when full. This is held

firmly between the magnetic field coils in a black-anodized sample block. Continuous sample illumination is provided by a mounted light emitting diode (LED), chosen to have a specific wavelength of light dependent on the system being used, which is powered by a high-power LED driver (ThorLabs). In most of the work presented in this thesis an LED with a wavelength of 385 nm and current 700 mA is used which has a very narrow wavelength range ±10 nm. The light from the LED is focused onto the sample using a collimator followed by a mounted lens. The fluorescence from the sample is collected at 90° to the incident beam, reflected by a prism and transmitted to the photomultiplier (PMT) housing by a liquid-filled light guide (LFLG). The PMT housing is a black-anodized, earthed μ-metal box containing the PMT assembly (Hamamatsu R928 PMT connected to a Hamamtsu C6271 high voltage power supply unit (PSU)); a variable resistor is mounted on the top face of the box to allow the user to make manual adjustments to the gain of the PMT such that the output voltage can be set constant across all experiments. Within the housing, a filter placed between the LFLG and the PMT will select the optimum wavelength for detection, corresponding to the largest exciplex fluorescence intensity relative to the size of other photochemical emissions which typically lies in the range of 400 nm - 600 nm.

The output to the PMT is T-pieced and connected to a SRS510 analogue lock-in amplifier (LIA) in two places. The first output provides the signal input for phase sensitive detection and the second is an auxiliary input which allows direct measurement of the PMT output voltage. The LIA is connected to a PC via an RS232 interface to allow two-way communication. The software, controlling the experiment, was written in National Instruments LABVIEW language to provide a graphical computer interface to the LIA, it allows control of a number of experimental parameters and also drives the dual power supply which controls the current to the coils. The LIA has two direct current (DC) analogue outputs. One controls the static field coils PSU and can produce a sweeping static magnetic field from 0 mT - 26 mT. The other drives the LIA internal signal generator, which produces a modulation frequency proportional to the input voltage and has both static and oscillating currents applied. The former current is manually controlled and can create a static-field offset of up to ±8 mT (to allow fields of the opposite direction

to be measured). The latter, audio-frequency (af) field, can have its amplitude adjusted (modulation depth), inducing fluctuations in the field dependent property, i.e. the fluorescence, which is measured by the PMT and subsequently monitored by the LIA. The total applied field is the sum of the static fields from the two sets of coils. Typically the applied field is swept from −3 mT - 23 mT. This was done to ensure that the spectra passes through zero field and that it is symmetrical around zero. A slight shift might be expected because of the Earth's magnetic field which is not screened out. The residual field was measured at the sample position and found to be 0.034 mT

Modulation Depth and Frequency

The magnitude of the modulation depth affects the size and the shape of both the MFE and the LFE. A greater modulation depth gives a larger Γ_{MFE} but can 'wash out' the LFE if the field modulation is comparable in size to the width of the LFE. The small changes in fluorescence intensity either side of zero field are averaged out by the modulation. If the signals are weak, larger modulation depths were used (typically 2.0 mT) to gain the largest Γ_{MFE} possible. However, in most systems it was satisfactory to use a smaller modulation depth (0.5 mT) and hence not lose the possibility of observing LFEs. Unless otherwise stated experiments were recorded with a modulation depth of 0.5 mT.

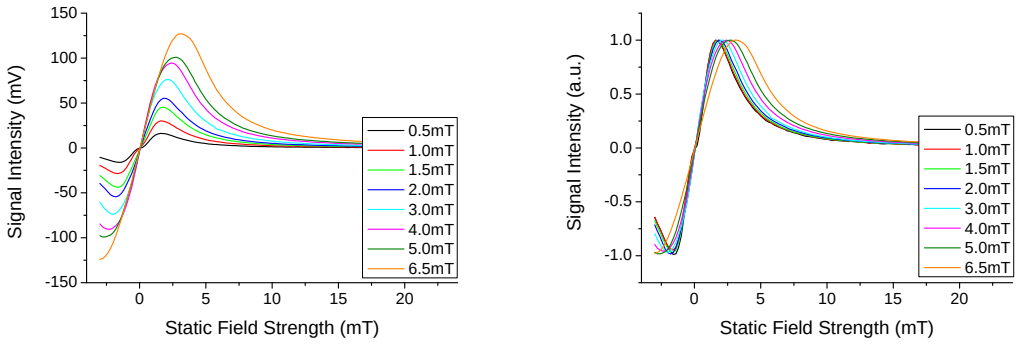

(a) Raw data (b) Normalised data

Figure 4.7: The effect of modulation depth on a MARY signal recorded using a Py/1,3DCB in cyclohexanol:acetonitrile (CH:ACN) (9:1) sample with a modulation frequency, 79 Hz. The left figure shows the raw data and the right hand figure shows the normalised data. The LIA time constant setting was 1 sec.

An investigation into the effect of the modulation frequency showed that different frequencies resulted in different MARY signals, (data not shown) and showed that at

lower modulation frequencies the MARY spectra exhibit a greater signal intensity. It was therefore necessary to calibrate the modulation field strengths for different frequencies. This was done for a Py/1,3-DCB sample Figure 4.7. The raw data shows that increasing the modulation depth increases the strength of the signal recorded (as described in Section 4.2.6) but at the cost of losing any observed low field effect (see inset Figure 4.7(a)). The normalised MARY data Figure 4.7(b) shows that for modulation depths larger than 2.0 mT, there is a broadening of the spectra. Hence, to avoid any deformation in the signal, modulation depths should not exceed 2.0 mT.

4.3 Results and Discussions

4.3.1 Polyarenes

In this section the RPs were generated from polyarenes acting as electron donors, namely naphthalene (Naph), pyrene (Py), chrysene (Chy), anthracene (Anth), phenathrene (Phen), tetracene (Tetr) and pentacene (Pent), and isomers of dicyanobenzene (DCB) acting as electron acceptors. The MARY spectra of these RPs were recorded in order to investigate systematically how increasing conjugation and changes in redox parameters may affect the exciplex formation and which parameters, if any, may be used to predict the occurrence of magnetic field effects.

All systems were studied using the solvent cyclohexanol:acetonitrile (CH:ACN) in the ratio 9:1 and concentrations of 0.4 mM for the electron donor and 40 mM for the electron acceptor unless stated otherwise. The optical absorption data for all molecules is shown in Figure 4.8 and a summary of details obtained from the fluorescence data for all systems (Appendix D) are shown in Table 4.1. The absorption data in Figure 4.8 illustrate that increasing conjugation of double bonds acts to shift the absorption maximum to longer wavelengths and the lowest excited state for polyarenes with small number of π-electrons (i.e. napthalene) occurs at short wavelengths. The three isomers of DCB have absorption bands in the region < 300 nm and these bands overlap with those of naphthalene and phenanthrene. The other polyarenes absorb in the region > 300 nm with the longest polyarenes (i.e. pentacene) absorbing at much longer wavelengths. In Figure 4.9 all

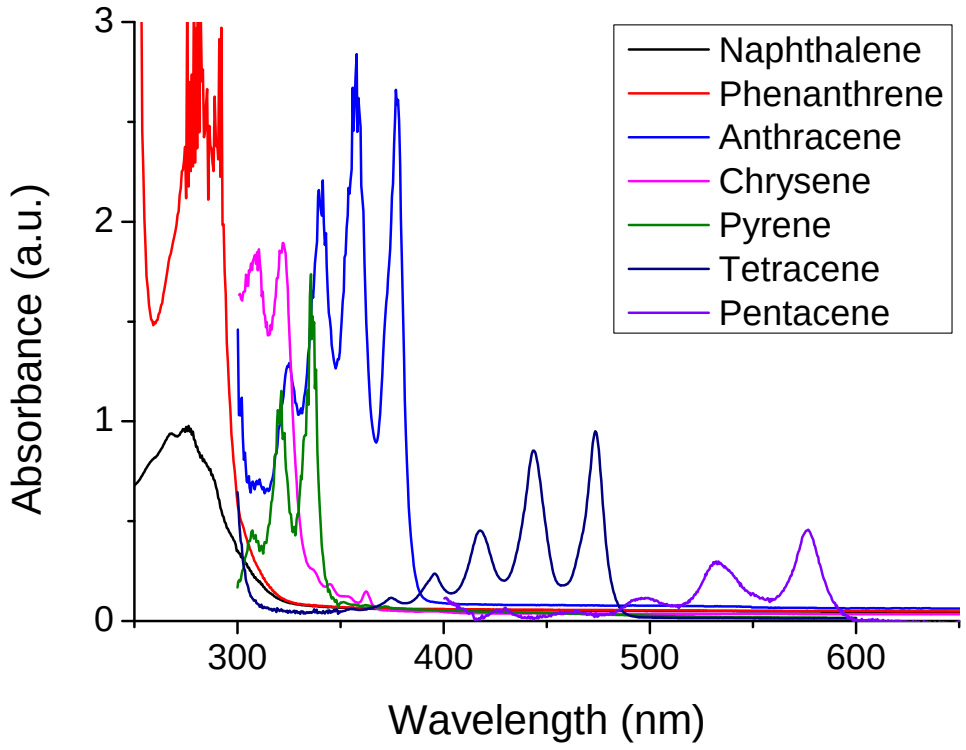

(a) Polyarene Absorption

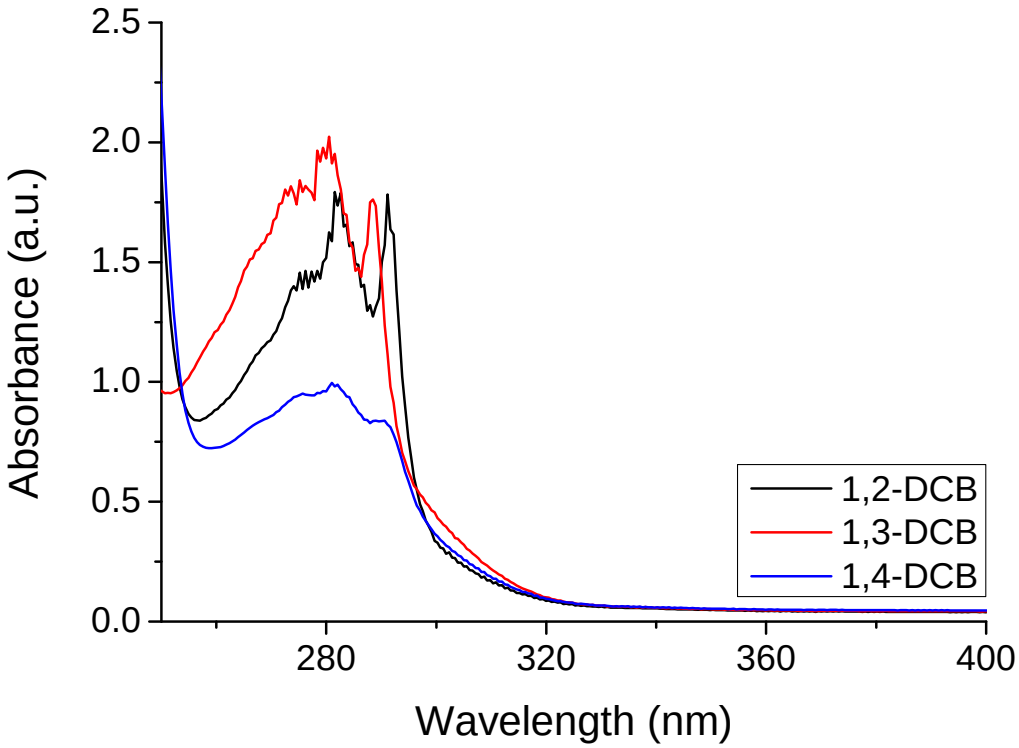

(b) DCB Absorption

Figure 4.8: UV/Vis absorption data for all polyarenes (Figure 4.8(a)) and DCB isomers (Figure 4.8(b)) used in this section. The solvent used was CH:ACN (9:1) ratio and concentrations of 0.4 mM for the electron donors and 40 mM for the electron acceptors.

obtained MARY data are presented alongside theoretical and experimental $B_{1/2}$ values, $B_{1/2}$(hfi) (Equation 4.3) and $B_{1/2}$(Pk-Pk) (Equation 4.4), respectively; the singlet state lifetime of the polyarenes in the absence of any electron acceptor at 77 K and a measure of the size of the MFE. For the purposes of this chapter these MFEs are given as a percentage of the largest field effect found in this study, namely that of Py/1,3-DCB. The data is presented in order of number of π-electrons in the polyarene. Theoretical $B_{1/2}$(hfi) values were calculated using hyperfine coupling constants as detailed in Appendix E.

	Excitation (nm)	Max. Monomer Emission (nm)
Naphthalene	300	350
Pyrene	350	400
Chrysene	320	375
Anthracene	385	400
Phenanthrene	320	320
Tetracene	465	510
Pentacene	550	620

Table 4.1: Summary of the optical data obtained from fluorescence experiments of all polyarene systems. The excitation wavelength corresponds to the maximum in the UV/Vis of the polyarene.

It can be clearly seen in all the data that the MARY spectra (not including tetracene and pentacene for which MFEs were not observed) demonstrate a shape characteristic of a second derivative spectra as described in Section 4.2.2. All data show a MARY plot which becomes constant with field by 12 mT (or below). In general, LFEs can be seen as very small deflections in the MARY signals around $B_0 = 0$ with the most significant LFE observed in the Phen/1,3-DCB system. It is possible that most of the LFE have been 'washed out' by large modulation depths but this was not investigated further. Comparison of the data also shows that if an MFE is observed for one isomer of DCB then MFEs will be observed for the others.

Experimentally determined $B_{1/2}$(Pk-Pk), correspond to those predicted theoretically (Figure 4.9) using Equation 4.3 (see Table 4.2 and Figure 4.10). In general, for all systems studied $B_{1/2}$(1,3-DCB) > $B_{1/2}$(1,2-DCB) > $B_{1/2}$(1,4-DCB) and hence spectra are broader for systems with 1,3-DCB. This is expected since the hyperfine couplings in 1,3-DCB are larger than those in 1,2-DCB and 1,4-DCB. The only system for which this trend is not observed is anthracene where the $B_{1/2}$(Pk-Pk) for 1,2-DCB and 1,4-DCB are equal. However, the signal to noise in the Anth/1,4-DCB is very small and results in a large

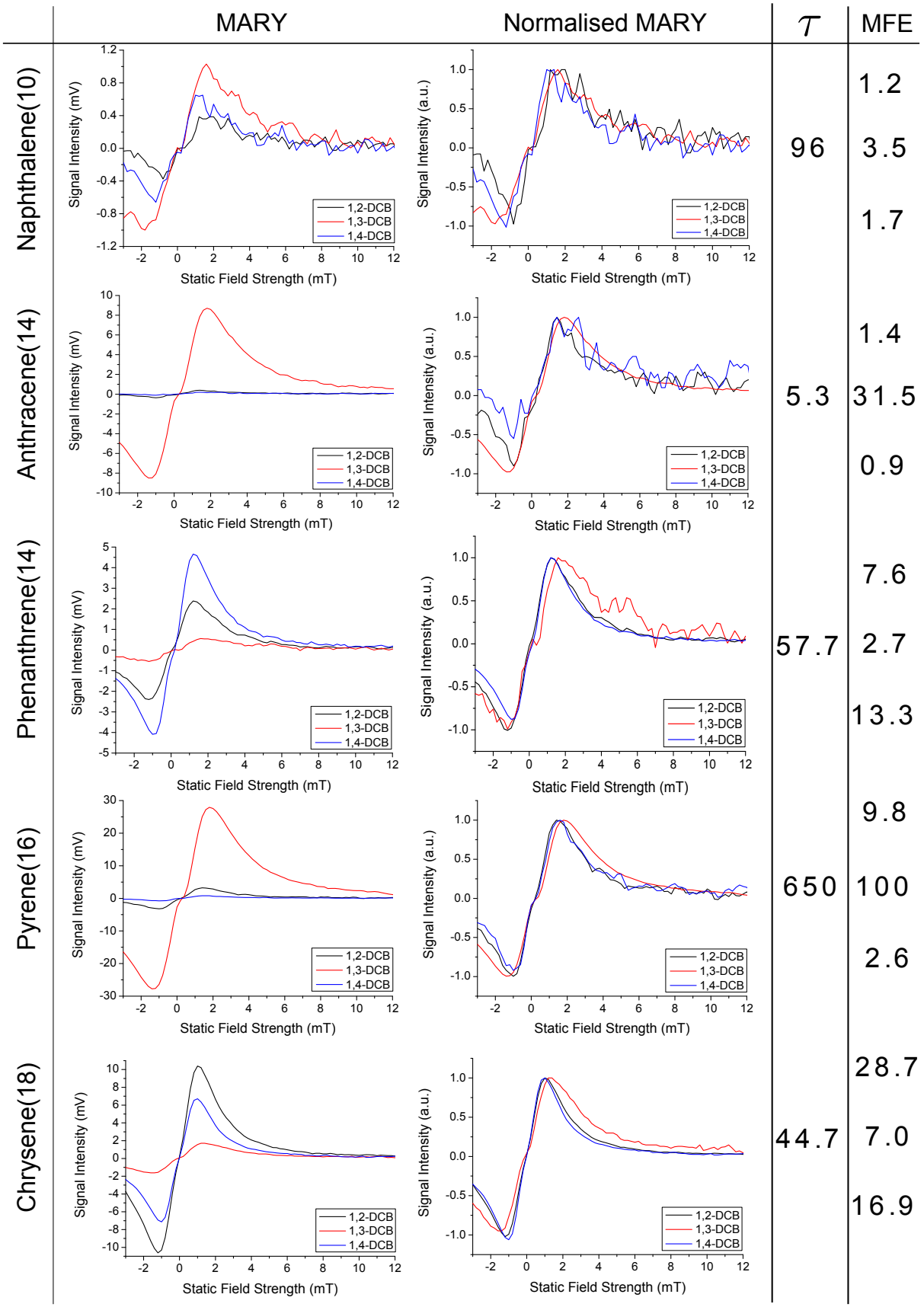

Figure 4.9: All obtained MARY data for the polyarene/DCB RP systems. Singlet state lifetimes, τ, (ns) of the polyarenes in the absence of any electron acceptor at 77 K [83]. All quoted values are in the order 1,2-DCB (top), 1,3-DCB(middle) and 1,4-DCB(bottom) respectively. Each curve obtained is the average of two scans.

	a_d		a_a	$B_{1/2}$ (hfi)	$B_{1/2}$(Pk-Pk)	$B_{1/2}$(MFE)
Naphthalene	1.28	1,2-DCB	0.80	2.17	2.43	3.87
		1,3-DCB	1.04	2.34	3.12	3.10
		1,4-DCB	0.53	2.12	2.23	3.00
Anthracene	1.20	1,2-DCB	0.80	2.08	2.25	2.56
		1,3-DCB	1.04	2.25	2.95	3.10
		1,4-DCB	0.53	1.99	2.25	2.81
Phenanthrene	1.16	1,2-DCB	0.80	2.03	1.91	2.11
		1,3-DCB	1.04	2.20	2.60	3.19
		1,4-DCB	0.53	1.93	1.73	1.94
Pyrene	1.03	1,2-DCB	0.80	1.86	2.25	3.20
		1,3-DCB	1.04	2.07	2.95	3.10
		1,4-DCB	0.53	1.72	2.08	3.95
Chrysene	0.99	1,2-DCB	0.80	1.82	2.25	2.51
		1,3-DCB	1.04	1.95	3.12	4.09
		1,4-DCB	0.53	1.67	2.08	2.40

Table 4.2: Calculated and experimental $B_{1/2}$ values for all polyarene systems which exhibited MFEs. $B_{1/2}$(hfi) were calculated using Equation 4.3, $B_{1/2}$(Pk-Pk) were calculated using Equation 4.4 and $B_{1/2}$(MFE) as shown in Figure 4.2. Hyperfine data obtained from [54, 84, 85] and are detailed in Appendix E. The effective hyperfine coupling constants for the donor and acceptor molecules are denoted a_d and a_a respectively. *All values are given in mT.*

error in $B_{1/2}$(MFE) and $B_{1/2}$(Pk-Pk) values.

The magnitudes of the observed MARY signals are different for all systems studied. Since the isomers of DCB are consistent for all systems, any differences in the observations of MFEs can be ascribed to the properties of the polyarene (electron donor) molecule when with the same DCB isomer in the RP. Although the size of the observed MARY signal does not correlate directly with the number of π electrons in the polyarenes, no MFEs were observed for the longest polyarene molecules, tetracene and pentacene. An attempt will be made to explain these findings in later discussions. The data shows the intensity of the MARY signal for the Py/1,3-DCB system is the largest obtained whilst the signal intensity of the MARY for Anth/1,4-DCB is the smallest. This is shown by presenting all MFEs as a percentage of the largest obtained, i.e. Py/1,3-DCB (Figure 4.9).

No consistent and comparable data for the polyarenes used in this thesis (CH:ACN (9:1) solvent at room temperature) were available in the literature and it was not possible to resolve the lifetimes using experiments available. Therefore, the singlet state lifetimes given in Figure 4.9 were recorded at 77 K which allows the comparison of the relative lifetimes between the polyarenes. They are, however, not true lifetimes for polyarenes in

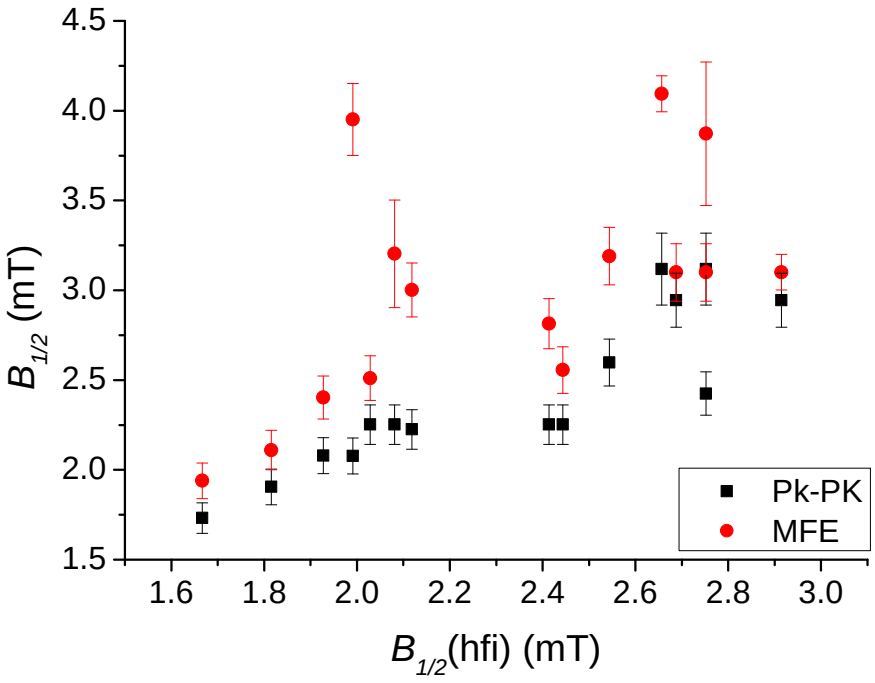

Figure 4.10: The relationship between $B_{1/2}$(Pk-Pk) (black) and $B_{1/2}$(MFE) (red) with the theoretically determined $B_{1/2}$(hfi), Table 4.2.

solution in the presence of electron acceptors (which would be much shorter) but they give some idea of the trends expected for singlet state lifetimes in polyarenes. For example, the singlet state in pyrene is much longer lived than in other polyarenes. There is therefore more chance of quenching by DCB and a higher chance of forming an exciplex. Hence larger signals are observed in pyrene systems.

The singlet state lifetimes cannot, however, solely account for all trends observed in the MARY spectra. For example, the singlet state lifetime for naphthalene is longer than other polyarenes but the observed MARY signal intensities are generally weaker. The singlet state lifetime of anthracene is much shorter than other polyarenes but Anth/1,3-DCB exhibited strong MARY signals whilst tetracene and pentacene did not exhibit any MFEs and their lifetimes are 6.4 ns [83] and 9.4 ns [86] respectively.

Furthermore, the fluorescence data shown in Appendix D help qualitatively in the discussion of some trends, e.g. for Naph/DCB systems, which demonstrate that there is very little quenching of the naphthalene monomer fluorescence by 1,2-DCB (explaining the low MARY signals observed), with more (but only slightly) quenching being observed by both 1,3-DCB and 1,4-DCB. However, the fluorescence data for pyrene shows that

there is significant quenching of the excimer on addition of 1,3-DCB. This difference in the quenching rate of the monomer fluorescence and corresponding exciplex formation contributes a further (so far, qualitative) argument for the explanation of different MFE signals.

The data in Table 4.2 shows the experimental and theoretical $B_{1/2}$ values for all polyarene systems studied. Generally, the $B_{1/2}$(hfi) values show a strong agreement with $B_{1/2}$(Pk-Pk) (Equation 4.4 see Figure 4.10). Whilst the agreement between $B_{1/2}$(MFE) and $B_{1/2}$(hfi) is not as strong. In general it can be seen that $B_{1/2}$(MFE) are larger than $B_{1/2}$(Pk-Pk). This discrepancy is found because Equation 4.4 is based on the assumption of an approximate Lorentzian line shape of the MARY spectrum [74] and therefore results in larger calculated $B_{1/2}$(Pk-Pk). The discrepancy between $B_{1/2}$(hfi) and $B_{1/2}$(MFE) could be caused by self-exchange reactions in the MARY process which cause the MARY to be broadened and exhibit larger $B_{1/2}$ values than estimated by Equation 4.3.

4.3.2 Energetics of Photoinduced Electron Transfers

The formation of an exciplex is one method for detecting the concentration of the singlet state and hence of magnetic field effects, by fluorescence methods. Other methods include detecting delayed fluorescence via triplet-triplet annihilation (Chapter 5). In this section the factors which effect the stability of the RP and exciplex will be investigated and will be used to predict under which circumstances an optimum balance is struck between the stability of RP and that of the exciplex. This approach has also been adapted by Kattnig *et al.* [68] who observed a linear relationship between the free energy of electron transfer and magnitude of MFE. The method employed by Kattnig [68] used a sophisticated and elegant way of calculating the free energy of electron transfer using free energy surfaces. Here, a more simplistic model is introduced which may provide a quick way of screening and referencing to check if systems are likely to exhibit MFEs or not.

Theories developed by R.A. Marcus and A. Weller [87–89] can be used to give a theoretical description of the energetics and rates of the electron transfer process providing an estimate of the 'driving force' for photoinduced charge separation in a solvent with relative permittivity, ϵ_S (dielectric constant). The 'Gibbs energy of photoinduced electron

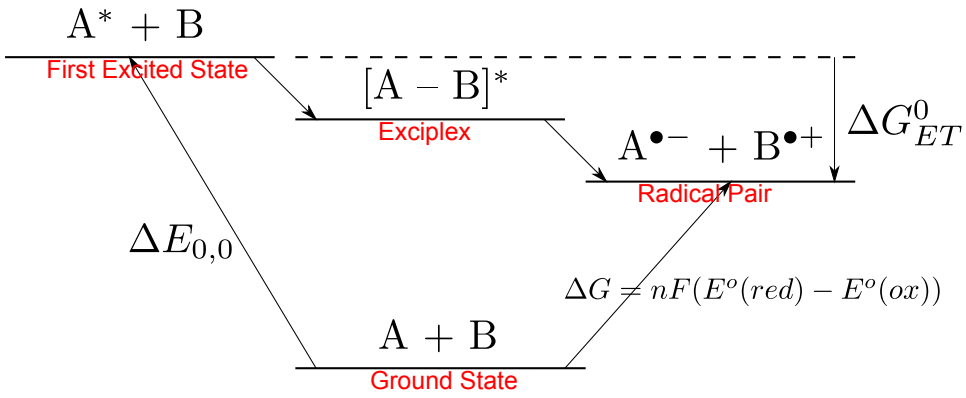

Figure 4.11: An illustration of the hess cycle required to find the 'Gibbs energy of photoinduced electron transfer', ΔG^0_{ET}. The electron donor is donated B and the electron acceptor A. $\Delta E_{0,0}$ is the energy of the lowest excited state transition and it is assumed that ΔS for this transition is equal to zero.

transfer', ΔG^0_{ET}, can be calculated [88]

$$\Delta G^0_{ET} = -nF(E^0(red) - E^0(ox)) - \Delta E_{0,0} - \frac{e^2 A}{\epsilon d 4\pi\epsilon_0}. \tag{4.8}$$

In this equation the redox potential $E^0(ox) = E^0(D^{+\bullet}/D)$ describes the process $D^{+\bullet} + e^- \rightarrow D$ and the redox potential $E^0(red) = E^0(A/A^{-\bullet})$ describes the process $A + e^- \rightarrow A^{-\bullet}$ where n is the number of transferred electrons ($n = 1$ in all redox reactions presented in this thesis) and F is the Faraday constant ($96\,485.3\,\mathrm{Cmol}^{-1}$). $\Delta E_{0,0}$ is the energy of the lowest excited state transition (0,0 band) and can be determined from UV/Vis spectra. This energy corresponds to the peak in the absorption band. It is assumed that the entropy, ΔS, for this transition is negligible as found to be the case in other electron transfer reactions [90]. The last term in Equation 4.8 is the coulombic attraction energy experienced by the ion pair following the electron transfer. ϵ is the dielectric constant of the solvent (for CH/ACN (9:1) it is approximately 16), d is the distance between the charges (typically $\leq$2 nm) and e is the charge of an electron. This last term makes a small contribution to the overall energy change [88] and since it is approximately constant for all systems given as the same solvent is always used it will be neglected in all that follows. These processes are shown in Figure 4.11.

The redox potential data for all donor and acceptor molecules along with the excitation energies for the donor molecules are shown in Table 4.3 and Table 4.4. The first oxidation

Donor	$E^0(ox)$/ V	$\Delta E_{(0,0)}$/ kJmol^{-1}
Naphthalene	1.54	427
Anthracene	1.09	315
Phenanthrene	1.50	398
Pyrene	1.16	352
Chrysene	1.35	373
Tetracene	0.77	252
Pentacene	0.78	206

Table 4.3: The oxidation potentials (vs SCE) in acetonitrile and excitation energies of the donor species [83]. The data for pentacene is taken from [91].

Acceptor	$E^0(red)$/ V
1,2-DCB	-2.12
1,3-DCB	-2.17
1,4-DCB	-1.97

Table 4.4: The reduction potentials (vs SCE) in acetonitrile of the acceptor species [83]

potential for a reversible redox system in the ground state [91] is given by

$$nFE^0(ox) = \Delta G_S^0 + IP + \Delta E^+ \tag{4.9}$$

where IP is the ionization potential for the electron donor (D) and ΔE^+ is the solvation energy difference between D^+ and D. The absolute potential of a reference electrode is given by $\Delta G_S^0 = -424.5\,\text{kJmol}^{-1}$(vs SCE) where $E^0(ox) - \Delta G_S^0 = IP_{solv}$ and IP_{solv} is the ionisation energy in solvents. ΔE^+, IP and IP_{solv} data for all polyarenes are shown in Table 4.5. It can be seen that, generally, the ionisation potentials (IP and IP_{solv}) decrease with increasing number of π-electrons in the polyarene but ΔE^+ is fairly constant across all systems especially compared with the differences in IP. It is hence assumed that the solvation effects are constant across all systems and will be therefore neglected for the purpose of this investigation.

These data were used to calculate the 'Gibbs energy of photoinduced electron transfer', ΔG_{ET}^0, for each system investigated using Equation 4.8. The results are displayed in Table 4.6 and show that for all systems which exhibit MFEs ΔG_{ET}^0 is negative and non-zero. For those systems which did not exhibit MFEs, i.e. tetracene and pentacene systems, ΔG_{ET}^0 is positive. Although these values should not be taken as absolute they can be used to describe trends in these systems. That is, from the data is it clear that RP formation

Donor	IP_{solv} / kJmol^{-1}	IP / kJmol^{-1}	ΔE^{+} / kJmol^{-1}
Naphthalene	786.36	599.17	187.18
Anthracene	720.75	551.9	168.85
Phenanthrene	758.37	592.42	165.95
Pyrene	714.96	548.04	166.92
Chrysene	733.29	577.95	155.34
Tetracene	679.26	519.09	160.17
Pentacene	650.31	499.79	150.52

Table 4.5: IP, IP_{solv} and ΔE^{+} for all electron donors, measured in an organic solvent (acetonitrile) [91] where $\Delta E^{+} = IP_{solv} - IP$.

is not favourable in tetracene and pentacene and no field effect can be observed.

The power of this method certainly lies in its simplicity. Although it neglects some contributions to the overall energetics, such as entropy and solvation effects, of the systems investigated it has produced the correct result. Therefore this method is likely to prove very useful as it can predict if an exciplex exhibits an MFE without the need for complex calculations. That is, if ΔG^{0}_{ET} is positive (calculated using data from literature for excitation profiles and electrochemistry) it is unlikely that a MFE will be observed for that exciplex system.

	ΔG^{0}_{ET} / kJmol^{-1}		
	1,2-DCB	1,3-DCB	1,4-DCB
Naphthalene	-74.23	-69.41	-88.69
Anthracene	-5.60	-0.78	-20.06
Phenanthrene	-49.09	-44.27	-63.54
Pyrene	-35.86	-31.04	-50.31
Chrysene	-38.54	-33.72	-53.00
Tetracene	26.55	31.37	12.10
Pentacene	73.52	78.34	59.06

Table 4.6: Calculated ΔG^{0}_{ET} for all systems studied Equation 4.8. Systems below the double line did not exhibit any MFEs.

The data in Table 4.7 summarises all the energies calculated for Equation 4.8. These values are depicted graphically in Figure 4.12 for all systems with 1,3-DCB. The data shows that in general both $\Delta E_{(0,0)}$ and ΔG decrease with increasing number of π-electrons of the polyarenes. The fact that ΔG Figure 4.11 is smaller for systems with more π-electrons (i.e. tetracene and pentacene) means that the energy of the RP will lie lower than in other polyarene systems. Alone, ΔG values might suggest that the production of the RP in these systems will be more favourable. However, combining data for ΔG with

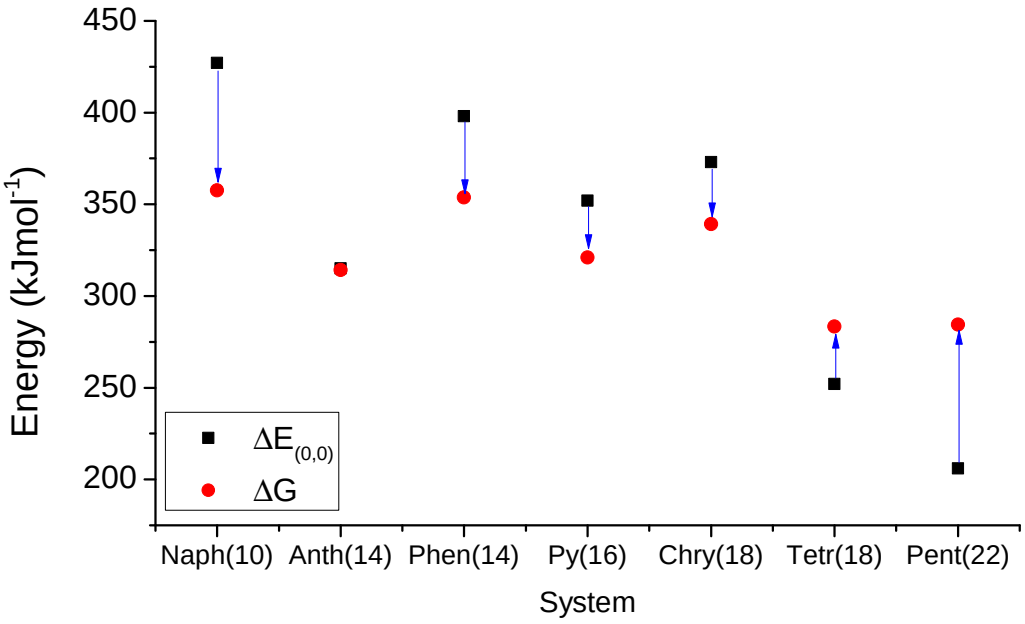

Figure 4.12: Schematic of the energy of the RP compared with the energy of the excited state molecule for 1,3-DCB systems Table 4.7.

the data for $\Delta E_{(0,0)}$ shows that the energy difference, ΔG^0_{ET}, between the two becomes positive with increasing number of π-electrons and hence RP formation is less favourable in tetracene and pentacene systems.

Although ΔG^0_{ET} values might help in determining if systems are likely to exhibit MFEs the model cannot be used to explain the relative size of the MFE from system to system. For example, in the pyrene systems ΔG^0_{ET}(1,4-DCB) $<$ ΔG^0_{ET}(1,2-DCB)$<$ ΔG^0_{ET}(1,3-DCB) but the observed MFE has a different order $\mathrm{MFE}_{(1,3-\mathrm{DCB})} > \mathrm{MFE}_{(1,2-\mathrm{DCB})} > \mathrm{MFE}_{(1,4-\mathrm{DCB})}$. For chrysene systems ΔG^0_{ET} values are more negative than those for pyrene systems but the pyrene systems showed larger MFEs. For chrysene, as with pyrene, ΔG^0_{ET}(1,4-DCB) $<$ ΔG^0_{ET}(1,2-DCB)$<$ ΔG^0_{ET}(1,3-DCB), however, the 1,2-DCB system gives the largest signal, then 1,4-DCB and 1,3-DCB gives the lowest signal, almost the opposite effect to that seen in pyrene.

If the Gibbs energy of photoinduced electron transfer was the major driving force for the observation of MFEs then it would not be possible to explain why all systems with 1,4-DCB do not exhibit the largest MFEs because for these systems ΔG^0_{ET} is the most favourable. In order to fully explain these results a different model must be explored and

π-electrons	Donor	Acceptor	ΔG^0_{ET}	$\Delta E_{0,0}$	ΔG
10	Naphthalene	1,2-DCB	-74.23	427	352.77
		1,3-DCB	-69.41	427	357.59
		1,4-DCB	-88.69	427	338.31
14	Anthracene	1,2-DCB	-5.60	315	309.4
		1,3-DCB	-0.78	315	314.22
		1,4-DCB	-20.06	315	294.94
14	Phenanthrene	1,2-DCB	-49.09	398	348.91
		1,3-DCB	-44.27	398	353.73
		1,4-DCB	-63.54	398	334.46
16	Pyrene	1,2-DCB	-35.86	352	316.14
		1,3-DCB	-31.04	352	320.96
		1,4-DCB	-50.31	352	301.69
18	Chrysene	1,2-DCB	-38.54	373	334.46
		1,3-DCB	-33.72	373	339.28
		1,4-DCB	-53.00	373	320.00
18	Tetracene	1,2-DCB	26.55	252	278.55
		1,3-DCB	31.37	252	283.37
		1,4-DCB	12.10	252	264.10
22	Pentacene	1,2-DCB	73.52	206	279.52
		1,3-DCB	78.34	206	284.34
		1,4-DCB	59.06	206	265.06

Table 4.7: Shows the energies ΔG^0_{ET}, $\Delta E_{0,0}$ and ΔG for all systems studied, as depicted in Figure 4.11. *All energies are given in* $kJmol^{-1}$.

the structure of the exciplexes must be investigated further.

It is possible that the observation of an MFE might suggest some relationship between the stability of exciplex compared with the stability of the radical ion pair (Figure 4.11), i.e. if the exciplex is very stable then very little RP will be formed or that back electron transfer from the RP to the exciplex will take place on a timescale quicker than the rate of $S-T$ mixing and hence, addition of a magnetic field will not affect the reaction yield. In [68], the energy of the exciplex and the RP are assumed to be equal and the validity of this assumption will be examined.

In [68] a linear correlation between the MFE intensity and ΔG^0_{ET} was observed (Figure 4.13). However, a combination of the data produced during their investigations and during the investigations in this thesis confirmed no such correlation in our data (Figure 4.13). The two systems which are consistent to both studies are circled: Py/1,3-DCB (black ellipse) and Anth/1,3-DCB (green ellipse). It can be seen from the data that not surprisingly ΔG^0_{ET} for both of these systems differ between the two approaches. This is

because the theoretically superior methods used in [68] are based on energy hypersurfaces where solvent effects are accounted for. In the basic method described here solvent effects have been neglected and a much simplified approach using redox potentials has been employed. However, it can be seen that the systems studied in this thesis do increase the range of ΔG^0_{ET} investigated compared to those in [68] and produce similar relative field effects for the two systems studied taking into account that different conditions (concentration and solvents) were used.

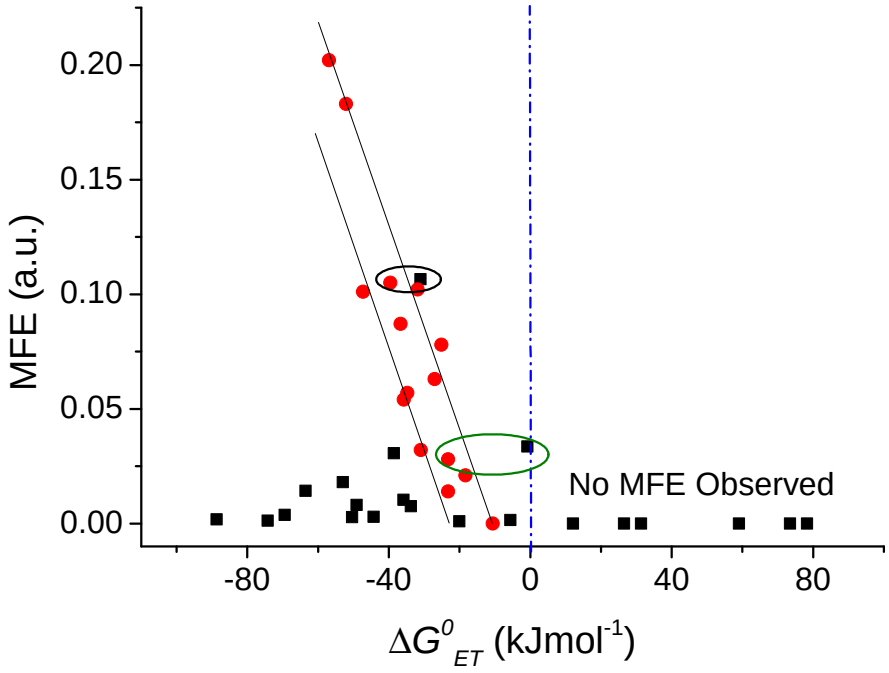

Figure 4.13: Dependence of the MFE on the free energy of electron transfer. Systems include those studied in this thesis (black squares) and those studied in [68] (red circles). The area shown between the two black lines show the linear relationship found in [68]. The blue dashed line shows $\Delta G^0_{ET} = 0$, for which no MFEs are observed for energies less than this value. The black and green eclipses group data points for systems which are consistent between the data from [68] and in this thesis.

4.3.3 Frontier Molecular Orbital Theory for Photoinduced Electron Transfer Reactions

Since a photoinduced electron transfer reaction occurs from a molecular orbital of the donor to a fully vacant orbital of the acceptor it follows that orbital overlap between the occupied and unoccupied orbitals must play an important role in electron transfer reactions.

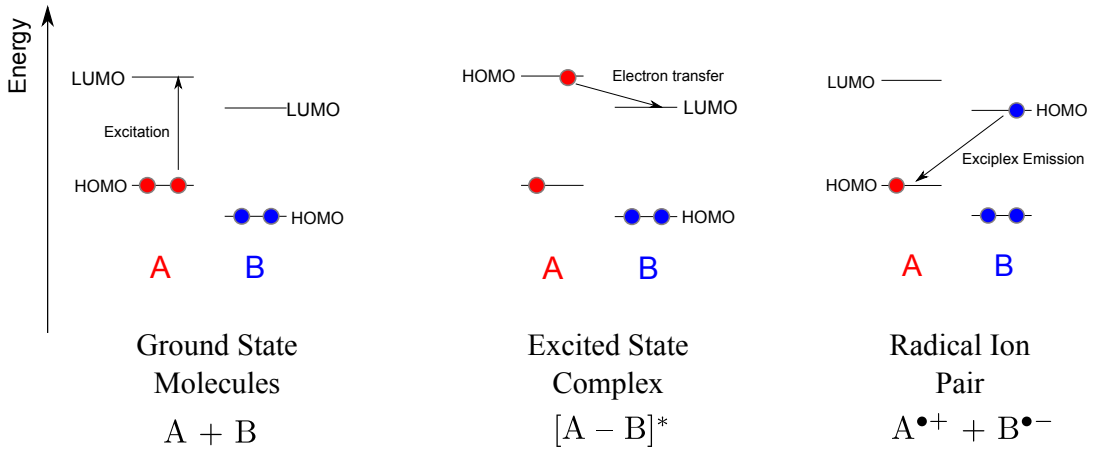

Figure 4.14: Energy diagram showing the HOMO and LUMO levels of a photoinduced electron transfer reaction.

Frontier molecular orbital theory is an application of molecular orbital theory describing the interactions between the highest occupied molecular orbital (HOMO) of one molecule and the lowest unoccupied molecular orbital (LUMO) of another. It was realised that a good approximation for reactivity could be found by comparing the HOMO/LUMO of the reacting pair, the energy between them and their symmetry [92]. According to Mulliken charge-transfer theory [93], formulated to explain the existence of weak molecular complexes between molecules with electron donor and electron acceptor properties, the transition state for electron transfer (exciplex) will be stabilised by partial electron transfer from the donor HOMO to the acceptor LUMO, Figure 4.14. This can be described through frontier molecular orbital methods where reactivity can be rationalised by examination of preferred HOMO-LUMO interactions and HOMO-LUMO energy differences [94].

Here the HOMO and the LUMO of the donors and acceptors were calculated using density functional theory (DFT) and Amsterdam Density Functional (ADF) [95], a computational chemistry program, using the graphical user interface (GUI). Molecular structures were initially generated in ChemBioDraw Ultra 11 and their energy was minimised using the inbuilt molecular modelling program in ChemBio3D Ultra 11 which uses the MM2 forcefield [96]. The x,y,z coordinate files were exported into ADF to allow further optimisation by DFT calculations of the geometries for the electronic ground states of the molecules. Ground state geometry optimisations were performed using a GGA-BLYP (Becke for the exchange part and Lee, Yang and Parr for the correlation part)

functional, which provides an approximation for the exchange and correlation energies of the Hamiltonian, and a TZ2P (triple Z, 2 polarisation function) basis set was used to create molecular orbitals. From these calculations the ground state LUMOs of the electron donors could be visualised using ADF GUI. For electron donor molecules it was necessary to perform an excited state geometry optimisation. Information regarding the excitations was found by calculating the excitation spectrum for the electron donor molecule using a single point energy calculation. The functionality used to calculate excitation energies is based on time dependent DFT (TDDFT). Using the information regarding which excitation formed the first excited singlet state, a single electron was excited manually from the ground state configuration and a geometry optimisation was subsequently performed. This corresponds to the geometry optimisation of the excited state molecule. From these calculations the HOMOs of the electron donors could be visualised using ADF GUI.

Energy / kJmol^{-1}			
HOMO		LUMO	
Naphthalene	-176.34	1,2-DCB	-313.42
Pyrene	-216.63	1,3-DCB	-305.50
Chrysene	-199.65	1,4-DCB	-329.67
Anthracene	-213.28		
Phenanthrene	-177.65		
Tetracene	-267.94		
Pentacene	-293.44		

Table 4.8: Calculated HOMO and LUMO energies for all electron donors and acceptors. The HOMO corresponds to the geometry optimisation of the first excited state and the LUMO corresponds to the geometry optimisation of the ground state.

Two important features of the interacting frontier orbitals determine the extent of favourable charge transfer (preceding electron transfer) from the HOMO of one molecule to the vacant LUMO of another: firstly the energy gap between the HOMO and the LUMO, $\Delta E_{\mathrm{HO-LU}}$, and secondly the degree of constructive interference of the HOMO and LUMO wavefunctions, i.e. the value of the overlap integral $< \psi_{HO} | \psi_{LU} >$ [97].

The fundamental underlying principle of FMO theory is the assumption that the majority of chemical (photochemical) reactions should take place most easily (i.e. have the lowest activation energy) at the position of, and in the direction of, maximum overlap of the HOMO and LUMO of the interacting species. Perturbation theory [97] can be used to predict the stabilisation energy change on interaction of two species, E_{stab}, of the

charge transfer complex due to overlap of FMOs:

$$E_{stab} \propto < \psi_{HO}|\psi_{LU} >^2 / \Delta E_{\mathrm{HO-LU}} \tag{4.10}$$

where $\Delta E_{\mathrm{HO-LU}}$ is the energy difference between the important interacting FMOs, E(HOMO) - E(LUMO). This stabilisation energy applies only to HOMO/LUMO interactions and not coloumbic interactions. The general rules for orbital-orbital interaction are as follows: (1) interaction between orbitals close in energy provides the most significant energy gain; (2) interacting orbitals must be of matching symmetry and (3) efficient overlap between interacting orbitals is required (the larger the overlap integral the more favoured the interaction).

$\Delta E_{\mathrm{HO-LU}}$ / kJmol^{-1}			
	1,2-DCB	1,3-DCB	1,4-DCB
Naphthalene	137.08	129.16	153.67
Anthracene	100.14	92.22	116.39
Pyrene	96.79	88.87	113.04
Chrysene	113.77	105.85	130.02
Phenanthrene	135.77	127.85	152.02
Tetracene	45.48	37.56	61.73
Pentacene	19.98	12.06	36.23

Table 4.9: Shows the HOMO-LUMO gap for the charge transfer complex for all systems studied in Figure 4.14.

The calculated energies for all HOMOs and LUMOs are shown in Table 4.8 and the corresponding HOMO - LUMO gaps, $\Delta E_{\mathrm{HO-LU}}$, for all systems in Table 4.9. The data shows that in general a decrease in the HOMO-LUMO gap is observed as the number of π-electrons in the polyarene increases. This is similar to the trend observed for ΔG^o_{ET} which was shown to decrease in exergonicity with increasing number of π-electrons. For the longest polyarenes, pentacene and tetracene, $\Delta E_{\mathrm{HO-LU}}$ is the smallest. This would suggest the stability of the exciplex, E_{stab}, may be large for longer polyarenes if $E_{stab} \propto \frac{1}{\Delta E_{\mathrm{HO-LU}}}$ yet they do not show the existence of an exciplex, according to the fluorescence data (Appendix D), nor do they exhibit MFEs. Even if an exciplex is formed, if the exciplex is more stable than the radical pair it is possible that either no radical pair is formed or that back electron transfer from the radical pair is so rapid the spin state does not have time

to evolve and no MFE is observed. It is very surprising that the pyrene/DCB systems all exhibit relatively large MFEs given that their HOMO - LUMO gaps are relatively large (Table 4.9). Anthracene/1,3-DCB exhibits the next largest MFE (Figure 4.9) and has a $\Delta E_{\mathrm{HO-LU}}$ of 92.22 kJ mol^{-1}. In general, we can summarise by saying all systems with $\Delta E_{\mathrm{HO-LU}} > 90\,\mathrm{kJ\,mol^{-1}}$ showed a MFE, even if the magnitude of the MFE is very small, and that no system with a HOMO-LUMO gap $< 80\,\mathrm{kJ\,mol^{-1}}$ exhibited a MFE. The one system that has a larger observed MFE than any other is Py/1,3-DCB, the supporting evidence for this is shown in the MARY spectra in Figure 4.9.

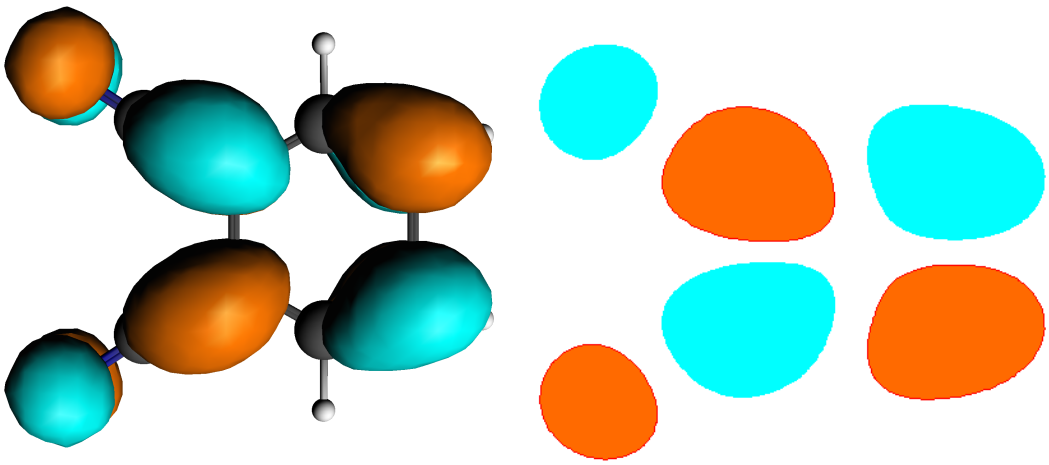

(a) 3-D (b) 2-D

Figure 4.15: A 3-D plot of the LUMO for 1,2-DCB (left) and a 2-D projection of the LUMO for 1,2-DCB (right).

	S'/a.u.		
	1,2-DCB	1,3-DCB	1,4-DCB
Naphthalene	41.25	39.78	39.65
Anthracene	35.14	37.37	49.42
Phenanthrene	36.21	40.48	34.27
Pyrene	34.05	36.41	37.97
Chrysene	42.58	35.51	40.08
Tetracene	36.27	37.94	44.9
Pentacene	34.49	34.93	33.71

Table 4.10: The maximum overlap area, S', calculated for all systems.

The second contribution to FMO theory, the value of the overlap integral, $S = \langle\psi_{HO}|\psi_{LU}\rangle$, was approximated by calculating the orbital overlap between the HOMO of the excited donor molecule and the LUMO of the acceptor molecule. This was achieved by firstly projecting the calculated HOMO and LUMO orbitals onto a 2-D plane (Fig-

ure 4.15) and secondly calculating the maximum overlap area for a range of different orientations. The 2-D projections were obtained using the ADF program *Densf*, which generates values of molecular orbitals, charge densities and potentials in a user-specified grid. The output file of Densf, TAPE41, was then processed by cntrs, a separate utility program which generates contour plot data. The contour plots were next imported into a Matlab program (Appendix F) and the overlap area, S', between the HOMO and LUMOs was calculated and optimised for a large set of orientations. The value of the maximum overlap area, S', for each system is shown in Table 4.10.

The maximum overlap areas and their corresponding donor-acceptor geometry are shown in Figure 4.16 for pyrene/DCB systems. All other systems are shown in Appendix H. The relative geometry of the donor and acceptor molecules represents the pre-organisation of the reactants prior to electron transfer. It can be seen in the geometry of the exciplex (Figure 4.16) that the maximum overlap achieved corresponds to the stacking of the two benzene moieties of the donor and acceptor molecules. In order to achieve a significant electronic interaction between donor and acceptor molecules the donor/acceptor pair must be arranged in a tight complex to allow optimum coupling of the benzene moieties. This geometry has been previously shown in arene/quinone systems using near-IR absorption [98].

	$S'^2/\Delta E_{\mathrm{HO-LU}}$/a.u.		
	1,2-DCB	1,3-DCB	1,4-DCB
Naphthalene	12.41	12.25	10.23
Anthracene	12.33	15.14	20.98
Phenathrene	9.66	12.82	7.73
Pyrene	11.98	14.92	12.75
Chrysene	15.94	11.91	12.36
Tetracene	28.93	38.32	32.66
Pentacene	59.54	101.17	31.37

Table 4.11: Approximation for E_{stab} using $S'^2/\Delta E_{\mathrm{HO-LU}}$ (Equation 4.10) for all systems studied.

From the data it can be seen that there is no correlation between the number of π-electrons in the electron donor and the maximum overlap. The maximum stabilisation energy change on interaction of two species, E_{stab}, can be approximated by dividing the obtained maximum overlap area, S'^2, by the HOMO-LUMO gap, $\Delta E_{\mathrm{HO-LU}}$, (Table 4.11).

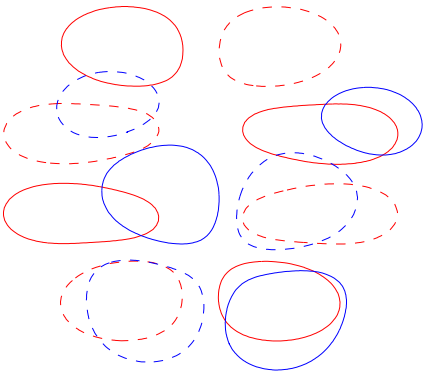

(a) 1,2-DCB

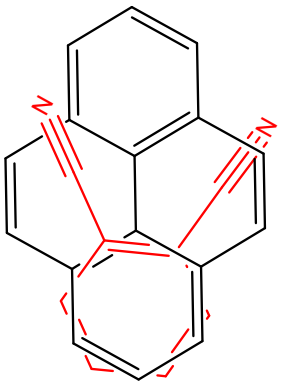

(b) 1,2-DCB

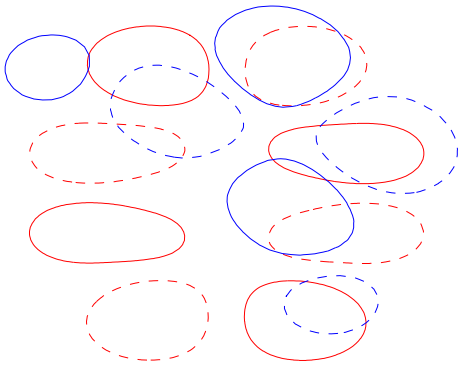

(c) 1,3-DCB

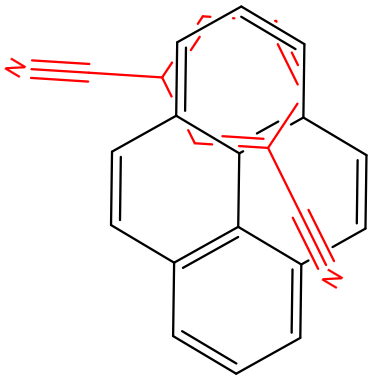

(d) 1,3-DCB

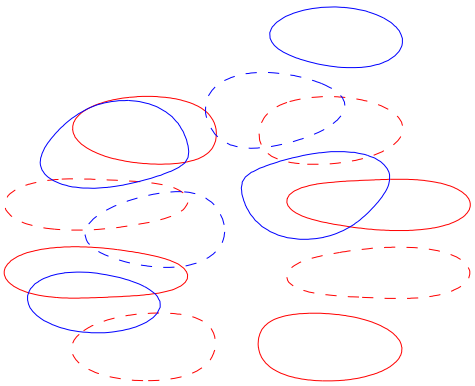

(e) 1,4-DCB

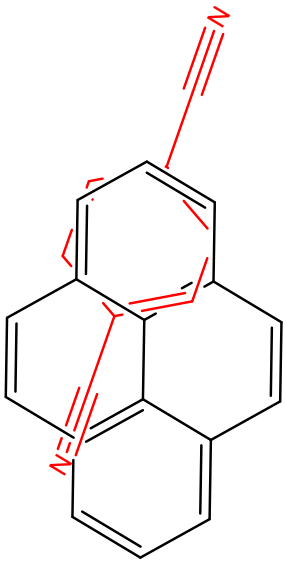

(f) 1,4-DCB

Figure 4.16: Orientation of HOMO(red) and LUMO(blue) which achieves the maximum orbital overlap for pyrene/DCB systems as performed in DFT (see text). The HOMO-LUMO orbitals are shown on the left and the corresponding exciplex geometry on the right.

The data shown in Table 4.11 can shed some light on the observed MFEs in polyarene/DCB systems. It can be clearly seen from the data that the largest E_{stab}(Equation 4.10) are observed for tetracene and pentacene systems. However, it has already been shown that RP formation in these systems is not favourable and $\Delta G^0_{ET} > 0$ and hence no MFEs are observed for these systems. There are some interesting points to be made about this data (Table 4.11) regarding the systems which do exhibit MFEs. It can be seen that for chrysene systems, $S'^2/\Delta E_{\mathrm{HO-LU}}$ is largest for Chy/1,2-DCB and smallest for Chy/1,3-DCB. Interestingly, this corresponds to the trend observed in the MFE intensity, i.e. $\mathrm{MFE_{Chy/1,2-DCB}} > \mathrm{MFE_{Chy/1,4-DCB}} > \mathrm{MFE_{Chy/1,3-DCB}}$. Similarly for pyrene, it can seen that $S'^2/\Delta E_{\mathrm{HO-LU}}$ is largest for the Py/1,3-DCB system and smallest for the Py/1,2-DCB system. This too corresponds to the trend observed in MFE intensity for pyrene systems, i.e. $\mathrm{MFE_{Py/1,3-DCB}} > \mathrm{MFE_{Py/1,4-DCB}} > \mathrm{MFE_{Py/1,2-DCB}}$. This trend holds true for all systems with the exception of phenanthrene. In this system the overlap areas with all three DCB isomers are shown to be small relative to other polyarene systems. It is possible therefore that the orbital overlap, while determining the stability of the exciplex, is not in this case the dominating factor for determining the observed MFE intensities for different DCB isomers. Instead, in the phenanthrene they are determined by ΔG^0_{ET} which are larger in these systems compared with other polyarenes.

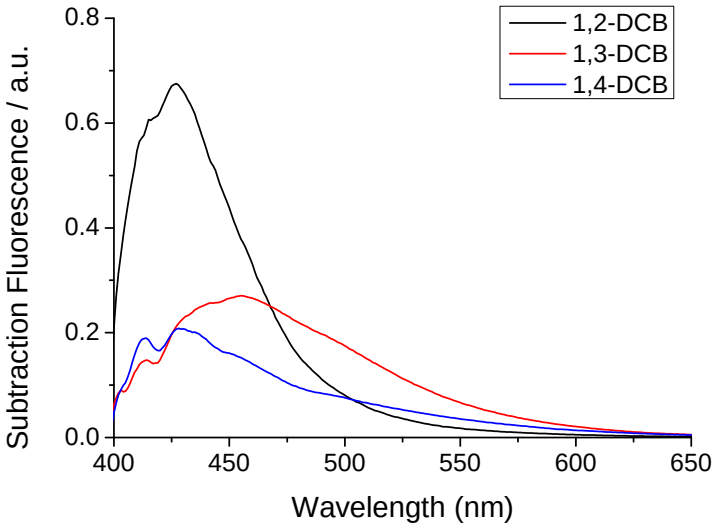

Figure 4.17: The exciplex emission band for Py/DCB systems in CH:ACN (9:1) solvent.

A closer look at the fluorescence data for these systems may shed some further in-

sight on these findings. Take the fluorescence data for Pyrene systems as an example (Appendix D, Figure D.2). Subtraction of the normalised monomer fluorescence (absence of quencher) from the normalised fluorescence of the sample in the presence of the quencher may show the wavelength profile of the exciplex emission. This data for Py/DCB systems is shown in Figure 4.17. The data shows that the peak wavelength for the Py/1,2-DCB, Py/1,3-DCB and Py/1,4-DCB are given by 425 nm, 455 nm and 430 nm respectively. Hence the energy of exciplex emission for Py/1,3-DCB is lower than that for Py/1,4-DCB and the highest energy of exciplex emission is seen for Py/1,2-DCB. This corresponds to the trend observed in E_{stab}, however, the two should not be directly compared since one is derived from a quantum mechanical model (E_{stab}) and the other is thermodynamic. However, the fact that their trends agree is very pleasing.

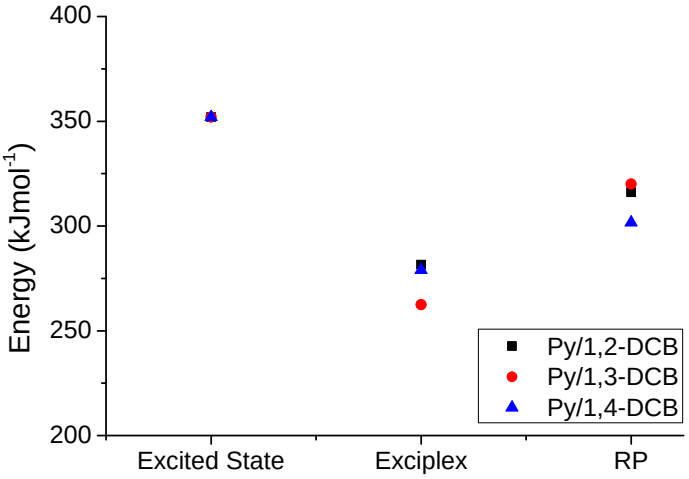

Figure 4.18: The energy of the excited state (from UV/Vis data), exciplex and RP for all three Py/DCB systems. The exciplex energy was derived from the maximum of the exciplex fluorescence profile and the energy of the RP is derived from redox potentials (Table 4.7). This schematic is only an approximation of the true energies since no solvation is accounted for.

Comparison of the energy derived from the exciplex fluorescence data compared with that of the RP, derived from redox potentials, is shown in Figure 4.18. These values are not absolute since solvation effects have not been fully accounted for (e.g. calculation of ΔG for the RP), however, the data show that the exciplex and RP are of similar energy. This has been shown to be the case where the activation enthalpy for electron transfer is negligible but has a very large negative activation entropy [99]. Unfortunately it was

not possible to conduct the same comparative study using any of the other system due to poor S:N ratio in the exciplex regions of their respective fluorescence spectra prohibiting any reliable extraction of the exciplex emission wavelength.

4.4 Conclusion

The magnetic field effects of a variety of exciplex donor-acceptor systems have been investigated. These systems differ in their energetics and magnetic properties and therefore lend themselves for the investigation of the radical pair mechanism in the context of exciplex forming systems. The energetics involved in RP formation have been explored, in particular the free energy difference between the excited fluorophore and the RP, and their implications for magnetic field effects have been discussed. It has been shown that the free energy of charge separation, ΔG^0_{ET}, plays a very important role in establishing if an exciplex will exhibit magnetic field effects. That is, formation of the RP will occur spontaneously if ΔG^0_{ET} is negative. However, no correlation between MFE and ΔG^0_{ET} was observed, contrary to the previous observations [68], and other properties of the system were explored, in particular the relative energies of the exciplex and RP states and factors which may effect the stability of the exciplex.

The stabilisation energy change on interaction of two species, E_{stab}, of the charge transfer complex was investigated using the model proposed by Turro [97]. This was approximated by calculating the maximum overlap area, S', and energy difference between the HOMO and LUMO of the interacting species, $\Delta E_{\mathrm{HO-LU}}$ as detailed in Table 4.10. The results of which afforded, not only, information on the stability of the exciplex but also the possible geometries for donor acceptor molecules in the exciplex state. With the exception of phenanthrene all systems showed a correlation between the approximate E_{stab} and the size of MFE observed with the three DCB isomers. Using Py/DCB systems as an example case it was also shown that the trends observed in E_{stab} corresponded with those observed in exciplex energy (Figure 4.17). Although the two were derived from different models (quantum mechanical and thermodynamic respectively) and hence, should not be compared directly their agreement was satisfying.

The results presented in this chapter highlight the need to consider different properties of the radical pair mechanism in the context of magnetic field effects, the energetics of which have been previously studied [68]. Although some factors were neglected in this model e.g. solvation effects and kinetics which have only been briefly discussed, the results are very pleasing and show that the model proposed can be used as a quick method for testing if exciplex systems will exhibit MFEs. Further work should concentrate on methods to be quantify overlap integrals as therein seems to lie the big difference between systems showing small and large MFEs.

Chapter 5

Exploring New Chemical Compass Systems

In this chapter, radical pair systems are investigated with respect to their potential to act as chemical compasses. A series of well-characterised chemical systems with a considerable sensitivity to applied magnetic fields show promise for magnetic field direction dependence. To date, the only system to show an anisotropic response to a magnetic field is a triad molecule consisting of carotenoid, porphyrin and fullerene (C-P-F) moieties [100]. Upon photoexcitation this molecule forms a biradical which exhibits magnetic field strength dependent recombination kinetics. The orientation selection in this system was achieved in two ways: (1) strongly aligned molecules in the nematic phase of the liquid crystal E7 and (2) photoselection. However, as a model system for the fundamental basis of bird magnetoreception, the triad molecule has its limitations: namely, magnetoresponse could only be detected at physiologically non-relevant conditions, namely at very low temperatures, 100 K and in methyl/THF solutions. Although the triad molecule showed an anisotropic magnetic response at magnetic field strengths of 3.4 mT, none was observed at the Earth's field strength. Regardless, these experiments established the feasibility of chemical magnetoreception and gave first insights into the structural and dynamic design features required for optimal detection of the direction of the Earth's magnetic field, which will be further explored in this work.

5.1 Introduction

In this chapter, fluorescent model chemical compass systems will be investigated using modulated-MARY techniques and a variety of methods for the investigation of anisotropic MFEs will be employed. The systems studied form exciplex intermediates and magnetic field effects are investigated by detecting exciplex fluorescence using highly sensitive modulation techniques. All systems investigated were either immobilised in a solid matrix and investigated using photoselection techniques or were aligned in ordered media. The added benefit of the latter systems is that the aligned media themselves can form part of the RP and thus can be easily orientated with respect to an applied external magnetic field.

5.1.1 Photoselection

The fluorescence of a molecule is characterised by an emission wavelength band and by a direction of polarization, i.e. a defined direction of the electrical field vector. The emission and absorption of electromagnetic radiation have an associated transition dipole moment of emission and absorption respectively. The polarisation of the radiation in a fluorescent sample is dependent on the orientation of the emission transition dipole moment and hence on the molecular orientation. Polarisation of light can be achieved using polarisers which can be rotated in order to select different directions for polarisation.

The fluorescence anisotropy, A, in a sample is defined as

$$A = \frac{I_{||} - I_{\perp}}{I_{||} + 2I_{\perp}} \tag{5.1}$$

where $I_{||}$ is the intensity of fluorescence with the polarisers in the excitation and emission beams parallel to each other and $I_{\perp}$ is the intensity of fluorescence with the polarisers perpendicular to each other, see Appendix I. The measurement of A for a sample quantifies the degree of alignment since the transition dipole moment for single photon absorption or emission in a molecule is defined with respect to the molecular coordinate system. If A is non-zero, the fluorophores in the sample are not free to rotate or diffuse.

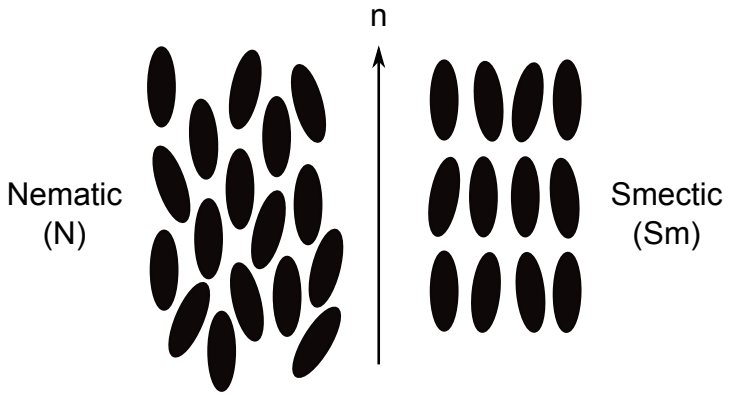

Figure 5.1: Pictorial representation of the nematic (N) and smectic (Sm) phases of a liquid crystal, where n is the director.

5.1.2 Liquid Crystals

Liquid crystals (LCs) are characterised by properties intermediate between those of a conventional liquid and those of a solid crystal. For instance, a LC may behave like a liquid due to its imperfect long-range order in one direction, but its molecules may be orientated in a crystal-like manner in a least one other direction. The tendency of the LC molecules to point along the director leads to anisotropy in the sample and thus potential chemical compass systems.

The distinguishing characteristic of the liquid crystalline state is the tendency of the molecules (mesogens) to point along a common axis, called the director, n. This is in contrast to molecules in the liquid phase, which have no intrinsic order. An order parameter, S, is used to quantify ordering in LCs.

LCs can be classified into different phases, depending on the amount of order in the material. The most common phases of liquid crystals are: nematic (N) where rod-like molecules point on average along the director, n (see Figure 5.1), and smectic (Sm) where the molecules additionally form layers of thickness corresponding to approximately one molecular length (see Figure 5.1). A direction perpendicular to the layers' plane is defined as the layer normal, z.

There are two general alignment methods for enforcing a director upon a nematic LC: surface and field direction alignment. Surface direction techniques are generally used for thin film LC studies and do not tend to be suitable for experiments that require a larger bulk material in order to achieve strong optical signals, i.e. MARY.

Field direction alignment can be achieved by the use of either electric or magnetic fields. The response of liquid crystal molecules to an electric field is the major characteristic utilised in industrial applications, for example in liquid crystal displays. The ability of the director to align with an external field stems from the permanent electric dipoles of the molecules. Electric fields are attenuated in LCs with low electric permittivity, and as such, alignment can be weaker in the centre of the sample. This field strength reduction can be considerable especially when using a direct current (DC) field and occurs as the ionic impurities in the LC are gradually drawn to the surface, causing the field to be attenuated.

Magnetic field alignment of LCs is analogous to electric field alignment, but magnetic fields demonstrate a weaker ability to control the alignment of LCs. Alignment in magnetic fields is still possible but high field strengths are required ($> 100\,\mathrm{mT}$).

5.1.3 Polymers

Polymers are potential candidates for model chemical compass systems for many reasons: they can be used as solid matrices for photoselection experiments; they have been shown to form exciplexes in their monomeric forms [101, 102] and thus might potentially show MFEs in polymeric form; and lastly, they can be aligned and hence have the potential to show anisotropic effects. Methods of aligning polymers include spin coating and polymer stretching.

5.1.4 Single Crystals

A single crystal is a material in which the crystal lattice of the entire sample is continuous and unbroken to the edges of the sample, with no grain boundaries. These monocrystals have unique mechanical, optical and electrical properties, which can be anisotropic, depending on the type of crystallographic structure. Single crystals have long been of interest but their exploitations in the context of model chemical compass systems have yet to be fully realised.

The thermodynamic driving force for crystallisation is supersaturation. When the

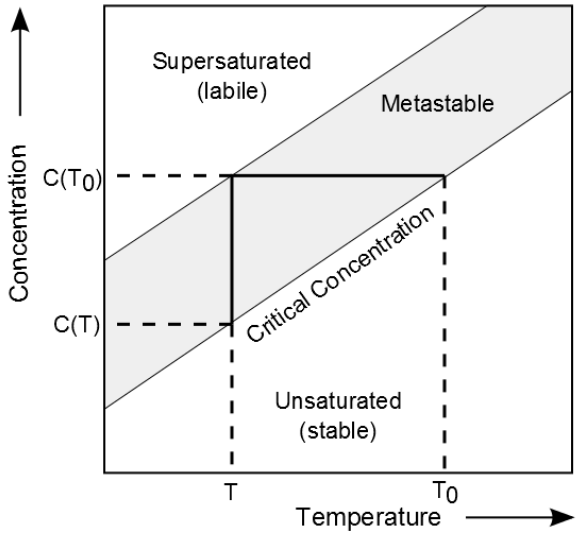

Figure 5.2: Phase diagram for a binary solid-liquid system.

concentration gradually increases (for example on solvent evaporation) and reaches the value sufficient to overcome the nucleation energy barrier, spontaneous precipitation of the crystalline powder occurs. Single crystals of large single domain size are grown under special conditions, when the concentration is very close to the critical point of nucleation. At such concentrations the molecular aggregates (which form and fall apart in solution), achieve a critical size and convert into nuclei of future crystals. When the concentration (e.g. for supersaturated solution) is higher than the critical concentration, spontaneous nucleation occurs throughout the solution and a crystalline (multi-domain) powder is produced. At concentrations lower than the critical concentration, nucleation does not occur spontaneously but artificial introduction of crystal nuclei by seeding can encourage crystal growth if the concentration is sufficiently close to the critical concentration.

Figure 5.2 shows a phase diagram for a two component system with a solute characterised by a positive temperature coefficient of solubility, $dC/dT > 0$. The diagram shows three zones: (1) the stable zone of unsaturated solution where nucleation is impossible; (2) the metastable zone where spontaneous nucleation is not likely but crystal growth can be encouraged with use of a seed, and (3) the labile zone of spontaneous nucleation. Seeding of a crystal at supersaturation is the simplest way to accelerate crystal growth. However, avoiding spontaneous nucleation at high supersaturation is a major challenge.

5.2 Experimental Considerations

5.2.1 Liquid Crystals

The nematic liquid crystal 4-Cyano-4'-pentylbiphenyl (5CB) (Figure 5.3) was used for all liquid crystal experiments. 5CB is the main constituent of E7, the liquid crystal used in the triad experiments [100], and was preferentially used in the following studies as it is cheaper and more readily available than E7. The clearing point (liquid crystal-isotropic transition temperature) of 5CB is 35 °C [103]; i.e., for temperatures below 35 °C the LC is nematic and for higher temperatures the LC is isotropic.

The dopant was added to the sample and was sonicated to ensure that all had dissolved resulting in a uniform mixture. UV/Vis absorption spectra of these samples were recorded on a UV/Vis spectrophotometer in 10 mm × 2 mm quartz cuvettes.

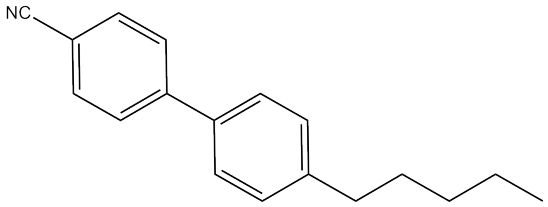

Figure 5.3: The structure of 5CB.

Alignment of 5CB

The degree of 5CB alignment was investigated using optical absorption techniques, mainly UV/Vis spectroscopy by measuring the liquid crystal's birefringent properties. A LC's refractive index is dependent on the polarisation and propagation direction of light; hence, the transparency of the crystal depends on the relative polarisation of light. Crossed polarisers are typically used to detect the existence of liquid crystal phases in a solution.

When heated above 35 °C, 5CB is completely transparent, corresponding to the isotropic phase. At room temperature 5CB is cloudy, corresponding to the nematic phase, but shows no evidence of overall sample alignment when using cross polarisers. The reason for this is that at room temperature, the nematic liquid crystal phase consists of many domains. Within each domain the molecules are orientated in the same direction but there is no overall director in the sample [104].

The molecules in a nematic phase align in an externally applied electric field above a

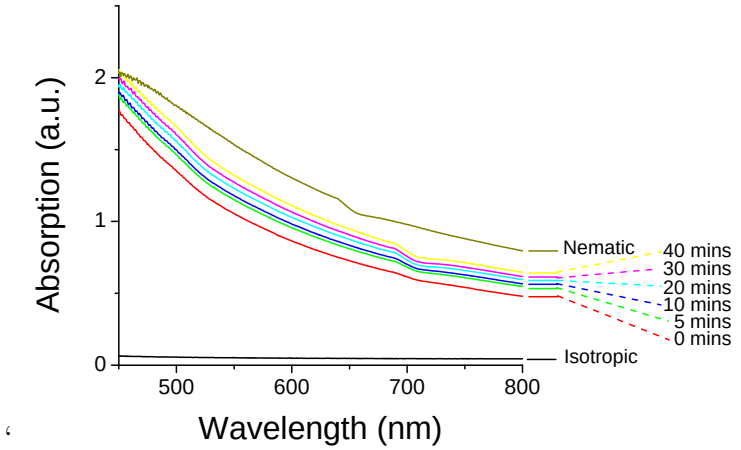

Figure 5.4: UV/Vis spectra of a pure 5CB sample, aligned in a $\pm 7\,\mathrm{kV\ m^{-1}}$ electric field. Spectra are shown at different time intervals after removal from the electric field and are compared to the spectra for an isotropic sample (45 °C) and the unaligned nematic sample.

certain critical threshold field which is $5\,\mathrm{kV\ m^{-1}}$ for 5CB [105]. Above V_c, LC molecules that have a dipole moment parallel to the long molecular axis and hence a positive dielectric anisotropy, $\Delta\epsilon$, are attracted by the electric field. The opposite case holds for LC molecules with $\Delta\epsilon < 0$. For 5CB, $\Delta\epsilon$ is positive and it will align with its major axis parallel to the electric field.

Alignment using AC electric fields was achieved using a home-built electric field alignment box (EFAB). A sample of 5CB was placed in the EFAB for one hour and a field of $\pm 7\,\mathrm{kV\ m^{-1}}$ was applied. The sample was removed from the box and immediately placed into a UV/Vis spectrometer and its spectrum recorded. Several more spectra were recorded at different time intervals, t, after removal from the electric field (see Figure 5.4). The sample was then heated and allowed to cool and the absorption spectrum of the unaligned nematic LC was recorded. The lifetime, τ, for the decay of alignment of 5CB was calculated as it was important that the lifetime was known, such that MFE studies were conducted under the condition of maximum and persistent alignment.

The absorption spectrum for 5CB in the isotropic phase is characterised by an absorption peak in the UV region of the spectrum, $\approx 300\,\mathrm{nm}$ (not shown in Figure 5.4). After one hour in a $\pm 7\,\mathrm{kV\ m^{-1}}$ electric field field, the absorption spectrum of 5CB differed from that of the nematic unaligned sample and showed less scattering, suggesting that the sample had been aligned by the electric field. After 40 mins, the alignment had

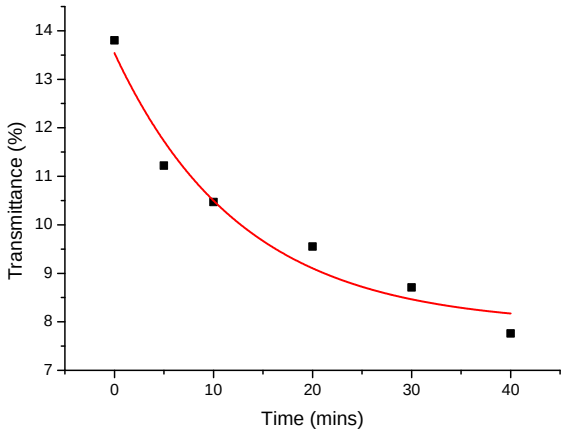

Figure 5.5: The transmittance of the sample at 600 nm as a function of time (mins) after removal from the ±7 kV electric field. Data fitted using an exponential decay curve and a rate constant $k_{decay} = 1.30 \times 10^{-3}\,\mathrm{s}^{-1}$.

partly subsided, but some alignment still remained (Figure 5.4). The transmittance of the sample at 600 nm was plotted as a function of time and fitted with an exponential decay (Figure 5.5), $k_{decay} = 1.30 \times 10^{-3}\,\mathrm{s}^{-1}$ and therefore the lifetime, τ is given by 768 s (12.8 min).

Electric field alignment was chosen over magnetic field alignment because it could be applied during the course of an MFE experiment without affecting the magnetic field experienced by the sample. The EFAB was designed so as to fit inside the MARY apparatus. The application of a 23 mT magnetic field orthogonal to the electric field would have a very minor effect on the decay rate of the alignment since the critical magnetic field required to obtain initial sample alignment is ≈ 600 mT [106].

5.2.2 Polymers

The polymer polyvinylcarbazole (PVCz) (see Figure 5.6) is a tough, glassy thermoplastic and consists of repeated monomer units of N-ethylcarbazole (ECz). PVCz is an organic semiconductor with remarkable photoconductivity and electroluminescence in the visible and UV region [107]. These properties arise because of its good electron donor properties and the high electron hole mobility owing to good π orbital overlap in the monomer units.

The sample was prepared using an evaporation method. PVCz (average $\mathrm{M_w} = 1{,}100{,}000$) purchased from Sigma Aldrich was purified before preparing the films. This was achieved

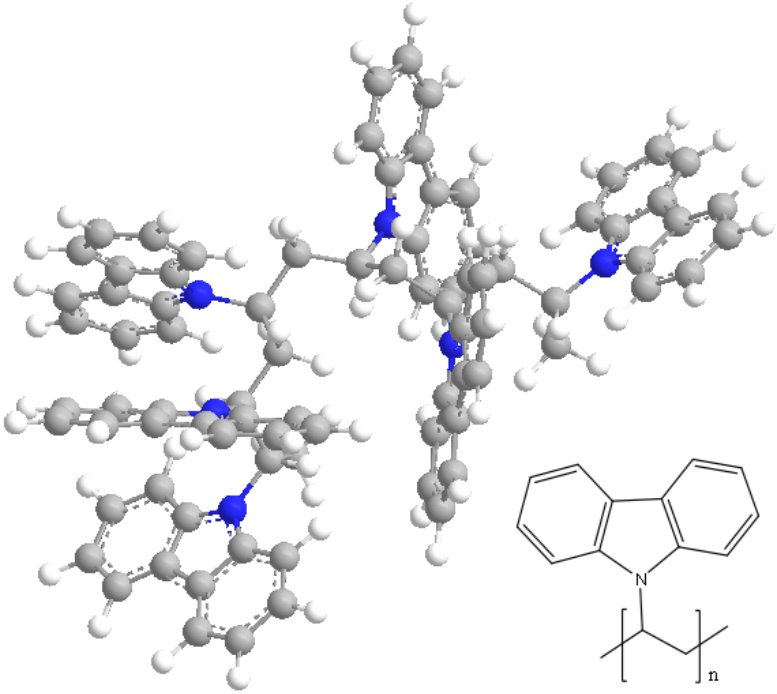

Figure 5.6: The structure of Polyvinylcarbazole with six monomer units.

by dissolving the polymer in THF, adding it drop-wise to ethanol and filtering for the purified product. The PVCz powder and the required electron acceptor (by percentage weight) were dissolved in a minimal volume of toluene. The solution was heated and the solvent evaporated resulting in a thick, viscous solution, which was poured onto glass slides and left in a dessicator overnight forming a thin, brittle and transparent film with an approximate thickness of 0.1 mm. The films were cut into 10 mm wide rectangles for use in MFE studies.

The photoconductivity properties of PVCz lend themselves to the study of magnetic field effects in systems where free diffusion of RPs is not possible and the PVCz can form part of the RP. In the case of PVCz the salient points of the radical pair mechanism are maintained where the radical ion pair molecules are separated, not by diffusion in solution, but by electron hole mobility in the polymer [108]. The charge mobility in PVCz may be viewed as a two stage process involving generation and transport of carriers which can be explained using a one-dimensional lattice model. After light excitation an excited complex between the polymer (electron donor) and dopant (electron acceptor) is formed. This creates an electron-hole (ion) pair in an analogous fashion to the radical pair mechanism.

The electron hole on the PVCz will hop between adjacent carbazyl side chains. In this manner the electron and hole separate and approach one another by stepwise hole hops [109, 110].

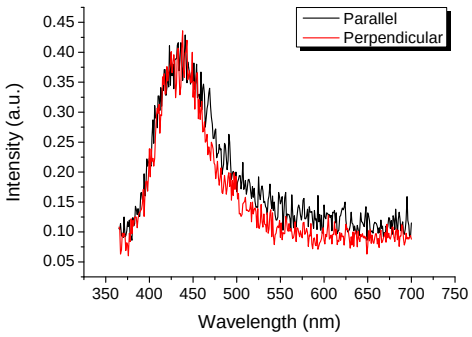

Figure 5.7: Fluorescence polarisation experiment for a PVCz film, excited at a wavelength of 350 nm.

To confirm the presence of the electron hole hopping mechanism and the characteristic random walk distribution of monomer units in the polymer, a fluorescence experiment was conducted. In the experiment the excitation beam was polarised and the emission beam was polarised either parallel or perpendicular with respect to the excitation beam. The fluorescence spectrum of the PVCz film was recorded for both arrangements, Figure 5.7. If electron hole hopping occurs in a polymer with a random walk distribution, the original direction of polarisation would be lost (analogous to the case in a solution) and fluorescence emission would be independent on the direction of polarisation. Evidence of electron-hole hopping is provided by the fluorescence of PVCz, Figure 5.7, where the difference in intensity of the parallel and perpendicular fluorescence is very small. The reason for this small difference is that the lifetime of the singlet state in PVCz is not long enough for electron hopping to occur such that all of the original polarisation would be lost. However, this difference is too small to conduct anisotropy experiments using fluorescence techniques.

Creating a uniformly aligned polymer film is difficult, particularly for the area of sample that MARY experiments require. An attempt to align the polymer was made using spin-coating techniques. However, it was difficult to achieve a uniform alignment for a sample of area of 1 cm^3 which is required for MARY experiments. Consequently the anisotropy experiments in polymers were conducted by photoselection, see Section 5.3. In these experiments the emission of the sample was polarised in order to select the fluorescence emission in a certain orientation with respect to the magnetic field.

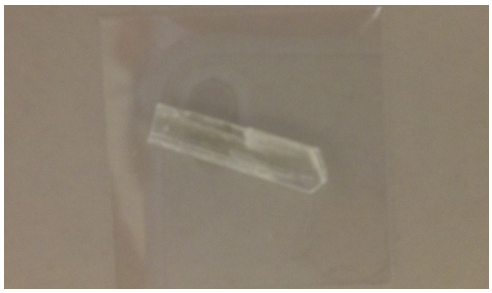

Figure 5.8: Anthracene single crystal grown by an evaporation technique. The crystal was 14 mm in length and 4 mm wide.

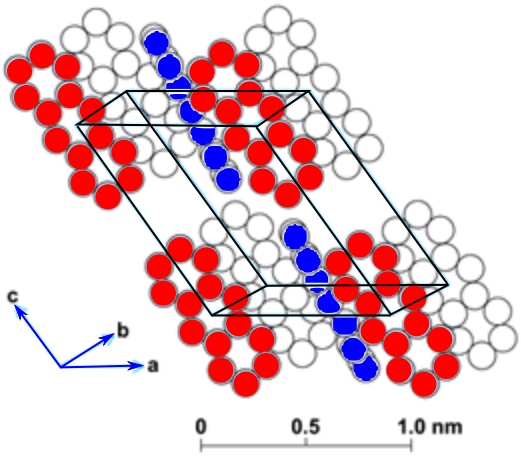

Figure 5.9: The unit cell of an anthracene single crystal. Red and white structure show different layers and the blue show the 'herringbone' anthracene molecules between each layer.

5.2.3 Anthracene Single Crystals

The best and most common method for making large, good quality crystals was found to be the evaporation technique. Anthracene was purchased from Sigma Aldrich with a purity of 97%. A 100 mM solution of anthracene consisting of THF/DMF (ratio of 9:1) was placed in a sealed glass vial. Two small holes were pierced into the lid of the glass vial to ensure that evaporation of solvent was very slow. The solutions were left in a fume hood until crystals formed. Although this method produced large crystals, it was a slow process and often took as long as 10 days for crystals to form, Figure 5.8.

Anthracene has a monoclinic structure with lattice constants a = 8.561 Å, b = 6.036 Å, c = 11.163 Å and $\beta = 124°$ (Figure 5.9). The structure is composed of layers of molecules stacked along the c-direction with 'herringbone' packing within each layer (Figure 5.9) [111] resulting in two different anthracene orientations. It has been shown that the periodicity constructed by each plane is extremely high [111].

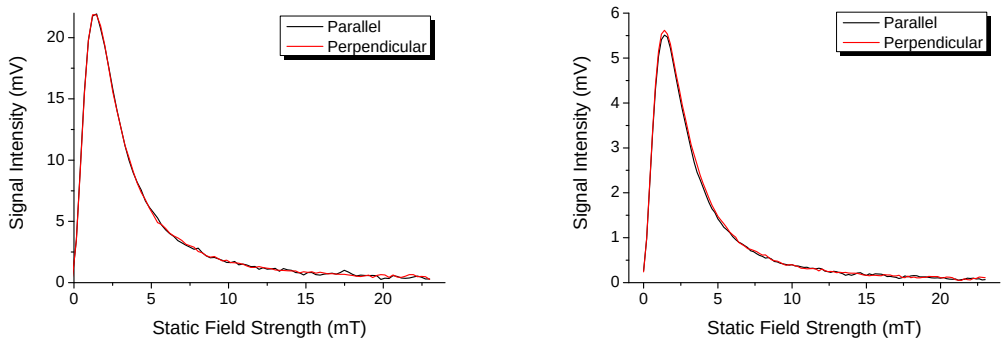

(a) Liquid (b) Glass

Figure 5.10: The results of a polarisation experiment for 0.4 mM Py/40 mM 1,3- DCB in ACN/CH (9:1) solvent (left) and of a polarisation experiment for 0.4 mM Py/40 mM1,3- DCB in THF:Glycerol:CH (3:2:2) glass at 77 K (right). Excitation was provided by UV light and emission was detected using a 548 nm filter.

5.3 Results

5.3.1 Pyrene/DCB in a Glass Matrix

A validation experiment was first performed to confirm that polarisation experiments in an isotropic solution would yield zero anisotropy. Another experiment was also performed in a frozen solution to investigate the anisotropy of the hyperfine coupling within the exciplex system. Py/1,3-DCB was a good choice of system for this investigation because of its large MFEs, as previously described in Chapter 4. The solvent chosen for the isotropic solution (at room temperature) was CH:ACN(9:1) and that chosen for the frozen system was a glass of tetrahydrofuran:glycerol:cyclohexanol (3:2:2) at 77 K. MARY experiments were performed using a UV polariser in the excitation beam and a visible polariser in the emission beam where the relative orientation of the two polarisers were perpendicular or parallel to each other. The results of these experiment are shown in Figure 5.10. For the liquid sample, the MARY plots are identical within the S:N (Figure 5.10(a)), exhibiting a $B_{1/2}$ value 2.06 mT. This corresponds well with the theoretically determined $B_{1/2}$(hfi) (Table 4.2) value for a Py/1,3-DCB RP which is 2.11 mT. The data for the glass matrix (Figure 5.10(b)) produces again identical MARY data for both orientations. The same $B_{1/2}$ value of 2.18 mT was obtained for both polariser orientations, i.e. there is no observable anisotropy in the MFE.

In order to interpret the absence of any anisotropy in the MFE, the hyperfine coupling

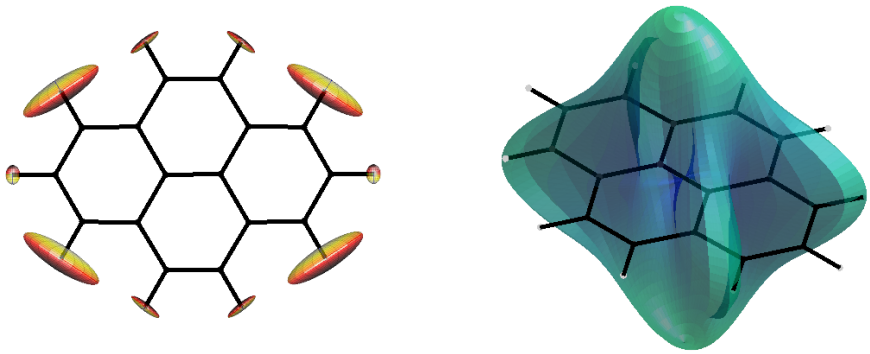

(a) HFC of $Py^{\bullet+}$ (b) Total HFC for $Py^{\bullet+}$

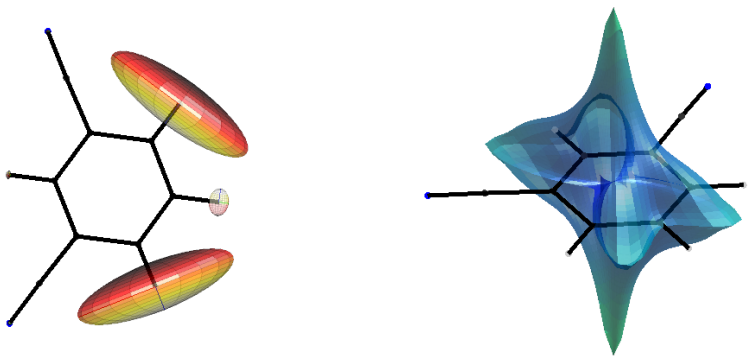

(c) HFC of 1,3-$DCB^{\bullet-}$ (d) Total HFC for 1,3-$DCB^{\bullet-}$

Figure 5.11: Plots of the hyperfine couplings (left) and the corresponding total anisotropy (right) for $Py^{\bullet+}$ (top) and 1,3-$DCB^{\bullet-}$ (bottom).

constants were calculated for the radical pair using DFT (BLYP functional and TZ2P basis set) and displayed in Figure 5.11(a) - Figure 5.11(c). The calculations show that a small amount of anisotropy exists in the principal hyperfine couplings of 1,3-DCB and Py (see Figure 5.11). Projection of these hyperfine coupling constants onto the molecular axes are detailed in Table 5.1. It can be seen that the hyperfine coupling constants along two of the axes are approximately equal and larger than the coupling along the third axis. If the donor and acceptor molecules align such that the axes with largest effective hyperfine coupling are parallel, the maximum $B_{1/2}$ is 2.39 mT and if the axes with the smallest effective hyperfine coupling are parallel the minimum is 1.64 mT. The average of the minimum and maximum $B_{1/2}$ is 2.02 mT, which corresponds to the theoretically and experimentally determined values (Figure 5.11). These, however, are arbitrary since the absolute orientation of the exciplex is not well defined and it is likely that no anisotropy is detected in these systems due to multiple orientations of the donor/acceptor pair which average out the hyperfine coupling constants.

Table 5.1: Hyperfine coupling constants (mT) along the molecular axes x, y and z of 1,3-DCB$^{\bullet-}$ and Py$^{\bullet+}$ and the effective hyperfine coupling constant along the molecular axes. Calculated using DFT (BLYP/TZ2P in ADF).

	1,3-DCB$^{\bullet-}$			
	2N	2H	H	Effective
x	0.039	-1.05	0.16	1.29
y	0.03	-0.76	0.23	0.95
z	0.51	-0.78	0.01	1.14
	Py$^{\bullet+}$			
	4H	4H	2H	Effective
x	0.13	-0.59	-0.23	1.08
y	0.18	-0.29	-0.16	0.63
z	0.05	-0.55	-0.27	1.01

5.3.2 Liquid Crystals

5CB/Pyrene

Pyrene was the first dopant used to test for MFEs in a liquid crystal system. It was used due to its success in producing strong MARY signals as a counter radical in the Py/DCB systems (Chapter 4). 5CB may possess properties analogous to those of DCB when acting as an electron acceptor in the 5CB/Py RP system due to the attached cyano group.

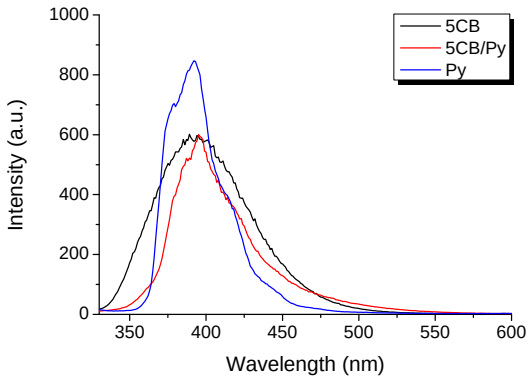

Figure 5.12: Fluorescence of 5CB, 5CB/Py (2% by mass) and 0.1 mM Py in ACN/CH(1:9), excited with a wavelength 325 nm, corresponding to the first excitation transition of 5CB.

Fluorescence spectra of the 5CB/Py system were recorded in order to elucidate the emission band of any possible exciplex in a Py/5CB sample (0.02 mole fraction tested in a 2 mm × 2 mm cuvette). This concentration was optimised to give the largest signal intensity in MARY experiments. The results are shown in Figure 5.12 where the presence of exciplex emission is shown at approximately 500 nm. The narrow spectrum observed with addition of pyrene is due to the pyrene absorption peak in the UV region which dominates the appearance of the emission spectrum. This is supported by fine structure which is evident in the fluorescence emission

band of 5CB/Py.

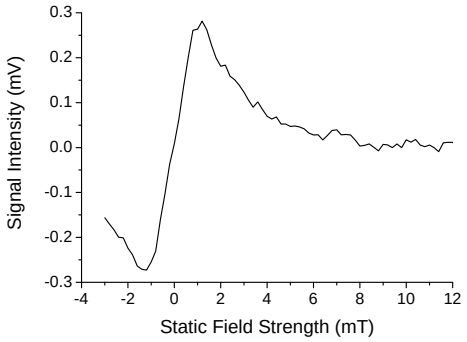

Figure 5.13: MARY for a (0.02 mole fraction) Py/5CB sample. The spectra were recorded by exciting in the UV region and detecting exciplex emission using a 507 nm filter.

The MARY data of the unaligned sample was recorded by photoexcitation in the UV region and detecting fluorescence emission using a 507 nm filter (Figure 5.13). The experimental $B_{1/2}$ value was found to be 2.08 mT, which corresponds to a $5CB^{\bullet-}/Py^{\bullet+}$ RP whose theoretically determined $B_{1/2}$, $B_{1/2}(\text{hfi})$, is equal to 1.71 mT. It is unlikely to be a $5CB^{\bullet+}/Py^{\bullet-}$ RP because this pair has a $B_{1/2}(\text{hfi}) = 3.53$ mT which would result in a much broader profile and also because 5CB is most likely to act as an electron acceptor. It is possible that the experimentally determined $B_{1/2}$ values are larger than the theoretically predicted $B_{1/2}$ values because of self exchange between $5CB^{\bullet-}$ molecules which are present in high concentration, ≈ 5 M.

MARY experiments were performed on a Py/5CB sample (0.02 mole fraction tested in a 2 mm × 2 mm cuvette), oriented in a ± 7 kV AC electric field. The MARY of the aligned sample was measured by exciting in the x, y and z direction (Figure 5.14) in turn and were compared in order to investigate any anisotropy in the sample. The sample block was designed such that excitation light could enter the sample from the side (x direction) or from the bottom (z direction). To record a MARY plot in the third plane it was necessary to turn off the electric field alignment and turn the sample around. This was assumed to be a reasonable procedure since the alignment has been shown (Figure 5.4) to still exist after the time it would take to perform enough averages to produce a plot with a good S:N ($\approx$ 25 min). The results of these MARY experiments

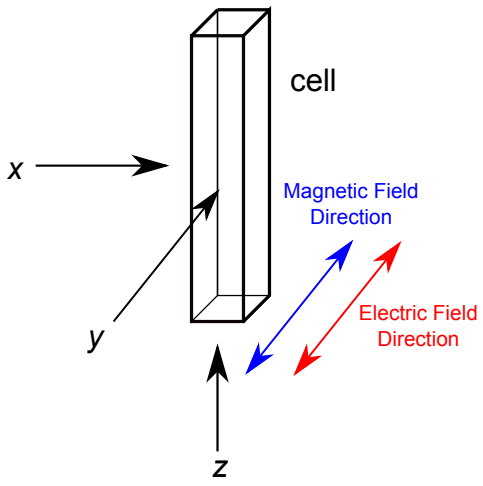

Figure 5.14: Schematic of excitation direction with respect to alignment of the electric field.

are shown in Figure 5.15. It can be seen that the MARY profiles for each plane differ in magnitude because of the different optical transparency of the liquid crystal in different directions. However, normalisation of the MARY plots (Figure 5.15(b)) shows that there is no difference in the shape of the plots and therefore they share the same approximate $B_{1/2}$ value. These results show that there is no observable anisotropy in the MFE. The hyperfine coupling constants were calculated for $5CB^{\bullet-}$ and are detailed in Table 5.2 and the hyperfine coupling constants are shown Figure 5.16(a) along with the corresponding total hyperfine coupling with respect to the molecular axes. It can be seen that the total hyperfine coupling is anisotropic with its magnitude being larger in the plane perpendicular to the benzene moieties. However, it is probable that the anisotropy in the MFE is lost in the 5CB/Py system because of the random orientation of the pyrene molecule with respect to 5CB.

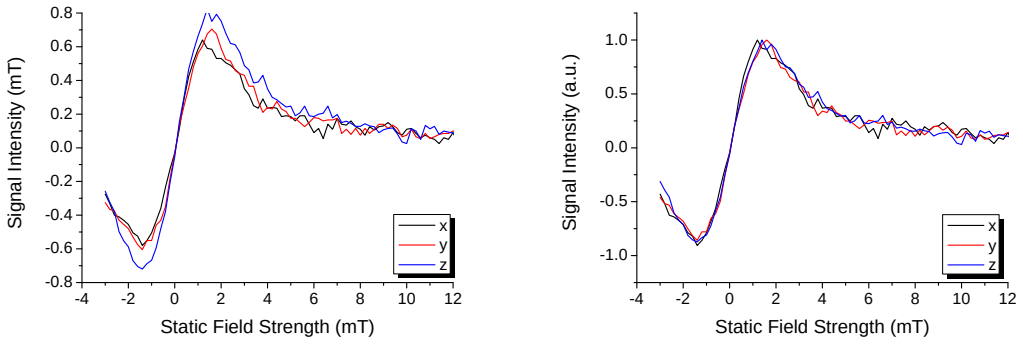

(a) MARY (b) Normalised

Figure 5.15: MARY(left) and normalised MARY(right) for a Py/5CB sample (0.02 mole fraction). The spectra were recorded by exciting in the UV region and detecting exciplex emission using a 507 nm filter. Alignment was achieved in a ± 7 kV AC electric field.

Table 5.2: Hyperfine coupling constants (mT) along the molecular axes x, y and z of $5CB^{\bullet-}$ and the effective hyperfine coupling constant along the molecular axes. Calculated with ADF using a GGA-BLYP exchange-correlation functional and a TZ2P basis set.

	$5CB^{\bullet-}$				
	N	2H	2H	1H	Effective
x	0.05	-0.14	-0.22	0.75	0.98
y	0.07	-0.09	-0.12	0.67	0.85
z	0.66	-0.18	-0.21	0.67	1.29

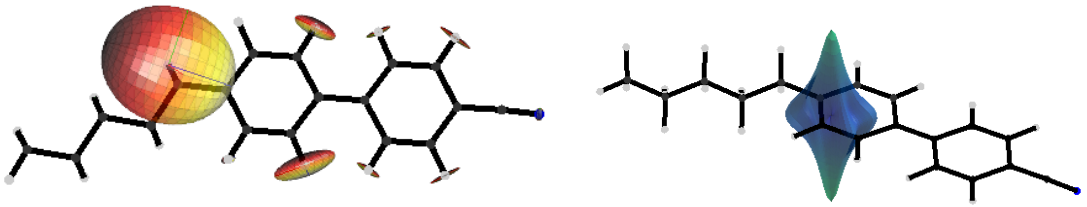

(a) HFC (b) Total HFC

Figure 5.16: The proton and nitrogen hyperfine couplings (Table 5.2) for $5CB^{\bullet-}$ (left) and the corresponding total HFC with respect to the molecular axes (right), calculated with DFT using a GGA-BLYP exchange-correlation functional and a TZ2P basis set.

5CB/Diphenylbutadiene

Trans, trans-1,4-diphenyl-1,3-butadiene (DPB) (Figure 5.17) was chosen as a dopant for 5CB because of its favourable geometry supporting alignment in a LC and its ability to form exciplexes with DCB as shown in previous MFE investigations [112]. Again, the 5CB should act as an electron acceptor because of the cyano group on the benzene moiety. It was hoped that the DPB would preferentially align parallel to the long axis of the 5CB, to maximise π-orbital overlap in the exciplex, and therefore increase the chance of observing anisotropic MFEs in 5CB/DPB systems.

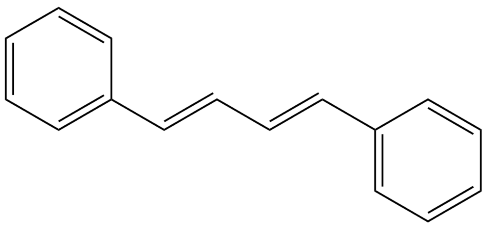

Figure 5.17: Structure of trans, trans-1,4-diphenyl-1,3-butadiene (DPB).

Fluorescence emission spectra and UV/Vis ground state absorption experiments were carried out in order to deduce the optimum wavelengths for excitation and detection for MARY experiments. The absorption bands of 5CB and DPB overlap in the UV region of the spectrum (data not shown) such that selective photoexcitation was difficult and it was not possible to deduce the optimum emission wavelength detection for emission of fluorescence. Optimisation of the wavelength to produce the largest MARY signal was achieved by recording MARY for different filters (data not shown) and comparing signal intensities. It was found that using a 548 nm filter for emis-

sion detection produced highest S:N. The optimum concentration of DPB in the sample which produced the largest MFE signals was 0.1% by mass composition (data not shown). The MARY and MFE plots for the unaligned 5CB/DPB sample are shown in Figure 5.18.

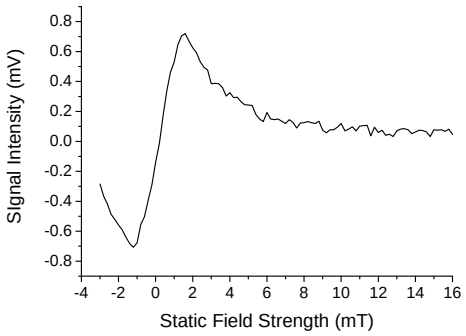

Figure 5.18: MARY plot for an unaligned 5CB/DPB(0.1% by mass) sample. MARY spectra were recorded using a wavelength of 350 nm for excitation and a 548 nm filter for detection.

From the redox potentials for 5CB and DPB it is found that 5CB is more likely to be the electron acceptor ($E_{red} = -1.9\,\mathrm{V}$ [113]) and DPB the electron donor ($E_{ox} = 1.1\,\mathrm{V}$ [114]) A $5CB^{\bullet -}/DPB^{\bullet +}$ RP has a $B_{1/2}$(hfi) of 1.61 mT and would result in a comparatively narrow MARY. The $B_{1/2}$ value deduced from the experimental data was 2.60 mT ($\pm 0.25\,\mathrm{mT}$). The experimentally observed $B_{1/2}$ is larger than the theoretically determined $B_{1/2}$ and this is likely to be due to electron exchange between the 5CB molecules which are present in a high concentration [74].

MARY experiments were performed on a DPB/5CB sample (1.2×10^{-3} mole fraction in a 2 mm $\times$ 2 mm cuvette), aligned in a $\pm$ 7 $\mathrm{kVm^{-1}}$ AC electric field (data shown in Figure 5.19). The signal intensities observed in the aligned sample are smaller than those observed for the isotropic sample. This is because the alignment of 5CB will alter the relative transmittance of light through the sample. It is apparent from the MARY data that the observed signal intensities for the three orientations are different. As before, the signal intensity observed when the excitation beam enters the sample cell from underneath (z direction) is larger than the signal intensities observed when the excitation beam enters the sample cell from the sides (x and y direction). Normalisation of the MARY curves show there is, again, very little difference in the shapes of the observed MARY plots with experimentally determined $B_{1/2}$ values of 3.30 mT ($\pm 0.05\,\mathrm{mT}$). Hence no anisotropic magnetic response was observed in 5CB/DPB system. This could be due to a number of

reasons: (1) the hyperfine coupling constants of 5CB and DPB are not anisotropic; (2) a random orientation of the molecules with respect to the field and with respect to each other cancels any anisotropy or (3) no anisotropy is observed because of fast self-exchange of $5CB^{\bullet-}$ meaning that only the anisotropy in the hyperfine couplings of $DPB^{\bullet+}$ would matter.

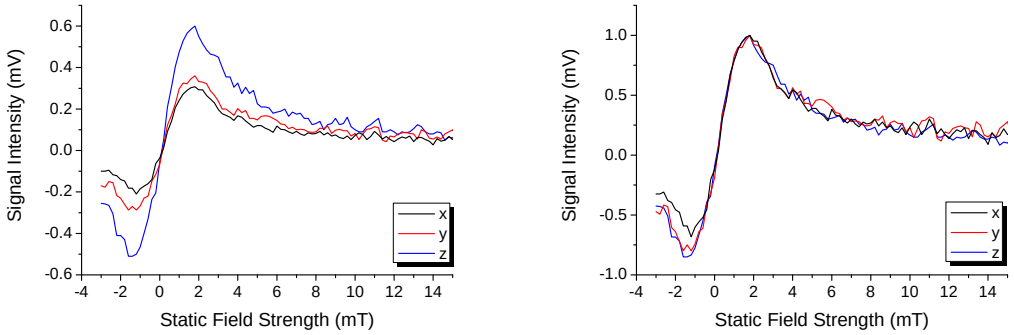

(a) MARY (b) Normalised MARY

Figure 5.19: MARY plot (left) and normalised MARY (right) for an aligned 5CB/DPB (1.2×10^{-3} mole fraction) sample. MARY spectra were recorded using a wavelength of 350 nm for excitation and a 548 nm filter for detection.

Further investigation of the hyperfine coupling constants may shed light on the reasons why no anisotropy was observed in these aligned systems other than self exchange reasons. The hyperfine coupling constants for $5CB^{\bullet-}$ and $DPB^{\bullet+}$ were calculated by DFT using a GGA-BLYP exchange correlation functional and a TZ2P basis set. These calculations are shown in Figure 5.16 and Figure 5.20 and Table 5.3. From the data it can be seen that the largest hyperfine coupling constants of $5CB^{\bullet-}$ and $DPB^{\bullet+}$ are observed on protons at the α position with respect to the ring and are 0.70 mT and 0.40 mT, respectively. The hyperfine coupling constants for $5CB^{\bullet-}$ and $DPB^{\bullet+}$ are given in Table 5.3 along the axes x, y and z of the molecular frame.

The data shows that for $5CB^{\bullet-}$ the effective hyperfine coupling along the z axis (1.29 mT) is larger than those in the x and y axes (Figure 5.16), 0.98 mT and 0.85 mT, respectively, but only by a small amount. In $DPB^{\bullet+}$ the difference between the hyperfine coupling constants along the three axes is even smaller than those in $5CB^{\bullet-}$. Again, in the best case scenario, when the axes of the molecules are aligned such that two axes with the largest effective hyperfine coupling constants (z direction) are parallel, the maximum

$B_{1/2}$ achievable would be 2.2 mT. If the axes with the smallest effective hyperfine coupling constants (perpendicular to z direction) are parallel the minimum would be 1.74 mT. However, the difference between the minimum and maximum obtainable $B_{1/2}$ values is relatively small even in this case.

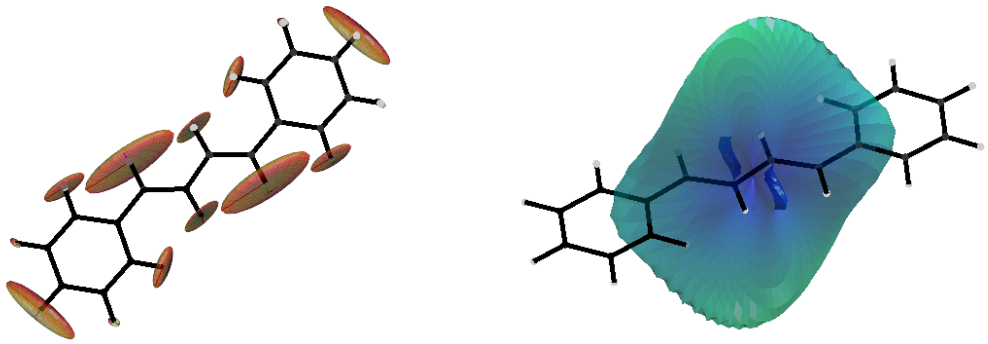

(a) HFC (b) Total HFC

Figure 5.20: The proton hyperfine couplings for $DPB^{\bullet+}$ (left) and the corresponding total HFC with respect to the molecular axes (right), calculated by ADF using a GGA-BLYP exchange-correlation functional and a TZ2P basis set.

Table 5.3: Hyperfine coupling constants (mT) along the molecular axes x, y and z of $5CB^{\bullet-}$ and $DPB^{\bullet+}$ and the effective hyperfine coupling constant along the molecular axes. Calculated with DFT using a GGA-BLYP exchange-correlation functional and a TZ2P basis set.

	$5CB^{\bullet-}$				
	N	2H	2H	1H	Effective
x	0.05	-0.14	-0.22	0.75	0.98
y	0.07	-0.09	-0.12	0.67	0.85
z	0.66	-0.18	-0.21	0.67	1.29
	$DPB^{\bullet+}$				
	2H	4H	2H	2H	Effective
x	-0.34	-0.1	-0.48	-0.17	0.78
y	-0.28	-0.24	-0.30	-0.14	0.68
z	-0.34	-0.24	-0.44	-0.26	0.86

There are several possible reasons for why no anisotropy has been observed in the 5CB systems investigated. The first reason is that the anisotropy of the hyperfine coupling within the RP may be too small to observe an anisotropic magnetic response, particularly when taking into account the random distribution of the orientation of the two molecules with respect to the field direction and with respect to each other. The second possibility is that fast self exchange between 5CB molecules causes the anisotropy to be lost. Hence there is the need to investigate different systems which may exhibit an anisotropic

magnetic response. For example, polymer films in which anisotropy is investigated using photoselection techniques.

5.3.3 Polymers

PVCz/C_{60}

C_{60} was chosen to partner with PVCz, because of its lack of hyperfine couplings and known ability to partake in electron transfer reactions [115]. If C_{60} is used as a dopant in PVCz films, the hyperfine coupling anisotropy of PVCz can be investigated since C_{60} does not contribute to the hyperfine interactions within the RP because of the low abundance of ^{13}C. PVCz films doped with a small amount of C_{60} have been reported to show excellent photoconductivity because the C_{60} acts as an electron acceptor in the polymers [116]. If PVCz had considerable hyperfine anisotropy the PVCz/C_{60} RP system might be an ideal candidate for chemical compass behaviour. UV/Vis ground state absorption and fluorescence emission spectra were used to optimise the wavelength for excitation and emission detection and to confirm that the monomer fluorescence of PVCz would be quenched in the presence of the dopant. Unfortunately no exciplex emission band was observed and it was not possible to elucidate the optimum wavelength for detection of exciplex emission. Therefore the wavelength for detection was optimised for the highest S:N in MARY plots by performing Modulated-MARY experiments using different filters for fluorescence emission detection and was found to be 548 nm (±20 nm) (data not shown). Experiments were also performed to optimise the concentration for the highest S:N in MARY plots and was found too be 0.25% by mass (Figure 5.21).

Since C_{60} has no significant hyperfine couplings the width of the MARY spectrum is due to the hyperfine coupling constants of PVCz only. Assuming that the hyperfine couplings on C_{60} are approximated by zero, the theoretical $B_{1/2}$ for the RP will be given by:

$$B_{1/2} = 2a_{\mathrm{PVCz}} \tag{5.2}$$

where a_{PVCz} is the effective hyperfine coupling for the $\mathrm{PVCz}^{\bullet+}$ radical. The $B_{1/2}$ value estimated from the MARY spectrum for PVCz/C_{60} in the absence of photoselection (Fig-

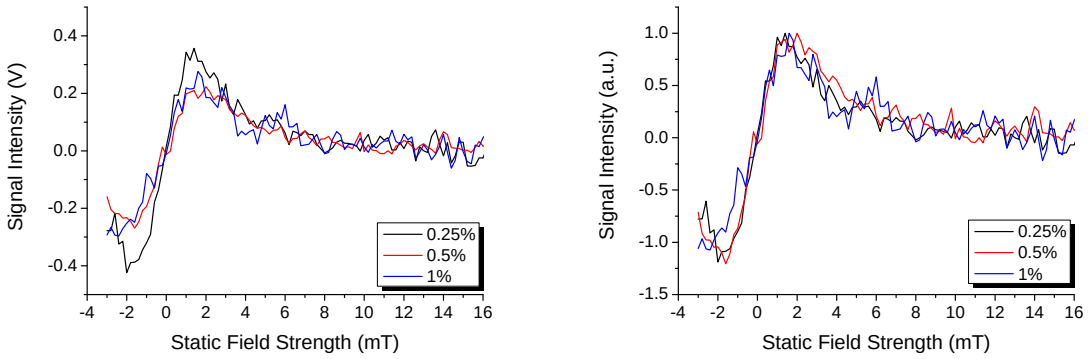

(a) MARY (b) Normalised MARY

Figure 5.21: MARY(left) and normalised (right) plots for PVCz/C_{60} for various concentrations. A 79 Hz, 2.0 mT modulation field was used and a 548 nm filter was employed for fluorescence emission detection.

ure 5.22) is 2.60 mT (±0.69 mT) which is comparable to the effective hyperfine coupling constant of $PVCz^{\bullet+}$ (1.46 mT [116, 117]), $B_{1/2}$ = 2.92 mT within the error limit.

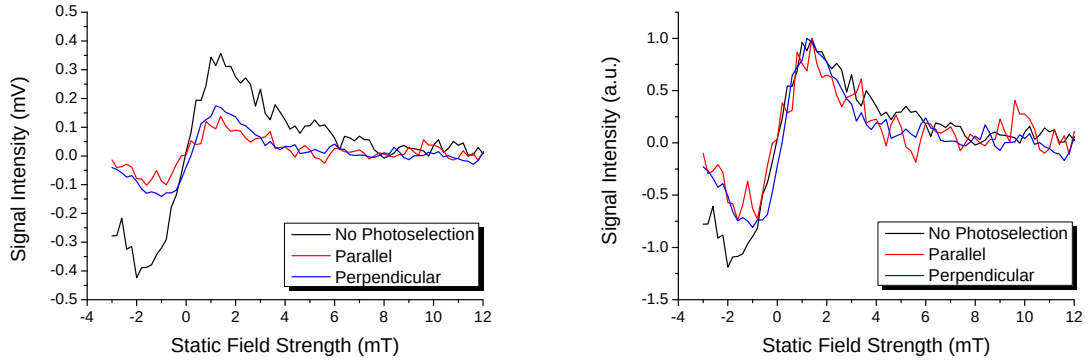

(a) MARY (b) Normalised MARY

Figure 5.22: MARY(left) and normalised (right) plots for PVCz/C_{60} (0.25% by mass). A 79 Hz, 2.0 mT modulation field was used and a 548 nm filter was employed for fluorescence emission detection.

Photoselection experiments were performed using a polariser in the visible region (300 nm - 800 nm) in the emission beam. The reason for not placing the polariser in the excitation beam was because electron hole hopping in the polymer would result in a loss of initial polarisation. Any anisotropy would be investigated by comparing the shapes of the MARY spectra for perpendicular polarisation and parallel polarisation of the fluorescence emission. The photoselection experiments were performed using UV excitation and a 548 nm (± 20 nm) filter for detection of exciplex emission. The results are shown in (Figure 5.22). The most obvious feature of the data is the reduction in the intensity of the observed MARY signal for parallel and perpendicular (of photodetection plane and

magnetic field direction) orientations when compared to unpolarised light excitation - as expected for application of a polariser. Normalisation of the MARY data and calculations of their $B_{1/2}$ values allows the shapes of the spectra to be compared. As can be seen in Figure 5.22(b) the spectra are similar in shape (within the S:N) with $B_{1/2}$ values of 2.40 mT ($\pm$0.69 mT) in the absence of photoselection; 2.08 mT ($\pm$0.36 mT) for parallel orientations of magnetic field direction and photodetection and 1.73 mT ($\pm$0.88 mT) for perpendicular arrangements. Unfortunately it was not possible to perform more averages on the sample to achieve a better S:N due to inherent degradation in the PVCz/C_{60} films which meant that the films only lasted about 20 runs before the signal intensity was reduced to almost zero. Although the experimental $B_{1/2}$ as given seem reasonably different at first sight the S:N in the MARY plots is very low making it less possible to quantify any observed anisotropy and the $B_{1/2}$ values are in the wrong order, since the value in the absence of any photoselection should be intermediate between the two cases where photoselection is present.

Calculation of anisotropic hyperfine coupling constants for PVCz is non-trivial since it requires calculations of a vast number of connected monomer units. However, an attempt was made to find an approximation of how anisotropic the hyperfine coupling constants might be by studying individual monomer unit and secondly how hyperfine coupling constants varied with the addition of another monomer unit, i.e. $(ECz)_2$, (Figure 5.23). The total hyperfine coupling constants were also compared for the monomer and dimer molecules. For both it can be seen that the total hyperfine coupling is anisotropic with its largest magnitude perpendicular to the plane of the ring. The hyperfine coupling constants for $ECz^{\bullet+}$ and $(ECz)_2{}^{\bullet+}$ along the molecular axes are given in Table 5.4. The first observation is that the hyperfine coupling constants of the monomer $ECz^{\bullet+}$ are larger than those in the dimer, $(ECz)_2{}^{\bullet+}$ the effective hyperfine coupling being 2.86 mT and 0.79 mT respectively. It can also be seen that both possess an anisotropy such that the effective hyperfine coupling constants along the z direction of the molecular frame are larger than those in the x and y axes. However, since no anisotropy was observed in the magnetic field response of the PVCz/C_{60} it is probable that the anisotropy of the hyperfine couplings within the PVCz are averaged in some way. There are several possible reasons

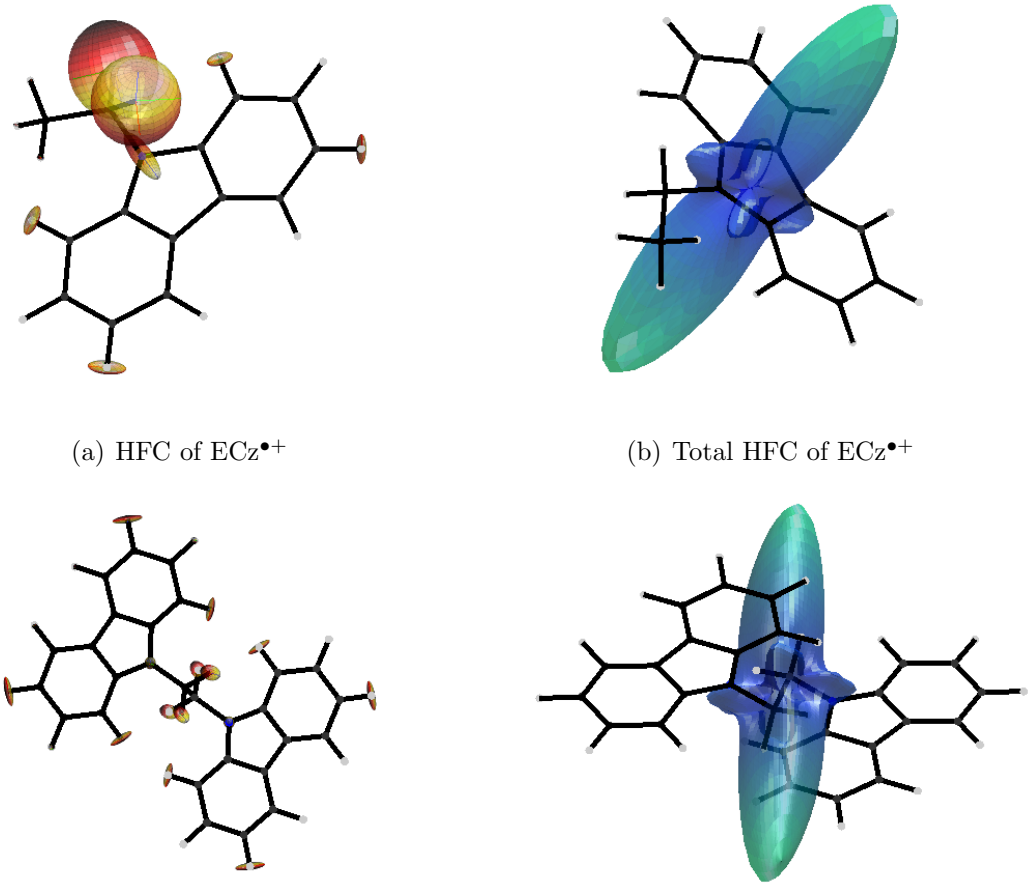

(a) HFC of $ECz^{\bullet+}$

(b) Total HFC of $ECz^{\bullet+}$

(c) HFC of $(ECz)_2{}^{\bullet+}$

(d) Total HFC of $(ECz)_2{}^{\bullet+}$

Figure 5.23: Calculated hyperfine couplings (left) and total hyperfine coupling with respect to the molecular axes (right) in $ECz^{\bullet+}$ (top) and the dimer $ECz_2^{\bullet+}$ (bottom), calculated using DFT.

for this. The first is because it is possible that averaging of the hyperfine couplings occur because of the random orientation of the monomer within the plane of photoselection direction and the second possibility is that electron hole hopping may 'smear out' any anisotropic hyperfine coupling constants within the RP. It must also be noted that the hyperfine coupling constants have only been investigated for the monomer and the dimer of ECZ. This is a very hypothetical situation compared with that of PVCz, which consists of thousands of connected monomer units.

PVCz/Fluorinated Compounds

The use of fluorinated compounds as dopants in PVCz films was motivated by the potential for fluorine to have large anisotropic hyperfine coupling constants. Fluorinated compounds used included mono-fluorobenzonitriles and perfluoronaphthalene (PFN) (an

	$ECz^{\bullet+}$					
	N	2H	2H	1H	1H	Effective
x	0.56	-0.52	-0.17	1.84	1.84	2.48
y	0.69	-0.25	-0.60	1.85	2.01	2.68
z	1.75	-0.36	-0.43	1.93	1.77	3.43
	$(ECz)_2{}^{\bullet+}$					
	N	2H	2H	1H	1H	Effective
x	0.13	-0.24	-0.09	0.21	0.23	0.45
y	0.13	-0.14	-0.35	0.22	0.18	0.55
z	0.91	-0.23	-0.24	0.17	0.15	1.36

Table 5.4: Hyperfine coupling constants (mT) along the molecular axes, x, y and z of $ECz^{\bullet+}$ and $(ECz)_2{}^{\bullet+}$ and the effective hyperfine coupling constant along the molecular axes. Calculated with DFT using a GGA-BLYP exchange-correlation functional and a TZ2P basis set.

oblong molecule with large hyperfine coupling constants [118]). The calculated hyperfine coupling constants of the three mono fluoro-substituted benzonitriles are shown in Table 5.5. The data indicates that the hyperfine coupling constants of the fluorine in 4-fluorobenzonitrile (4-FBN) are large compared to the hyperfine coupling constant of the fluorines in 2-fluorobenzonitrile (2FBN) and 3-fluorobenzonitrile. In the literature [119] it is stated that the hyperfine coupling constants of the fluorine in 4-FBN are strongly anisotropic. No data was found detailing the anisotropy of the 2-FBN and 3-FBN in the literature. However, in order to investigate the anisotropy of the FBN molecules, DFT calculations were performed using a BLYP exchange-correlation functional and a TZ2P basis set on a system where PVCz is the electron donor and FBN the electron acceptor, $PVCz^{\bullet+}/FBN^{\bullet-}$. The hyperfine coupling constants for $2\text{-}FBN^{\bullet-}$, $3\text{-}FBN^{\bullet-}$ and $4\text{-}FBN^{\bullet-}$are shown as 3D plots in (Figure 5.24). The hyperfine coupling constants along the molecular axes are given in Table 5.6.

Benzonitrile	a_N	a_F	a_{H-2} a_{H-6}	a_{H-3} a_{H-5}	a_{H-4}
2-FBN	0.217	0.554	0.341	0.111 0.047	0.914
3-FBN	0.226	0.251	0.474 0.294	0.057	0.787
4-FBN	0.208	2.296	0.438	0.084	-

Table 5.5: Experimentally determined hyperfine coupling constants (mT) for fluorobenzonitrile radical anions [120].

From the hyperfine coupling data (Table 5.6) it can be seen that $4\text{-}FBN^{\bullet-}$ and $PFN^{\bullet-}$

possess the largest effective hyperfine coupling constants 2.41 mT and 3.07 mT, respectively. The data show that the hyperfine coupling constants for 4-FBN are anisotropic with the largest coupling along the z axis - as predicted in the literature [119]. The hyperfine coupling constants of $PFN^{\bullet-}$ are experimentally unknown but have been determined using theoretical calculations [118] via DFT. From the plots (Figure 5.24), the anisotropy of the hyperfine couplings on fluorine can be seen to be largest in magnitude in the plane perpendicular to the ring. The hyperfine couplings of PFN are also anisotropic with the largest hyperfine coupling constants along the y axis. This can be seen to be the plane perpendicular to the ring (Figure 5.24). Both 2-FBN and 3-FBN also show hyperfine coupling constants which are anisotropic perpendicular to the plane of the benzene ring; however, these anisotropies were not as large as in the case of 4-FBN and PFN and hence were not investigated as dopants in PVCz films.

	$2\text{-FBN}^{\bullet-}$						
	F	N	H	H	H	H	Effective
x	-0.19	0.10	-0.54	0.11	-1.24	-0.13	1.20
y	-0.17	0.07	-0.41	0.09	-0.50	-0.07	0.60
z	1.12	1.01	-0.48	-0.06	-0.69	-0.19	1.88
	$3\text{-FBN}^{\bullet-}$						
	F	N	H	H	H	H	Effective
x	-0.15	0.10	-0.19	0.00	-1.04	-0.18	0.95
y	-0.13	0.15	-0.16	-0.21	-0.44	-0.69	0.78
z	-0.55	1.02	-0.25	-0.18	-0.56	-0.47	1.67
	$4\text{-FBN}^{\bullet-}$						
	F	N	H	H	H	H	Effective
x	-0.43	0.08	-0.34	0.03	0.07	-0.60	0.72
y	-0.02	0.10	-0.42	0.09	0.04	-0.16	0.42
z	6.80	1.05	-0.41	-0.07	-0.07	-0.41	6.09
	$PFN^{\bullet-}$						
	4F	4F					Effective
x	0.02	-0.10					0.18
y	4.42	1.64					8.17
z	-0.49	-0.14					0.88

Table 5.6: Hyperfine coupling constants (mT) along the molecular axes x, y and z of fluorobenzonitriles and perfluoronaphthalene and the effective hyperfine coupling constant along the molecular axes. Calculated with DFT using a GGA-BLYP exchange-correlation functional and a TZ2P basis set.

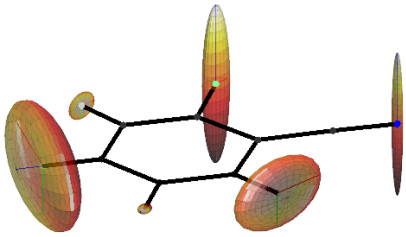

(a) HFC 2-FBN$^{\bullet-}$

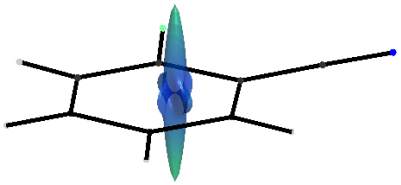

(b) Total HFC 2-FBN$^{\bullet-}$

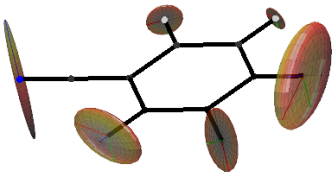

(c) HFC 3-FBN$^{\bullet-}$

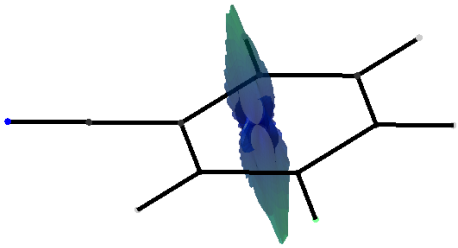

(d) Total HFC 3-FBN$^{\bullet-}$

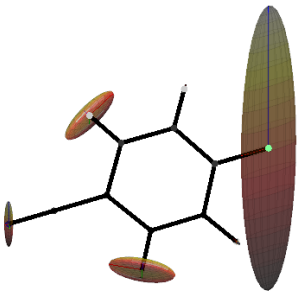

(e) HFC 4-FBN$^{\bullet-}$

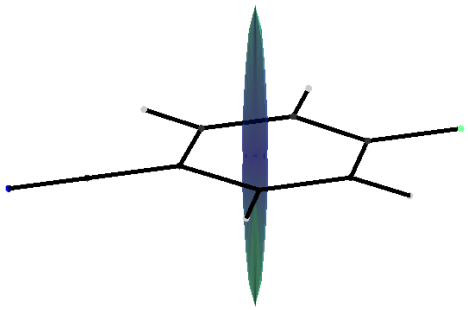

(f) Total HFC 4-FBN$^{\bullet-}$

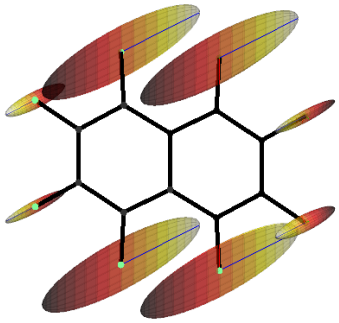

(g) HFC PFN$^{\bullet-}$

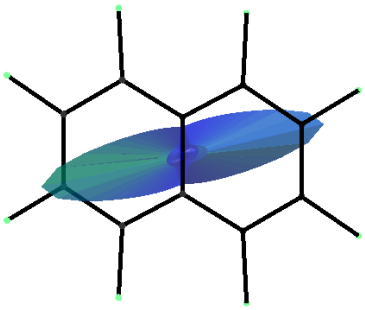

(h) Total HFC PFN$^{\bullet-}$

Figure 5.24: The hyperfine coupling constants (mT) of the fluorobenzonitriles calculated in DFT using a BLYP exchange-correlation functional and a TZ2P basis set and their corresponding total hyperfine coupling with respect to the molecular axes.

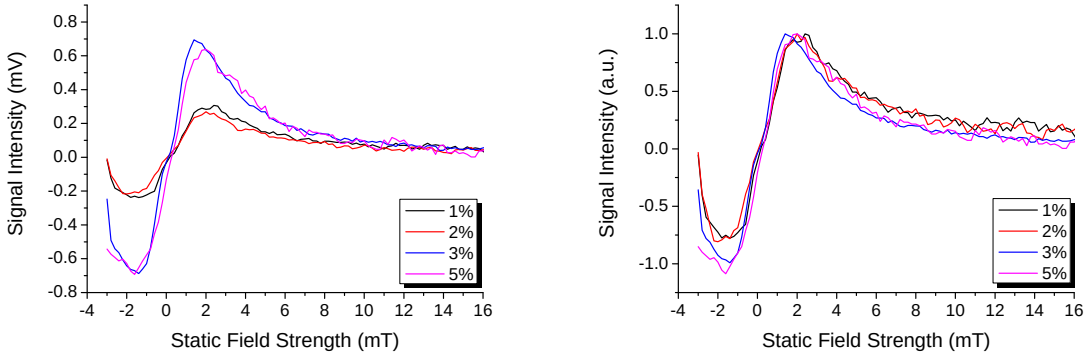

(a) MARY (b) Normalised MARY

Figure 5.25: MARY (left) and normalised MARY (right) plots for PVCz/4-FBN for various concentrations. A 79 Hz, 2.0 mT modulation field was used and a 548 nm filter was employed for fluorescence emission detection.

4-FBN and PFN strongly absorb in the UV region and so their absorption spectra overlap with that of PVCz. Because of this it was not possible to determine the wavelength of any exciplex emission from the fluorescence emission spectra of the films. However, optimisation of the wavelength was performed by recording MARY using different emission filters for detection. The best MARY signal was recorded using the 548 nm filter for both 4-FBN and PFN dopants (data not shown). The concentration of dopant was optimised for largest signal intensity and found to be 3% (by mass) for both 4-FBN (Figure 5.25) and PFN (data not shown). With such high concentrations it is highly likely that self exchange will occur between dopant molecules. Determination of self exchange rates in these systems is difficult due to the inability to go to much higher or lower concentrations because the films become brittle at high concentrations and low concentrations result in too low a S:N. However, from Figure 5.25 it can be seen that a decrease in the width of the MARY data is observed with increasing 4-FBN concentration. It may therefore be concluded that there is fast exchange of 4-FBN$^{\bullet-}$ and experimental $B_{1/2}$ values will be lower than those predicted theoretically. The average distance between FBN molecules in the polymer films is approximately 2 nm. In solids the distance dependence of electron transfer rates is approximately exponential and at a distance of 2 nm the rate of electron transfer can be as large as $1 \times 10^{10}\,\mathrm{s}^{-1}$ [121].

The MARY data for PVCz/4-FBN and PVCz/PFN films in the absence and in the presence of parallel and perpendicular photoselection are shown in Figure 5.26. The

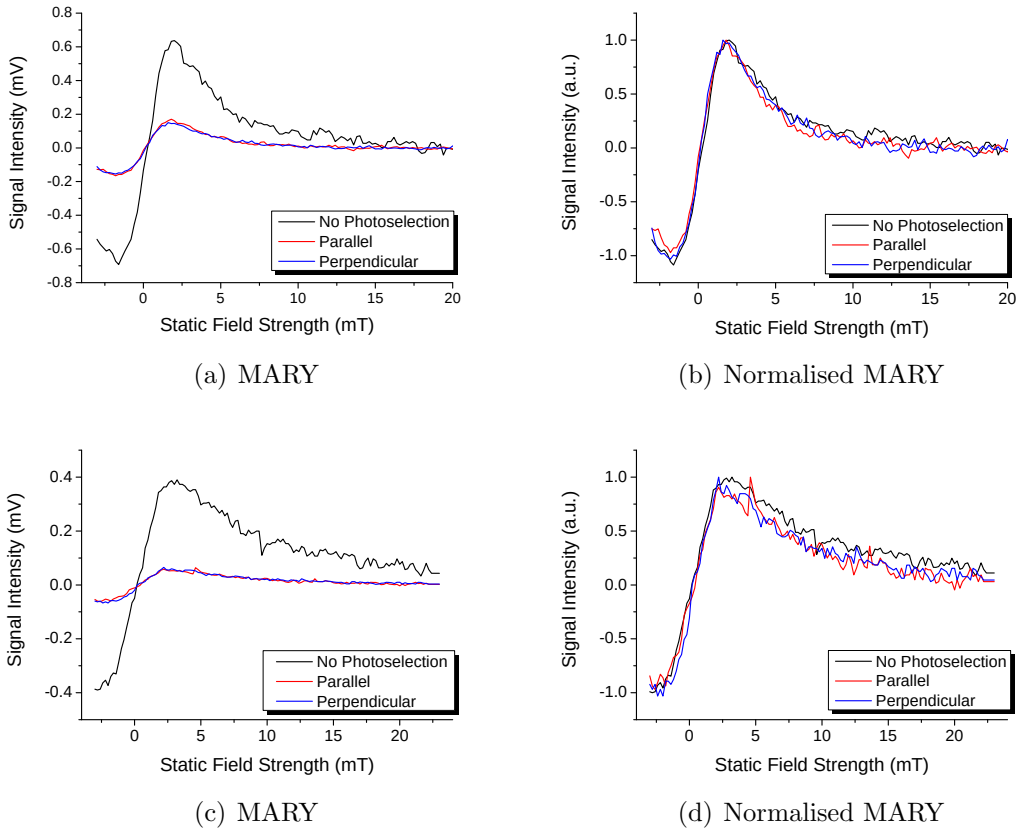

(a) MARY (b) Normalised MARY

(c) MARY (d) Normalised MARY

Figure 5.26: MARY (left) and normalised MARY (right) data for a PVCz/4-FBN (3% by mass) film (top) and for a PVCz/PFN (3% by mass) film (bottom). The spectra were recorded using UV light for excitation and a 548 nm filter for detection of exciplex fluorescence. A 79 Hz, 2.0 mT modulation field was applied.

theoretical $B_{1/2}$ for a PVCz$^{\bullet+}$/4-FBN$^{\bullet-}$ is given by 3.65 mT, where the effective hyperfine coupling constants for PVCz$^{\bullet+}$ and 4-FBN$^{\bullet-}$ are 1.46 mT and 2.08 mT, respectively. This suggests that MARY would have a large peak to peak separation, resulting in a broad MFE plot. The normalised MARY data show that all three MARY curves have approximately the same shape within the S:N. In the absence of any photoselection $B_{1/2}$(Pk-Pk) is 3.29 mT ($\pm$0.12 mT) and for parallel and perpendicular photoselection, the $B_{1/2}$ (Pk-Pk) values are 2.94 mT ($\pm$0.20 mT) and 2.94 mT ($\pm$0.26 mT), respectively. All experimental $B_{1/2}$ values are smaller than the theoretical value predicted using Equation 4.3 ($B_{1/2}$(hfi) = 3.64 mT). The reason for this could be due to a number of effects: (1) self exchange (Section 4.2.5) between 4-FBN$^{\bullet-}$ molecules, which will reduce the width of the MARY plot or (2) reduction of 4-FBN upon electron transfer to lose a fluorine. The latter may occur in 4-FBN because the presence of cyano-groups on fluorobenzenes labilises the C - F bond and thus a reduction, resulting in the loss of fluorine anions, may occur [122].

However, disproportionation of 4-FBN radical anion to produce a fluoride anion and a benzonitrile radical occurs with a rate constant $k = 11\,\mathrm{s}^{-1}$ which is much slower than the rate of electron transfer, i.e. $k \approx 1 \times 10^{10}\,\mathrm{s}^{-1}$. It is most likely, therefore, that experimental $B_{1/2}$ values are smaller than those determined theoretically because of self exchange effects on 4-FBN$^{\bullet-}$ (Figure 5.25).

The MARY data for PVCz/PFN (Figure 5.26(c)) show very broad spectra particularly in the absence of photoselection. Since the hyperfine coupling constants of PFN are larger than those of 4-FBN, it is expected that the MFE spectra will be broader with larger $B_{1/2}$ values. Inspection of the normalised MARY data (Figure 5.26(d)) shows that the spectra are broad with large $B_{1/2}$ values given by 4.84 mT (±0.40 mT), 4.55 mT (±0.40 mT) and 4.48 mT (±0.62 mT) without photoselection, for parallel and for perpendicular photoselection respectively. The $B_{1/2}$ values for the MARY in the presence of photoselection are both smaller than the theoretically determined $B_{1/2}$(hfi) value of 5.10 mT. Again, the narrowing of the experimental data could be due to self exchange (Section 4.2.5), as believed to be the case for 4-FBN. The normalised MARY data show that plot in the absence of any photoselection is broader than those in the presence of photoselection. However, the S:N, and hence error, in these system are large and it is not possible to quantify any anisotropy in the PVCz/PFN film. It may be that rotation of the molecule with respect to the direction of photoselection causes the anisotropic hyperfine couplings (perpendicular to the plane of the ring) to be averaged and thus no anisotropic magnetic field response is observed.

The failure to observe any anisotropic response to an applied magnetic field in these fluorinated systems is very disappointing. Particularly as the anisotropies of the hyperfine coupling constants on 4-FBN and PFN are so large (Figure 5.24). This highlights the need to find aligned systems in which no self-exchange occurs so as to increase the chance of observing an anisotropic magnetic response.

5.3.4 Single Crystals

In 1967, it was discovered that the rate of triplet-triplet annihilation in anthracene single crystals is magnetic-field dependent at room temperature [123]. Triplet-triplet annihila-

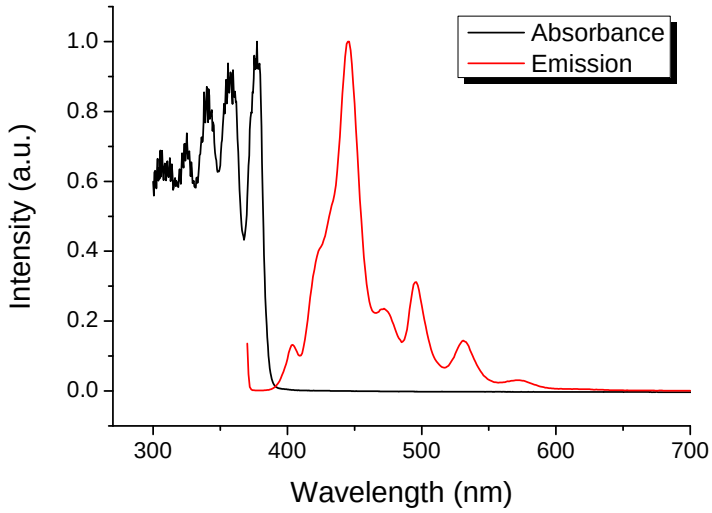

Figure 5.27: The normalised absorption and emission spectra of an anthracene single crystal. The emission spectrum is recorded using an excitation wavelength of 365 nm and slit width of 2.5 nm.

tion of anthracene triplet excited state molecules leads to a higher-energy singlet whose radiative decay gives rise to delayed fluorescence. Furthermore, the field effect was shown to exhibit a dependence on the orientation of the magnetic field with respect to the crystal [123].

The absorption and emission spectra of an anthracene single crystal are shown in Figure 5.27, where the emission spectrum is recorded using a excitation wavelength of 365 nm and a slit width of 2.5 nm. The data shows that anthracene absorbs in the UV region 300 nm - 400 nm with the largest absorbance at approximately 365 nm (0,0 band). The emission spectrum shows a collection of bands centred at 450 nm and corresponds to the monomer emission of anthracene.

The MARY for anthracene single crystals was recorded using continuous UV excitation and a 450 nm filter for detection (Figure 5.29). This filter corresponds to the monomer fluorescence of anthracene and was used in order to detect prompt fluorescence. The anisotropy of the crystal was investigated by rotating the crystal in the apparatus, where the crystal face lies parallel to the magnetic field direction or perpendicular to the magnetic field direction (Figure 5.28). For parallel orientations the static magnetic field is parallel to the *ac* plane of the anthracene crystal and for perpendicular orientations the applied static field is perpendicular to the *ac* plane.

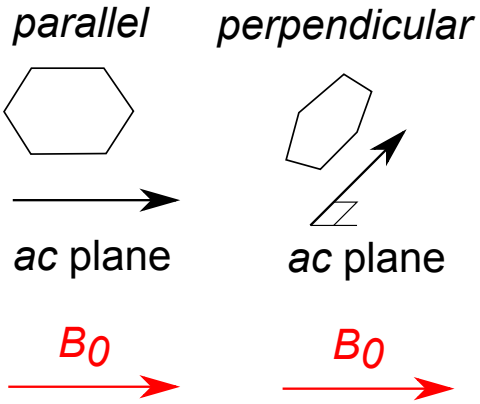

Figure 5.28: The orientation of the anthracene crystal with respect to the applied static magnetic field. The *ac* plane of the crystal is either parallel (left) or perpendicular (right) to the direction of the field.

The spectra were broad and hence it was necessary to record from −13 mT to 23 mT in order to see the peak at negative fields. The magnitude of the magnetic field effect in the single crystal was found to depend on the square of the light intensity dependence (data not shown) and is thus characteristic of that observed for a triplet-triplet mechanism. The triplet-triplet mechanism is known to take place frequently in molecular crystals [10]. This mechanism is different to those that have already been presented in this thesis and will therefore be briefly discussed.

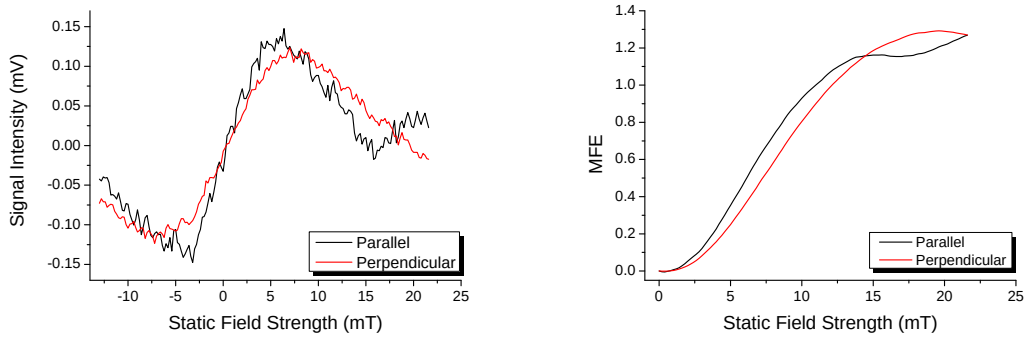

(a) MARY Data (b) MFE Data

Figure 5.29: MARY (left) and MFE (right) data for an anthracene single crystal. These results were recorded using UV excitation and a 450 nm filter for detection of emission fluorescence. A 79 Hz, 2.0 mT modulation field was applied.

The triplet-triplet mechanism arises when a pair of triplets interact by transferring electronic energy (annihilation), involving a change of multiplicity. The two non-interacting triplet excitons come together to form pairs and either annihilate to yield an excited singlet state or dissociate. It can hence lead to higher energy excited singlets, producing delayed fluorescence. The triplet-triplet annihilation process which leads to an excited

singlet state will be discussed in terms of the mechanism [124]:

$$\mathrm{T} + \mathrm{T} \;\rightleftharpoons\; (\mathrm{TT}) \;\rightarrow\; \mathrm{S}^{*} \tag{5.3}$$

The initial state manifold $|i_k|$ consists of the set of coupled spin states (nine states in the case of a TT pair) which are coupled together to energy eigenstates depending on the strength and direction of the external magnetic field. The spin Hamiltonian for a triplet exciton consist of two terms: the Zeeman interaction and the dipolar, or zero field, splitting term.

$$\hat{H} = g\beta\mathbf{B}.\mathbf{S} + DS_z^2 + E(S_x^2 - S_y^2) \tag{5.4}$$

where the first term describes the Zeeman interaction and the remaining terms represent the fine structure which results from the interaction between the two magnetic dipoles of the two unpaired electrons. D and E are the zero-field splitting parameters predicted to be $-5.6\,\mathrm{mT}(\pm 1\,\mathrm{mT})$ and $35\,\mathrm{mT}(\pm 1\,\mathrm{mT})$, respectively [123]. The consequence of the second term is to lift the degeneracy of the three triplet sub-levels which would exist at zero field in the absence of the dipolar coupling. The exciton Hamiltonian differs from the molecular one for two reasons. The first is that hyperfine interaction, present in the molecular Hamiltonian, is averaged to zero by rapid motion of the exciton. Secondly, the fine structure tensor for the excitons is an average over the various inequivalent molecules in the crystal structure. The zero-field eigenstates are given by;

$$|x\rangle = \frac{1}{\sqrt{2}}(|-1\rangle - |+1\rangle) \tag{5.5}$$

$$|y\rangle = \mathrm{i}\frac{1}{\sqrt{2}}(|-1\rangle + |+1\rangle) \tag{5.6}$$

$$|z\rangle = |0\rangle \tag{5.7}$$

whose energies are $D - E$, $D + E$ and 0 respectively. The spin states are quantised with respect to the z-axis of the dipolar tensor which is given as an average over all the inequivalent molecules of a unit cell for triplet excitons [125].

At zero field the *pair* eigenstates are given by

$$\text{Singlet}: \quad |S\rangle = \frac{1}{\sqrt{3}}(|xx\rangle + |yy\rangle + |zz\rangle) \tag{5.8}$$

$$\text{Triplets}: \quad |T_x\rangle = \frac{1}{\sqrt{2}}(|yz\rangle - |zy\rangle) \tag{5.9}$$

$$\text{Quintets}: \quad |Q_a\rangle = \frac{1}{\sqrt{2}}(|xx\rangle - |yy\rangle) \tag{5.10}$$

$$|Q_b\rangle = \frac{1}{\sqrt{6}}(|xx\rangle + |yy\rangle - 2\,|zz\rangle) \tag{5.11}$$

$$|Q_x\rangle = \frac{1}{\sqrt{2}}(|yz\rangle + |zy\rangle) \tag{5.12}$$

where the states $|T_y\rangle$, $|T_z\rangle$ and $|Q_y\rangle$, $|Q_z\rangle$ are obtained from $|T_x\rangle$ and $|Q_x\rangle$ by cyclic permutation of x, y, and z [124]. Note that, the singlet pair and quintets are symmetric with respect to spin exchange and the pair triplet states are antisymmetric. In terms of these single-particle functions the singlet pair is $\frac{1}{\sqrt{3}}(|xx\rangle + |yy\rangle + |zz\rangle)$ and hence at zero field only three of the nine states have a singlet component. Application of a weak field ($B_0 <$ zero field splitting (ZFS)) causes the zero-field states to mix resulting in additional pair states with singlet character. This will result in an increase of the rate of triplet annihilation and a subsequent increase in the intensity of delayed fluorescence.

For high-fields, where the Zeeman splitting is large compared to the zero-field splitting, the spin states will now be quantised along the field and are given by [124];

$$|S\rangle = \frac{1}{\sqrt{3}}(|00\rangle - |+-\rangle - |-+\rangle) \tag{5.13}$$

$$|T_0\rangle = \frac{1}{\sqrt{2}}(|+-\rangle - |-+\rangle) \tag{5.14}$$

$$|Q_0\rangle = \frac{1}{\sqrt{6}}(2\,|00\rangle + |+-\rangle + |-+\rangle) \tag{5.15}$$

$$|T_{\pm 1}\rangle = \frac{1}{\sqrt{2}}(|\pm 0\rangle - |0\pm\rangle) \tag{5.16}$$

$$|Q_{\pm 1}\rangle = \frac{1}{\sqrt{2}}(|\pm 0\rangle + |0\pm\rangle) \tag{5.17}$$

$$|Q_{\pm 2}\rangle = |\pm\pm\rangle \tag{5.18}$$

where three of the states have a singlet component, i.e., $|00\rangle$, $|+-\rangle$ and $|-+\rangle$. Hence as the field increases the rate of triplet annihilation decreases to that of the zero-field

case and the intensity of delayed fluorescence will decrease. However, the $|+-\rangle$ and $|-+\rangle$ states are degenerate and the symmetric and antisymmetric combinations will be the true eigenstates in the presence of an arbitrarily weak triplet-triplet interaction. The antisymmetric combination is a pure triplet state; hence there are only two pair states with singlet character. Thus, in the high field limit there are fewer states with singlet character than at zero field and the rate of triplet annihilation reduces to lower than that at zero-field and consequently the intensity of the delayed fluorescence will decrease to below that of the zero-field case.

The general shape expected for an MFE arising from the triplet-triplet mechanism is an increase at low fields, i.e. when the Zeeman splitting is small compared to the dipolar splitting (ZFS), followed by a decrease at higher fields and finally a levelling off at a value below the zero-field value when the magnitude of the Zeeman splitting has exceeded that of the zero-field splitting. Unfortunately, the high field strengths used in reference [123] were unattainable in the MARY apparatus used in this thesis; however, in reference [123] the low field triplet-triplet mechanism effects were shown to a low resolution in anthracene single crystals (Figure 5.30). Here we concentrate on exploring this low-field region in more detail.

In the high field limit, i.e. when the Zeeman splitting is large compared to the dipolar splitting (ZFS) such that the dipolar terms in Equation 5.4 may be treated as a first-order perturbation theory, the only two (symmetric) eigenstates of the pair spin Hamiltonian that have singlet component have energies given by:

$$E_0 = 2(D-E)\cos^2\alpha + 2(D+E)\cos^2\beta \tag{5.19}$$

$$E_1 = D(1+\cos^2\gamma) + E(\cos^2\alpha - \cos^2\beta) \tag{5.20}$$

where α, β and γ are the angles made by $\hat{H}$ and the x, y and z axes, respectively, of the dipolar tensor. Hence, the first order energies now depend on the angles that the magnetic field makes with the x and y principal axes of the dipolar tensor.

These qualitative descriptions of the theory are in accord with the MFEs observed in anthracene single crystals (Figure 5.29) which agree with the previously observed results

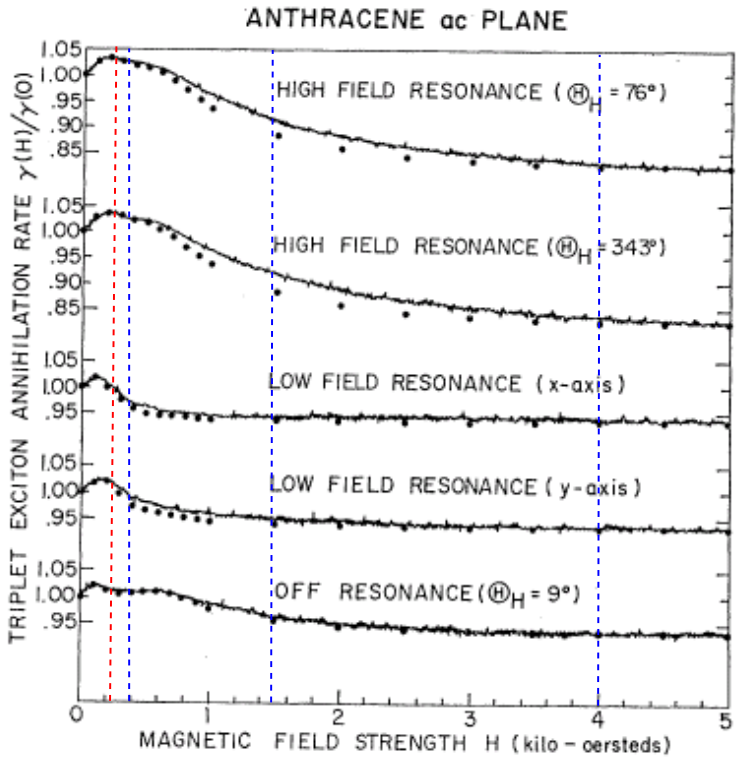

Figure 5.30: Experimental measurements and theoretical calculations (dots) of the field dependence of the triplet annihilation rate for several representative directions in the *ac* plane of anthracene. The x and y axes of the dipolar tensor are at 29.5° and 299.5° respectively. The red dashed line shows the maximum field strengths used in this work and the blue dashed lines show the field strengths at which anisotropy was observed in reference [123]. [Adapted from [123]. Copyrighted by the American Physical Society.]

in reference [123]. Although few points in the low field regime were collected in reference [123] the two sets of data correlate well at low fields. That is, an observed increase in the fluorescence intensity with increasing field strength which reaches a maximum at approximately 20 mT and then subsequently decreases. For the experimental data collected in this work (Figure 5.29), a 'kink' in the MFE curve for parallel orientations is observed ($\approx$ 20 mT and this is also observed in the data obtained from [123] for $\theta = 9°$.

An anisotropy in the triplet annihilation rate has been previously observed in anthracene single crystals at 40 mT, 150 mT and 400 mT [123] in the *ac* plane of the crystal Figure 5.9. These field strengths are higher than those used in this thesis and are shown in Figure 5.30. However, the data presented in Figure 5.29 proves that anisotropy in the magnetic field effects of anthracene single crystals also exists at much lower static field strengths. In fact, the two graphs diverge from 1 mT but the modulation depth is 2 mT. The anisotropy in the anthracene single crystal can be shown as a subtraction of the parallel MFE data from the perpendicular MFE data (Figure 5.31). It can be seen

that anisotropy changes as a function of static field strength, as predicted in [123], and its magnitude changes sign. At field strengths $B_0 < 15\,\mathrm{mT}$ the anisotropy is negative and above this field strength the anisotropy detected is positive. The significance of the field strength at which anthracene single crystals show no anisotropy is unknown but it is in agreement with theoretical predictions [123] and this result is very encouraging when considering anthracene single crystals as model chemical compass systems.

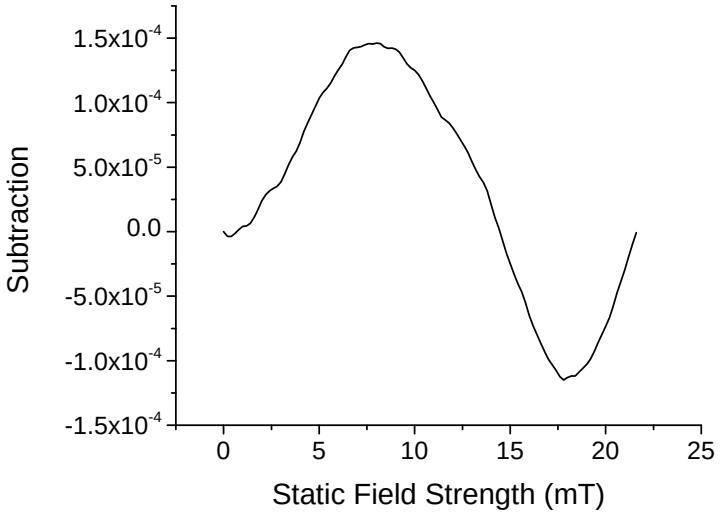

Figure 5.31: The subtraction parallel MFE data from perpendicular MFE data for anthracene single crystals. A 79 Hz, 2.0 mT modulation depth was applied.

5.4 Conclusion

In this chapter, exciplex systems have been investigated for their potential to act as chemical compasses using MARY spectroscopic techniques. Systems investigated used either alignment media or photoselection in order to test for anisotropic field effects. These systems included liquid crystals which were aligned in electric fields; polymer doped films which used photoselection techniques and organic crystals.

A method of aligning liquid crystals was investigated and used to probe anisotropic magnetic field effects in exciplex systems. It was shown that not only could 5CB be used to align radicals, but can itself form part of a RP. Its properties as an electron acceptor, analogous to that of DCB, proved useful when probing the magnetic field effects of long thin aromatic molecules, such as DPB. However, the anisotropic hyperfine couplings within

the 5CB/DPB system were small, and no anisotropic field effects were observed within the S:N of the data. Unfortunately the presence of fast self exchange between $5CB^{\bullet-}$ is likely to destroy any anisotropy which may be observed in the system. 5CB systems with larger more pronounced anisotropic hyperfine couplings, such as fluorinated compounds were investigated, but no MFEs were observed. This was because both molecules will act as electron acceptors (favourable reduction potentials) and therefore RP formation was not favourable.

Photoselection experiments in polymer films were utilised and investigated to probe anisotropic magnetic field effects in exciplex systems. New exciplex systems which exhibit MFEs have been discovered, where the monomer form of PVCz forms part of the RP. These include: C_{60} and fluorinated compounds such as fluorobenzonitriles and perfluoronaphthalene. In polymer films it was shown that despite being able to use RPs with significant anisotropic hyperfine couplings (fluorinated benzonitriles) no anisotropy in the field response could be observed due to self exchange and electron hopping effects.

Further inspection of exciplex systems may shed light into why, despite having very large anisotropic hyperfine coupling, no anisotropy in the magnetic field effect was observed. The requirements for anisotropy to be observed in photoselection experiments are: the hyperfine coupling constants within the RP must be anisotropic; the relative orientation of the donor and acceptor molecules in the exciplex is fixed and that the molecules have a fixed orientation with respect to the externally applied magnetic field. Since the first has already been established to be true, particularly in fluorinated systems, it is likely that no anisotropy is observed because of the random orientation of the acceptor and donor molecules with respect to each other and with respect to the applied magnetic field. In solution, molecules can diffuse freely such that the geometry of the exciplex is one where maximum orbital overlap (see Chapter 4) is achieved. In solids, however, this is not the case because molecules cannot diffuse freely and the relative orientation between the acceptor and donor pair is random. The consequence of the random orientation of the two molecules is that the transition dipole moment of the exciplex is no longer well defined with respect to the hyperfine couplings within the RP and any anisotropy present would be 'averaged' out. In addition to this, the electron hopping mechanism might also

be a contributing factor in the failure to observe any anisotropy in polymer systems. The reason for this is that the original orientation of two molecules when the RP is formed may not correlate to the orientation of the molecules when back electron transfer to form the exciplex occurs. Consider a 3D lattice of repeated monomer units, the RP is created at a given site, site A, via electron transfer: the electron hole will now hop from one monomer unit to another in polyvinylcarbazole with a rate constant of $\approx 4 \times 10^8\,\mathrm{s}^{-1}$ [116] but recombination can only occur from the contact ion pair at site A. However, the electron hole may return to site A on a different carbazole monomer unit with a different orientation to the originally created RP and therefore the transition dipole moment of the emitting exciplex is not well defined with respect to the originally created RP and its corresponding hyperfine coupling tensors. In addition to electron hole hopping effects, self-exchange occurring between dopant molecules will also contribute to the 'averaging' of the hyperfine coupling and hence diminish any anisotropic field response that might otherwise be observed.

For the reasons outlined above, it is speculated that the observation of anisotropic magnetic field effects in exciplex systems in unlikely. However, a promising system investigated was that of the anthracene single crystal. Here, it has been shown the anisotropic nature of the triplet mechanism would result in anisotropic magnetic field effects in fields as low as 1 mT through the measurement of delayed fluorescence. This anisotropic behaviour in anthracene single crystals has also be observed in reference [123] but at much higher field strengths than those used in this thesis and with a lower resolution at low static field strengths $< 10\,\mathrm{mT}$.

An interesting system for future work on investigating model chemical compass systems could build on a combination of these systems, e.g. an aligned polymer in which the triplet mechanism operates. Such a system could be a molecularly imprinted polymer. In previous work, fluorescence anisotropy was shown for a spin-coated sample of anthracene-imprinted polyurethane [126]. It would be interesting to investigate anisotropic magnetic field effects in this kind of system. Another possibility for future work would be to investigate exciplex systems in frozen solution, in particular fluorinated compounds at low concentration, but then the current modulated-MARY apparatus would need to be

redesigned to include a cooling system.

Chapter 6

Angle Modulated Experiment for Lock-In Detection of Anisotropy

In this chapter a progress report is presented which discusses the design and construction of an experiment aimed at measuring the anisotropic field response of an aligned or photoselectively excited biradical system. The experiment is related to the previously employed, Rota-MARY apparatus, [127] which used a rotating magnetic field to detect the anisotropy in the photosynthetic bacterium *Rhodopseudomonas viridis* [128]. In [127], anisotropy experiments were performed by polarising the excitation beam and rotating the magnetic field with respect to the direction of the E-vector of the exciting light using two perpendicular pairs of coil. The concentration of the triplet species being detected (triplet-triplet annihilation mechanism) is modulated by the rotating magnetic field and hence also the emitted light (which is field dependent). The anisotropy of *Rhodopseudomonas viridis* was observed as a function of emission wavelength at various field strengths and as a function of static field strength for fixed emission wavelengths.

In this new experiment, Angle Modulated Experiment for Lock-In Detection of Anisotropy (AMELIA), anisotropy will be detected by measuring changes in fluorescence intensity. Rotation of the field around the sample allows for the comparison of the magnetic field effect in a given direction to the magnetic field effect perpendicular to it, i.e. magnetic field angle modulation, and can therefore measure anisotropy in the sample.

This work was done in collaboration with Jonathan Storey who assisted with the initial

stages of design, including the programming of the graphical interface for the experiment.

6.1 Experimental Procedure

The AMELIA experiment was designed to measure small changes in signal that would be due to the anisotropic field response in the sample. Problems such as these (measuring small changes on a large background) lend themselves to the use of lock-in detection. The theory of lock-in detection is well established but it is useful to examine how it specifically applies to AMELIA in order to understand how anisotropy is detected.

The response of the sample to the field in one direction is the same as the response to the field in the opposite direction, therefore, assuming that there is only two distinct signals one in the 90° and one in the 0° direction (namely when the field is perpendicular and parallel to a given direction in the laboratory frame such as specified by the orientation in a sample) the input signal from the sample, V_{sig}, will be given by;

$$\mathrm{V}_{sig} = I(0^\circ)\cos^2(\omega_s \mathrm{t}) + I(90^\circ)\sin^2(\omega_s \mathrm{t}) \tag{6.1}$$

where $I(0^\circ)$ and $I(90^\circ)$ are the signal intensities for parallel and perpendicular orientations, respectively and ω_s is the frequency of the input signal. From trigonometry the input signal may be written:

$$\mathrm{V}_{sig} = I(0^\circ)\frac{1+\cos(2\omega_s \mathrm{t})}{2} + I(90^\circ)\frac{1-\cos(2\omega_s \mathrm{t})}{2} \tag{6.2}$$

and thus

$$\mathrm{V}_{sig} = \frac{1}{2}([I(0^\circ) + I(90^o)] + [I(0^o) - I(90^\circ)]\cos(2\omega_s \mathrm{t})). \tag{6.3}$$

The LIA receives the input signal and then multiplies it by the lock-in reference using a phase sensitive detector or a multiplier. When a sinusoidal function of frequency, ω_s is multiplied by another sinusoidal function of frequency, $\omega_L \neq \omega_s$ and the product integrated over a time much longer than the period of the two functions, the result tends to zero. In the case when $\omega_s = \omega_L$, and the two functions are in phase, the average value is equal to

half of the product of the amplitudes.

$$\mathrm{V}_{out} = \frac{1}{T}\int_0^T \mathrm{V}_{sig}\mathrm{V}_{lock-in}\,\mathrm{d}t \tag{6.4}$$

where T is the time constant of the LIA and $V_{lock-in}$ is the reference signal generated by the LIA. Using the double frequency mode of the LIA, $\mathrm{V}_{lock-in}$ will be proportional to $\cos(2\omega_s\mathrm{t})$ and the integral then becomes

$$\mathrm{V}_{out} = \frac{1}{2T}\int_0^T ([I(0^\circ) + I(90^o)]\cos(2\omega_s t) + [I(0^o) - I(90^\circ)]\cos^2(2\omega_s\mathrm{t}))\,\mathrm{d}t \tag{6.5}$$

For large T the first part of the integral ($[I(0^\circ) + I(90^o)]\cos(2\omega_s t)$) tends to zero and the second tends to be proportional to I(0°) - I(90°) the anisotropic response.

The experimental apparatus will now be detailed. A block diagram of the system is shown in Figure 6.1. Excitation of the sample is achieved using UV light from a Thermo-Oriel 6293 1000 W Xenon arc lamp which is powered by a Thermo-Oriel 69920 power supply unit and maintains constant power output. A water filter (not shown) absorbs infra-red (IR) radiation and prevents over-heating. Filters are chosen which select the correct wavelength of light for photolysis. Light was directed to and from the sample using 40 mm diameter BG7 glass lenses. The coils (Figure 6.1) are designed to hold the sample firmly in the centre and a mount was designed so that the sample could be easily placed within coils. Sample fluorescence is detected perpendicular to the incoming light and is focused onto a PMT through a filter which selects the correct wavelength for detection of the exciplex emission.

6.1.1 The Coils

The rotating static field is produced by two sets of water cooled Helmholtz coils which were designed and constructed in house. The coils were made using delrin and aluminium, used to create a heat sink, and were water cooled to avoid over heating. The design of the coils were informed by considerations of a minimisation of the inductance, associated with AC fields, a limiting factor for the maximum field strength achievable. The outer

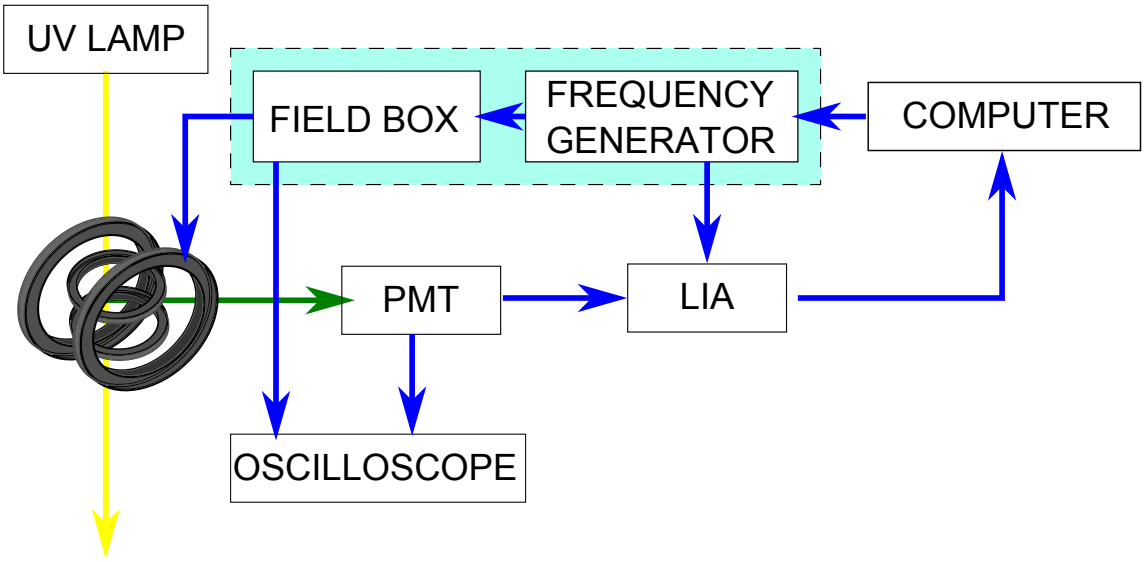

Figure 6.1: Simple block diagram of the AMELIA set up. The yellow arrow represents the excitation beam, which enters the sample from the rear of the coils, and the green arrow represents the emission beam. The wavelength for the emission is varied from sample to sample. The emission is focused onto the photomultiplier tube (PMT) using a glass lens (40 mm) and the corresponding signal is fed to the lock-in amplifier (LIA). Further details are given in Section 6.1.1 - Section 6.1.3.

coil has a radius of 120 mm and the inner coil has a radius 70 mm.

An inductor can store energy in its magnetic field, and tends to resist any change in the amount of current flowing through it. Inductance can be described by the differential equation,

$$V = L\frac{\mathrm{d}I}{\mathrm{d}t} \tag{6.6}$$

where V is the voltage, L is the inductance, I is current and t is time. The inductance is proportional to the field strength;

$$L = \frac{NBA}{I} \tag{6.7}$$

and

$$B = \left(\frac{4}{5}\right)^{3/2} \frac{\mu_0 NI}{R} \tag{6.8}$$

where N is the number of turns, B is the field strength, A is the cross-section area of the coils and R is the coil radius.

The capacity of an inductor is controlled by four factors:

- The number of turns.
- The material that the coil is wrapped around (the core).

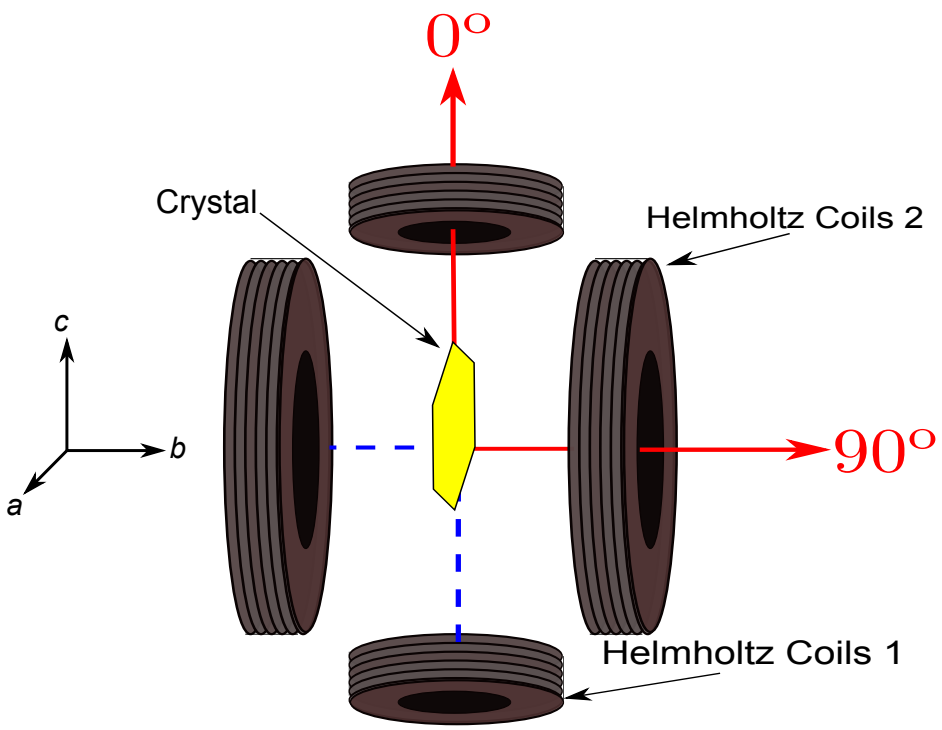

Figure 6.2: Schematic of the coils showing parallel to the *ac* plane of the crystal (0°) and perpendicular to the *ac* plane of the crystal (90°) field directions.

- The cross-sectional area of the coils. A larger area gives a higher inductance.
- The length of the coil.

The magnetic field strength in one coil is given by $B = a\sin(\omega t)$, (where a is the maximum field strength). Since field strength is directly proportional to the current flowing through the coils $I = b\sin(\omega t)$ (where b is the maximum current) and $\mathrm{d}I/\mathrm{d}t = \omega b\cos(\omega t)$. If the voltage, V, supplied to the coils, given by Equation 6.6, is constant and the inductance is high $\mathrm{d}I/\mathrm{d}t$ will be limited. If a high field strength is required ω needs to be small (low frequency). Similarly if a high frequency is required b must be small and hence results in small magnetic field strengths. Working at low frequencies would cause issues with lock-in detection in the experiment because this would mean that longer time constants would be required to gain accurate measurements resulting in a long acquisition time. The only option to gain reasonable field strengths was to decrease the surface area of the coils.

The static field is produced by two time-dependent sinusoidal voltages which are applied to each set of coils. The two sinusoidal voltages have a phase difference of 90° and

the overall field is given by the resultant of the two resulting fields. A schematic of the coils is shown in Figure 6.2.

6.1.2 The Frequency Generator and Field Box

Sinusoidal waves are produced using a RIGOL DG1022 Dual-Channel Function/Arbitrary Waveform Generator which can provide stable, high-precision and low distortion sine signals. The RIGOL waveform generator also has a function to create an external modulation source. This is synchronised to the channel one output of the waveform generator and is connected to the reference wave input of the LIA. The waveform generator is connected to the computer via USB to allow for user control. This means that the experiment can run automatically, sweeping the static field strength, without having to manually change parameters and record results. The two channel outputs of the waveform generator then connect to the two channels of the field box which controls the current supplied to the two pairs of coils. The field box simply acts as a voltage controlled current source and amplifies the small voltages supplied by the waveform generator into the large currents required to create magnetic fields in the coils.

6.1.3 The Graphical User Interface

The graphical interface was designed and programmed by Mr Jonathan Storey. It has the following features:

- Accepts parameters to run the experiment
- Controls the experimental apparatus
- Performs real time averaging
- Saves data and parameters to files

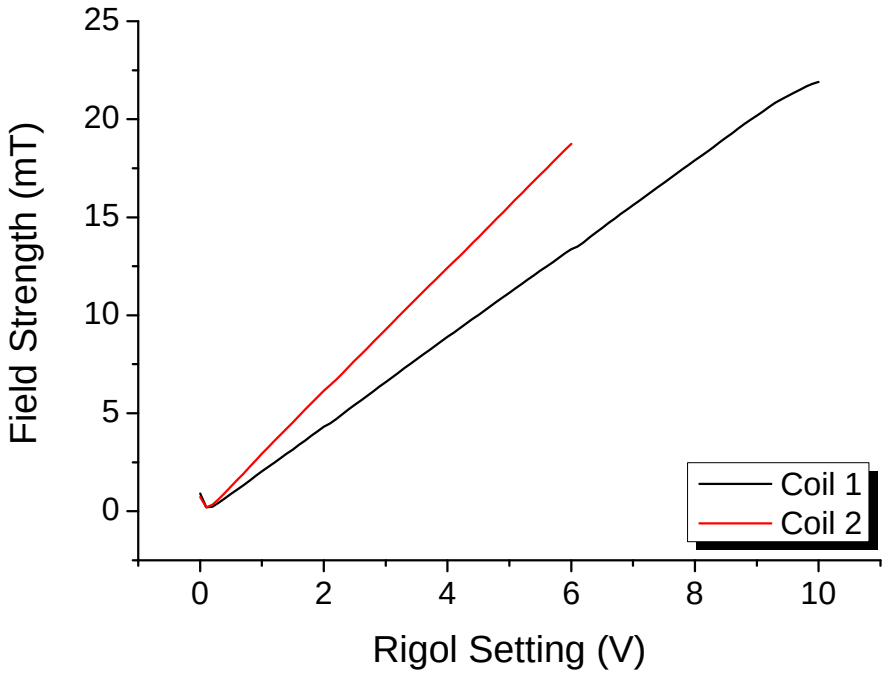

Figure 6.3: Calibration of the magnetic field strength

6.2 Calibration

6.2.1 Static Field Strength

It was first necessary to calibrate the static field strength such that the waveform generator could be programmed to generate two sinusoidal waves which would generate a static magnetic field of constant magnitude in all directions. Firstly, a Gauss meter, connected to the signal input of the LIA, was placed in the sample position (centre of the coils) and its response (LIA signal) recorded as a function of sweeping voltage of the waveform generator (data not shown). The Gauss meter was then connected to the oscilloscope and the field strength was measured for several voltages and a conversion factor between LIA signal intensity and field strength was calculated. Finally, the field strength was plotted as a function of voltage setting on the waveform generator.

6.2.2 Lock-In Amplifier Settings

Frequency

The frequency of the field rotation was optimised at 81 Hz: higher frequencies will lead to lower noise. This is otherwise known as $1/f$-noise (or pink noise) and is characteristic of lock-in amplifiers (Figure 6.4). However, at high frequencies the magnitude of the signal decreases. This is due to the inverse relationship between impedance and frequency:

$$Z = \frac{1}{2\pi f C} \tag{6.9}$$

where Z is the impedance of the capacitor, f the frequency of field rotation and C the capacitance.

Time Constant

The time-constant of the lock-in amplifier is the integration period and selects the setting of the band pass filter of the LIA output, i.e. how much low-frequency noise of the input signal is allowed to pass. The time constant is defined by $1/(2\pi\Delta f)$ where Δf is the frequency bandwidth of the filter (Figure 6.4). If the time constant is large Δf will be small. The notion of time constant arises from the fact that the actual output is supposed to be a DC signal. A Low-Pass filter actually corresponds to a time averaging of the signal. If there is a change in the signal, a longer time constant is required for the averaging to settle to a stable result. An infinitely sharp filter would imply an infinitely long time constant. Thus, there is a trade off between the short time-scale of a measurement, and how much noise the data can tolerate.

Wait Factor

The wait factor determines how long the program waits between measurements of the signal intensity at each field strength. The wait factor was investigated for two types of data sampling, random and non-random (Figure 6.5). The response of the gauss meter was recorded as a function of field strength. The data clearly shows that in the case of random sampling there is noise in the spectra unless the wait factor is longer than 210 ms

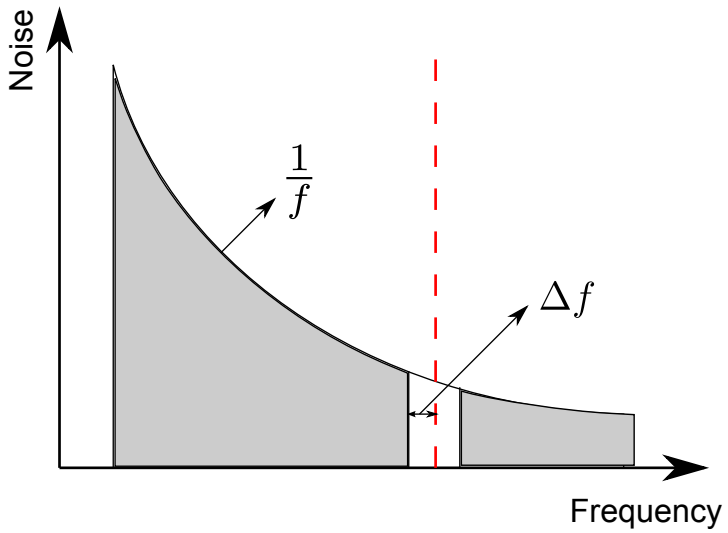

Figure 6.4: The magnitude of noise in the input signal as a function of frequency. The time constant selects the width of the band pass filter whose purpose is to reject noise at lower and higher frequencies. The red dashed line shows the modulation frequency (frequency of field rotation).

whilst for linear sampling there is little noise in the data even for a wait factor of 30 ms. It can also be seen that for linear sampling there is a non-linearity at low static field strengths.

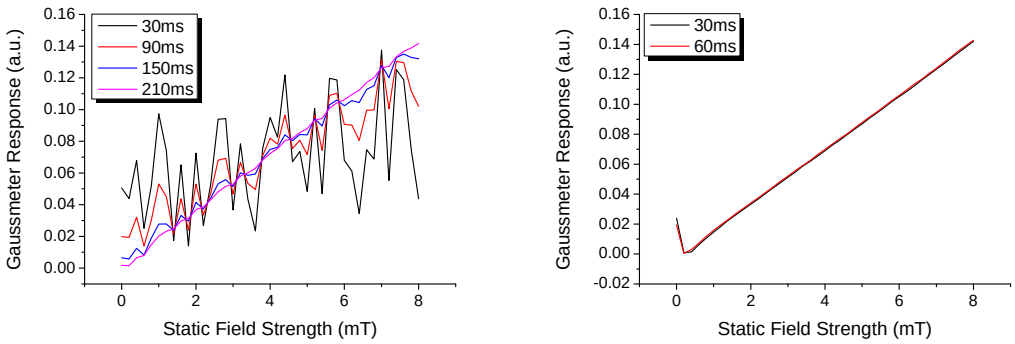

(a) Random Sampling (b) Linear Sampling

Figure 6.5: Optimisation of the wait factor (legend) for two different methods of data sampling.

To remove this non-linearity the pre-run wait factor (the time period between each average run) was optimised, Figure 6.6. This is the time the program waits between averages and is necessary to allow the signal output of the LIA to reach its true value. The pre-wait factor was varied whilst the wait factor was fixed at 30 ms for linear data sampling. The data clearly shows that when the pre-run wait factor is much larger than the wait factor (5 times) the deformation at low static field strengths is removed.

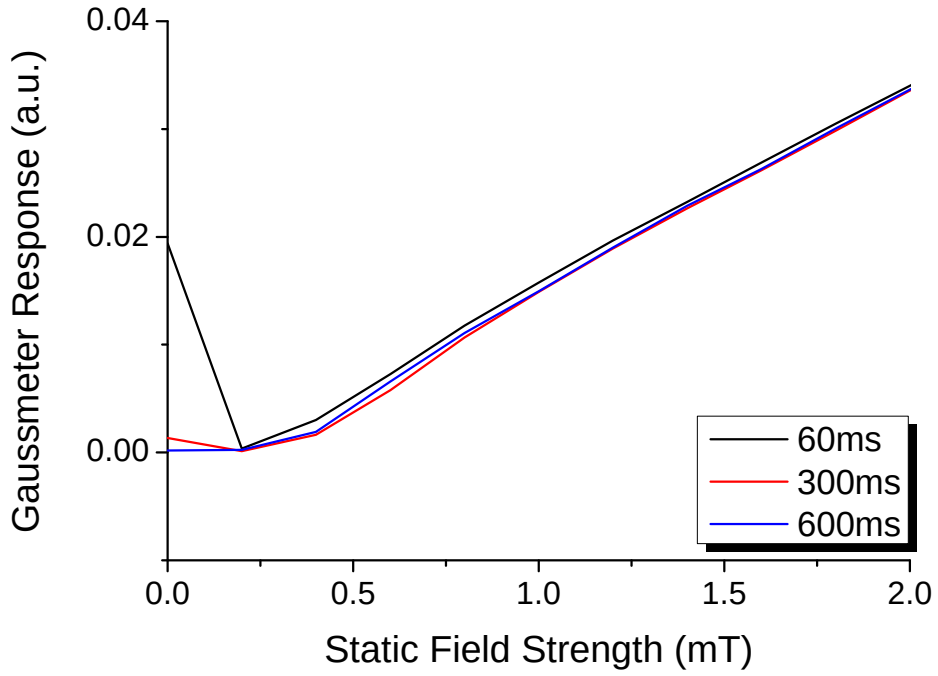

Figure 6.6: Pre-run wait factor (legend) optimisation with linear sampling for a wait factor 30 ms.

6.3 Preliminary Results

Preliminary tests were performed using isotropic solutions to verify that the apparatus was calibrated and to investigate the sensitivity limits of the experiment. Firstly, each pair of coils were connected in turn and a field sweep experiment (MARY) was performed to see if an MFE curve would be observed (Figure 6.7). In this situation, the static field strength in one direction (determined by the disconnected coils) is zero and therefore the corresponding signal intensity in the given direction is zero. The signal observed will therefore be determined by the static field strength through one set of coils, i.e. analogous to a MARY experiment. However, because there is an AC current applied to the coils, at a given field strength, B_0, the static field strength will oscillate around zero with a maximum and minimum of B_0 and $-B_0$, respectively. In contrast, when both coils are connected the field strength will rotate around the sample with a given frequency, f, and the anisotropic response will be measured.

Experiments were performed using Py/1,3-DCB (0.4 mM/40 mM) in CH:ACN (9:1), a system previously shown to exhibit large MFEs (Chapter 4). The solution was circulated using a flow cell to prevent degradation of the sample. A wait factor of 7 s was used to

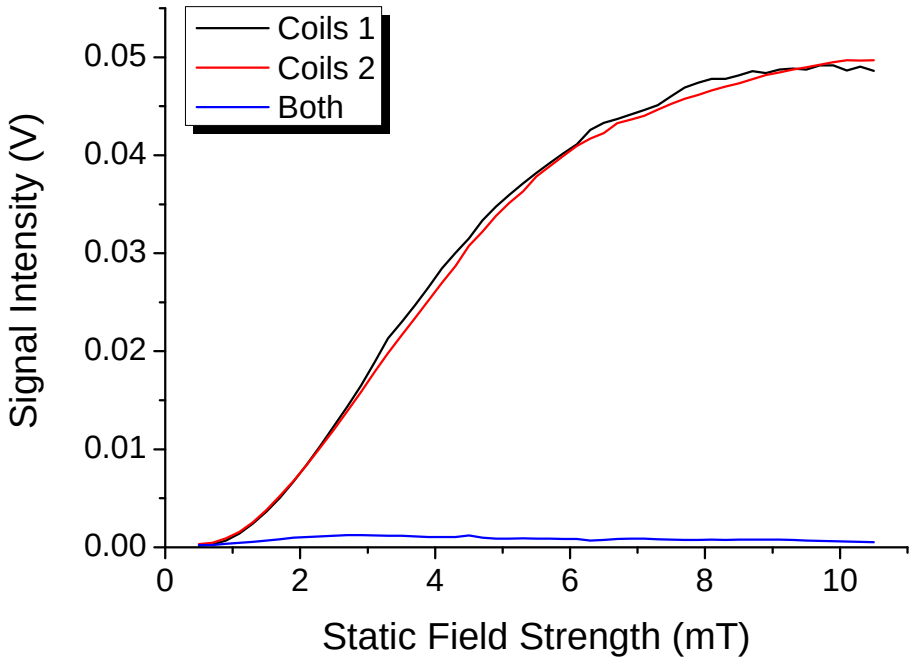

Figure 6.7: AMELIA experiments performed on a Py/DCB (ACN:CH(1:9)) solution with Helmholtz Coils 1 and Helmholtz Coils 2 connected and with both coils connected simultaneously. UV excitation was used and a 507 nm filter was employed for detection of fluorescence emission. The time constant, t = 3 s, wait factor = 7 s and pre-run wait factor = 15 s.

reduce noise in the sample and allow for the signal to reach its true value and a 15 s pre-run wait factor was used such that the signal would settle between average runs (field sweeps). It was necessary to use longer wait factors than those used in calibration experiments because there was a much lower S:N when using a fluorescent sample compared with using a Gaussmeter.

The data (Figure 6.7) show that the MFE plot obtained when the two pairs of coils were connected independently of each other (i.e. one pair of Helmholtz coils are connected and the other pair is disconnected) are identical within the S:N. This is very pleasing and demonstrates that the coils are accurately calibrated.

A comparison between the MFE curves obtained using Modulated-MARY and AMELIA apparatus is shown in Figure 6.9. This shows that the two curves have an approximately similar shape within the field strengths investigated. The expected shape of the MFE curves observed using Modulated-MARY and AMELIA apparatus were simulated (Figure 6.8) and the results are shown in Figure 6.10. It was assumed that the MFE of a RP exhibits a shape which can be described by a Lorentzian, assuming that

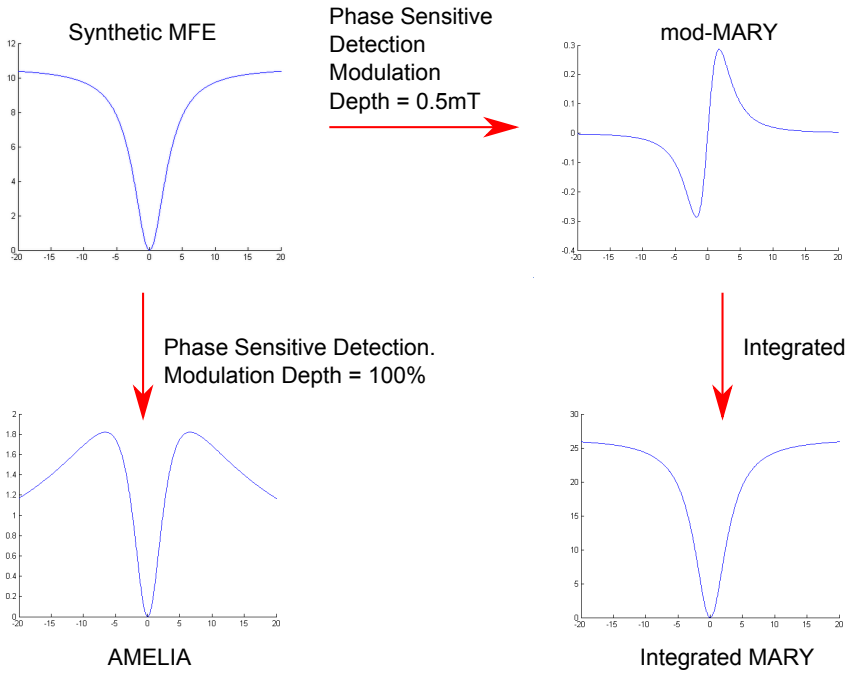

Figure 6.8: Method for simulating MFE curves observed using AMELIA and Modulated-MARY apparatus.

no LFE is observed, with a given intensity and width. The MFE curve observed using Modulated-MARY is simulated by applying a static field modulation which oscillates around a static field strength B_0 with a amplitude equal to the modulation depth, ΔB = 0.5 mT, to obtain a first derivative spectrum and subsequently integrating the curve to obtain the MFE. The MFE curve observed using AMELIA was simulated by applying a static field modulation which for a given field strength, B_0, oscillates about zero with an amplitude B_0. It can be seen that the agreement between experimental and simulated results is very strong.

A third experiment was performed on Py/1,3-DCB (0.4 mM/40 mM) in CH:ACN (9:1) solution with both pairs of Helmholtz coils connected. This was to verify that the anisotropic response would be zero, as expected for an isotropic solution whose MFE would be the same magnitude, regardless of direction. This data is also shown in Figure 6.7 (blue line). It can be clearly seen that anisotropy (measured when both pair of Helmholtz coils were connected) is indeed approximately zero within the error ± 4.8%.

The same experiments, with Helmholtz Coils 1 and Helmholtz Coils 2 connected independently and with both coils connected together, were performed using an anthracene

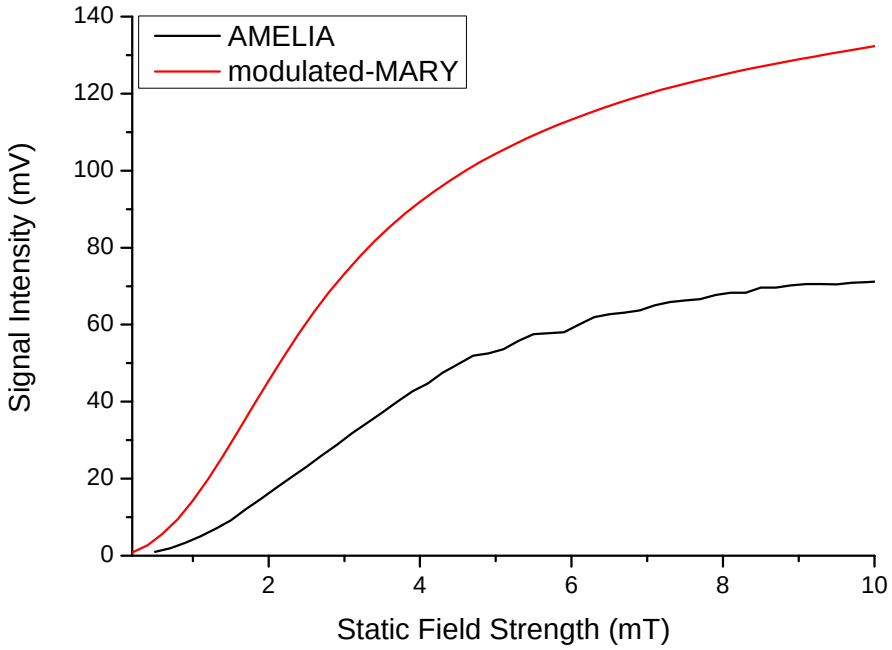

Figure 6.9: Modulated-MARY experiment of Py/1,3-DCB in CH:ACN (9:1) plotted with the MARY plots obtained using AMELIA apparatus.

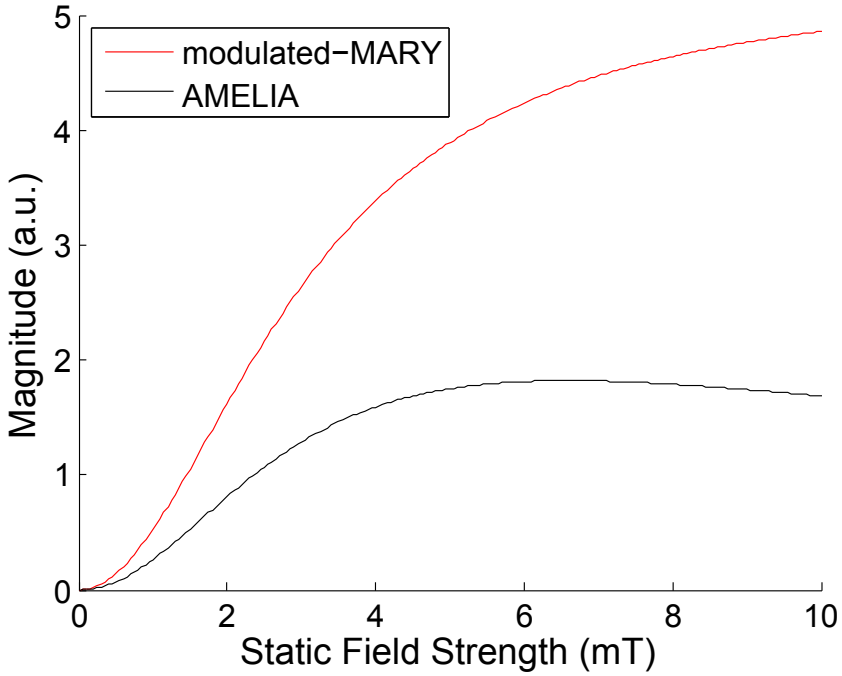

Figure 6.10: Simulated MFE curves for Modulated-MARY and AMELIA apparatus.

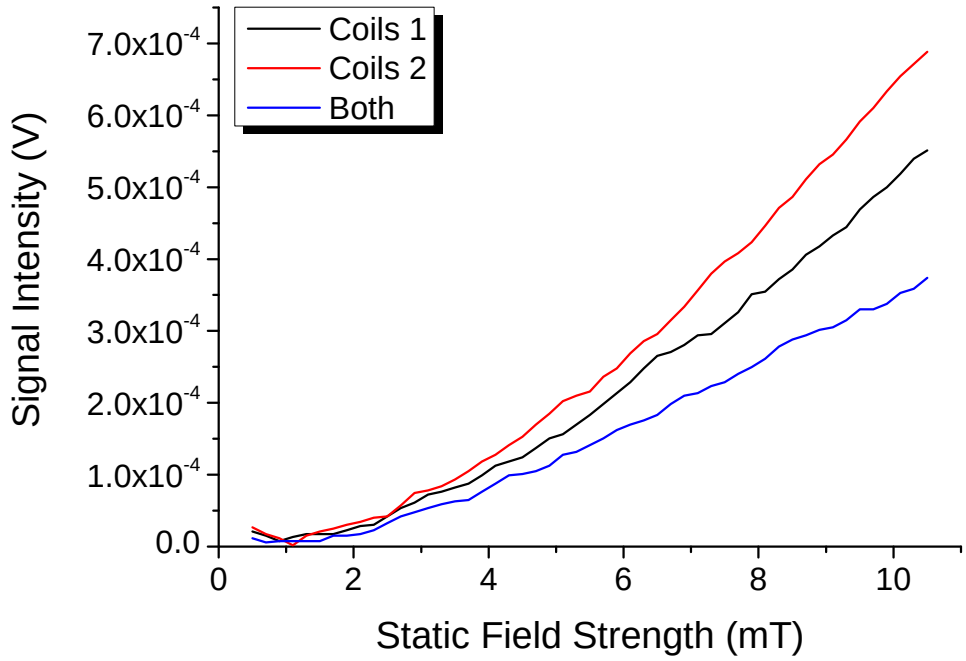

Figure 6.11: AMELIA experiments performed on an anthracene single crystal with Helmholtz Coils 1 and Helmholtz Coils 2 connected independently and with both pairs of coils connected together. UV excitation was used and a 450 nm filter was employed for detection of fluorescence emission. The time constant, $t = 3$ s, wait factor = 7 s and pre-run wait factor = 15 s.

single crystal. The same parameters, time constant, $t = 3$ s, wait factor = 7 s and pre-run wait factor = 15 s, were used as for the isotropic solution. The sample was excited using UV light and a 450 nm was employed for detection of monomer fluorescence, Figure 6.11. The data show that the MFE intensity, measured with each pair of coils connected independently, increases with increasing field strength but does not saturate within the field strengths investigated. In the case where both pairs of Helmholtz coils are connected a non-zero signal is observed demonstrating some anisotropy of the magnetic response of the single crystal. This is seen to increase with increasing static field strength. A subtraction of the data when the pair of Helmholtz Coils 1 and Helmholtz Coils 2 are connected independently shows that the subtraction signal will increase with increasing static field strength (Figure 6.12).

Comparing the results obtained using the AMELIA with those obtained using the Modulated-MARY apparatus shows some interesting similarities. When the pair of Helmholtz coils 1 is connected and Helmholtz coils 2 are disconnected the magnetic field is perpendicular to the *ac* plane of the single crystal (Figure 6.2). This is also true

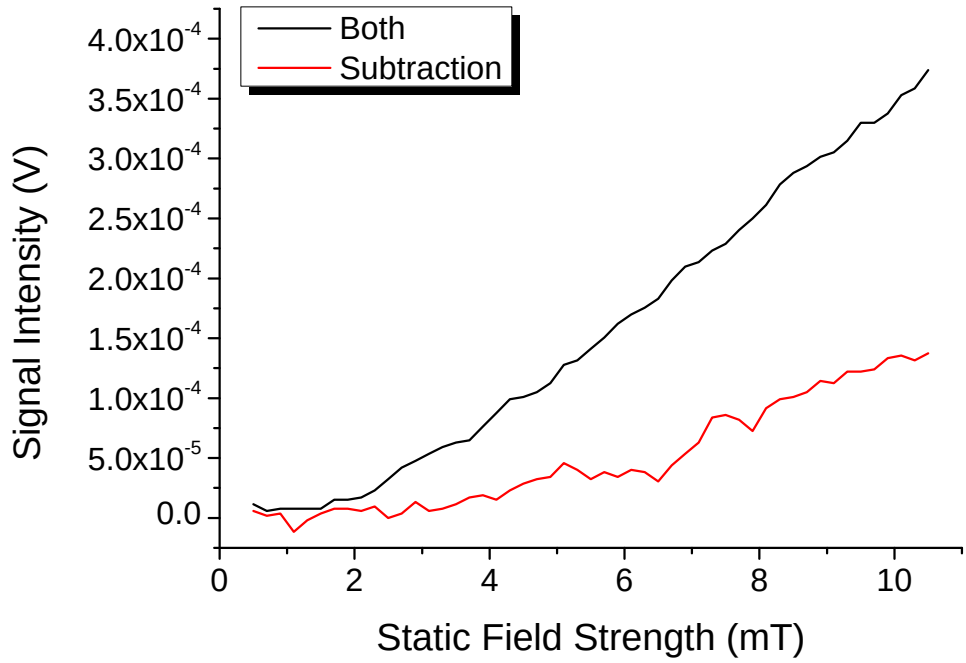

Figure 6.12: The AMELIA signal when both magnetic field coils are connected (black) and the AMELIA signal obtained by a subtraction of the data when Coil 1 and Coil 2 are connected independently (red) for an anthracene single crystal.

for the magnetic field in perpendicular orientations in the Modulated-MARY experiment (Figure 5.29). When the Helmholtz coils 2 are connected and Helmholtz coils 1 are disconnected the magnetic field is parallel to the *ac* plane of the anthracene single crystal which is equivalent to parallel orientations in the Modulated-MARY experiment (Figure 5.29).

Comparison of MFE plots obtained for AMELIA and Modulated-MARY experiments (Figure 6.13) show that different MFE plots are observed when the magnetic field is parallel or perpendicular to the *ac* plane of the crystal. The agreement between the shapes of the MFE plots obtained for each experiment is very pleasing. For both experiments it can be seen that MFE is larger when the magnetic field is parallel to the *ac* plane of the crystal (Coil 2 for AMELIA). In both cases it can be seen that the MFE is still rising at a static field strength 10 mT and there is a significant difference between the magnitude of the MFEs obtained when the magnetic field is parallel or perpendicular to the *ac* plane of the anthracene single crystal. However, in the data obtained using Modulated-MARY it can be seen that anisotropy in the MFE exists at static field strengths of 2 mT whilst the data obtained using AMELIA no anisotropy can be seen for static field strengths less than

3.5 mT. A reason for this discrepancy in these field strengths is because of the different modulation techniques used, as detailed above Figure 6.8.

The anisotropy data obtained using AMELIA (Figure 6.11) was compared with the anisotropy data obtained by subtracting MFE curves in parallel and perpendicular orientations using Modulated-MARY (Figure 5.31) experiments. The data shows that for static field strengths below 4 mT the plots are very similar but above this field strength the curves are different. The anisotropy in an anthracene single crystal is still rising at a static field strength 10 mT, whilst the anisotropy observed using Modulated-MARY experiments rises, reaches a maximum at 8 mT and subsequently starts to decrease. The reason for this discrepancy is because the anisotropy measured in AMELIA is not a comparison of the signal intensity of the parallel and perpendicular orientations but the anisotropy of all angles. Nonetheless, both curves confirm, without doubt, the presence of anisotropy in anthracene single crystals which is in agreement with previous results [123].

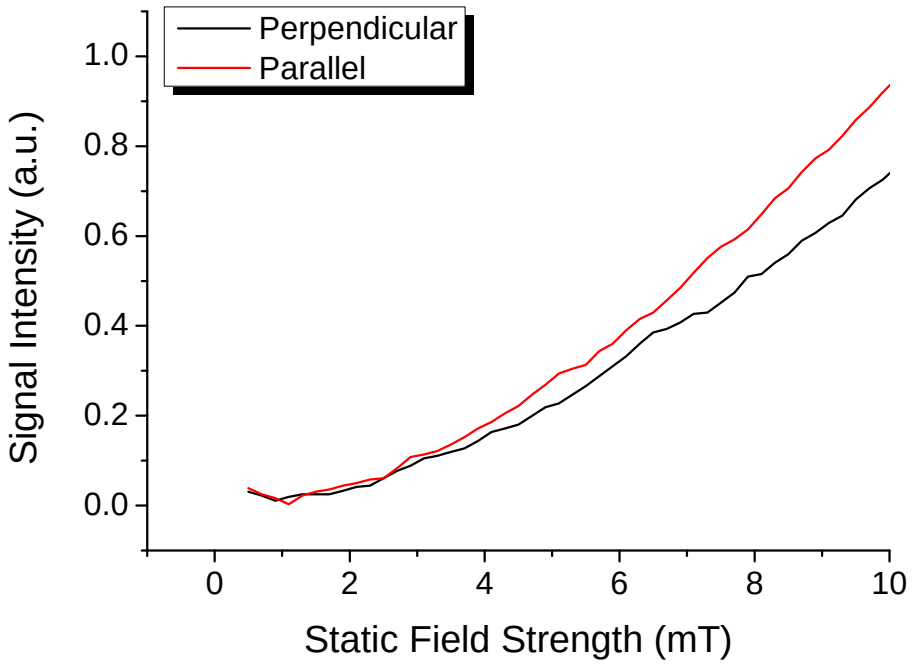

(a) AMELIA

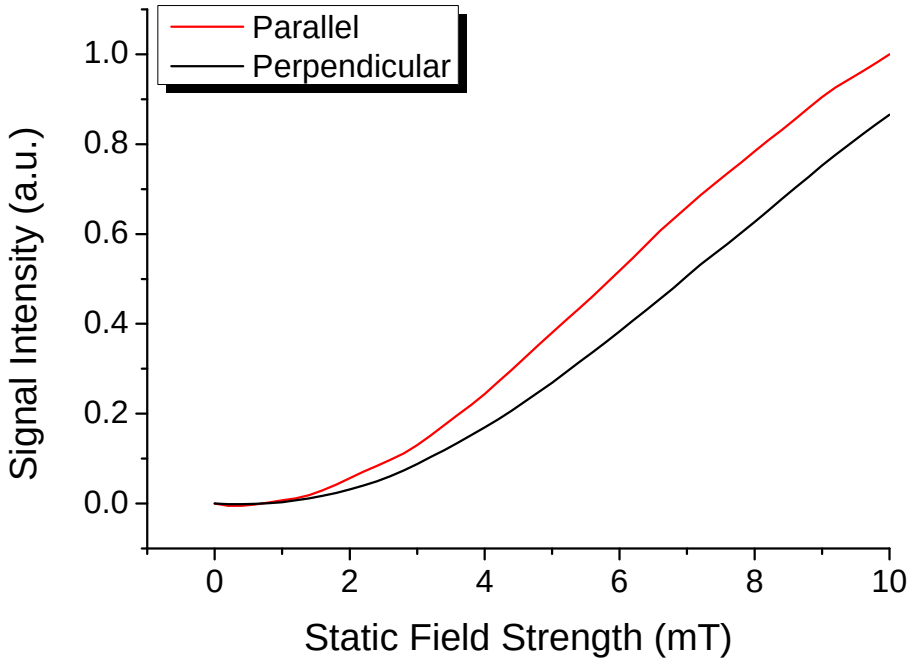

(b) Modulated-MARY

Figure 6.13: Normalised MFE plots obtained using AMELIA (a) and Modulated-MARY (b) for a anthracene single crystal. Parallel and perpendicular plots obtained using AMELIA correspond to the magnetic field being parallel or perpendicular *ac* plane, respectively of the single crystal. Parallel and perpendicular plots obtained using MARY correspond to the magnetic field parallel to the *ac* and *bc* plane, respectively of the single crystal.

6.4 Conclusion

In this chapter the design and development of a novel experiment, AMELIA, which measures directly the anisotropic magnetic field effect, is presented. Using isotropic solutions it was possible to show that the apparatus are well calibrated and the field effects measured are understood and reproduced well using synthetic and simulated data. Using the anthracene crystals, previously shown to exhibit anisotropic field effects at high fields (100 mT - 400 mT) in flashphotolysis studies and in low fields (2 mT to 23 mT) using modulated-MARY studies, AMELIA has been shown to enable the direct measurement of the field effect anisotropy. Unlike in the Modulated MARY experiment, there is no need to move the sample for different field orientations thereby significantly reducing the operator-associated error on the measurements. Any signal observed in the AMELIA experiment is due to an anisotropic field effect whereas all other previous methods (with the notable exception of rota-MARY based on TA detection [128]) rely on the small modulation of a large signal with the relative angle between the field and the radical pair under study. The single crystal anthracene used here for 'proof of principle' studies will, in future, be of little interest as a chemical compass since the typical low field effects of interest are only observed in systems whose magnetosensitivity is dominated by the hyperfine coupling mechanism.

However, the results presented in this thesis are pointing towards other promising chemical systems that might benefit from the application of AMELIA, such as fluorinated compounds (fluorobenzonitrile) covalently connected to an electron donor (in analogy to the Py/DMA systems originally synthesized and investigated by Weller) in frozen solutions (and low concentrations so that exchange processes do not quench the anisotropic response as found in the polymer systems discussed). For that, AMELIA needs to be modified so as to allow for cooling of the sample cell. Another exciting development is the use of flavin incorporating hen egg white lysozyme single crystals. In solution FMN (flavin mononucleotide) and HEWL (hen egg white lysozyme) are known to exhibit large MFEs [129]. If the flavin is incorporated in specific binding sites within the single crystal, anisotropic magnetic field effects should be detectable. However, presently, the single

crystals cannot be grown to larger than 0.4 mm. Hence, the sensitivity of the apparatus will have to be further improved. Possible solutions include the redesign of the coils to allow for double modulation techniques, i.e. modulated field strength and modulated field angle, which will lead to a further increase of the apparatus sensitivity.

Appendix A

RotRYDMR Data

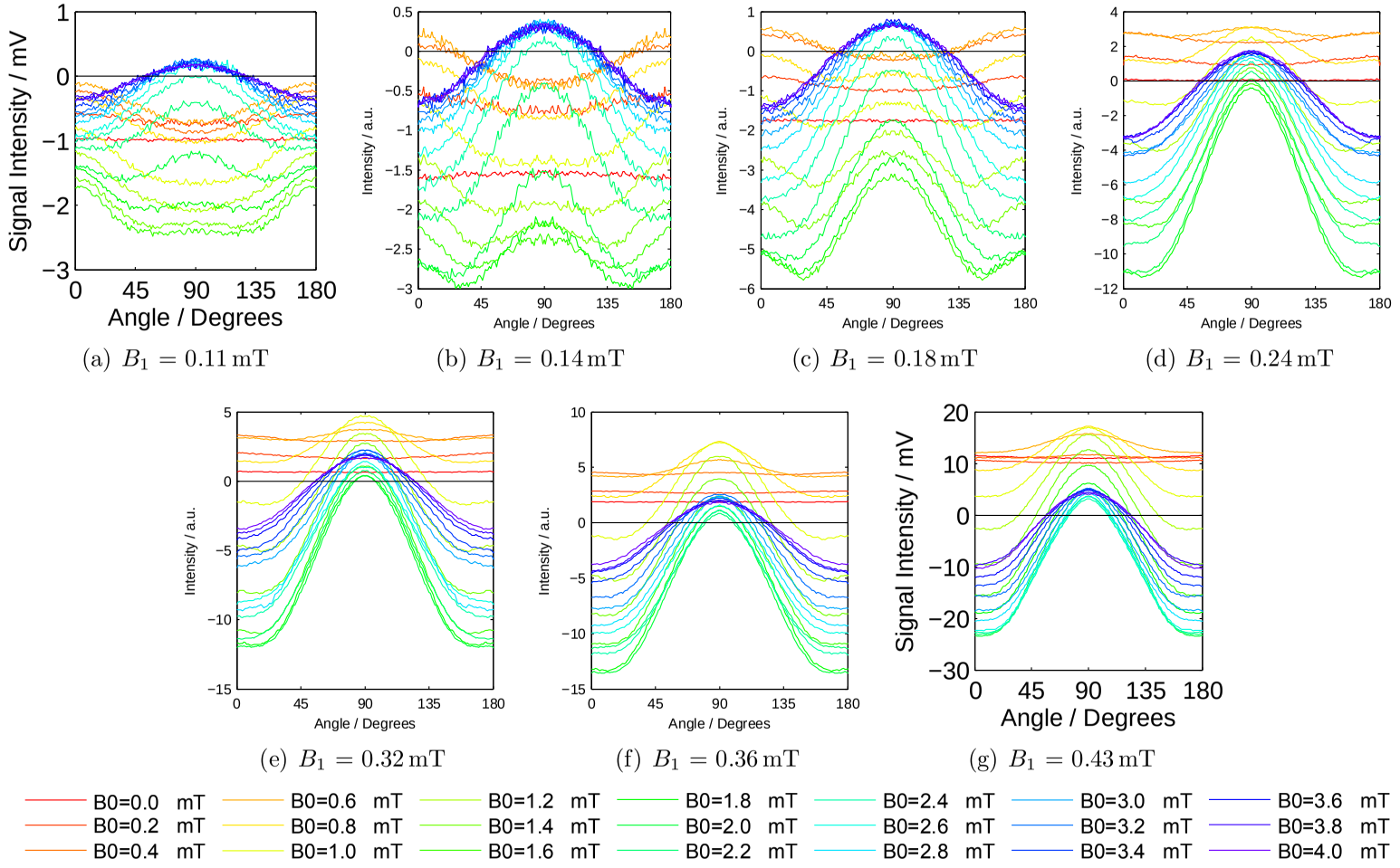

(a) $B_1 = 0.11\,\mathrm{mT}$ (b) $B_1 = 0.14\,\mathrm{mT}$ (c) $B_1 = 0.18\,\mathrm{mT}$ (d) $B_1 = 0.24\,\mathrm{mT}$

(e) $B_1 = 0.32\,\mathrm{mT}$ (f) $B_1 = 0.36\,\mathrm{mT}$ (g) $B_1 = 0.43\,\mathrm{mT}$

Figure A.1: Experimental rot-RYDMR results for $\mathrm{Py_{h10}}$/1,3-DCB. B_0 field strengths ranging from 0.0 - 4.0 mT are shown within panels. Spectra were recorded for different B_1 field strengths, 0.11 mT - 0.43 mT, shown in different panels.

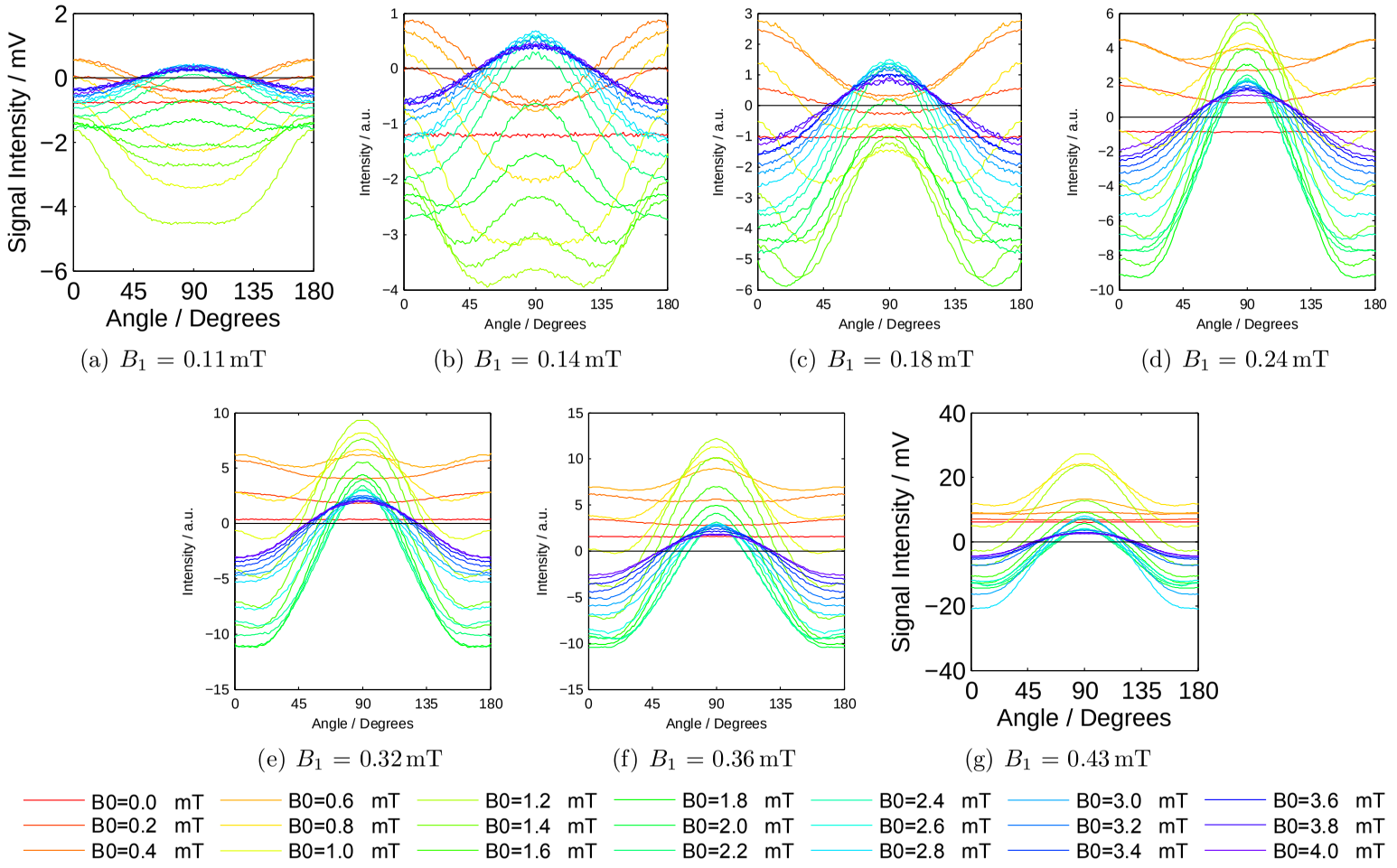

(a) $B_1 = 0.11\,\mathrm{mT}$ (b) $B_1 = 0.14\,\mathrm{mT}$ (c) $B_1 = 0.18\,\mathrm{mT}$ (d) $B_1 = 0.24\,\mathrm{mT}$

(e) $B_1 = 0.32\,\mathrm{mT}$ (f) $B_1 = 0.36\,\mathrm{mT}$ (g) $B_1 = 0.43\,\mathrm{mT}$

Figure A.2: Experimental rot-RYDMR results for $\mathrm{Py_{d10}}$/1,3-DCB. B_0 field strengths ranging from 0.0 - 4.0 mT are shown within panels. Spectra were recorded for different B_1 field strengths, 0.11 mT - 0.43 mT, shown in different panels.

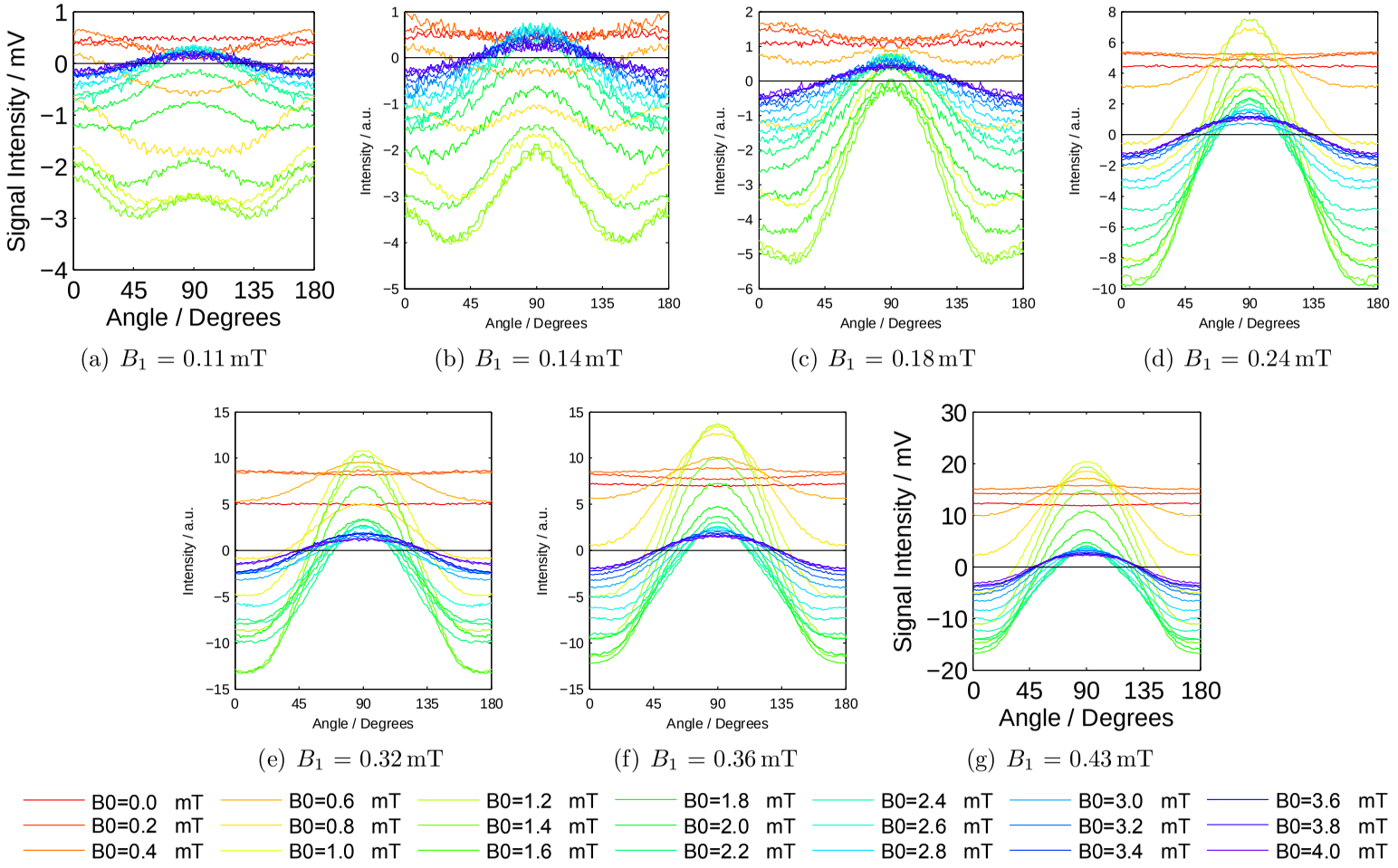

(a) $B_1 = 0.11\,\mathrm{mT}$ (b) $B_1 = 0.14\,\mathrm{mT}$ (c) $B_1 = 0.18\,\mathrm{mT}$ (d) $B_1 = 0.24\,\mathrm{mT}$

(e) $B_1 = 0.32\,\mathrm{mT}$ (f) $B_1 = 0.36\,\mathrm{mT}$ (g) $B_1 = 0.43\,\mathrm{mT}$

Figure A.3: Experimental rot-RYDMR results for $\mathrm{Chy_{h12}}$/1,4-DCB. B_0 field strengths ranging from 0.0 - 4.0 mT are shown within panels. Spectra were recorded for different B_1 field strengths, 0.11 mT - 0.43 mT, shown in different panels.

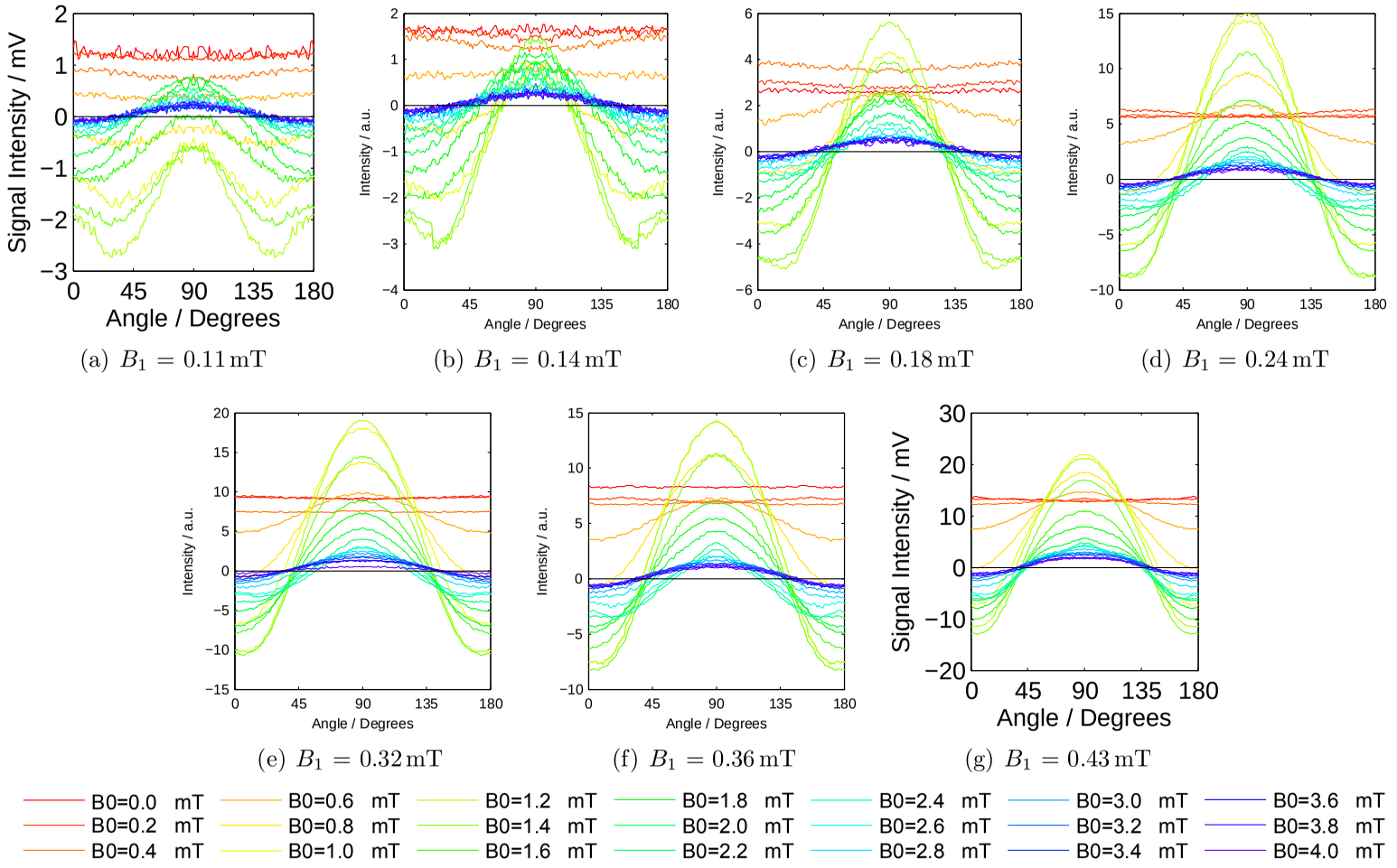

(a) $B_1 = 0.11\,\mathrm{mT}$ (b) $B_1 = 0.14\,\mathrm{mT}$ (c) $B_1 = 0.18\,\mathrm{mT}$ (d) $B_1 = 0.24\,\mathrm{mT}$

(e) $B_1 = 0.32\,\mathrm{mT}$ (f) $B_1 = 0.36\,\mathrm{mT}$ (g) $B_1 = 0.43\,\mathrm{mT}$

Figure A.4: Experimental rot-RYDMR results for $\mathrm{Chy}_{\mathrm{d12}}$/1,4-DCB. B_0 field strengths ranging from 0.0 - 4.0 mT are shown within panels. Spectra were recorded for different B_1 field strengths, 0.11 mT - 0.43 mT, shown in different panels.

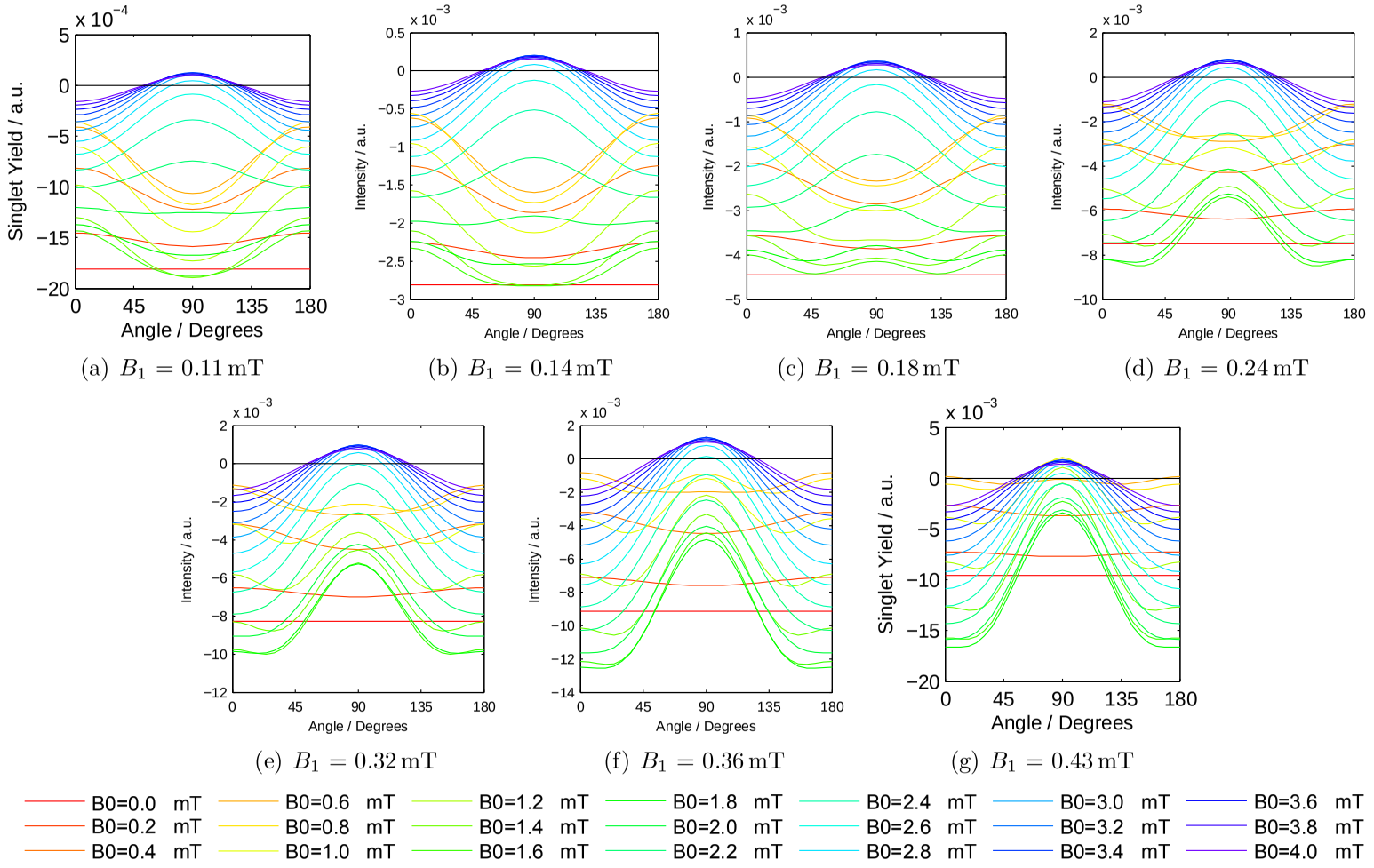

(a) $B_1 = 0.11\,\mathrm{mT}$ (b) $B_1 = 0.14\,\mathrm{mT}$ (c) $B_1 = 0.18\,\mathrm{mT}$ (d) $B_1 = 0.24\,\mathrm{mT}$

(e) $B_1 = 0.32\,\mathrm{mT}$ (f) $B_1 = 0.36\,\mathrm{mT}$ (g) $B_1 = 0.43\,\mathrm{mT}$

Figure A.5: Theoretical rot-RYDMR results for $\mathrm{Py_{h10}}$/1,3-DCB, $k = 86.16\,\mu\mathrm{s}^{-1}$. B_0 field strengths ranging from 0.0 - 4.0 mT (legend) are shown within panels. Spectra were calculated for different B_1 field strengths, 0.11 mT - 0.43 mT, shown in different panels.

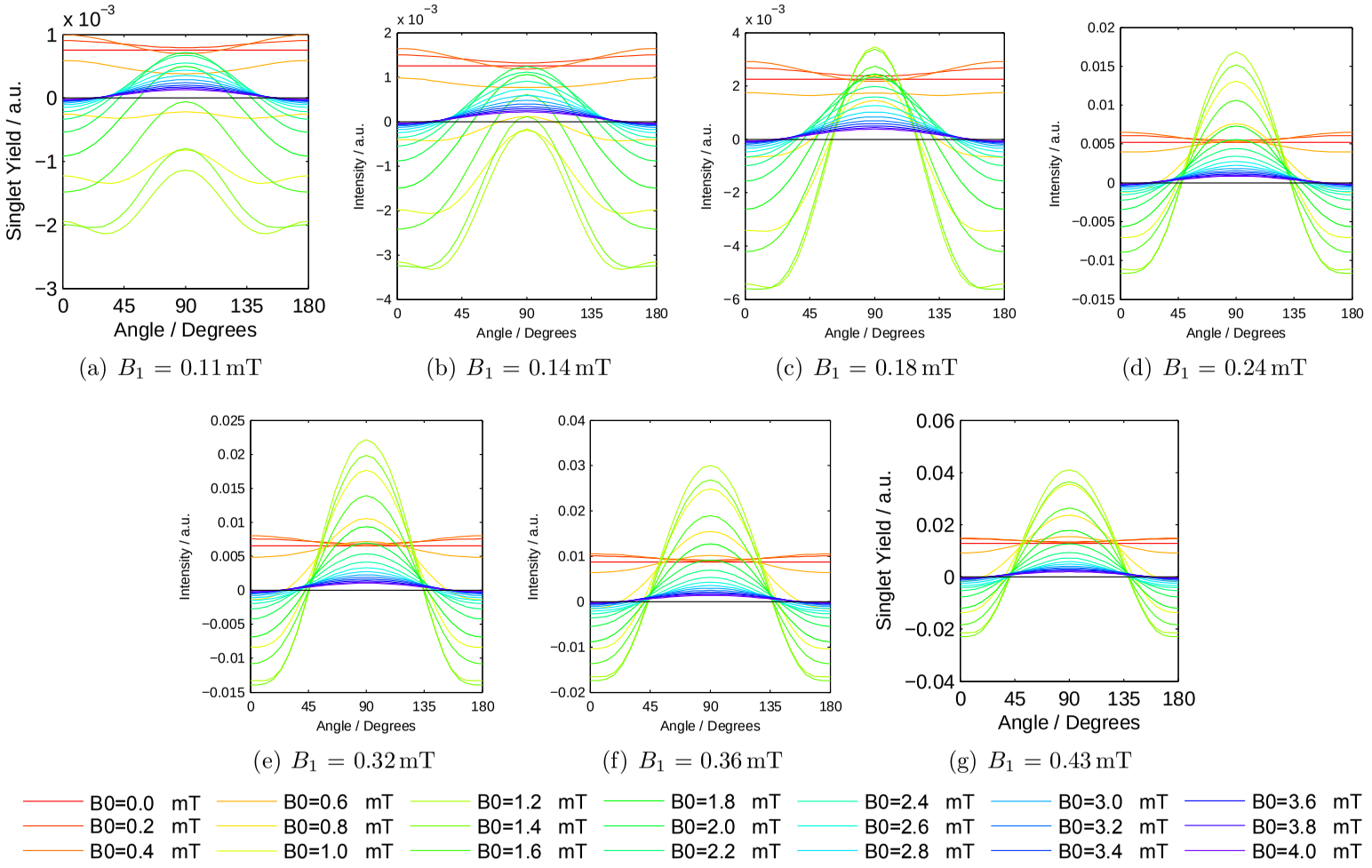

(a) $B_1 = 0.11\,\mathrm{mT}$ (b) $B_1 = 0.14\,\mathrm{mT}$ (c) $B_1 = 0.18\,\mathrm{mT}$ (d) $B_1 = 0.24\,\mathrm{mT}$

(e) $B_1 = 0.32\,\mathrm{mT}$ (f) $B_1 = 0.36\,\mathrm{mT}$ (g) $B_1 = 0.43\,\mathrm{mT}$

Figure A.6: Theoretical rot-RYDMR results for $\mathrm{Chy_{d12}}$/1,4-DCB, $k = 55.34\,\mu\mathrm{s}^{-1}$. B_0 field strengths ranging from 0.0 - 4.0 mT (legend) are shown within panels. Spectra were calculated for different B_1 field strengths, 0.11 mT - 0.43 mT, shown in different panels.

Appendix B

RYDMR Data

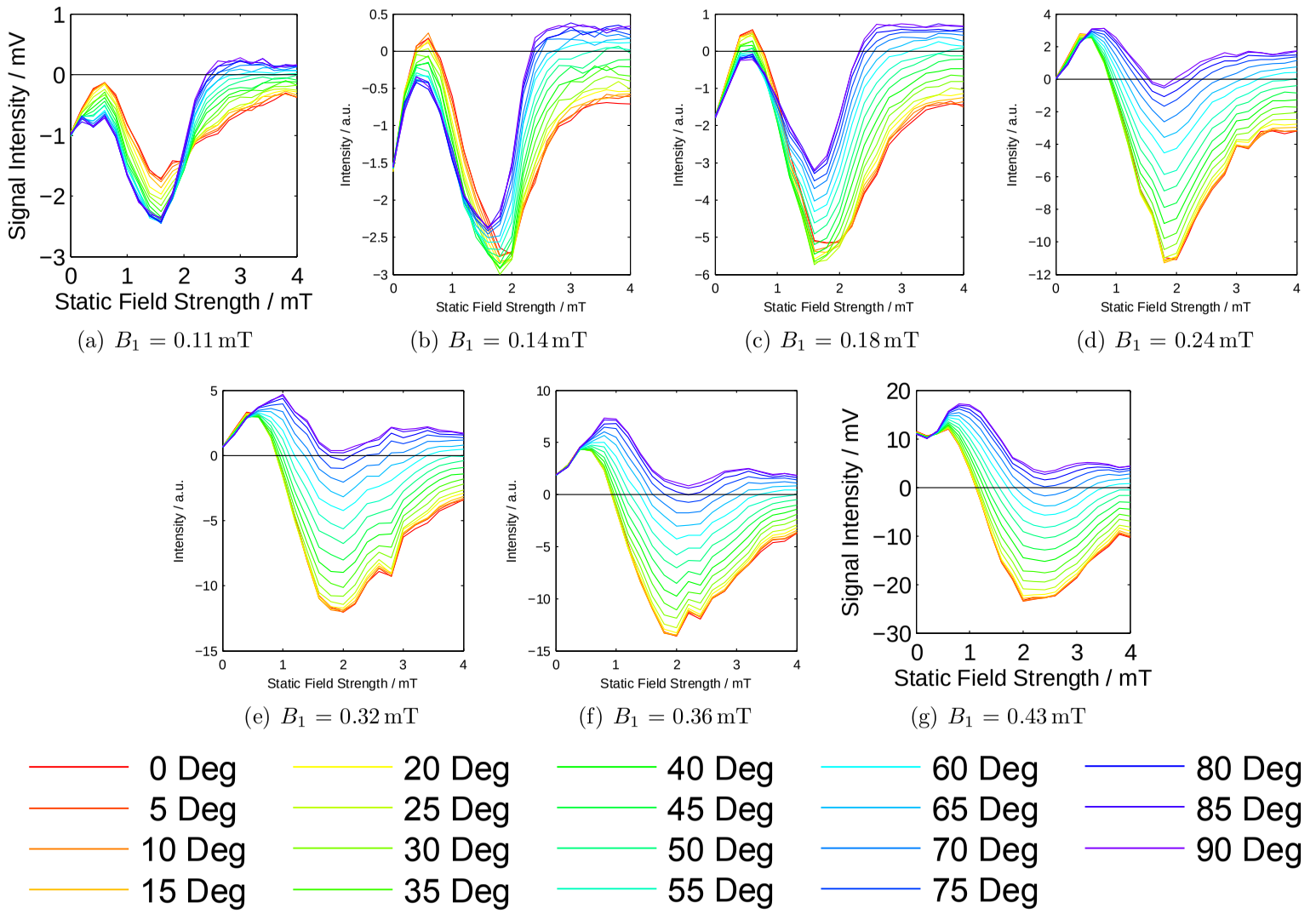

(a) $B_1 = 0.11\,\mathrm{mT}$ (b) $B_1 = 0.14\,\mathrm{mT}$ (c) $B_1 = 0.18\,\mathrm{mT}$ (d) $B_1 = 0.24\,\mathrm{mT}$

(e) $B_1 = 0.32\,\mathrm{mT}$ (f) $B_1 = 0.36\,\mathrm{mT}$ (g) $B_1 = 0.43\,\mathrm{mT}$

Figure B.1: Experimental RYDMR results for Py_{h10}/1,3-DCB. B_0 field strengths ranging from 0° - 90° are shown within panels. Spectra were recorded for different B_1 field strengths, 0.11 mT - 0.43 mT, shown in different panels.

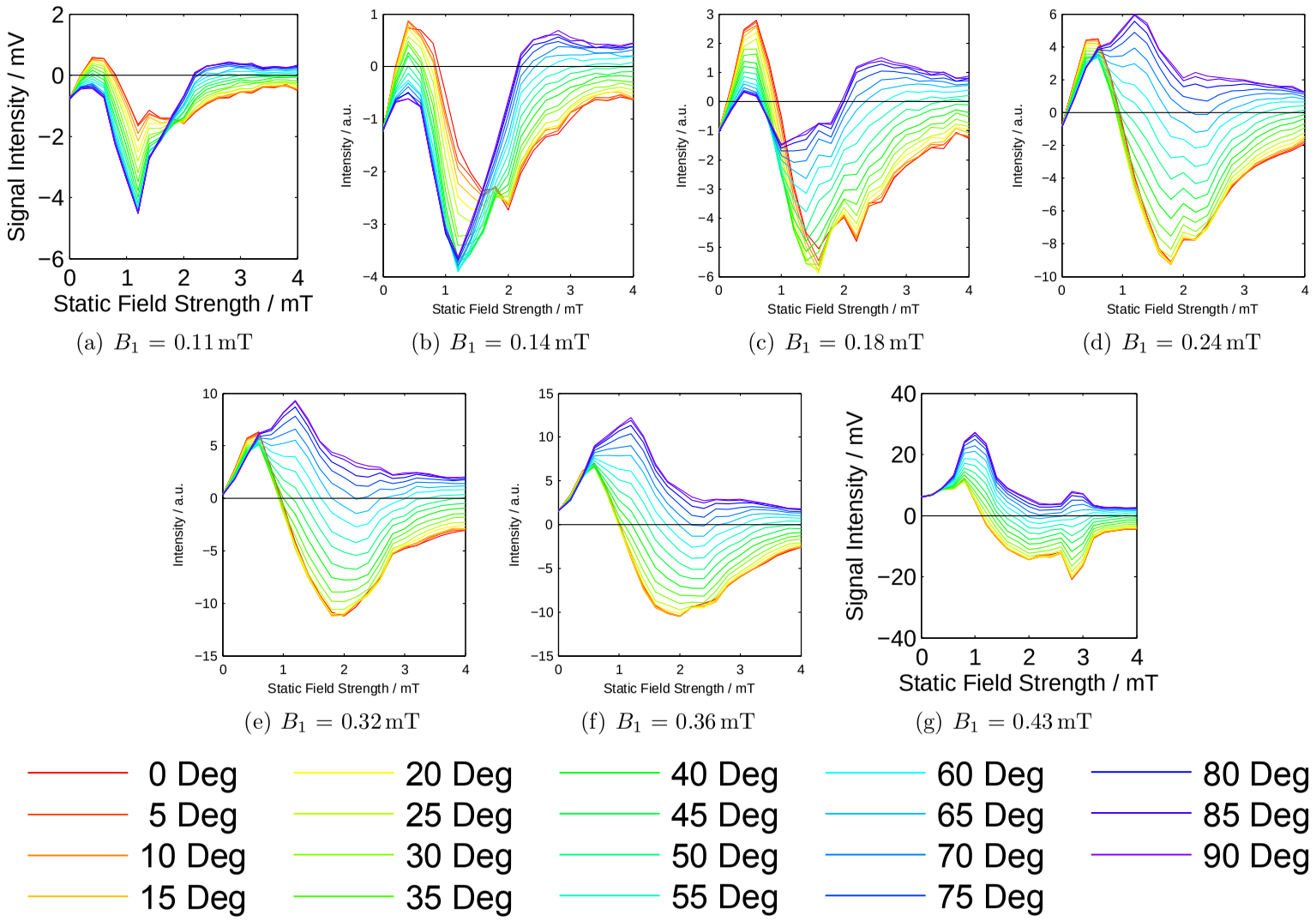

(a) $B_1 = 0.11\,\mathrm{mT}$ (b) $B_1 = 0.14\,\mathrm{mT}$ (c) $B_1 = 0.18\,\mathrm{mT}$ (d) $B_1 = 0.24\,\mathrm{mT}$

(e) $B_1 = 0.32\,\mathrm{mT}$ (f) $B_1 = 0.36\,\mathrm{mT}$ (g) $B_1 = 0.43\,\mathrm{mT}$

Figure B.2: Experimental RYDMR results for $\mathrm{Py_{d10}}$/1,3-DCB. B_0 field strengths ranging from 0° - 90° are shown within panels. Spectra were recorded for different B_1 field strengths, 0.11 mT - 0.43 mT, shown in different panels.

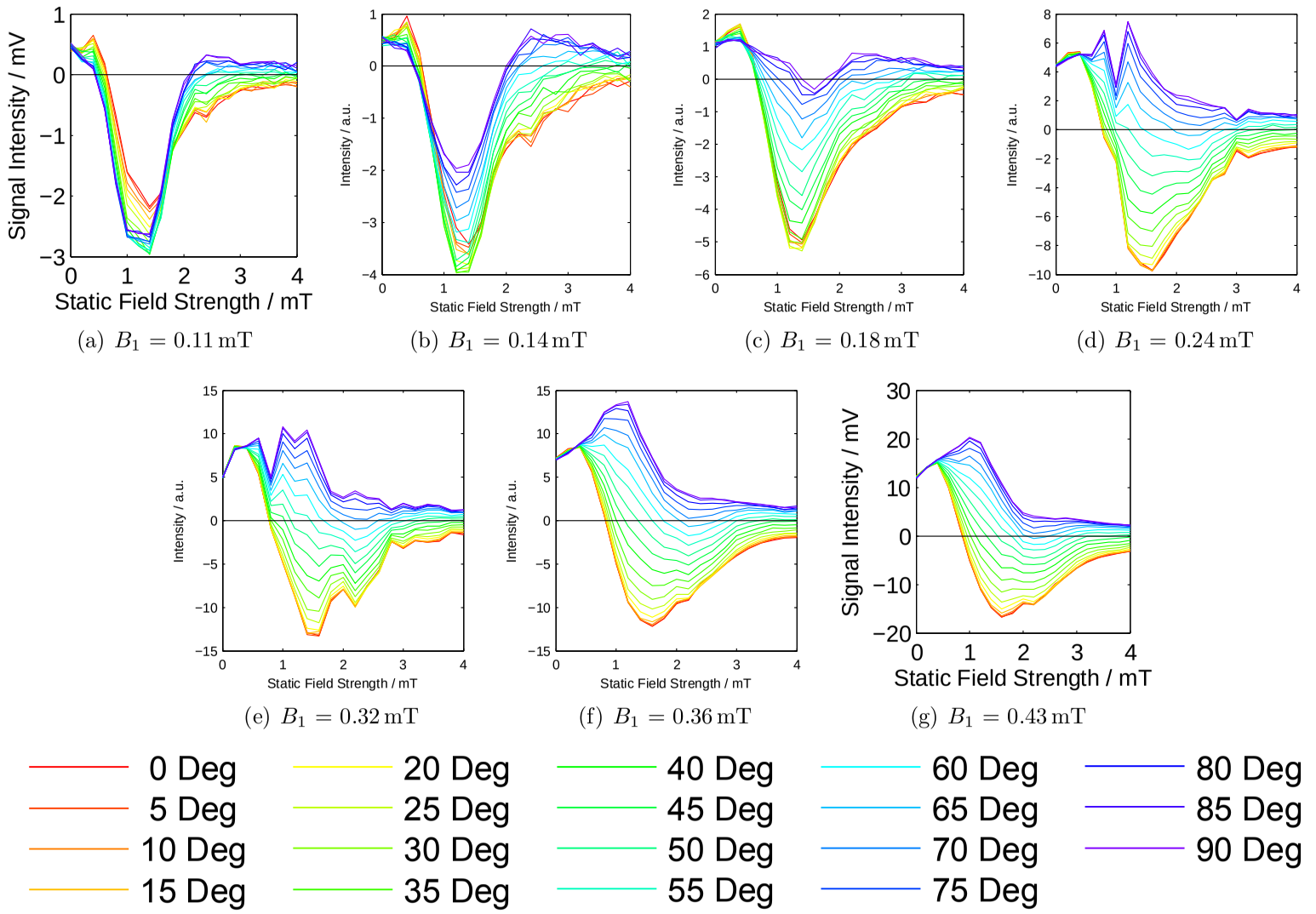

(a) $B_1 = 0.11\,\mathrm{mT}$ (b) $B_1 = 0.14\,\mathrm{mT}$ (c) $B_1 = 0.18\,\mathrm{mT}$ (d) $B_1 = 0.24\,\mathrm{mT}$

(e) $B_1 = 0.32\,\mathrm{mT}$ (f) $B_1 = 0.36\,\mathrm{mT}$ (g) $B_1 = 0.43\,\mathrm{mT}$

Figure B.3: Experimental RYDMR results for $\mathrm{Chy_{h12}}$/1,4-DCB. B_0 field strengths ranging from 0° - 90° are shown within panels. Spectra were recorded for different B_1 field strengths, 0.11 mT - 0.43 mT, shown in different panels.

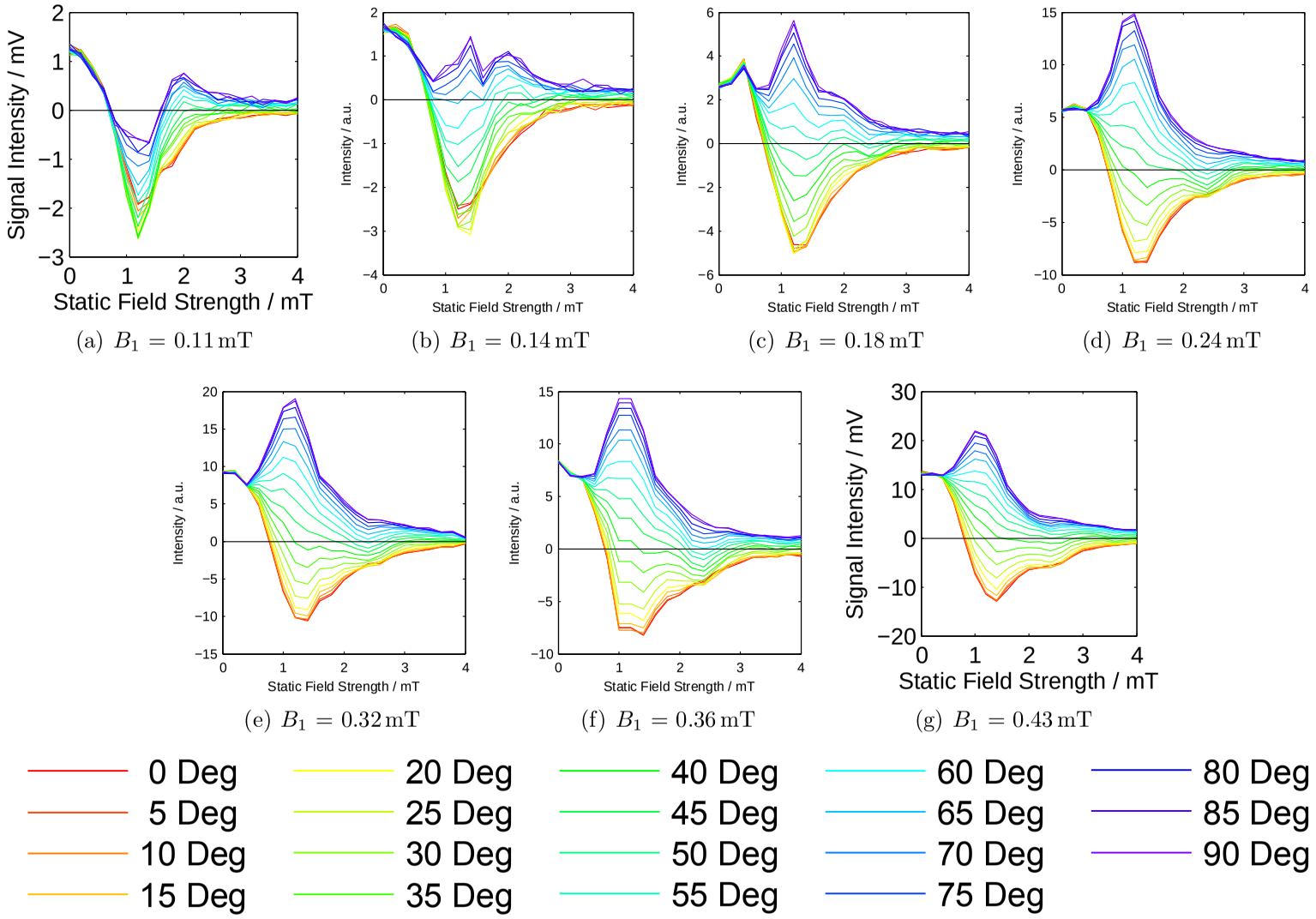

(a) $B_1 = 0.11\,\mathrm{mT}$ (b) $B_1 = 0.14\,\mathrm{mT}$ (c) $B_1 = 0.18\,\mathrm{mT}$ (d) $B_1 = 0.24\,\mathrm{mT}$

(e) $B_1 = 0.32\,\mathrm{mT}$ (f) $B_1 = 0.36\,\mathrm{mT}$ (g) $B_1 = 0.43\,\mathrm{mT}$

Figure B.4: Experimental RYDMR results for $\mathrm{Chy}_{\mathrm{d12}}$/1,4-DCB. B_0 field strengths ranging from 0° - 90° are shown within panels. Spectra were recorded for different B_1 field strengths, 0.11 mT - 0.43 mT, shown in different panels.

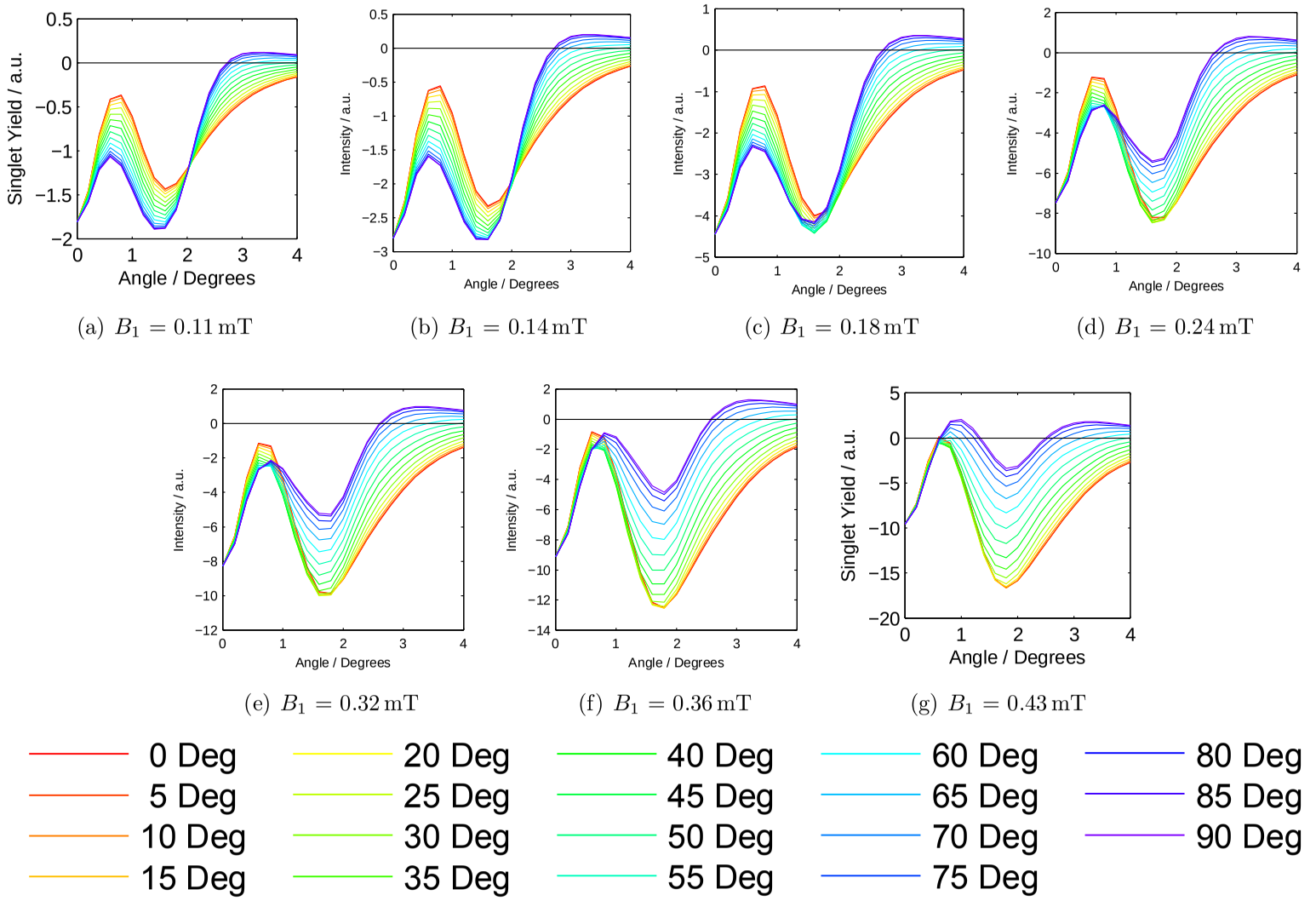

(a) $B_1 = 0.11\,\mathrm{mT}$ (b) $B_1 = 0.14\,\mathrm{mT}$ (c) $B_1 = 0.18\,\mathrm{mT}$ (d) $B_1 = 0.24\,\mathrm{mT}$

(e) $B_1 = 0.32\,\mathrm{mT}$ (f) $B_1 = 0.36\,\mathrm{mT}$ (g) $B_1 = 0.43\,\mathrm{mT}$

Figure B.5: Theoretical RYDMR results for $\mathrm{Py_{h10}}$/1,3-DCB, $k = 86.16\,\mu\mathrm{s}^{-1}$. B_0 field strengths ranging from 00° - 90° (legend) are shown within panels. Spectra were calculated for different B_1 field strengths, 0.11 mT - 0.43 mT, shown in different panels.

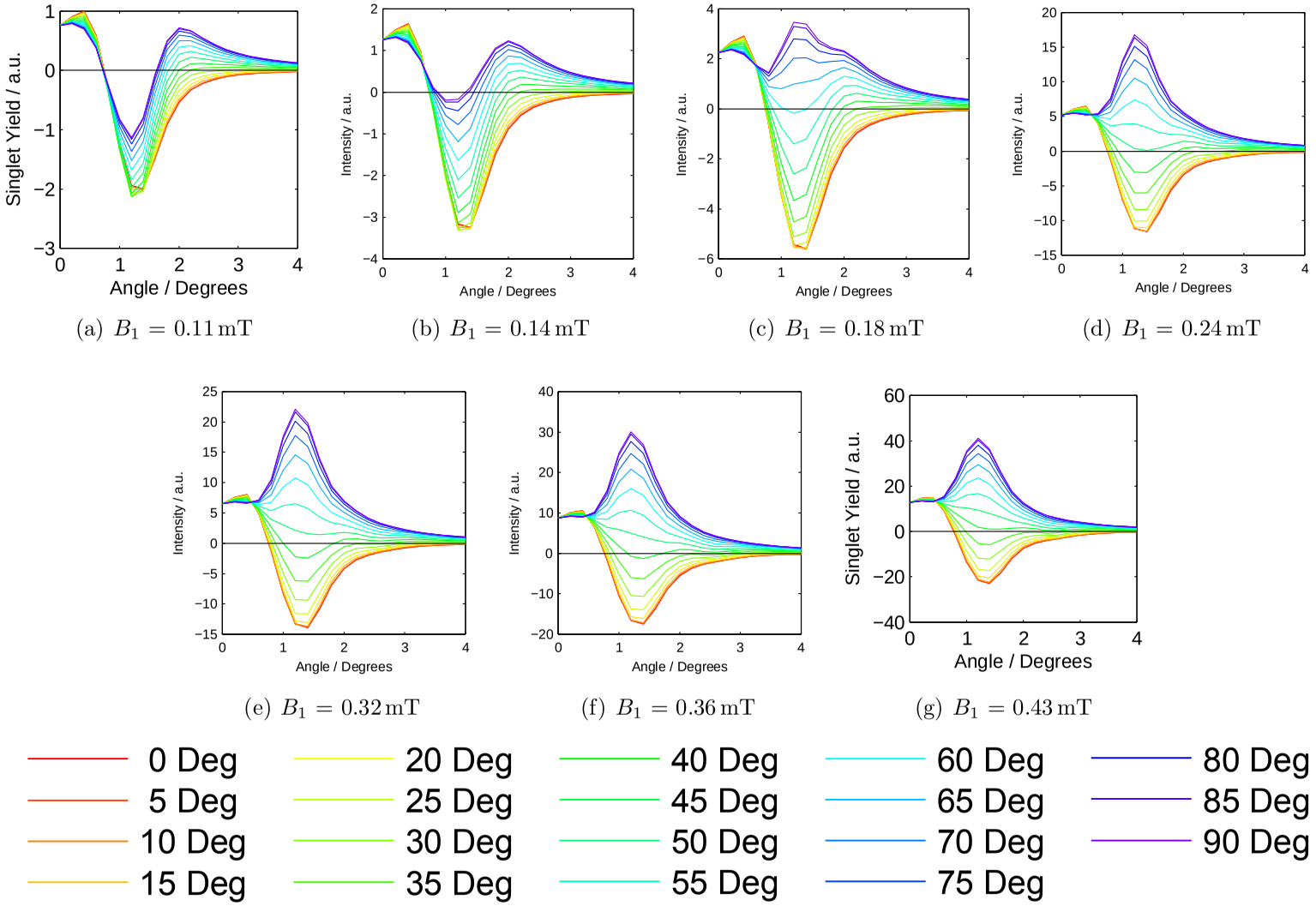

(a) $B_1 = 0.11\,\mathrm{mT}$ (b) $B_1 = 0.14\,\mathrm{mT}$ (c) $B_1 = 0.18\,\mathrm{mT}$ (d) $B_1 = 0.24\,\mathrm{mT}$

(e) $B_1 = 0.32\,\mathrm{mT}$ (f) $B_1 = 0.36\,\mathrm{mT}$ (g) $B_1 = 0.43\,\mathrm{mT}$

Figure B.6: Theoretical RYDMR results for $\mathrm{Chy_{d12}}$/1,4-DCB, $k = 55.34\,\mu\mathrm{s}^{-1}$. B_0 field strengths ranging from 0° - 90° (legend) are shown within panels. Spectra were calculated for different B_1 field strengths, 0.11 mT - 0.43 mT, shown in different panels.

Appendix C

Modulation Techniques

For simplification let's first assume, the singlet yield, Φ_S, can be approximated to have a linear dependence on B_1;

$$\Phi_S(B_1) = k_1 B_1 + k_0 \tag{C.1}$$

where $k_0 = \Phi_S(B_1 = 0) = \Phi_S^0$. Then the signal output, S, of the LIA is the integral of the products of Equation C.1 and a reference cosine function over one modulation period.

$$S = \int_0^{t_m} \Phi_S(B_1) \cos(2\pi\nu_{AF} t) \mathrm{d}t \tag{C.2}$$

where ν_{AF} is the frequency of the AF and $t_m = \frac{1}{\nu_{AF}}$. The time dependence of the B_1 field can be simplified because the RF has a negligible effect on the LIA.

$$B_1(t) = B_1^{max}(1 - M \sin^2(\pi\nu_{rf} t)) \tag{C.3}$$

where M is the fractional modulation depth. Equation C.3 can be substituted into Equation C.1, and then into Equation C.2. After evaluating the integral, the signal is:

$$S = \frac{B_1^{max} M}{4\nu_{AF}} k_1 \tag{C.4}$$

Now substitution of Equation C.4 for k_1 into Equation C.1 yields

$$S = \frac{M}{4\nu_{AF}} (\Phi_S(B_1^{\max}) - \Phi_S^0) = \frac{M}{4\nu_{AF}} \Phi_S^{\mathrm{diff}} \tag{C.5}$$

where $\Phi_S^{\mathrm{diff}} = \Phi_S(B_1^{\max}) - \Phi_S^0$.

When this linearity breaks down, things are not so simple and Φ_S will instead be given by;

$$\Phi_S(B_1) = k_4 B_1^4 + k_3 B_1^3 + k_2 B_1^2 + k_1 B_1 + k_0. \tag{C.6}$$

The signal, S that will result will hence be

$$S = k_4 \frac{B_1^{\max 4}}{2\nu_{RF}} \left(-\frac{7M^4}{16} + \frac{15M^3}{8} - 3M^2 + 2M \right) + k_3 \frac{B_1^{\max 3}}{4\nu_{RF}} \left(\frac{15M^3}{16} - 3M^2 + 3M \right) + k_2 \frac{B_1^{\max 2}}{2\nu_{RF}} \left(\frac{M^2}{2} + M \right) + k_1 \frac{B_1^{\max} M}{4\nu_{RF}} \quad \text{(C.7)}$$

The observed signal will therefore also be a polynomial in B_1.

Appendix D

Fluorescence

Naphthalene

Naphthalene is a polyarene consisting of two fused benzene rings, resulting in a flat aromatic system. It's absorption spectrum is shown in Figure 4.8 along with that of 1,2-DCB, 1,3-DCB and 1,4-DCB. The absorption spectrum shows that Naphthalene absorbs in the UV region of the spectrum with a maximum at 280 nm and an absorption of 2 at 300 nm. This corresponds to the first excited state of Naphthalene, i.e. the $S_0 - S_1$ transition. The corresponding fluorescence spectra for Naphthalene is shown in Figure D.1 along with the fluorescence for all three Naph/DCB systems. The monomer fluorescence of Naphthalene occurs as a series of peaks centred at 320 nm and the excimer fluorescences occurs as a broad peak at 400 nm (overlapping with monomer fluorescence). Addition of DCB is shown to quench the monomer fluorescence of Naphthalene Figure D.1(a) but shows an additional peak at 400 nm. This peak is due to the monomer fluorescence of DCB since the absorption spectra of DCB and naphthalene overlap and hence both molecules are excited at 300 nm. The fluorescence data Figure D.2(b) shows possibility of some exciplex emission at approximately 550 nm.

Pyrene

Pyrene is a polyarene consisting of four fused benzene rings, resulting in a flat aromatic system. It's absorption spectrum is shown in Figure 4.8 along with that of 1,2-DCB, 1,3-DCB and 1,4-DCB. The absorption spectrum shows that Pyrene absorbs in the UV region

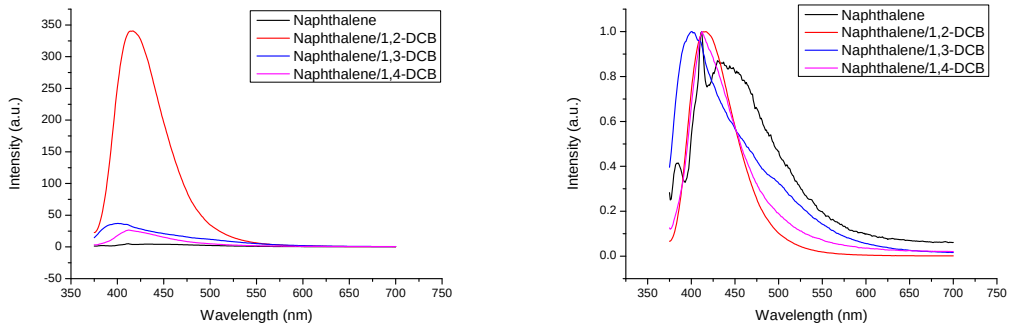

(a) Raw data (b) Normalised data

Figure D.1: Fluorescence data for all Naph/DCB systems. Spectra were recorded in acetonitrile/cyclohexanol (1:9) and the excitation wavelength was chosen to be 280 nm.

of the spectrum with a maximum at 350 nm. This corresponds to the first excited state of Pyrene, i.e. the $S_0 - S_1$ transition. The corresponding fluorescence spectra for Py is shown in Figure D.2 along with the fluorescence for all three Py/DCB systems. The monomer fluorescence of Py occurs at approximately 400 nm and the excimer fluorescence occurs at approximately 470 nm. Addition of the electron donor DCB is shown to quench the monomer fluorescence of Py, Figure D.2(a), and the fluorescence spectra of Py/DCB shows an extra peak at 500 - 550 nm. Normalisation of the fluorescence data, Figure D.2(b), shows that this peak at 500 - 550 nm is largest for the Py/1,3-DCB system and may correspond to the exciplex emission for the system.

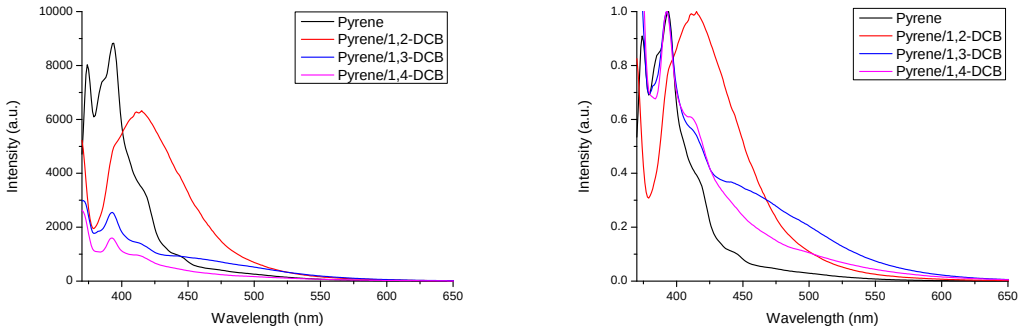

(a) Raw data (b) Normalised data

Figure D.2: Fluorescence data for all Py/DCB systems. Spectra were recorded in acetonitrile/cyclohexanol (1:9) and the excitation wavelength was chosen to be 350 nm.

Chrysene

Chrysene is another polyarene consisting of four fused benzene rings, resulting in a flat aromatic system. Its absorption spectrum (recorded in a 9:1 cyclohexanol:acetonitrile solvent) is shown in Figure 4.8 and shows that it absorbs in the UV region of the spectrum at a wavelength 320 nm corresponding to the first excited state, i.e. the $S_0 - S_1$ transition. The fluorescence spectrum for chy is shown in Figure D.3 along with the fluorescence of all three Chy/DCB systems. The fluorescence spectrum of chrysene consists of sharp bands with their origin at 375 nm corresponding to monomer fluorescence. Addition of DCB quenches the monomer fluorescence and another peak between 500 - 550 nm appears due to exciplex emission.

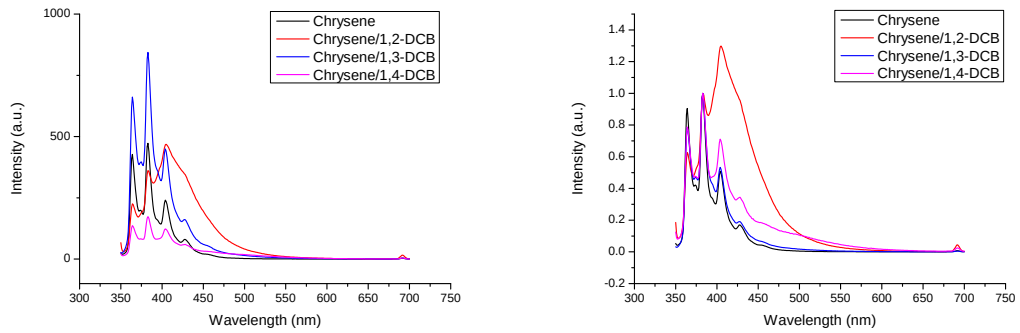

(a) Raw data (b) Normalised data

Figure D.3: Fluorescence data for all Chrysene/DCB systems. Spectra were recorded in acetonitrile/cyclohexanol (1:9) and the excitation wavelength was chosen to be 345 nm.

Anthracene

Anthracene is a polyarene consisting of three fused benzene rings, resulting in a flat aromatic system. Its absorption spectrum, Figure 4.8, shows that the Anth absorbs in UV region of the spectrum with a maximum peak at 385 nm corresponding to the first excited state transition i.e. the $S_0 - S_1$ transition. The fluorescence spectrum for Anth is shown in Figure D.4 along with the fluorescence of all three Anth/DCB systems. The emission spectrum of Anth consists of sharp bands centred at 400 nm and corresponds to monomer fluorescence. Addition of DCB isomers acts to quench the monomer fluorescence but shows no visible sign of an exciplex peak in the emission spectra.

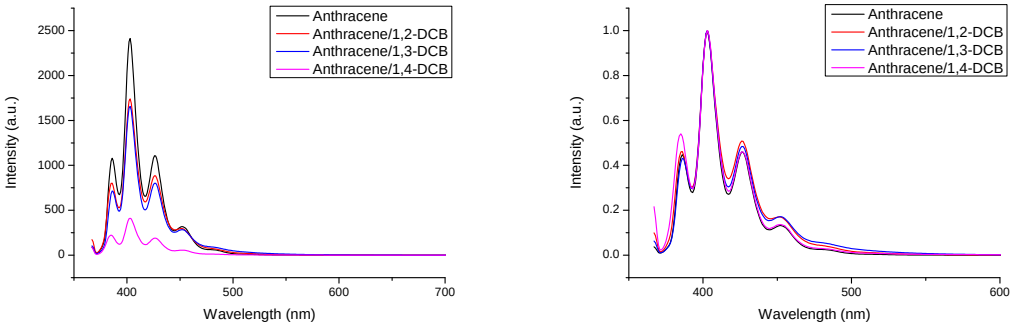

(a) Raw data (b) Normalised data

Figure D.4: Fluorescence data for all Anth/DCB systems. Spectra were recorded in acetonitrile/cyclohexanol (1:9) and the excitation wavelength was chosen to be 365 nm.

Phenanthrene

Phenanthrene is a polyarene consisting of three fused benzene rings resulting in a flat aromatic system. It's absorption spectrum, Figure 4.8, shows an absorption peak in the UV region of the spectrum 300 nm corresponding to the first excited state transition i.e. the $S_0 - S_1$ transition. The fluorescence spectrum for phenanthrene is shown in Figure D.5 along with the fluorescence of all three Phen/DCB systems, all excited at 300 nm. The data for phenanthrene alone shows monomer fluorescence consisting of several sharp peaks, centred at 370 nm which is quenched in the presence of DCB. Normalisation of the data, Figure D.5(b), shows evidence of exciplex fluorescence in the region 500 - 550 nm.

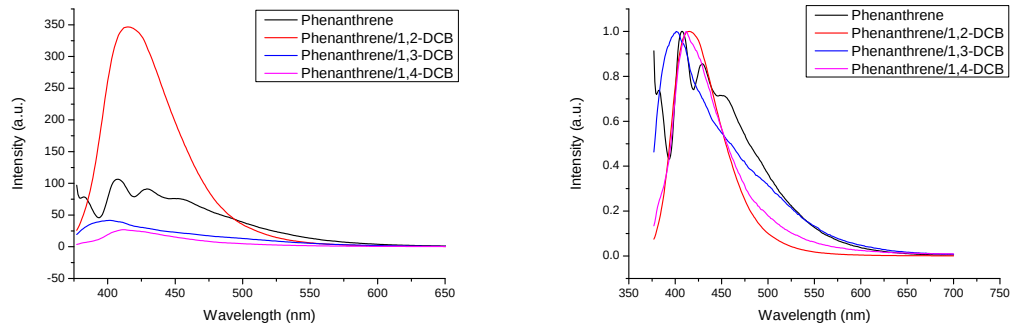

(a) Raw data (b) Normalised data

Figure D.5: Fluorescence data for all Phananthrene/DCB systems. Spectra were recorded in toluene and the excitation wavelength was chosen to be 565 nm.

Tetracene

Tetracene is a polyarene consisting of four fused benzene rings resulting in a flat aromatic system. Its absorption spectrum, Figure 4.8, shows an absorption peak in the region 350 - 400 nm corresponding to the first excited state transition i.e. the $S_0 - S_1$ transition. The fluorescence spectrum for tetracene is shown in Figure D.6 along with the fluorescence of all three Tetr/DCB systems, all excited at 465 nm. The data for tetracene alone shows monomer fluorescence consisting of sharp bands centred at 510 nm which is quenched in the presence of DCB. Unfortunately, normalisation of the fluorescence data Figure D.6(b) shows no significant exciplex peak.

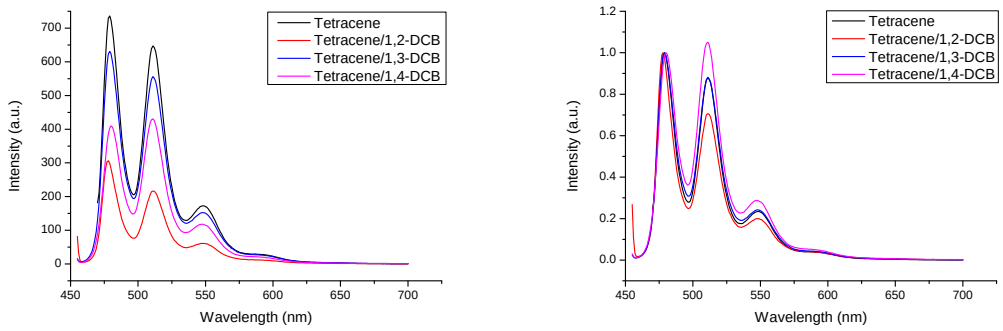

(a) Raw data (b) Normalised data

Figure D.6: Fluorescence data for all Tetracene/DCB systems. Spectra were recorded in acetonitrile/cyclohexanol (1:9) and the excitation wavelength was chosen to be 465 nm.

Pentacene

Pentacene is a polyarene consisting of five fused benzene rings resulting in a flat aromatic system. Its absorption spectrum, Figure 4.8, shows an absorption peak in the region 500 - 600 nm corresponding to the first excited state transition i.e. the $S_0 - S_1$ transition. The fluorescence spectrum for pentacene is shown in Figure D.7 along with the fluorescence of all three pent/DCB systems. The pentacene fluorescence shows monomer fluorescence consisting of bands centred at 620 nm which is quenched in the presence of DCB. Unfortunately, normalisation of the fluorescence data Figure D.7(b) shows no significant exciplex peak.

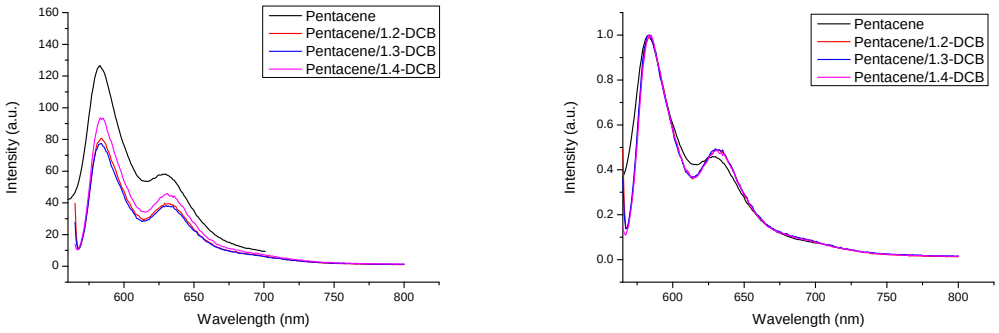

(a) Raw data (b) Normalised data

Figure D.7: Fluorescence data for all Pentacene/DCB systems. Spectra were recorded in toluene and the excitation wavelength was chosen to be 565 nm.

Appendix E

Hyperfine Coupling Data

Table E.1: Hyperfine coupling data (mT) for all polyarenes (electron donors) [130] and dicyanobenzenes (electron donors) [131]. The effective hyperfine coupling for the radical is also shown, as calculated using Equation 1.34.

	a_1	a_2	a_3	a_4	a_5	a_6	a_{mol}
Naphthalene	0.49(4H)	0.18(4H)					1.28
Anthracene	0.27(4H)	0.15(4H)	0.54(23H)				1.20
Tetracene	0.43(4H)	0.16(4H)	0.12(4H)				1.14
Phenanthrene	0.29(4H)	0.13(4H)	0.49(2H)				1.16
Pentacene	0.51(2H)	0.30(4H)	0.09(4H)	0.09(4H)			1.19
Chrysene	0.49(2H)	0.21(2H)	0.15(2H)	0.14(2H)	0.05(2H)	0.03(2H)	0.99
Pyrene	0.55(4H)	0.21(4H)	0.12(2H)				1.03
1,2-DCB	0.18(2N)	0.41(2H)	0.04(2H)				0.80
1,3-DCB	0.10(2N)	0.83(2H)	0.14(1H)				1.04
1,4-DCB	0.18(2N)	0.16(4H)					0.53

Appendix F

Matlab Code for Calculating Maximum Overlap

```
function [Contour_Plot] = Density_Plot(filename)
%-------------------------------------------------------------------------%
%                              Density Plots                              %
%-------------------------------------------------------------------------%
% This code will read in the output file from densf and cntrs
% calculations in DFT and plot the 2D density.
%% Open data and write each contour plot to a cell array

   fid = fopen(filename,'rt');
D = textscan(fid, '%f', 'Delimiter','\n');
fclose(fid);

   Data = D{1,1};

   A = isnan(Data);
B = find(A);
```

```
   C = [];

for K = 1;
    k = K;
    C{1} = Data(1:(B(k) - 1));
end

for K = 2:length(B)
    k = K;
    m = K - 1;
    C{k} = Data((B(m) + 1):(B(k) - 1));
end
Cont = [];
for M = 1:length(B)
    m = M;
    for P = 1:length(C{m})
        p = P;
        q = P - 1;
     if rem(p,2) == 0
         Cont{m}(q,2) = C{m}(p);
     else
         Cont{m}(p,1) = C{m}(p);
     end
    end
end

Contours = [];

for M = 1:length(B)
    m = M;
```

```
    Cont_Array = Cont{m};
    Cont_Array_New = Cont_Array(any(Cont_Array,2),:);
    Contours{m} = Cont_Array_New;
end

M_x = [];
M_y = [];

for M = 1:length(B)
    m = M;
    Mx = median(Contours{m}(:,1));
    My = median(Contours{m}(:,2));
    M_x = [M_x Mx];
    M_y = [M_y My];
end

Centre = [median(M_x) median(M_y)];

Contour_Plot = [];

for M = 1:length(B)
    m = M;
    Contour_Plot{m}=[(Contours{m}(:,1)-Centre(1))(Contours{m}(:,2)-Cent
end


Donor = Density_Plot('Py.txt');
Acceptor = Density_Plot('12DCB.txt');
savefile = 'Py_12DCB.mat';
Pos_D = 4;
```

```
Neg_D = 4;

Pos_A = 3;

Neg_A = 3;

%% Draw the original orbitals without displacement


for M = 1:Pos_D
    m = M;
    hold on
    plot(Donor{m}(:,1), Donor{m}(:,2),'r')
end


for M = (Pos_D + 1):length(Donor)
    m = M;
    hold on
    plot(Donor{m}(:,1), Donor{m}(:,2),'--r')
end


for N = 1:Pos_A
    n = N;
    hold on
    plot(Acceptor{n}(:,1),Acceptor{n}(:,2),'b')
end


for M = (Pos_A + 1):length(Acceptor)
    m = M;
    hold on
    plot(Acceptor{m}(:,1), Acceptor{m}(:,2),'--b')
end
```

```
%% Now let's calculate the overlap between the orbitals for different
%% orientations

% Define the displacement vectors

Ydis = [-5:1:5];
Xdis = [-5:1:5];
Theta = [0:pi/36:2*pi];

% Calculate the overlap for these displacements

h = waitbar(0,'Please wait...');

OI_theta_xy = [];

for T = 1:length(Theta)
    t = T;
    theta = Theta(t);
    waitbar(T / length(Theta));

OI_xy = [];

for Y = Ydis
    y = Y;

OI_x = [];

for X = Xdis
    x = X;
```

```
Total_Area_Pos = [];


for M = 1:Pos_D
    m = M;
lat1 = Donor{m}(:,1);
lon1 = Donor{m}(:,2);


Area = [];


        for N = 1:Pos_A
            n = N;
lat_2 = Acceptor{n}(:,1) + y;
lon_2 = Acceptor{n}(:,2) + x;
lat2 = lat_2.*cos(theta) - (lon_2.*sin(theta));
lon2 = lon_2.*cos(theta) + (lat_2.*sin(theta));
axesm miller
hold on
[loni,lati] = polybool('intersection',lon1,lat1,lon2,lat2);
[lati loni];
% geoshow(lati,loni,'DisplayType','polygon','FaceColor','y')
A = polyarea(lati,loni);
Area = [Area A];
        end
Total_Area_Pos = [Total_Area_Pos Area];
end


Total_Area_Neg = [];


for M = (Pos_D + 1):length(Donor)
    m = M;
```

```
lat1 = Donor{m}(:,1);
lon1 = Donor{m}(:,2);
Area = [];
        for N = (Pos_A + 1):length(Acceptor)
            n = N;
lat_2 = Acceptor{n}(:,1) + x;
lon_2 = Acceptor{n}(:,2) + y;
lat2 = lat_2.*cos(theta) - (lon_2.*sin(theta));
lon2 = lon_2.*cos(theta) + (lat_2.*sin(theta));
axesm miller
% plotm(lat1,lon1,'--r')
% plotm(lat2,lon2,'--b')
hold on
[loni,lati] = polybool('intersection',lon1,lat1,lon2,lat2);
[lati loni];
% geoshow(lati,loni,'DisplayType','polygon','FaceColor','y')
A = polyarea(lati,loni);
Area = [Area A];
        end
Total_Area_Neg = [Total_Area_Neg Area];
end

Overlap = sum(Total_Area_Pos) + sum(Total_Area_Neg);

OI_x = [OI_x Overlap];

end

OI_xy = [OI_xy; OI_x];
end
```

```
OI_theta_xy{t} = OI_xy;

end

close(h)

save(savefile, 'OI_theta_xy');


%% Find the maximum displacement obtained and draw the orbitals
%% corresponding to the best overlap

Donor = Density_Plot('Py.txt');
Acceptor = Density_Plot('12DCB.txt');
file = 'Py_12DCB.mat';
Values = load(file);

Data = Values.OI_theta_xy;

Pos_D = 4;
Neg_D = 4;
Pos_A = 3;
Neg_A = 3;

MaxC = [];
MaxI = [];

for k = 1:length(Data)
K = k;
```

```
[C,I] = max(Data{K});

MaxC = [MaxC; C];
MaxI = [MaxI; I];
end

[D, J] = max(MaxC);
[E, M] = max(D);

y = M;
t = J(M);
x = MaxI(t,y);

Xdis = [-5:1:5];
Ydis = [-5:1:5];
Theta = [0:pi/36:2*pi];

Orbital_Overlap = Data{t}(x,y)

f = figure;

% - Plot the donor molecule

for M = 1:Pos_D
    m = M;
    hold on
    plot(Donor{m}(:,1), Donor{m}(:,2),'r')
    xlabel('Angstrom')
    ylabel('Angstrom')
end
```

```
for M = (Pos_D + 1):length(Donor)
    m = M;
    hold on
    plot(Donor{m}(:,1), Donor{m}(:,2),'--r')
end

% - Plot the acceptor molecule with new geometry for maximum overlap

for N = 1:Pos_A
    n = N;
    hold on

    X = Acceptor{n}(:,1) + Xdis(x);
    Y = Acceptor{n}(:,2) + Ydis(y);

    x_rot = X.*cos(Theta(t)) - Y.*sin(Theta(t));
    y_rot = Y.*cos(Theta(t)) + X.*sin(Theta(t));

    plot(x_rot,y_rot,'b')
end

for M = (Pos_A + 1):length(Acceptor)
    m = M;
    hold on

    X = Acceptor{m}(:,1) + Xdis(x);
    Y = Acceptor{m}(:,2) + Ydis(y);

    x_rot = X.*cos(Theta(t)) - Y.*sin(Theta(t));
```

```
    y_rot = Y.*cos(Theta(t)) + X.*sin(Theta(t));

    plot(x_rot,y_rot,'--b')
end

save2pdf('Py_12DCB',f, 600)
```

Appendix G

HOMO and LUMO 2-D Contour Plots

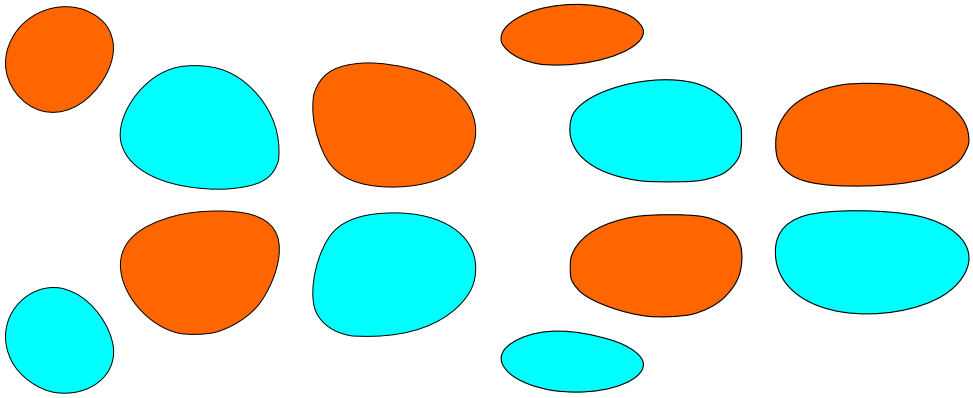

(a) 1,2-DCB

(b) 1,3-DCB

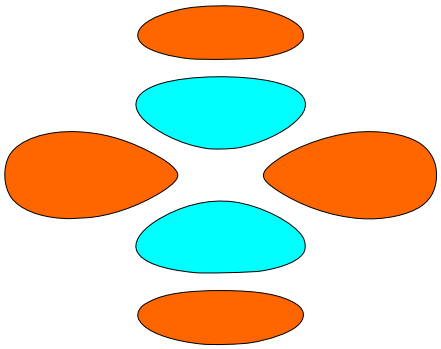

(c) 1,4-DCB

Figure G.1: Contour plots of LUMOs for DCB isomers

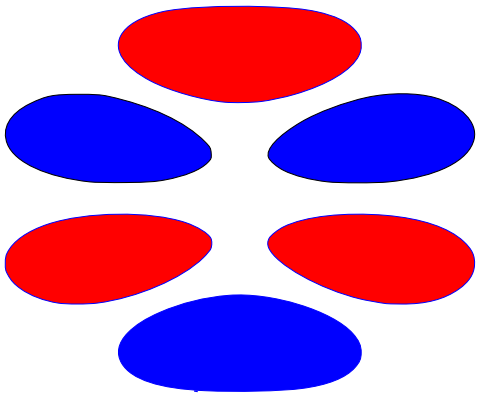

(a) Naphthalene

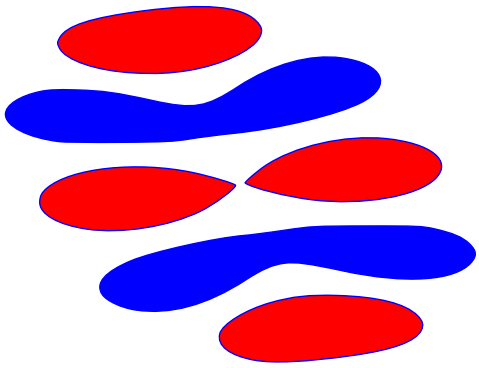

(b) Anthracene

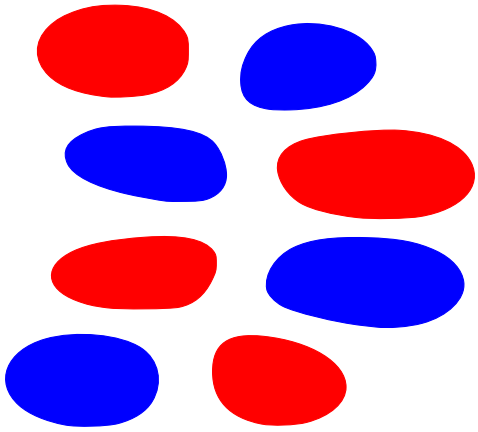

(c) Phenanthrene

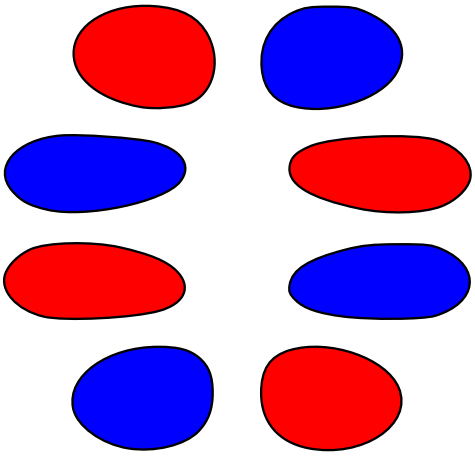

(d) Pyrene

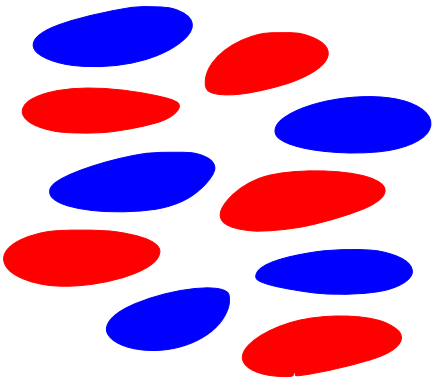

(e) Chrysene

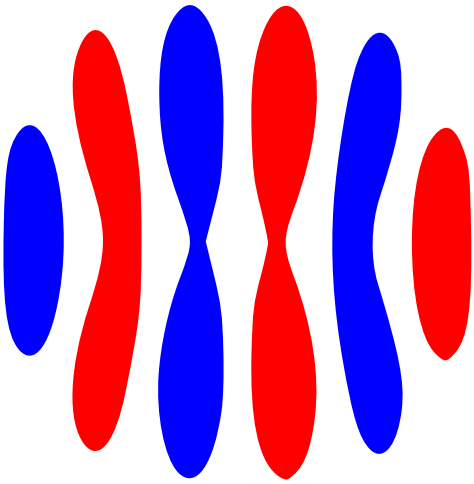

(f) Tetracene

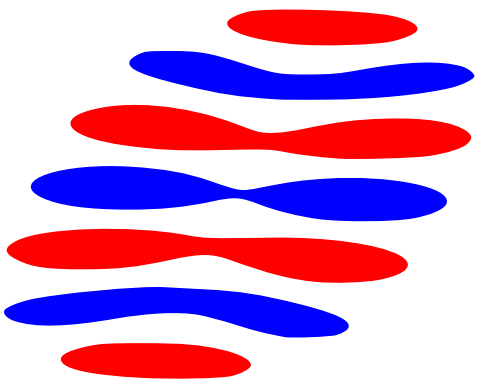

(g) Pentacene

Figure G.2: Contour plots of HOMOs for polyarene molecules.

Appendix H

Exciplex Geometry

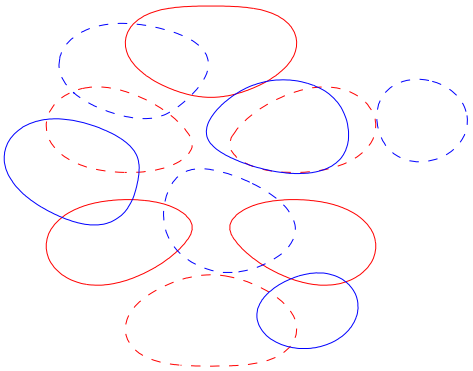

(a) 1,2-DCB

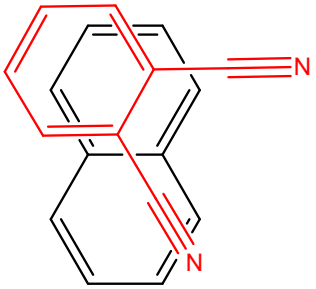

(b) 1,2-DCB

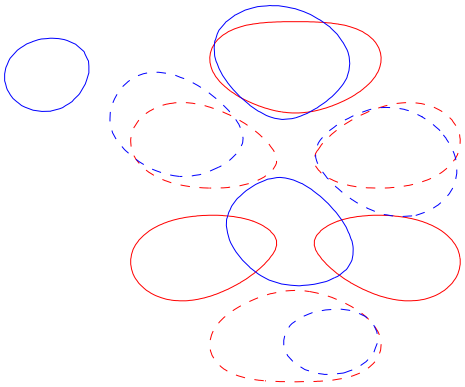

(c) 1,3-DCB

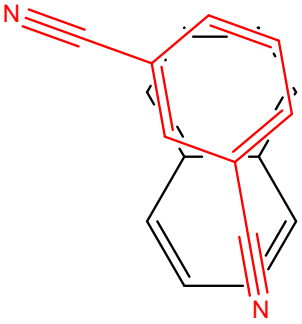

(d) 1,3-DCB

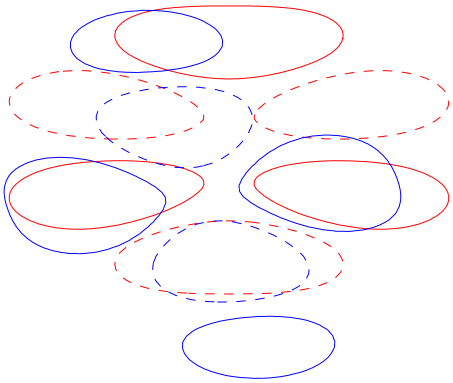

(e) 1,4-DCB

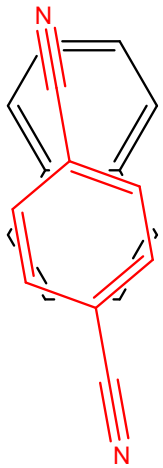

(f) 1,4-DCB

Figure H.1: Orientation of HOMO (red) and LUMO (blue) which achieves the maximum orbital overlap for naphthalene/DCB systems as performed in DFT. The HOMO-LUMO orbitals are shown on the left and the corresponding exciplex geometry on the right.

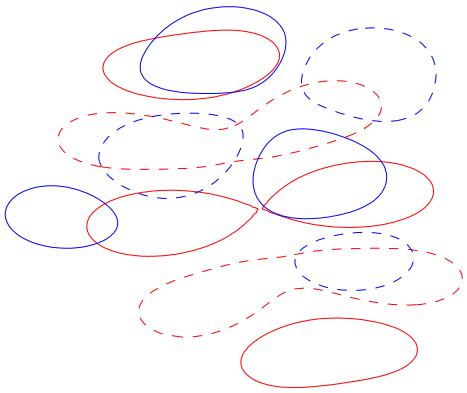

(a) 1,2-DCB

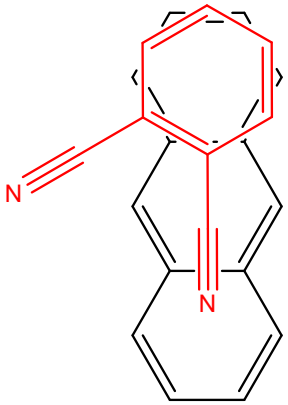

(b) 1,2-DCB

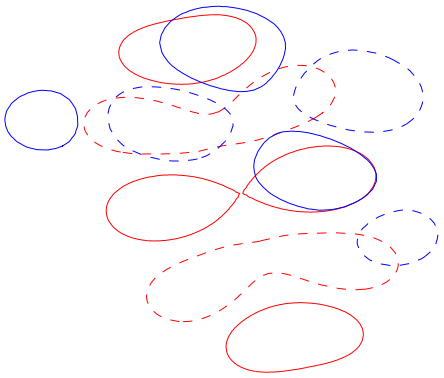

(c) 1,3-DCB

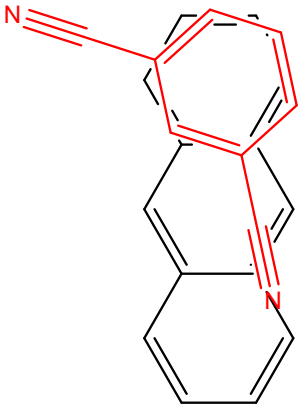

(d) 1,3-DCB

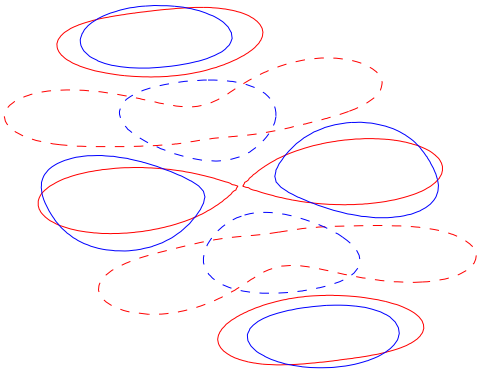

(e) 1,4-DCB

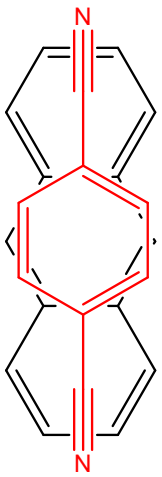

(f) 1,4-DCB

Figure H.2: Orientation of HOMO (red) and LUMO (blue) which achieves the maximum orbital overlap for anthracene/DCB systems as performed in DFT. The HOMO-LUMO orbitals are shown on the left and the corresponding exciplex geometry on the right.

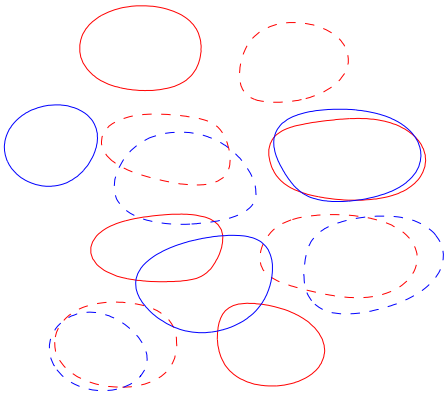

(a) 1,2-DCB

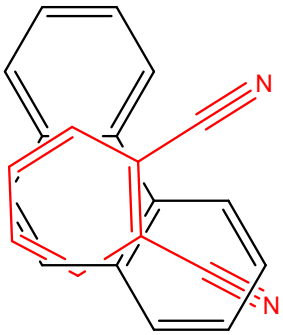

(b) 1,2-DCB

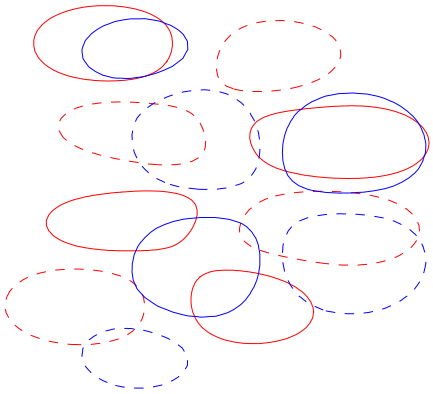

(c) 1,3-DCB

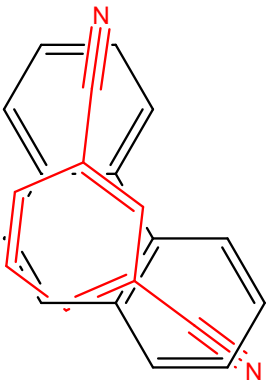

(d) 1,3-DCB

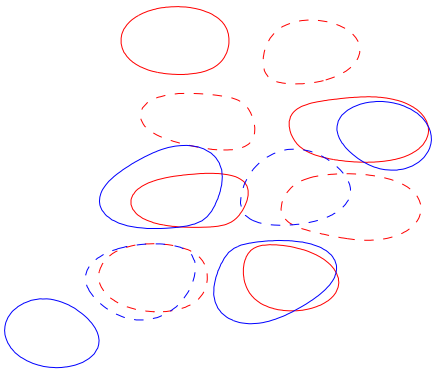

(e) 1,4-DCB

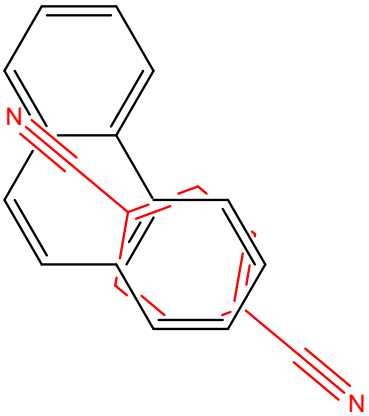

(f) 1,4-DCB

Figure H.3: Orientation of HOMO (red) and LUMO (blue) which achieves the maximum orbital overlap for phenanthrene/DCB systems as performed in DFT. The HOMO-LUMO orbitals are shown on the left and the corresponding exciplex geometry on the right.

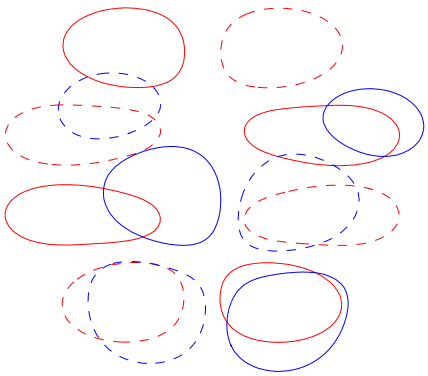

(a) 1,2-DCB

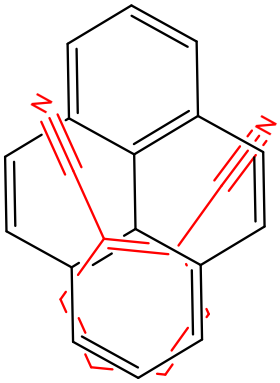

(b) 1,2-DCB

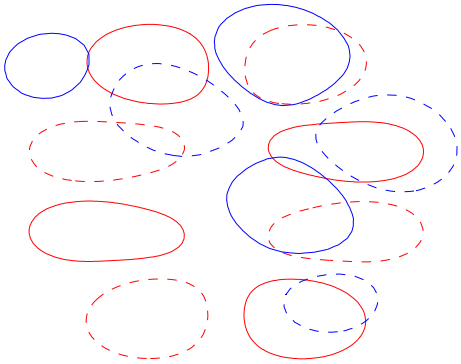

(c) 1,3-DCB

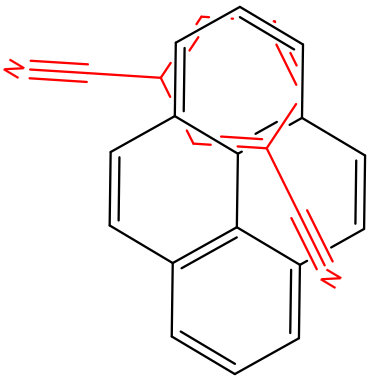

(d) 1,3-DCB

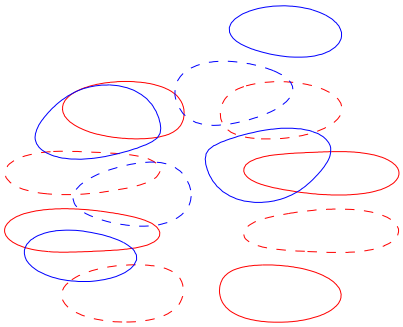

(e) 1,4-DCB

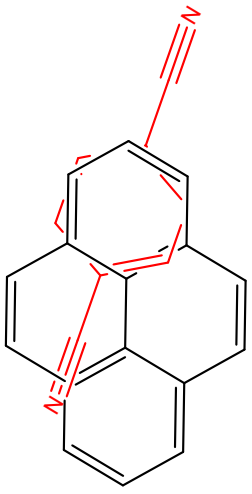

(f) 1,4-DCB

Figure H.4: Orientation of HOMO (red) and LUMO (blue) which achieves the maximum orbital overlap for pyrene/DCB systems as performed in DFT. The HOMO-LUMO orbitals are shown on the left and the corresponding exciplex geometry on the right.

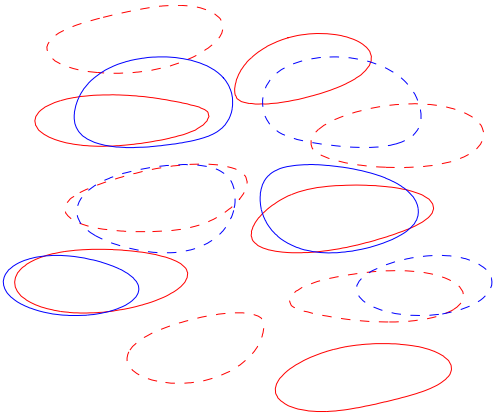

(a) 1,2-DCB

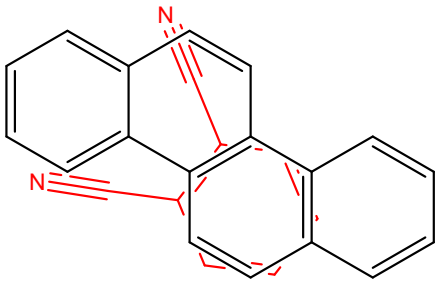

(b) 1,2-DCB

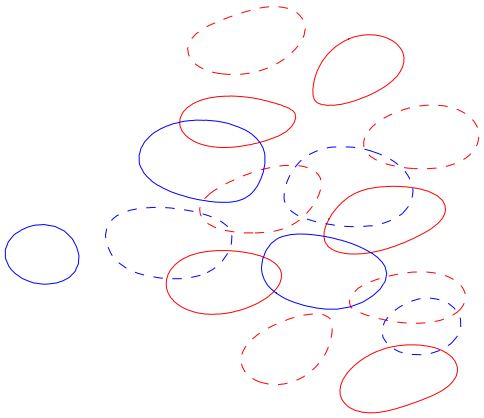

(c) 1,3-DCB

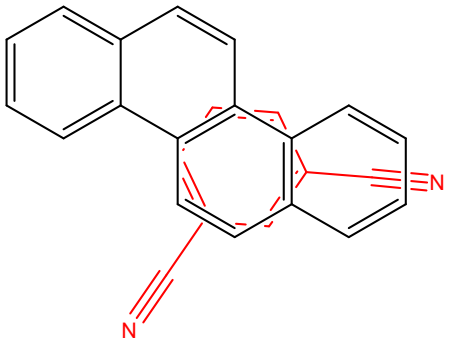

(d) 1,3-DCB

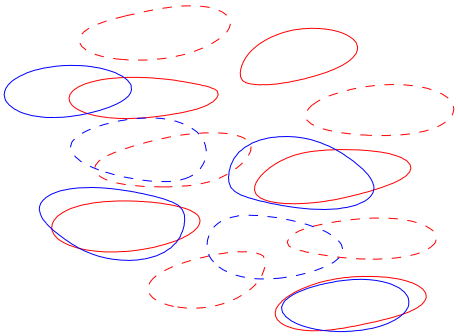

(e) 1,4-DCB

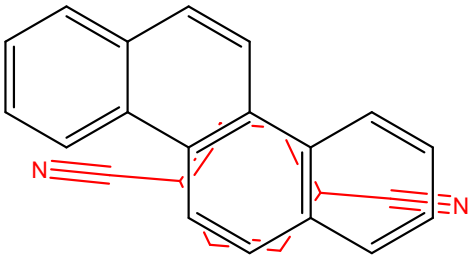

(f) 1,4-DCB

Figure H.5: Orientation of HOMO (red) and LUMO (blue) which achieves the maximum orbital overlap for chrysene/DCB systems as performed in DFT. The HOMO-LUMO orbitals are shown on the left and the corresponding exciplex geometry on the right.

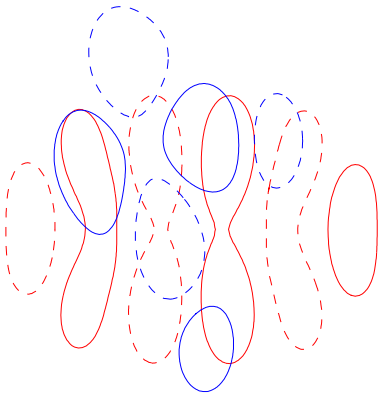

(a) 1,2-DCB

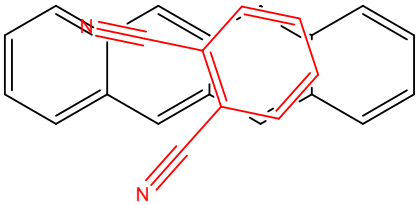

(b) 1,2-DCB

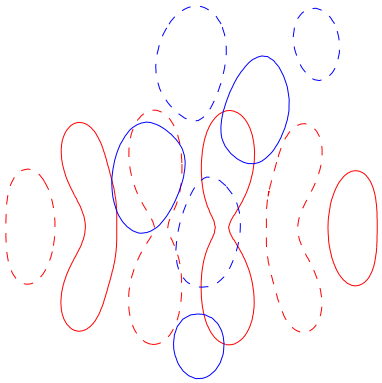

(c) 1,3-DCB

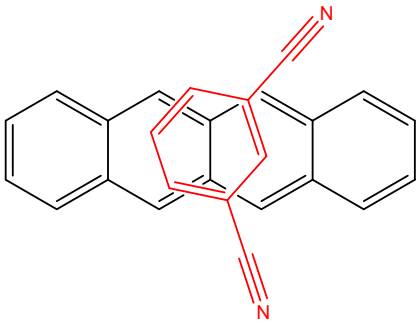

(d) 1,3-DCB

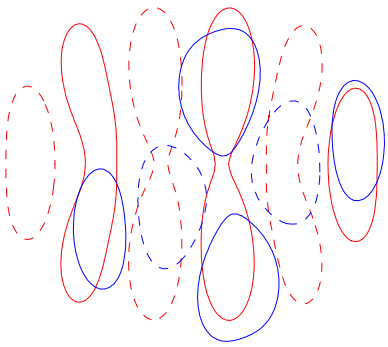

(e) 1,4-DCB

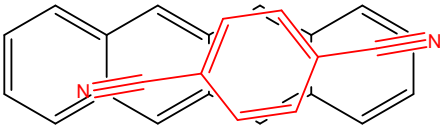

(f) 1,4-DCB

Figure H.6: Orientation of HOMO (red) and LUMO (blue) which achieves the maximum orbital overlap for tetracene/DCB systems as performed in DFT. The HOMO-LUMO orbitals are shown on the left and the corresponding exciplex geometry on the right.

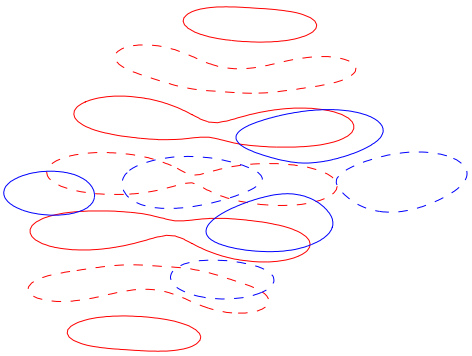

(a) 1,2-DCB

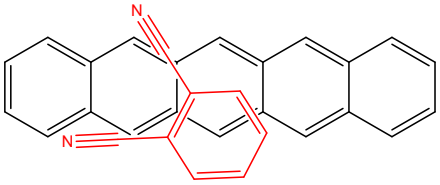

(b) 1,2-DCB

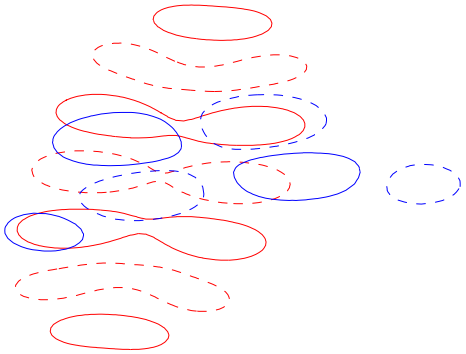

(c) 1,3-DCB

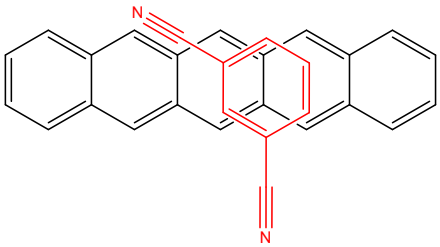

(d) 1,3-DCB

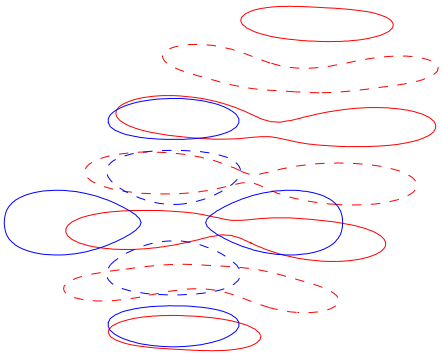

(e) 1,4-DCB

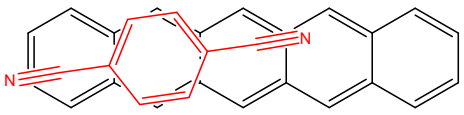

(f) 1,4-DCB

Figure H.7: Orientation of HOMO (red) and LUMO (blue) which achieves the maximum orbital overlap for pentacene/DCB systems as performed in DFT. The HOMO-LUMO orbitals are shown on the left and the corresponding exciplex geometry on the right.

Appendix I

Photoselection

For single photon excitation:

$$\rho_{\text{excitation}} \propto \mu_A.E \propto \cos^2\theta \tag{I.1}$$

A molecule with its dipole moment aligned in the direction of electric field will have the greatest probability of excitation whereas a molecule with dipole moment orthogonal to the excitation light will not be excited at all. First consider the simplest case, a single fluorophore with a fixed position of its transition dipole moment Figure I.1 where absorption and emission dipoles are assumed to be collinear. The probability of detection when fluorescence is detected parallel to the excited light polarisation is $f(\theta)$ and the corresponding fluorescence intensity is given by:

$$I_{||} = \int_0^{\pi/2} f(\theta)\cos^2\theta \mathrm{d}\theta \;=\; k < \cos^2\theta > \tag{I.2}$$

The corresponding intensity when fluorescence is detected perpendicular to the excited light polarisation is given by:

$$I_{\perp} = k\int_0^{\pi/2}\int_0^{\pi/2} f(\theta,\phi) sin^2\theta \sin^2\phi \mathrm{d}\theta\mathrm{d}\phi \;=\; k < \sin^2\theta >< \sin^2\phi > \tag{I.3}$$

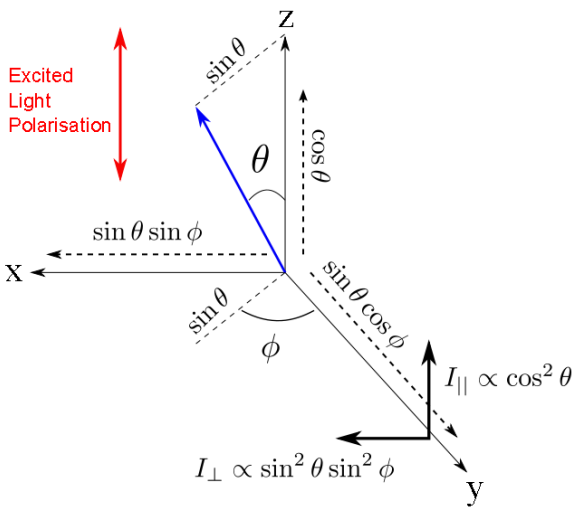

Figure I.1: A dipole interacting with a polarised electric field. For simplicity assume the orientation of absorption and emission dipole are collinear. The emitted light is the electromagnetic wave from a radiating dipole. $I_{||}$ and $I_{\perp}$ are equal to the fluorescence intensity in parallel and perpendicular (respectively) directions with respect to the polarised excitation light.

Now if we take an ensemble of molecules with random values of ϕ the above becomes

$$I_{\perp} = k \int_0^{\pi/2} \int_0^{\pi/2} f(\theta,\phi) sin^2\theta \frac{1}{2\pi} \sin^2\phi \mathrm{d}\theta \mathrm{d}\phi \; = \; \frac{k}{2} < \sin^2\theta > \tag{I.4}$$

The degree of polarisation in a sample is defined as

$$P = \frac{I_{||} - I_{\perp}}{I_{||} + I_{\perp}} \tag{I.5}$$

where $I_{||}$ is the intensity of fluorescence with the polarizers parallel and $I_{\perp}$ is the intensity of fluorescence with the polarizers perpendicular. A more important parameter the anisotropy factor, A, can also be defined which contains the contributions of all directions of polarisation and is expressed as,

$$A = \frac{I_{||} - I_{\perp}}{I_{||} + 2I_{\perp}} \; = \; \frac{3 < \cos^2\theta > -1}{2} \tag{I.6}$$

Bibliography

[1] G. E. Uhlenbeck and S. Goudsmit. Replacement of the hypothesis of unmechanical coercion by a requirement for the internal condition of every electron. *Naturwissenschaften*, 13(47):953–954, 1925.

[2] Jean-Francois Van Huele and Jared Stenson. Stern-gerlach experiments: Past, present, and future. http://www.physics.byu.edu/research/theory/SGPaper.pdf, October 2004.

[3] Robert S. Van Dyck, Paul B. Schwinberg, and Hans G. Dehmelt. New high-precision comparison of electron and positron g-factors. *Phys. Rev. Lett.*, 59:26–29, Jul 1987.

[4] Alan Carrington and Andrew D McLachlan. *Introduction to Magnetic Resonance with Applications to Chemistry and Chemical Physics*. Harper and Row, first edition, 1967.

[5] C Daul and J Weber. The electronic fine-structure of co(ii)-complexes with schiff-base ligandst. *Helvetica Chimica Acta*, 65(8):2486–2497, 1982.

[6] A. Weller, F. Nolting, and H. Staerk. A quantitative interpretation of the magnetic field effect on hyperfine-coupling-induced triplet formation from radical ion pairs. *Chemical Physics Letters*, 96(1):24–27, March 1983.

[7] Christopher T. Rodgers. *Magnetic Field Effects in Chemical Systems*. DPhil thesis, University of Oxford, 2007.

[8] Anthony R. O'Dea, Ailsa F. Curtis, Nicholas J. B. Green, Christiane R. Timmel, and P. J. Hore. Influence of dipolar interactions on radical pair recombination

reactions subject to weak magnetic fields. *Journal of Physical Chemistry Part A*, 109(5):869–873, January 2005.

[9] R. Kaptein and L. J. Oosterhoff. Chemically induced dynamic nuclear polarisation II: (relation with anomalous ESR spectra). *Chem. Phys. Lett.*, 4:195–197, 1969.

[10] Ulrich E. Steiner and Thomas Ulrich. Magnetic field effects in chemical kinetics and related phenomena. *Chemical Reviews*, 89:51–147, 1989.

[11] Brian Brocklehurst. Spin correlation in the geminate recombination of radical ions in hydrocarbons: Part 1. — theory of the magnetic field effect. *Journal of the Chemical Society, Faraday Transactions 2*, 72:1869–1884, 1976.

[12] C. R. Timmel, U. Till, B. Brocklehurst, K. A. McLauchlan, and P. J. Hore. Effects of weak magnetic fields on free radical recombination reactions. *Molecular Physics*, 95(1):71–89, 1998.

[13] Jeff M. Canfield, R. Linn Belford, Peter G. Debrunner, and Klaus Schulten. A perturbation theory treatment of oscillating magnetic fields in the radical pair mechanism. *Chemical Physics*, 182:1–18, 1994.

[14] K. M. Salikhov, Yu. N. Molin, R. Z. Sagdeev, and A. L. Buchachenko. *Spin Polarization and Magnetic Effects in Radical Reactions*, volume 22 of *Studies in Physical and Theoretical Chemistry*. Elsevier Science Publishers, Amsterdam, 1984.

[15] S. N. Batchelor, C. W. M. Kay, K. A. McLauchlan, and I. A. Shkrob. Time-resolved and modulation methods in the study of the effects of magnetic fields on the yields of free-radical reactions. *The Journal of Physical Chemistry*, 97:13250–132, 1993.

[16] Hanns Fischer. The effect of a magnetic field on the product yield of a geminate radical-pair reaction in homogeneous solution. *Chemical Physics Letters*, 100(3):255–258, September 1983.

[17] C. A. Hamilton, J. P. Hewitt, Keith A. McLauchlan, and Ulrich E. Steiner. High resolution studies of the effects of magnetic fields on chemical reactions. *Molecular Physics*, 65:423, 1988.

[18] A. von MIddendorff. Die isepiptesen russlands. *Mem. Acad. Sc.*, 1(8):1–143, 1859.

[19] S Johnsen and KJ Lohmann. The Physics and Neurobiology of Magnetoreception. *Nature Reviews Neuroscience*, 6(9):703–712, SEP 2005.

[20] Wolfgang Wiltschko and Roswitha Wiltschko. Magnetic orientation and magnetoreception in birds and other animals. *Journal of Comparative Physiology A*, 191(8):675–693, 2005.

[21] Thorsten Ritz, Salih Adem, and Klaus Schulten. A model for photoreceptor-based magnetoreception in birds. *Biophysical Journal*, 78:707–718, February 2000.

[22] W Wiltschko and R Wiltschko. Disorientation of innexperience young pigeons after trsnportation in total darkness. *Nature*, 291(5814):433–434, 1981.

[23] Robert J. Gegear, Lauren E. Foley, Amy Casselman, and Steven M. Reppert. Animal cryptochromes mediate magnetoreception by an unconventional photochemical mechanism. *Nature*, 463(7282):804–U114, 2010.

[24] Steven M. Reppert, Robert J. Gegear, and Christine Merlin. Navigational mechanisms of migrating monarch butterflies. *Trends in Neurosciences*, 33(9):399–406, 2010.

[25] KJ Lohmann and CMF Lohmann. Detection of magnetic field intensity by sea turtles. *Nature*, 380(6569):59–61, MAR 7 1996.

[26] W. Wiltschko and F. Merkel. Orientierung zugunruhiger rotkehlchen im statischen magnetfeld. *Verh. dt. zool. Ges*, 1(59):362–367, 1966.

[27] Roswitha Wiltschko and Wolfgang Wiltschko. Avian navigation: From historical to modern concepts. *Animal Behaviour*, 65(2):257 – 272, 2003.

[28] W Wiltschko and R Wiltschko. Magnetic orientation in birds. *Journal of Experimental Biology*, 199(1):29–38, JAN 1996.

[29] Wolfgang Wiltschko and Roswitha Wiltschko. Magnetic compass of european robins. *Science*, 176(4030):62–64, 1972.

[30] Wolfgang Wiltschko, Katrin Stapput, Peter Thalau, and Roswitha Wiltschko. Avian magnetic compass: Fast adjustment to intensities outside the normal functional window. *Naturwissenschaften*, 93(6):300–304, 2006.

[31] Herv Cadiou and Peter A. McNaughton. Avian magnetite-based magnetoreception: A physiologist's perspective. *Journal of The Royal Society Interface*, 2010.

[32] Murray R. W. The response of the ampullae of lorenzini of elasmobranchs to electrical stimulation. *Journal of Experimental Biology*, 39:119–128, 1962.

[33] Joseph L. Kirschvink and James L. Gould. Biogenic magnetite as a basis for magnetic field detection in animals. *BioSystems*, 13:181–201, 1981.

[34] Joseph L Kirschvink, Michael M Walker, and Carol E Diebel. Magnetite-based magnetoreception. *Current Opinion in Neurobiology*, 11:462–467, 2001.

[35] A.F. Davila, G. Fleissner, M. Winklhofer, and N. Petersen. A new model for a magnetoreceptor in homing pigeons based on interacting clusters of superparamagnetic magnetite. *Physics and Chemistry of the Earth, Parts A/B/C*, 28:647 – 652, 2003.

[36] Robert C. Beason and Peter Semm. Does the avian ophthalmic nerve carry magnetic navigational information? *The Journal of Experimental Biology*, 199:1241–1244, 1996.

[37] Manuela et al. Zapka. Visual but not Trigeminal Mediation of Magnetic Compass Information in a Migratory Bird. *NATURE*, 461(7268):1274–U108, 2009.

[38] Christoph Daniel Treiber, Marion Claudia Salzer, Johannes Riegler, Nathaniel Edelman, Cristina Sugar, Martin Breuss, Paul Pichler, Herve Cadiou, Martin Saunders, Mark Lythgoe, Jeremy Shaw, and David Anthony Keays. Clusters of Iron-Rich Cells in the Upper Beak of Pigeons are Macrophages not Magnetosensitive Neurons. *Nature*, 484(7394):367–U102, APR 19 2012.

[39] Klaus Schulten, Charles E. Swenberg, and Albert Weller. A biomagnetic sensory mechanism based on magnetic field modulated coherent electron spin motion. *Zeitschrift fuer Physikalische Chemie Neue Folge*, 111:1–5, 1978.

[40] Ilia A. Solov'yov, Henrik Mouritsen, and Klaus Schulten. Acuity of a Cryptochrome and Vision-Based Magnetoreception System in Birds. *Biophysical Journal*, 99(1):40–49, JUL 7 2010.

[41] JB Phillips and SC Borland. Magnetic compass orientation is eliminated under near-infrared light in the eastern red-spotted newt notophthalmus-viridescens. *Animal Behaviour*, 44(4):796–797, 1992.

[42] JB Phillips and SC Borland. Behavioural evidence for use of a light-dependent magnetoreception mechanism by a vertebrate. *Nature*, 359(6391):142–144, 1992.

[43] Wolfgang Wiltschko and Roswitha Wiltschko. Magnetic compass orientation in birds and its physiological basis. *Naturwissenschaften*, 89:445–452, 2002.

[44] W Wiltschko and R Wiltschko. The Effect of Yellow and Blue Light on Magnetic Compass Orientation in European Robins, Erithacus Rubecula. *Journal of Comparative Physiology A-Sensory Neural and Behavioural Physiology*, 184(3):295–299, 1999.

[45] Rachel Muheim, Johan Bäckman, and Susanne Åkesson. Magnetic compass orientation in european robins is dependent on both wavelength and intensity of light. *Journal of Experimental Biology*, 205:3845–3856, 2002.

[46] Thorsten Ritz, Peter Thalau, John B. Phillips, Roswitha Wiltschko, and Wolfgang Wiltschko. Resonance effects indicate a radical-pair mechanism for avian magnetic compass. *Nature*, 429:177–180, 2004.

[47] Peter Thalau, Thorsten Ritz, Katrin Stapput, Roswitha Wiltschko, and Wolfgang Wiltschko. Magnetic compass orientation of migratory birds in the presence of a 1.315 MHz oscillating field. *Naturwissenschaften*, 92(2):86–90, 2005.

[48] Mark Sharnoff. Esr-produced modulation of triplet phosphorescence. *Journal of Chemical Physics*, 46(8):3263–3264, April 1967.

[49] A V Koptyug and Yu A Grishin. S-band magnetron-based accessory for optical detection of esr spectra of radiation-induced radical-ion pairs. *Measurement Science and Technology*, 5(4):363, 1994.

[50] Jonathan R. Woodward, Christiane R. Timmel, Peter J. Hore, and Keith A. McLauchlan. Oscillating magnetic field effects on chemical reaction yields. *RIKEN Review*, 44:79–81, 2002.

[51] K. Stapput and R. Wiltschko. Behavioral evidence for the radical pair model of magnetoreception. *JOURNAL OF ORNITHOLOGY*, 147(5, 1):49–50, 2006.

[52] Roswitha Wiltschko, Katrin Stapput, Thorsten Ritz, Peter Thalau, and Wolfgang Wiltschko. Magnetoreception in birds: different physical processes for two types of directional responses. *HFSP Journal*, 2007.

[53] Thorsten Ritz, Peter J. Hore, Christiane R. Timmel, Christopher T. Rodgers, Katrin Stapput, Peter Thalau, Roswitha Wiltschko, and Wolfgang Wiltschko. Key features of the receptor molecule underlying the avian magnetic compass. *For submission to Nature*, 2007.

[54] Stuart A. Norman. *Magnetic Field Effects on Radical Pair Reactions.* PhD thesis, University of Oxford, 2006.

[55] Christopher J. Wedge. *Radiofrequency Magnetic Field Effects in Chemical Systems.* DPhil thesis, University of Oxford, 2009.

[56] A. V. Koptyug, V. O. Saik, O. A. Anisimov, and Yu. N. Molin. Spin-locking in concentration-narrowed od esr spectra. *Chemical Physics*, 138:173–178, 1989.

[57] S. N. Batchelor, K. A. McLauchlan, and I. A. Shkrob. Reaction yield detected magnetic resonance in exciplex systems. i. b_0 and b_1 spectra. *Molecular Physics*, 75(3):501–529, 1992.

[58] Christopher T. Rodgers. *Magnetic Field Effects in Chemical Systems.* DPhil thesis, University of Oxford, 2007.

[59] Malcolm H. Levitt. *Spin Dynamics: Basics of Nuclear Magnetic Resonance*. Wiley, 2001. Good introduction to the theory of NMR and spin chemistry. It carries on where PJH's second primer finishes.

[60] P Kukura. Oscillating magnetic field effects on rps. Part II thesis, Oxford University, June 2002.

[61] Hans Landolt and Richard Börnstein. *Landolt-Bornstein physikalisch-chemische Tabellen*. Springer-Verlag, Berlin, sixth edition, 1950.

[62] Kevin B. Henbest, Philipp Kukura, Christopher T. Rodgers, P. J. Hore, and Christiane R. Timmel. Radio frequency magnetic field effects on a radical recombination reaction: A diagnostic test for the radical pair mechanism. *Journal of the American Chemical Society*, 126(26):8102–8103, 2004.

[63] M. Hohwy, H. Bildsoe, H. J. Jakobsen, and N. C. Nielsen. Efficient spectral simulations in nmr of rotating solids. the *gamma*-compute algorithm. *Journal of Magnetic Resonance*, 136:6–14, 1999.

[64] Christiane R. Timmel. *Magnetic Field Effects on Radical Pair Reactions*. PhD thesis, Oxford University, Trinity 1998.

[65] C. J. Wedge, Christopher T. Rodgers, Stuart A. Norman, Neville Baker, Kiminori Maeda, Kevin B. Henbest, C. R. Timmel, and P. J. Hore. Radiofrequency polarization effects in low-field electron paramagnetic resonance. *Phys. Chem. Chem. Phys.*, 11:6573–6579, 2009.

[66] Laura I. Sacolick, Florian Wiesinger, Ileana Hancu, and Mika W. Vogel. B1 mapping by bloch-siegert shift. *Magnetic Resonance in Medicine*, 63(5):1315–1322, 2010.

[67] Christopher J Wedge, Jason C Lau, Kelly-Anne Ferguson, Stuart Norman, P J Hore, and Christiane Timmel. Spin-locking in low-frequency reaction yield detected magnetic resonance. *Phys. Chem. Chem. Phys.*, pages 16043–16053, 2013.

[68] Daniel R. Kattnig, Arnulf Rosspeintner, and Gunter Grampp. Magnetic field effects on exciplex-forming systems: the effect on the locally excited fluorophore and its dependence on free energy. *Phys. Chem. Chem. Phys.*, 13:3446–3460, 2011.

[69] Doyel Das, Deb Narayan Nath, Partha Pratim Parui, and Mihir Chowdhury. Magnetic field effect on pyrene-dma exciplex luminescence in non-aqueous aot reverse micelle. *Chemical Physics Letters*, 424(46):300 – 306, 2006.

[70] Grampp G., Justinek M., and Landgraf S. Magnetic field effects on the pyrene-dicyanobenzene system: Determination of electron self-exchange rates by mary spectroscopy. *Molecular Physics*, 100(8):1063–1070, 2002.

[71] Deb Narayan Nath and Mihir Chowdhury. Effect of environment on the magnetic field modulation of exciplex luminescence. *Chemical Physics Letters*, 109(1):13–17, August 1984.

[72] Keith A. McLauchlan and Steven R. Nattrass. Experimental studies of the spin-correlated radical pair in micellar and microemulsion media; MARY, RYDMR b_0 and RYDMR b_1 spectra. *Molecular Physics*, 65(6):1483–1503, 1988.

[73] Kevin B. Henbest, Kiminori Maeda, Eliana Athanassiades, P J. Hore, and Christiane R. Timmel. Measurement of magnetic field effects on radical recombination reactions using triplettriplet energy transfer. *Chemical Physics Letters*, 421:571576, 2006.

[74] M. Justinek, G. Grampp, and S. Landgraf. Determination of electron self-exchange rate constants with MARY spectroscopy: Dependence on the fluorophore. *PCCP*, 4:5550–5553, 2002.

[75] Klaus Schulten, H. Staerk, A. Weller, H.-J. Werner, and B. Nickel. Magnetic field dependence of the geminate recombination of radical ion pairs in polar solvents. *Zeitschrift für Physikalische Chemie*, 101(1–6):371–390, 1976.

[76] Kevin B. Henbest, Kiminori Maeda, P. J. Hore, Monika Joshi, Adelbert Bacher, Robert Bittl, Stefan Weber, Christiane R. Timmel, and Erik Schleicher. Mag-

netic field effect on the photoactivation reaction of escherichia coli dna photolyase. *Proceedings of the National Academy of Sciences of the United States of America*, 105:14395+, 2008.

[77] Eugene Frankevich, Anvar Zakhidov, Katsumi Yoshino, Yusei Maruyama, and Kyuya Yakushi. Photoconductivity of poly(2,5-diheptyloxy-*p*-phenylene vinylene) in the air atmosphere: Magnetic-field effect and mechanism of generation and recombination of charge carriers. *Phys. Rev. B*, 53:4498–4508, Feb 1996.

[78] Sharmistha Dutta Choudhury and Samita Basu. Magnetic field effect on n-ethylcarbazoledimethylterephthalate and n-ethylcarbazole1,4-dicyanobenzene: A comparative study focusing on steric effect. *Chemical Physics Letters*, 408(46):274 – 278, 2005.

[79] Darius Kuciauskas, Paul A. Liddell, Su Lin, Simon G. Stone, Ana L. Moore, Thomas A. Moore, and Devens Gust. Photoinduced electron transfer in carotenoporphyrin-fullerene triads: Temperature and solvent effects. *J. Phys. Chem. B*, 104(18):4307–4321, 2000.

[80] Klaus Schulten and Robert Bittl. Probing the dynamics of a polymer with paramagnetic end groups by magnetic fields. *Journal of Chemical Physics*, 84(9):5155–5161, May 1986.

[81] G. Grampp, B. Mladenova, D. Kattnig, and S. Landgraf. Esr and endor investigations of the degenerate electron exchange reactions of various viologens in solution. solvent dynamical effects. *Applied Magnetic Resonance*, 30:145–164, 2006. 10.1007/BF03166715.

[82] H. Staerk, R. Treichel, and A. Weller. Lifetime uncertainty broadening in photoinduced electron transfer. *Chemical Physics Letters*, 96(1):28–30, March 1983.

[83] I. Murov, S. L .and Carmichael and G. L. Hug. *Handbook of Photochemistry*. Marcel Dekker, Inc., second edition, 1993.

[84] JL Courtneidge and AG Davies. Hydrocarbon radical cations. *Accounts of Chemical Research*, 20(3):90–97, MAR 1987.

[85] Ffrancon Williams. *Electron Paramagnetic Resonance: Elementary Theory and Practical Applications, Second Edition (John A. Weil and James R. Bolton)*, volume 86. 2009.

[86] Hans J. Kupka. *Transitions in Molecular Systems*. Wiley, 1 edition, 2012.

[87] D Rehm and A Weller. Kinetics and mechanics of electron transfer during fluorescence quenching in acetonitrile. *Berichte Der Bunsen-Gesellschaft Fur Physikalische Chemie*, 73(8-9):834–&, 1969.

[88] D Rehm and A Weller. Kinetics of fluorescence quenching by electron and h-atom transfer. *Isreal Journal of Chemistry*, 8(2):259–&, 1970.

[89] Rudolf A. Marcus. Electron transfer reactions in chemistry: Theory and experiment (nobel lecture). *Angewandte Chemie International Edition in English*, 32(8):1111–1121, August 1993.

[90] CM PREVITALI. SOLVENT EFFECTS ON INTERMOLECULAR ELECTRON-TRANSFER PROCESSES. *PURE AND APPLIED CHEMISTRY*, 67(1):127–134, JAN 1995. 15th IUPAC Symposium on Photochemistry, PRAGUE, CZECH REPUBLIC, JUL 17-22, 1994.

[91] T Kubota, B Uno, K Kano, T Kawakita, and M Goto. Oxidation and reduction potentials and electron transfer interactions in photoexcited states. *Bulletin of the Chemical Society of Japan*, 63(2):516–519, FEB 1990.

[92] K Fukui, T Yonezawa, and H Shingu. A Molecular Theory of Reactivity in Aromatic Hydrocarbons. *J. Chem. Phys.*, 20(4):722–725, 1952.

[93] RS Mullliken. Molecular Compounds and their Spectra .2. *J. Am. Chem. Soc.*, 74(3):811–824, 1952.

[94] I. Fleming. *Molecular Orbitals and Organic Chemical Reactions, Student Edition*. Molecular Orbitals and Organic Chemical Reactions. John Wiley & Sons, 2010.

[95] SCM. Scientific computing and modelling, June 2009.

[96] Kenny Lipkowitz. Molecular mechanics. *Journal of Computational Chemistry*, 4(4):605–605, 1983.

[97] Nicholas J Turro. *Modern Molecular Photochemistry*. University Science Books, 55D Gate Five Road, Sausalito, CA 94965, 1991.

[98] Stephan M. Hubig, Rajendra Rathore, and Jay K. Kochi. Steric control of electron transfer. changeover from outer-sphere to inner-sphere mechanisms in arene/quinone redox pairs. *Journal of the American Chemical Society*, 121(4):617–626, 1999.

[99] E.V. Dolotova, I.V. Soboleva, and M.G. Kuz'min. Activation enthalpy and entropy for the decay of 9-cyanophenanthrene exciplexes. *High Energy Chemistry*, 37(4):231–240, 2003.

[100] F. Cintolesi I. Kuprov C. T. Rodgers P. A. Liddell D. Gust C. R. Timmel K. Maeda, K. B Henbest and P. J. Hore. Chemical compass model of avian magnetoreception. *Nature*, 453:387–390, May 2008.

[101] SD Choudhury and S Basu. Magnetic field effect on N-ethylcarbazole-dimethylterephthalate and N-ethylcarbazole-1,4-dicyanobenzene: A comparitive study focusing on steric effect. *CHEMICAL PHYSICS LETTERS*, 408(4-6):274–278, JUN 17 2005.

[102] Kamlesh Awasthi, Miwako Mizoguchi, Toshifumi Iimori, Takakazu Nakabayashi, and Nobuhiro Ohta. Magnetic field effect on fluorescence in a mixture of n-ethylcarbazole and dimethyl terephthalate in a polymer film in the presence of electric fields. *The Journal of Physical Chemistry A*, 112(19):4432–4436, 2008. PMID: 18426190.

[103] Hiroshi Yoshida, Yuko Nakajima, Shunsuke Kobinata, and Shiro Maeda. Determination of order parameters in liquid crystal by resonance raman method; 5cb as

probed by β-carotene. *Journal of the Physical Society of Japan*, 50(10):3525–3528, 1981.

[104] Daniel Porter, John R. Savage, Itai Cohen, Patrick Spicer, and Marco Caggioni. Temperature dependence of droplet breakup in 8cb and 5cb liquid crystals. *Phys. Rev. E*, 85:041701, Apr 2012.

[105] Wei-Shun Chang, Stephan Link, Arun Yethiraj, and Paul F. Barbara. Single molecule spectroscopy of conjugated polymer chains in an electric field-aligned liquid crystal. *The Journal of Physical Chemistry B*, 112(2):448–453, 2008. PMID: 17975912.

[106] Ying Xiang, textscLin Ziyang, textscLi Tao, textscLiang Xuxia, textscZhang Jieli, textscHuang Jin-wang, and textscJi Liang-nian. Magnetic-field-induced freedericksz transition of a homeotropical alignment liquid crystal doped with double-azo. *Japanese Journal of Applied Physics*, 38(Part 1, No. 10):6017–6018, 1999.

[107] T Ikoma, M Nakai, K Akiyama, S Tero-Kubota, and T Ishii. Direct observation of a distant ion pair generated in a photoconductive poly(N-vinylcarbazole) film with dopant. *Angewandte Chemie-international Edition*, 40(17):3234+, 2001.

[108] Tadaaki Ikoma, Toshinari Ogiwara, Yutaka Takahashi, Kimio Akiyama, Shozo Tero-Kubota, Yuka Takahashi, Tomohiro Suzuki, and Yusuke Wakikawa. Giant magnetoresistance due to electron-hole pair mechanism in poly(n-vinylcarbazole). *Synthetic Metals*, 160(34):285 – 290, 2010. ¡ce:title¿Spins in Organic Semiconductors 2009, Salt Lake City, Utah, February 4-7¡/ce:title¿ ¡ce:subtitle¿SPINOS 2009¡/ce:subtitle¿.

[109] James Lillington. Magnetic field effects on radical pair recombination in solid and liquid phase. Master's thesis, University of Oxford, 2007.

[110] Fuyuki Ito, Tadaaki Ikoma, Kimio Akiyama, Yasuhiro Kobori, and Shozo Tero-Kubota. Long-range jump versus stepwise hops: Magentic field effects on the charge-transfer fluorescence from photoconductive polymer films. *Journal of the American Chemical Society*, 125:4722–4723, 2003.

[111] Sadaharu Jo, Hitoshi Yoshikawa, Akane Fujii, and Mitsuru Takenaga. Epitaxial growth of anthracene single crystals on graphite substrate with physical vapor growth technique. *Surface Science*, 592(13):37 – 41, 2005.

[112] Tamal Sengupta and Samita Basu. Magnetic field effect on the exciplex between all-s-trans-1,4-diphenylbuta-1,3-diene and 1,4-dicyanobenzene: a comparative study with other ,-diphenyl polyenes. *Spectrochimica Acta Part A: Molecular and Biomolecular Spectroscopy*, 57(5):1103 – 1110, 2001.

[113] GP Wiederrecht. Photorefractive liquid crystals. *Annual Review of Materials Research*, 31:139–169, 2001.

[114] Nasser Safari and Farzad Bahadoran. Cytochrome p-450 model reactions: a kinetic study of epoxidation of alkenes by iron phthalocyanine. *Journal of Molecular Catalysis A: Chemical*, 171(12):115 – 121, 2001.

[115] G.Z. Li and N. Minami. Photoluminescence from fullerene-doped polyvinylcarbazole (pvk) prepared by solution casting under laser irradiation. *Chemical Physics Letters*, 331(1):26 – 30, 2000.

[116] Toshinari Ogiwara, Tadaaki Ikoma, Kimio Akiyama, and Shozo Tero-Kubota. Spin dynamics of carrier generation in a photoconductive c60-doped poly(n-vinylcarbazole) film. *Chemical Physics Letters*, 411(46):378 – 383, 2005.

[117] Tadaaki Ikoma, Kimio Akiyama, and Shozo Tero-Kubota. Carrier generation in photoconductive poly(*n*-vinylcarbazole) as revealed by multifrequency time-resolved esr. *Phys. Rev. B*, 71:195206, May 2005.

[118] Ajay Misra, Rina Dutta, Mintu Haldar, and Mihir Chowdhury. Magnetically sensitive non-polar exciplex: the perfluoronaphthaleneanthracene system. *Chemical Physics Letters*, 281(46):254 – 260, 1997.

[119] Yoshinori Asahi and Noboru Hirota. E.p.r. studies of the lowest excited triplet states of the halogen containing benzonitriles. *Molecular Physics*, 41(5):1211–1223, 1980.

[120] AR Buick, TJ Kemp, GT Neal, and TJ Stone. Electron spin resonance studies of reduction by solvated electrons in liquid amonia .i. aryl halides. *Journal of the Chemical Society A - Inorganic Physical Theoretical*, (4):666–&, 1969.

[121] E.B. Krissinel and S.I. Mackarchuck. Determination of the distance-dependent electron transfer rate constant employing the kinetics of luminescence quenching in solids. *Chemical Physics*, 208(2):259 – 266, 1996.

[122] Duane E. Bartak, Kent J. Houser, Bruce C. Rudy, and M. Dale Hawley. Electrochemical studies of the formation and decomposition of halogenated benzonitrile anion radicals. *Journal of the American Chemical Society*, 94(21):7526–7530, 1972.

[123] R. C. Johnson and R. E. Merrifield. Effects of magnetic fields on the mutual annihilation of triplet excitons in anthracene crystals. *Phys. Rev. B*, 1:896–902, Jan 1970.

[124] R.E Merrifield. Theory of Magnetic Field Effects on Mutual Annihilation of Triplet Excitons. . *Journal of Chemical Physics*, 48(9):4318–&, 1968.

[125] H Sternlicht and HM McConnell. Paramagnetic Excitons in Molecular Crystals. *Journal of Chemical Physics*, 35(5):1793–&, 1961.

[126] Yin-Chu Chen, Zheming Wang, Mingdi Yan, and Scott A. Prahl. Fluorescence anisotropy studies of molecularly imprinted polymers. *Luminescence*, 21(1):7–14, 2006.

[127] B. van Dijk, R. van der Vos, and A.J. Hoff. Rota-mary, a novel way of measuring anisotropic magnetic field effects on reaction yield. *Chemical Physics Letters*, 226(12):206 – 212, 1994.

[128] A.J. Hoff, E.J. Lous, K.W. Moehl, and J.A. Dijkman. Magneto-optical absorbance difference spectroscopy. a new tool for the study of radical recombination reactions. an application to bacterial photosynthesis. *Chemical Physics Letters*, 114(1):39 – 43, 1985.

[129] Emrys W. Evans, Charlotte A. Dodson, Kiminori Maeda, Till Biskup, C. J. Wedge, and Christiane R. Timmel. Magnetic field effects in flavoproteins and related systems. *Interface Focus*, 3(5), 2013.

[130] I. C. Lewis and L. S. Singer. Electron spin resonance of radical cations produced by the oxidation of aromatic hydrocarbons with sbcl[sub 5]. *The Journal of Chemical Physics*, 43(8):2712–2727, 1965.

[131] Hans Landolt and Richard Börnstein. *Landolt-Bornstein physikalisch-chemische Tabellen*. Springer-Verlag, Berlin, sixth edition, 1950.